The Thesis Committee for Mishal Mansour Al-Johar

Certifies that this is the approved version of the following thesis:

Constraining fracture permeability by characterizing fracture surface roughness

APPROVED BY

SUPERVISING COMMITTEE:

Supervisor:

John M. Sharp, Jr.

M. Bayani Cardenas

Richard A. Ketcham

Constraining fracture permeability

by characterizing fracture surface roughness

by

Mishal Mansour Al-Johar, B.S.

Thesis

Presented to the Faculty of the Graduate School of

The University of Texas at Austin

in Partial Fulfillment

of the Requirements

for the Degree of

Master of Science in Geological Sciences

The University of Texas at Austin

December 2010

Dedication

To my parents, Denise and Mansour, and my brothers, Waleed and Yoseph

Acknowledgements

I am grateful for the support, encouragement and mentorship by my supervisor Jack Sharp. I also thank my committee members Rich Ketcham and Bayani Cardenas for reviewing my thesis and providing helpful advice.

I thank my predecessors and colleagues Don Slottke, Wendy Robertson, and Clark Thompson for paving the way for my work. I am also exceptionally grateful to my friends Travis Swanson and Kuldeep Chaudhary for valuable feedback as I completed my research. I also thank Sarah Godner for her support and encouragement.

Finally, I am grateful for the financial support of the National Science Foundation (EAR-0439806), the Geological Society of America Graduate Student Research Grant, and the Jackson School of Geosciences.

December 2010

Abstract

Constraining fracture permeability by characterizing fracture surface roughness

Mishal Mansour Al-Johar, M.S.Geo.Sci.

The University of Texas at Austin, 2010

Supervisor: John M. Sharp, Jr.

Open and connected fractures, where present, control fluid flow and dominate solute transport. Flow through fractures has major implications for water resource management, underground waste repositories, contaminant remediation, and hydrocarbon exploitation. Complex fracture morphology makes it difficult to quantify and predict flow and transport accurately. The difficulty in usefully describing the complex morphology of a real fracture from a small 3-D volume or 2-D profile sample remains unresolved. Furthermore, even when complex fracture morphology is measured across three-dimensions, accurate prediction of discharge remains difficult. High resolution x-ray computed tomography (HXRCT) data collected for over 20 rock surfaces and fractures provide a useful dataset to study fracture morphology across scales of several orders of magnitude. Samples include fractured rock of varying lithology, including sandstone, volcanic tuffs and crystalline igneous and metamorphic rocks. Results suggest that the influence of grain size on surface roughness is not readily apparent due to other competing variables such as mechanics, skins and coatings, and weathering and erosion. Flow tests of HXRCT-scanned fractures provide real discharge data allowing the hydraulic aperture to be directly measured. Scale-invariant descriptions of surface roughness can produce constrained estimates of aperture variability and possibly yield better predictions of fluid flow through fractures. Often, a distinction is not made between the apparent and true fracture apertures for rough fractures measured on a 2-D

topographic grid. I compare a variety of local aperture measurements, including the apparent aperture, two-dimensional circular tangential aperture, and three-dimensional spherical tangential aperture. The mechanical aperture, the arithmetic mean of the apparent local aperture, is always the largest aperture. The other aperture metrics vary in their ranking, but remain similar. Results suggest that it may not be necessary to differentiate between the apparent and true apertures. Rock fracture aperture is the predominant control on permeability, and surface roughness controls fracture aperture. A variety of surface roughness characterizations using statistical and fractal methods are compared. A combination of the root-mean-square roughness and the surface-to-footprint ratio are found to be the most useful descriptors of rock fracture roughness. Mated fracture surfaces are observed to have nearly identical characterizations of fracture surface roughness, suggesting that rock fractures can be sampled by using only one surface, resulting in a significantly easier sampling requirement. For mated fractures that have at least one point in contact, a maximum potential aperture can be constrained by reflecting and translating a single surface. The maximized aperture has a nearly perfect correlation with the RMS roughness of the surface. These results may allow better predictions of fracture permeability thereby providing a better understanding of subsurface fracture flow for applications to contaminant remediation and water and hydrocarbon management. Further research must address upscaling fracture morphology from hand samples to outcrops and characterizing entire fracture networks from samples of single fractures.

Table of Contents

Chapter 1: Introduction

1.1 GROUNDWATER FLOW IN FRACTURED ROCK AQUIFERS

Rock fractures are secondary permeability features of extraordinary hydrogeologic importance. In the hydrogeologic sense, fractures are any sort of crack in rock, including features such as bedding plane partings, joints, and faults. Fractures are ubiquitous and they occur in aquifers and reservoirs of all types. Fractures typically have permeabilities many orders of magnitude larger than the permeability of the surrounding matrix rock. Furthermore, in hard rock terrains, fractures are often the only viable features for both the transmission and storage of groundwater (Gustafson and Krásný, 1994). However, rock fractures may play a significant role in groundwater systems of any lithology, even where significant matrix permeability exists (Sharp, 1993).

Characterizing fractured rock aquifers and reservoirs remains difficult due to the anisotropic and heterogeneous nature of fractures (Krásný and Sharp, 2007). This includes the distribution and connectivity of fractures in a fracture network, the orientation of fractures, the length and aperture (opening size) of individual fractures, fracture skins, the physical and chemical alteration of fracture surfaces, including mineral precipitation, and the infilling of fractures with sediment. This study considers the relationship between fracture morphology and permeability at the hand sample size scale. The primary objective is to develop an understanding of fractured rock aquifers from hand samples of natural rock fractures and the characterization of fracture morphology including aperture and surface roughness. Applying laboratory results to field studies requires fundamentally understanding how fracture morphology changes with scale.

The hydrogeology of fractured rock aquifers is difficult to characterize due to the discrete nature of fractures in contrast to the bulk medium properties of permeable sediments. A representative elemental volume (REV) can be found to describe the intrinsic permeability of a sandstone aquifer, but a similar analog describing permeability in a fractured rock aquifer is difficult to determine. This is due to the scale invariant

nature of fractures, including the morphology of individual fractures and the distribution of fractures in an aquifer.

1.2 PREDICTING FLOW IN FRACTURED ROCK

Some fundamental characteristics that control flow through fractures are the connectivity, length, and aperture of fractures. Fracture aperture is the length separation between the two fracture surface walls. Aperture can be described in a variety of ways, such as the global average separation across the entire fracture or an array of local apertures. The hydraulic aperture is the aperture computed using a simple parallel plate model with measured discharge and hydraulic gradient. The kinematic aperture is the maximum displacement of the fracture walls disregarding any mineral precipitation or infilling (Marrett et al., 1999). The apparent aperture is the local aperture measured at an orientation not perpendicular to the fracture plane.

The roughness of fracture surfaces is the characteristic deviation of the surface from a smooth plane and is a more intrinsic property of fractures than the aperture. When points of contact exist for the two fracture surfaces, the surface roughness can, in fact, control the fracture aperture. The roughness of fracture surfaces is an accumulation of many natural processes, starting with the primary process of fracture genesis and the breakage through or around grains of different sizes and mineralogy, the direction and path of fracture propagation, and secondary processes such as fracture skin formation, dissolution, precipitation, erosion, weathering, and sediment infilling.

Each fundamental characteristic of fractured rock aquifers and individual fractures introduces complexities to predicting flow through fractures. Beginning with the degree to which fractures are connected to one another (fracture connectivity), to the size of the fracture opening (fracture aperture) or the length of the fracture, each characteristic may change with the scale of interest. Predicting flow in fractures within aquifers requires an understanding of which fracture characteristics are most important and how fracture characteristics scale.

1.2.1 Parallel-plate model/The Cubic law

The simplest approximation used for flow through rock fractures is the parallel-plate model. The cubic law describes the volumetric discharge between two parallel plates as proportional to the "cubed" aperture. The equation for steady incompressible flow between parallel plates is one of the few closed-form solutions to the Navier-Stokes equations.

Figure 1.1 illustrates the parabolic velocity field for flow through parallel plates. Flow is in the *x*-direction, parallel to the orientation of the bounding plates, requiring $\frac{\partial}{\partial z} = 0$. The x-momentum equation is

$$0 = -\frac{\partial p}{\partial x} + \mu \frac{d^2 u}{dy^2} \tag{1.1}$$

where μ is dynamic viscosity and $\frac{\partial p}{\partial x}$ is the pressure gradient in the *x*-direction and assumed to be constant (pressure varies linearly along the *x*-axis). Integrating twice gives

$$0 = -\frac{y^2}{2}\frac{dp}{dx} + \mu u + Ay + B \tag{1.2}$$

The boundary conditions from Figure 1.1 are applied to solve for the constants of integration *A* and *B*. The velocity *u* is zero at the plates, or $u(y = 0, b) = 0$. This makes $B = 0$ and $A = \frac{b}{2}\frac{dp}{dx}$, leaving the equation for fluid velocity as

$$u = \frac{y}{2\mu}\frac{dp}{dx}(y - b) \tag{1.3}$$

Next, volumetric discharge per unit width is given by

$$Q = \int_0^b u \, dy = \int_0^b \left[\frac{y}{2\mu}\frac{dp}{dx}(y - b)\right] dy = -\frac{b^3}{12\mu}\frac{dp}{dx} \tag{1.4}$$

which shows that the volumetric discharge, *Q*, is proportional to the cube of the aperture, *b*, hence, the cubic law.

This solution provides a relatively simple and attractive approximation to calculate volumetric discharge for flow through a rock fracture. However, researchers

over the past 70 years continue to question the applicability of the parallel plate model due to its striking differences with real rock fractures (Lomize, 1951; Louis, 1969; Witherspoon et al., 1980; Brown, 1987; Zimmerman et al., 1991; Ge, 1997; Brown et al., 1998; Oron and Berkowitz, 1998; Brush and Thomson, 2003; Cardenas et al., 2007; Slottke, 2010).

1.2.2 Why is the parallel plate model not satisfactory?

Rock fracture morphology is composed of two rough surfaces set together with void space left in between them. The fracture surfaces are not flat plates nor are they always parallel. The distance between the surfaces is not constant but highly variable, with a lower limit of zero at points where the surfaces are in contact. The application of the parallel-plate model for the flow of fluids within rock fractures is problematic for many reasons. The most obvious obstacle is the difficulty in determining a suitable aperture to calculate the flow between the surfaces. Furthermore, the variable aperture throws into doubt the assumption of flow not varying in the third dimension, across the fracture. Indeed, channeling is a common observation in numerical models, laboratory experiments, and field studies of fracture flow (Brown, 1987; Brown et al., 1998; Auradou, 2006). And lastly, even if the fracture surfaces were parallel to each other, the flow path would still be tortuous as it follows the fracture's roughness, another phenomenon not addressed by the parallel plate model. Figure 1.2 illustrates examples of a real fracture profile measured from high-resolution x-ray computed tomography (HRXCT) data.

The complex morphology of rock fractures is the dominant control on fracture permeability and fracture flow and solute transport. Rock fracture morphology is a product of many competing factors including the fracture's mechanical genesis, fracture skins (secondary alterations, coatings, mineral precipitation, varnishes, and weathering) and secondary mechanics such as the effects of shear displacement and normal compression.

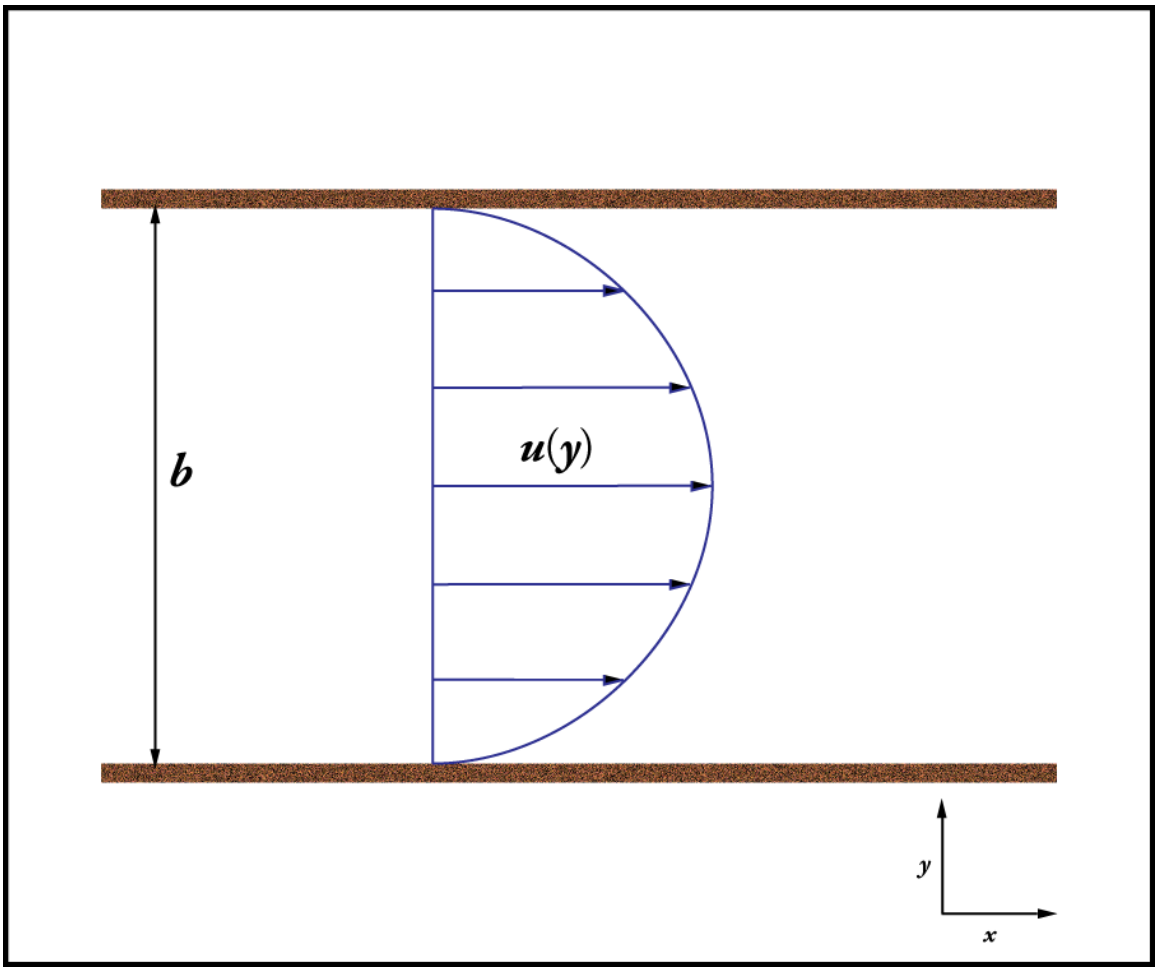

Figure 1.1 Parabolic velocity profile for Navier-Stokes flow between parallel plates, often used as an idealized model for flow in rock fractures. The aperture is *b*, and *u* is the velocity of the fluid. Discharge can be calculated using the cubic law equation.

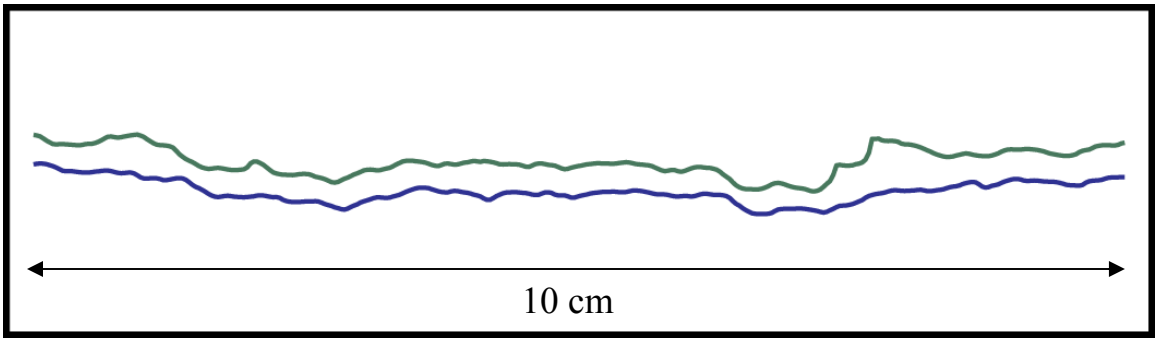

Figure 1.2 Profile of granite rock fracture GRV from HRXCT data. The surfaces are very rough and are similar but not completely identical. Furthermore, roughness also continues in the third dimension as this is only a fracture profile. The aperture varies along the profile, making it difficult to pick a single value for the cubic law. Furthermore, even if the aperture was constant (the surfaces were completely identical), the rough surfaces create a tortuous flow path. Fracture sample collected by Thompson (2005).

1.3 DIFFERENT KINDS OF APERTURE

Fracture aperture is a parameter of paramount importance to the prediction of fluid flow through fractures. Simply stated, aperture is the length-distance between the two surfaces of a fracture. For a fracture composed of smooth, parallel plates, the aperture is a constant. However, for rough and non-parallel natural rock fractures, aperture varies continuously from point to point throughout the fracture. The variability of fracture aperture presents a significant problem when attempting to characterize fractures in the field.

Many different definitions exist to describe the aperture of rock fractures. The mechanical aperture is defined as the average measured length-distance between the two surfaces. The kinematic aperture is used to describe the maximum 'paleo-mechanical aperture' of veins, fractures which may have been filled in by secondary mineralization. Both the mechanical and kinematic aperture will vary at any point throughout the fracture.

The hydraulic aperture is found by applying the parallel plate model to flow through a fracture. Unlike the mechanical or kinematic apertures, the hydraulic aperture is not directly measured. Rather, the hydraulic aperture is indirectly determined by measuring the hydraulic gradient and volume discharge for laminar flow through the fracture and using the cubic law (equation 1) to determine the fracture aperture. While the hydraulic gradient and volume discharge can easily be measured in a laboratory setting, the hydraulic aperture can also be measured in the field by using pump test data to find the aquifer's transmissivity.

Besides the flow of fluids, hydrogeologists are also interested in the transport of solutes within an aquifer. Like the hydraulic aperture, the transport aperture is calculated from experimental data applied to a conceptual model. McKay et al. (1993) perform experimental tracer tests on a weathered and fractured shale outcrop and calculate hydraulic and transport apertures within a factor of 3. They calculate the transport aperture by using a combined matrix diffusion-discrete fracture model.

1.4 CHARACTERIZING SURFACE ROUGHNESS AS A METHOD TO CONSTRAINING THE HYDRAULIC APERTURE

When fracture surfaces have points of contact, the void space between the surfaces (aperture) is primarily a function of the roughness of the surfaces. When fracture surfaces are not in contact, the variability of the fracture aperture is controlled by the roughness of the surfaces but the mean aperture is controlled by a global displacement between the surfaces. From these simple observations, the characterization of fracture surface roughness is inferred to be necessary for the prediction of fracture aperture and permeability.

1.4.1 Do mated fracture surfaces exhibit similar roughness parameters?

Practical field sampling of a complete fracture requires at least two additional fractures to allow the sample to be taken from the field to the laboratory. Mated fracture surfaces refer to the two matching surfaces which make up a fracture. If mated fracture surfaces are observed to have identical or nearly identical roughness characteristics, sampling requirements of fractures is greatly eased. Characterization of the roughness of a single fracture surface could provide useful data for constraining fracture permeability.

1.4.2 Which roughness characterization methods and parameters are most useful?

Rough surfaces have long been of interest to engineers and scientists. Many roughness characterization methods have been developed in a wide variety of research fields. Identifying the most useful roughness characterizations for investigations of natural rock fracture permeability is important for predicting fracture permeability from fracture surfaces. Surface roughness analysis traditionally consists of statistical or fractal methods.

1.4.3 How does surface roughness scale?

Practical analysis of rock fracture morphology requires fracture analysis that can be used across length-scales of several orders of magnitude. Is it possible to characterize

an entire fractured rock aquifer from a hand-sample? By analyzing fracture surface roughness for a range of sub-divided sample sizes, the scaling behavior of roughness characteristics can be determined for rock fractures.

1.4.4 What is the relationship between surface roughness and fracture aperture?

The parallel plate model describes two perfectly flat parallel plates separated by a constant aperture. However, rock fracture surfaces are often found to have at least several points of contact. If the fracture surfaces are in contact, then the void space between rock fracture surfaces is defined largely by the accumulation of the surface roughness. These fracture surfaces are referred to as 'mated fracture surfaces'. I hypothesize that the fracture surfaces have very similar roughness characteristics. However, this does not mean that the fracture surfaces are exactly identical. If the fracture surfaces were identical, with a matching arrangement and in contact, then the void space between the fracture would not exist. Considering this observation, constraining fracture permeability by characterizing fracture surface roughness appears to be in the realm of possibility. Figure 1.3 illustrates this hypothesis.

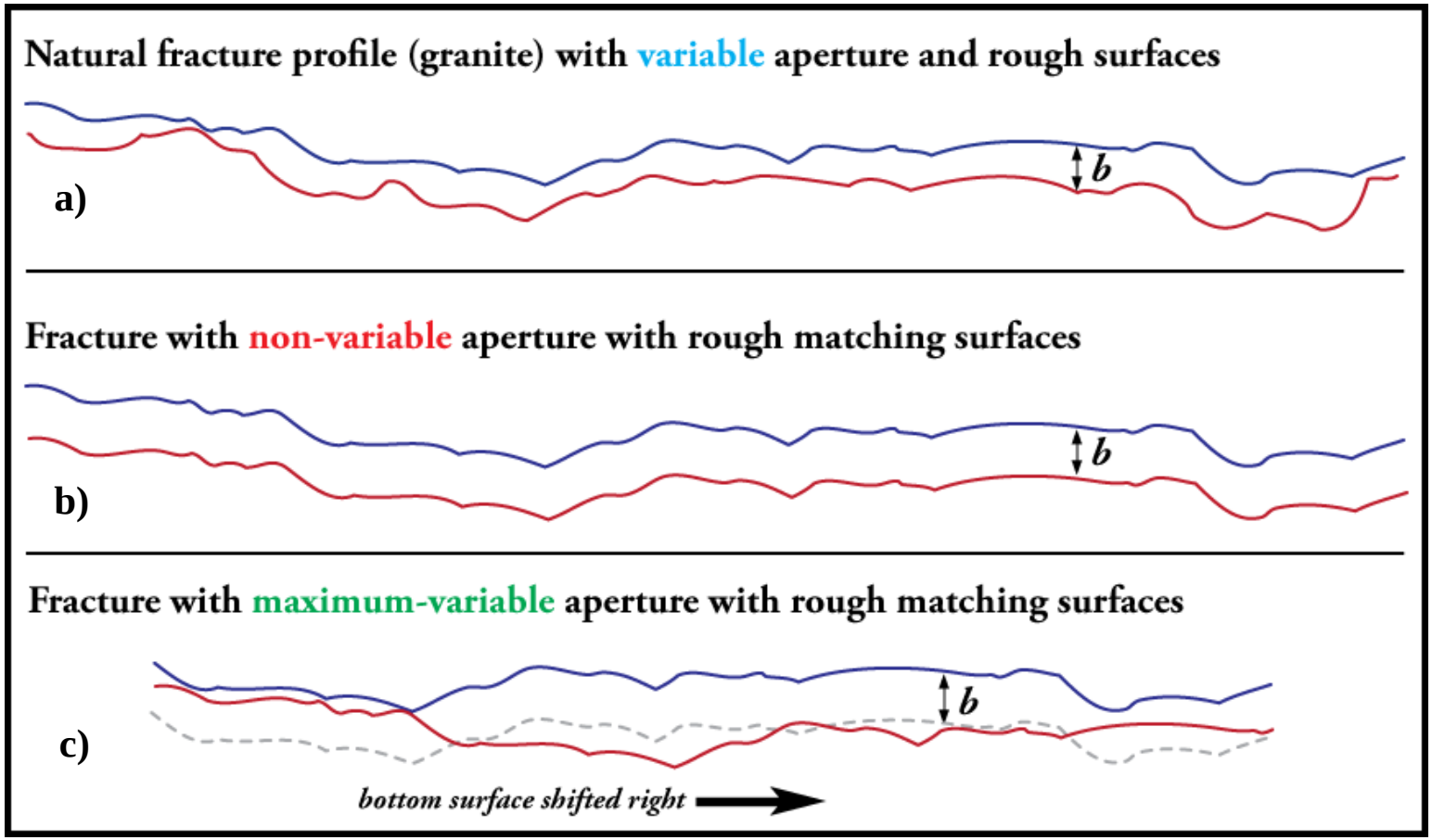

Figure 1.3 Three fracture profiles illustrating different 'mated fractures': (a) is a natural fracture profile in granite; (b) is a conceptual fracture with a constant aperture, no points of contact, and identical rough surfaces, created by copying the blue surface in fracture (a); (c) is a fracture with identical surfaces, but with one surface translated so that the aperture is at a maximum when the surfaces are in contact. If (b) had points of contact, there would be no aperture because the surfaces are identical and aligned to match.

Chapter 2: Literature Review

Here I provide an overview of the extensive literature on fracture morphology and flow through fractures over the last 60 years. Major observations from fracture flow experiments, implications from fracture flow modeling, and methods developed to characterize fracture morphology are provided.

2.1 FRACTURE MORPHOLOGY

One obstacle to predicting flow through fractures is the complexity of fracture morphology. The roughness and variation of natural rock fractures is a topic of interest to many researchers, including rock mechanicians, hydrogeologists, geochemists, and geophysicists. Fracture morphology is often considered simply as the deviation from parallel plates. However, this perspective is fundamentally flawed because open rock fractures in the subsurface would be unlikely to exist if they were parallel plates, as the typical stress field found in the subsurface would close them. In other words, the complexity of fracture morphology (the roughness and variability in fracture aperture) is the fundamental property which keeps fractures open and makes flow through fractures significant and important to subsurface fluid flow. Below I review approaches to characterizing fracture morphology and the subsequent section discusses the treatment of fracture morphology in fracture flow studies.

2.1.1 Surface Roughness

The roughness of fracture surfaces is the primary component contributing to the complexity of fracture morphology and, consequently, the phenomenon of fracture flow. Initially, fracture roughness is determined by the propagation of the fracture through rock and largely controlled by heterogeneities in the matrix (grain boundaries, structural weaknesses, mineral cleavage planes, bedding surfaces, etc) (Bouchaud, 1997).

However, in a hydrogeologic sense, fracture roughness cannot be considered simply based on primary processes from the initial fracture genesis but must include

secondary processes such as mineralization, dissolution, and weathering of fracture surfaces, processes which are part of the fracture skin (Fu et al., 1994; Fuller and Sharp, 1992; Moench, 1984; Garner et al., 2007; Kreisel, 1996; Robinson et al., 1998). Fracture skins include both the fracture surface and a zone of permeability between the fracture and the rock matrix, both resulting from the secondary processes of mineralization, dissolution, and weathering of fracture surfaces (Moench, 1984). However, fracture skins are generally treated as porous media, separate from discrete fracture flow or as dual-porosity media, where fluids flow *within* the fracture skins. For solute transport, fracture skins have also been considered in terms of sorption (either increasing or decreasing retardation) (Robinson et al., 1998; Garner et al., 2007). However, this study concerns fluid flow only between the fracture surfaces.

Fluid flow through natural fractures developed through long periods of geologic time scales generally can be considered to have roughness developed by both primary and secondary processes and considering the difference simply highlights the complex diversity of processes which contribute to fracture morphology. However, when considering anthropogenically-induced fractures in hydrocarbon reservoirs, the different processes which develop fracture roughness may yield important insights which can be exploited. There is a dearth of work which directly confronts the difference between the morphology of natural rock fractures (loosely defined in hydrogeology, with justification, as any thin, planar permeability feature including joints *and* faults *and* bedding plane partings) and the morphology of artificial rock fractures created in a laboratory under controlled conditions, without the effects of secondary processes, and strictly defined by fracture mechanics theory.

The study of rough surfaces applies to a variety of fields in science and engineering. Different methods and approaches have been developed to characterize rough surfaces, but only some are applicable to natural rock fracture surfaces or surface height data from high resolution x-ray computed tomography (HRXCT). Here, two major approaches are briefly reviewed. One group of metrics, referred to as “Statistical Metrics”, describes the roughness of a surface without considering changes with scale.

The other approach, referred to as "Fractal Analysis", describes the scale invariance of surfaces. In the following chapter, specific metrics and methods implemented in this study are defined and described.

2.1.1.1 Statistical Metrics

Statistical metrics describing rough surfaces are generally taken from the field of elementary statistics. Characterizing extreme values, variability, and averages of surface height values are the major focus of this approach to roughness (Thomas, 1999). Typically, these metrics require the measured surface profile or array to be 'flattened' by removing the mean linear or planar trend. This approach is easily applied to three-dimensional treatments of surfaces (Stout, 2000). Table 2.1 is a summary of the 14 Stout surface roughness parameters. In studies specific to flow through fractured rocks, the most common parameter used has been the root-mean-square roughness (Amitrano and Schmittbuhl, 2002; Barton and de Quadros, 1997; Brown, 1995). Thompson (2005) performed statistical roughness analysis of a granite and sandstone sample and investigated the statistical stationarity of the surface samples. The subsequent study by Slottke (2010) introduced a surface-to-footprint ratio roughness parameter which is explained in detail in Chapter 3 of this study.

Table 2.1 Stout or Birmingham 14 Surface Roughness Parameters

Name	Description	Equation
Root-mean-square deviation of the surface	RMS value of surface height	$S_q = \sqrt{\frac{1}{MN}\sum_{j=1}^{N}\sum_{i=1}^{M}\lvert z^2(x_i, y_i)\rvert}$
Ten point height of the surface	Average of five highest peaks and valleys	$S_z = \frac{\sum_{i=1}^{5}\lvert z_p\rvert + \sum_{i=1}^{5}\lvert z_v\rvert}{5}$
Skewness of topography height distribution	Assymetry of surface height deviations from the mean plane	$S_{sk} = \frac{1}{MNS_q^3}\sum_{j=1}^{N}\sum_{i=1}^{M} z_{i,j}^3$
Kurtosis of topography height distribution	Peakedness or sharpness of surface height distribution	$S_{ku} = \frac{1}{MNS_q^4}\sum_{j=1}^{N}\sum_{i=1}^{M} z^4(x_i, y_j)$
Density of summits of the surface	Number of summits in a unite sampling area	$S_{ds} = \frac{number\ of\ summits}{(M-1)(N-1)\cdot\Delta x\cdot\Delta y}$
Texture aspect ratio of the surface	Identifies texture pattern	
Texture direction of the surface	Direction of surface texture relative to the *y*-axis	$S_{td} = \begin{cases} -\beta & \beta \le \frac{\pi}{2} \\ \pi - \beta & \frac{\pi}{2} < \beta \le \pi \end{cases}$
Fastest decay autocorrelation length	Length parameter that describes character of areal autocorrelation	$S_{al} = \min\left(\sqrt{\tau_x^2 + \tau_y^2}\right), \tilde{R}(\tau_x, \tau_y) \le 0.2$
Root-mean-square slope of the surface	Root mean square of the slope	$S_{\Delta q} = \sqrt{\frac{1}{(M-1)(N-1)}\sum_{j=2}^{N}\sum_{i=2}^{M}\rho_{ij}^2}$
Arithmetic mean summit curvature of the surface	Average of the curvatures of the summits	$S_{sc} = -\frac{1}{2}\cdot\frac{1}{n}\sum_{k=1}^{n}\left(\frac{\partial z^2(x,y)}{\partial x^2} + \frac{\partial z^2(x,y)}{\partial y^2}\right)$
Developed interfacial area ratio	Ratio of the area of the surface over the sampling area	$S_{dr} = \frac{A}{(M-1)(N-1)\Delta x\cdot\Delta y}$
Surface bearing area ratio	Ratio of the total contact area after truncating the surface summits	
Core fluid retention index	Ratio of the void volume of the unit sampling area to the RMS deviation at the core zone	
Valley fluid retention index	Ratio of the void volume of the unit sampling area to the RMS deviation for valleys	

2.1.1.2 Fractal Analysis

Fracture surfaces are a classic example of self-affine fractal geometry and included in the seminal work on fractals by (Mandelbrot, 1977). Many natural surfaces are fractal; their roughness increases with scale (Thomas, 1999). Brown and Scholz (1985) are the first to apply fractal geometry to the study of natural rock fracture surfaces. One popular example is of a coastline, where as the scale changes the coastline will change (more nooks and crannies will appear as the scale increases). A fractal dimension describes the size of the new geometric features that appear as the scale changes. For self-similar fractals, changing the scale of the horizontal and vertical dimensions by the same amount will produce a statistically identical geometry. For self-affine fractals (like fracture surfaces), the horizontal and vertical dimensions must be scaled by different amounts to produce an identical geometry across different scales. In Figure 2.2, Brown and Scholz (1985)'s fractal analysis of eight different rock fracture surfaces show that the RMS roughness increases as a power law with length-scale and that the power spectral density function has a strong negative power law trend (or "red-noise"), characteristic of fractal geometry.

One insightful explanation for the power-law behavior of natural rough surfaces (such as rock fractures) is given by Sayles and Thomas (1978) who invoke the Central Limit Theorem. Rough surfaces are the cumulative product of many random processes across scales. The amplitude distribution of rough samples is Gaussian, and the variance of the Gaussian height distribution (the RMS roughness) increases with length scale. When considering the roughness of natural rock fractures, it might be instinctual to consider the surface roughness as dominated by the effects of petrographic features such as grain-size or mineralogy. However, these processes are limited to a very narrow length-scale of interest. It can be inferred from the theoretical framework provided by Sayles and Thomas (1978) that the rough surface of a fracture is the cumulative product of processes across a very wide range of length-scales, producing a fractal behavior that does not approach statistical stationarity within the length-scale window of the surface.

a)

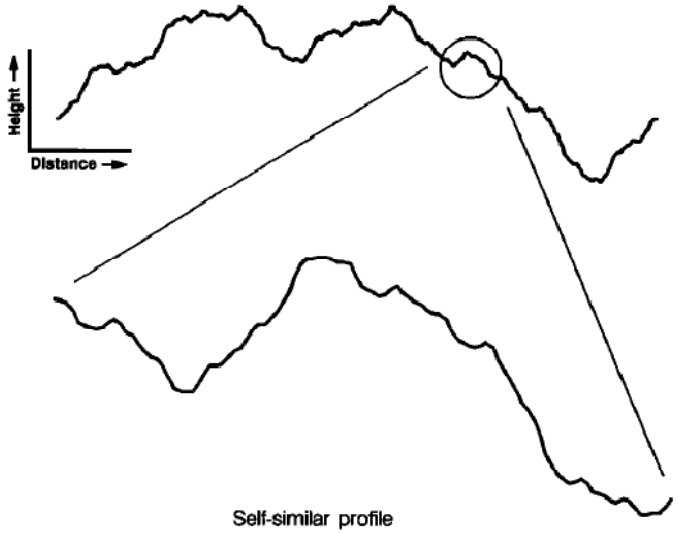

b)

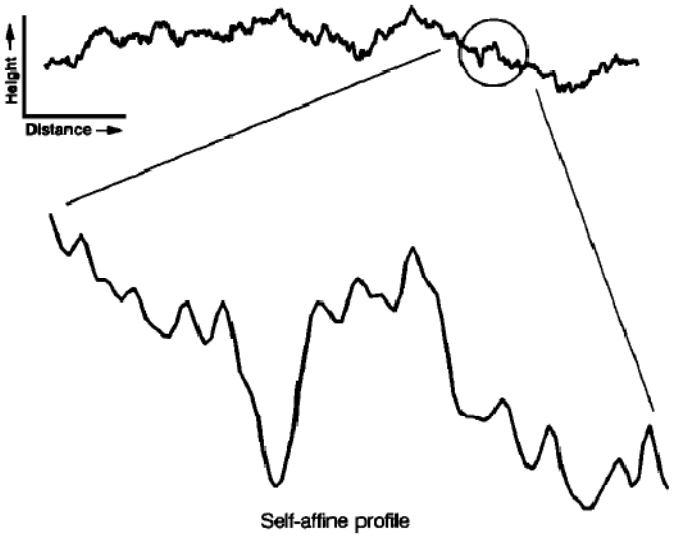

Figure 2.1 Illustration comparing self-similar and self-affine fractals where (a) is a sample of a self-similar profile that is statistically similar to the larger profile and (b) is a sample of a self-affine profile that shows different statistical and geometric properties from the larger sample. (Power and Tullis, 1991)

a) b)

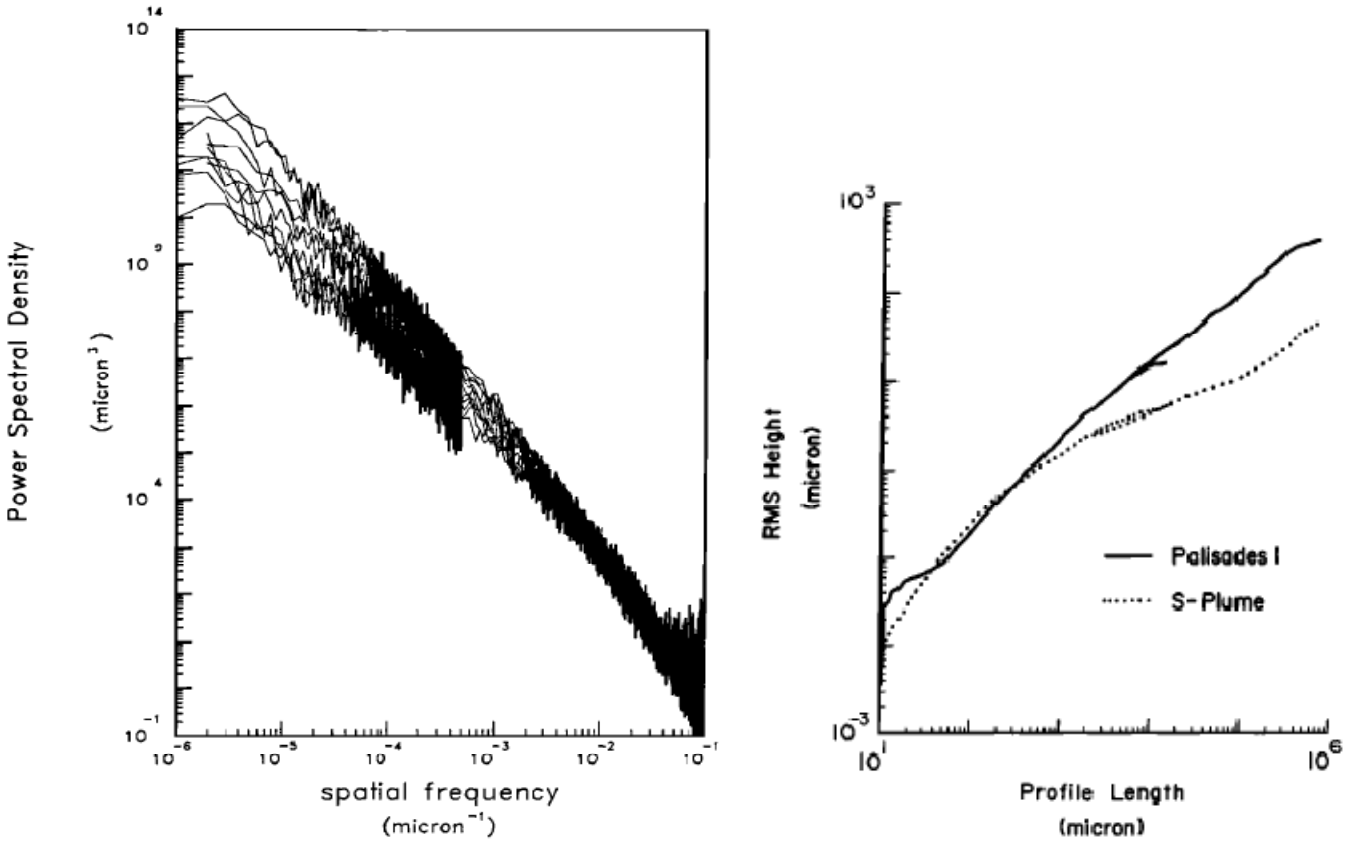

Figure 2.2 Fractal analysis of rock fracture surfaces using (a) the power spectral density and (b) the RMS roughness-length methods (Brown and Scholz, 1985). Fractal analysis shows that rock surface roughness parameters can scale as a power law within a range of length-scales. (a) is an ensemble of fracture surfaces and (b) is analysis done only for the two extreme samples in (a).

2.1.2 Fracture Aperture

The fracture aperture is the size of the opening between the two rough surfaces that bound a fracture. For a fracture made up of parallel plates, the aperture is a constant value and the discharge of flow through the fracture is proportional to the cube of the aperture. For fractures with rough surfaces, aperture measurement is not straightforward nor is the aperture constant. In many early studies of fracture flow, aperture was treated a constant value modified by a roughness parameter (Lomize, 1951; Louis, 1969; Witherspoon et al., 1980). Robertson (2006) uses modern high-precision methods to measure aperture, flow modeling, and flow experiments to confirm the utility of Lomize (1951) and Louis (1969)'s modified cubic law to predict flow across a limited range of hydraulic gradient. In other studies, aperture variability was considered only perpendicular or parallel to fracture flow (Neuzil and Tracy, 1981). More recent studies of fracture flow treated aperture as variable in all three dimensions (Brush and Thomson, 2003; Zimmerman et al., 2004; Slottke, 2010). Additionally, some studies treat flow through fractures experimentally or numerically with only one rough surface opposite a parallel plate (Zimmerman and Bodvarsson, 1996; Méheust and Schmittbuhl, 2000). With new technological developments in measuring surface topography at a fine scale, characterizing fracture aperture came under focus in the last two decades and is the focus of this section (Mourzenko et al., 1995; Ge, 1997; Oron and Berkowitz, 1998).

The roughness of fracture surfaces is the major obstacle to measuring fracture aperture. Rough surfaces introduce significant variability in aperture where the aperture can range from zero at points of contact to a maximum value determined by the magnitude of the surface roughness. However, even more importantly, rough surfaces obfuscate the actual measurement of fracture aperture due to the continuous change in fracture orientation and the non-parallel nature of fracture surfaces. This complexity of rock fracture aperture is not commonly addressed in studies of fracture flow, but has been discussed by a few authors.

Mourzenko et al. (1995) are the first to tackle this issue directly and suggest using a variably-sized conceptual sphere to measure the aperture at each point in the fracture, where the aperture is the diameter of the largest sphere which can fit between the surfaces. Ge (1997) takes a different approach and develops a governing equation for flow through fractures that addresses the aperture variability that is commonly observed in natural rock fractures, the difference in defining aperture for parallel plates and rough surfaces, and the tortuosity in flow paths through a rough fracture. Ge defines the apparent aperture as the local aperture measurement determined using a global coordinate system, while the true aperture is measured using a local coordinate system which changes at each point in the fracture. The equation to measure the true aperture at any point locally along a fracture profile is

$$b_T = 2b_A \frac{\cos\alpha_t \cos\alpha_b}{\cos\frac{\alpha_t - \alpha_b}{2}(\cos\alpha_t + \cos\alpha_b)} \tag{2.1}$$

where b_T is the true aperture, b_A is the apparent aperture, α_t is the local angle of the top fracture surface, and α_b is the local angle of the bottom surface. Ge (1997) explains that the true aperture is measured perpendicular to the local direction of fluid flow, estimated as the bisecting angle between the top and bottom surface.

Oron and Berkowitz (1998) propose a new version of the local aperture, where the true aperture is measured normal to a local coordinate system for local length segments, not at each point as in Ge (1997). Figure 2.3 presents all four types of local apertures. The medium-dashed line represents the local aperture measured on a global coordinate orientation, the small-dashed circle represents the aperture using the method of Mourzenko et al. (1995), the small-dashed line represents the aperture using the method of Ge (1997), and the large-dashed line represents the aperture using the method of Oron and Berkowitz (1998).

Types of Fracture Aperture		
Mechanical Aperture	The arithmetic mean of the measured physical distance between the fracture walls (Renshaw, 1995).	
Hydraulic Aperture	The aperture parameter computed when applying the parallel plate model to measured experimental flow through a rock fracture.	
Transport Aperture	Like the hydraulic aperture, this parameter is computed by applying experimental data to a fracture transport model, such as combining advection through a discrete fracture with diffusion through the matrix.	
Kinematic Aperture	The kinematic aperture is the maximum displacement of the fracture walls including any mineral precipitation or infilling (Marrett et al., 1999)	
Local Aperture Measurements		
Apparent Aperture	The local aperture measured by finding the difference between the height of the top and bottom surfaces measured on a coordinate system applied to the whole fracture.	
Mourzenko Aperture	The local aperture is the diameter of the circle or sphere which is tangent to the top and bottom surfaces.	
Ge Aperture	The local aperture measured perpendicular to the angle which bisects the angles of the top and bottom surfaces.	
Oron-Berkowitz Aperture	The local aperture is not measured at each point within a fracture but for fracture segments where the small-scale roughness has been filtered out. The aperture is measured perpendicular to the particular orientation of each segment.	
Mean Apertures		
Arithmetic	$b_A = \frac{1}{NM}\sum_{j=1}^{N}\sum_{i=1}^{M} b(i,j)$	The most common mean aperture and often referred to as the mechanical aperture. Typically greater than the hydraulic aperture (Slottke, 2010)
Geometric	$b_G = \sqrt[NM]{b_1 b_2 \cdots b_{NM}}$	Roughly equal to the hydraulic aperture (Slottke, 2010)
Harmonic	$b_H = \frac{NM}{\sum_{i=1}^{NM}\frac{1}{b_i}}$	Typically less than the hydraulic aperture (Slottke, 2010)

Table 2.2 Summary of fracture aperture definitions from the literature

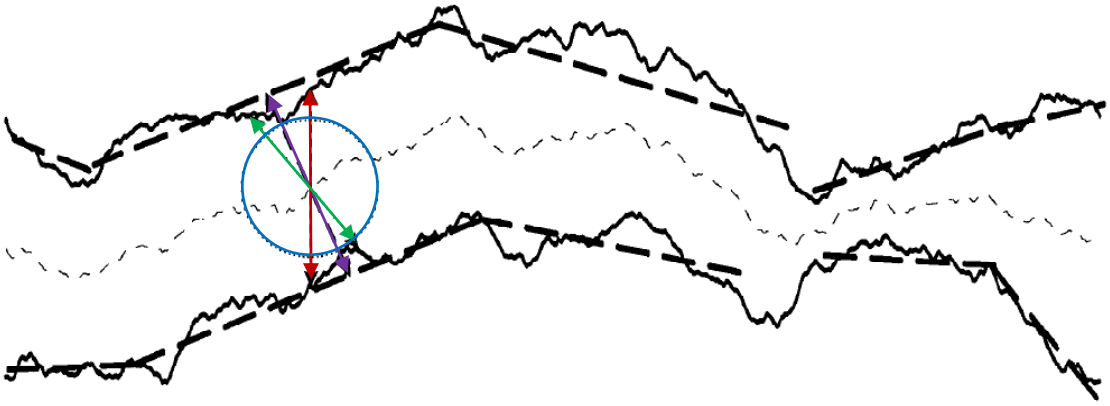

Figure 2.3 Illustration of four different methods to calculate local aperture. The apparent local aperture (red line) is calculated simply by finding the difference in surface height between the top and bottom surfaces. The Mourzenko et al. (1995) true aperture (blue circle) is measured by finding the largest diameter circle (or sphere) tangent to the top and bottom surface at each point. The Ge (1997) true aperture (green line) is measured perpendicular to the line which bisects the top and bottom surfaces. Finally, the Oron and Berkowitz (1998) true aperture (purple line) is measured similar to Ge but, rather than measuring at each point in the fracture, measure aperture only for representative segments of the fracture, disregarding small scale roughness. Figure modified from Oron and Berkowitz (1998).

Hakami and Larsson (1996) perform experimental flow tests on a natural granite fracture sampled with a drill core and measure the fracture's morphology by injecting epoxy into the fracture and performing image analysis on slices of the epoxy cast. After measuring actual flow through the fracture and characterizing the fracture geometry, they find that the mean mechanical aperture is 1.4 times larger than the hydraulic aperture. Based on aperture measurements of profiles of a single rock fracture, Hakami and Larsson (1996) suggest that a 2-D profile characterization of fracture aperture is sufficient to predict flow to a low level of accuracy. However, Slottke (2010) finds that this hypothesis has no validity based on findings from studying a suite of fractures in tuff and granite.

Chen et al. (2000) present a method to measure mean fracture aperture directly using gas volume balance and find that for 3 granite samples 48mm x 90mm in size, the mean mechanical aperture vastly overestimates the hydraulic aperture (measured in flow experiments).

Tsang and Witherspoon (1983) model the effects of normal and shear stress on fracture flow. Fractures used in the model are generated by using profiles of natural rock joint surfaces and using each profile for both the top and bottom fracture surface. They show that shear stress increases fracture flow due to the fracture surfaces becoming mismatched. Normal stress decreases fluid flow more quickly for fractures with well-matched surfaces, but less quickly if the fracture surfaces do not match.

Thompson and Brown (1991) show with numerical simulations that anisotropy of fracture surface roughness can inhibit flow when perpendicular to flow direction or enhance flow when parallel to flow direction. Anisotropy is integrated into the fracture surface generation used in Brown (1987).

Isakov et al. (2001) introduce methods to measure fracture geometry by imaging dyed water in high fidelity fracture models.

Lee and Cho (2002) investigate laminar fracture flow experimentally under normal and shear stress. Fracture geometry is measured with a laser profilometer. They find that permeability decreases exponentially with normal stress up to 5MPa and

permeability increases with shear stress until reaching a maximum value 2 orders of magnitude larger after 7-8mm of shear displacement. Lee and Cho (2002) suggest that the maximum permeability threshold is due to infilling materials from surface degradation. They also show that with cyclical shear stress, laterally displacing the fracture surfaces forward and backward, fracture permeability behaves as a hysteretic phenomenon.

Oron and Berkowitz (1998) also show that under increasing normal stress, the effective hydraulic conductivity of fractures decreases non-linearly as the contact area ratio increases. They doubt the validity of applying the Reynolds equation (the local cubic law) for flow through rock fractures due to the wide variability of aperture in natural fractures, including the high percentage of contact regions. Conditions where the assumptions required by the Reynolds equation are valid decreases rapidly as the normal stress increases.

2.2 FLOW THROUGH DISCRETE ROCK FRACTURES

The complexity of fracture morphology is the major obstacle preventing a complete understanding of flow through rock fractures. This results in two general problems: 1) correctly modeling flow through a fracture with precise and accurate measurements of fracture morphology and 2) predicting discharge through fractures based on samples or average metrics of fracture morphology. Flow channeling is another phenomenon of fracture flow that is important to contaminant transport. Flow channeling is observed numerically and experimentally and is associated with aperture variability and distribution. However, predicting the degree of channeling and location of channels in the field remains a challenge.

2.2.1 Experimental studies of fracture flow

Experimental studies of fracture flow are useful for observing fracture flow phenomena in action, such as channeling. Some studies use analogs of rock fractures,

epoxy casts of real rock fractures, or real rock fractures themselves. A summary of experimental studies and their observations follows.

Brown et al. (1998) conduct flow experiments in a transparent epoxy replica of a natural rock fracture to observe flow channeling and measure flow velocity. They find that flow velocities in rock fractures can vary over several orders of magnitude and observe the maximum flow velocity to be 5 times higher than the mean velocity for a fracture size of 12 x 7.8 cm.

Nicholl et al. (1999) use three analog fractures to test the validity of the Reynolds equation for describing flow in rock fractures. The analog fractures consist of one pair of smooth glass plates, one pair of textured glass plates, and one pair consisting of one textured and one smooth glass plate. Explanation of the suitability of the analog fractures constructed to understanding flow through natural rock fractures is not provided. The local aperture used in this study is the apparent aperture, measured as the difference between the top and bottom surface height values.

Méheust and Schmittbuhl (2000) study flow experimentally and numerically with an artificially created granite fracture 100 cm^2 in size. The experimental setup consists of a single rock fracture surface and a plexiglass plate. The rock fracture surface was imaged with a mechanical profilometer. In the flow experiments, the fluid consisted of a glycerol water mixture to insure laminar flow. They conduct flow experiments in two different perpendicular directions. In one direction, the hydraulic aperture is about 85% of the mechanical aperture, while in a perpendicular orientation the hydraulic aperture is roughly 105% of the mechanical aperture.

2.2.2 The parallel plate model and the cubic law

Flow through rough rock fractures has been a subject of interest for over half a century. The most common approach involves modifying the solution for flow through parallel plates derived from the Navier-Stokes Equations by including some roughness factor that takes into account aperture variability. This approach requires some estimate of the average aperture within the fracture.

Witherspoon et al. (1980) perform experimental studies of laminar flow through artificially created rock fractures and investigate the validity of the cubic law. Aperture is determined indirectly by measuring the discharge, gradient, length, and width. Witherspoon et al. introduce normal loading to the experimental setup, decreasing the mean aperture from 250 to 4 μm. Discharge and gradient are observed to be proportional throughout the range of experimental conditions, confirming laminar flow. Witherspoon et al. (1980) observe an apparent decrease in discharge due to the deviation of the rock fracture from the parallel plate model and conclude with a modified form of the cubic law

$$Q = \frac{1}{f}\frac{\rho g b^3}{12\mu}\frac{\Delta h}{L}w \tag{2.2}$$

where f is a modifier ranging from 1.04 to 1.65. An illustration from Witherspoon et al. (1980) is included in Figure 2.4 showing the difference between the morphology of open and "closed" (described as "mated" elsewhere in this text) fractures.

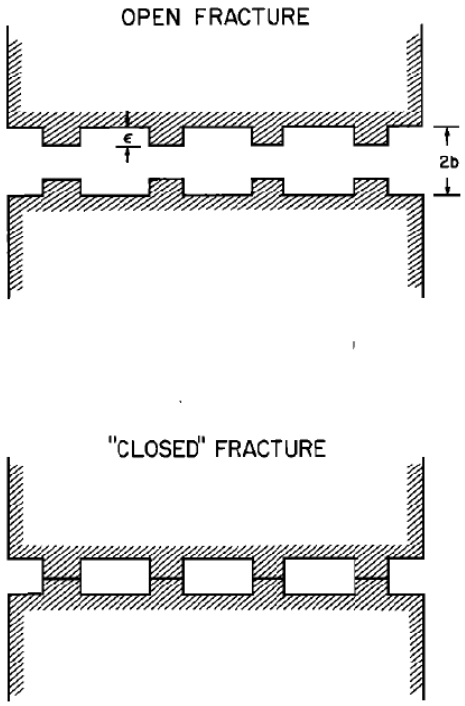

Figure 2.4 Illustration comparing an open fracture where the surfaces have no points of contact and a closed (or mated) fracture with points of contact (Witherspoon et al., 1980)

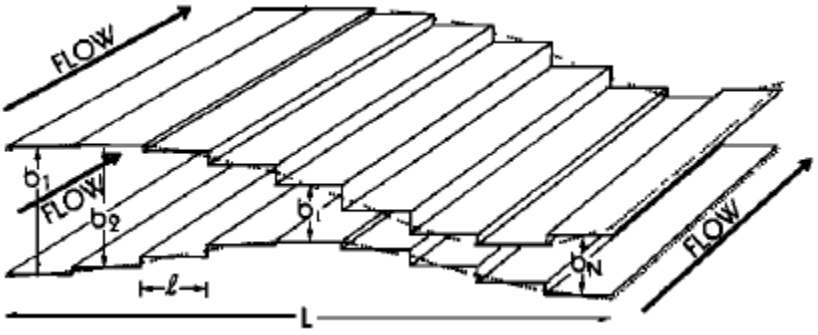

Figure 2.5 Simple early conceptual model for cubic law modified with normalized aperture frequency distribution, only considering aperture variation parallel to the flow path (Neuzil and Tracy, 1981).

Neuzil and Tracy (1981) very clearly identify the major problems of applying the parallel plate model to flow through rock fractures as the fracture's rough surfaces and variable aperture. They present a model of a fracture made up of parallel plates with apertures varying perpendicular to the flow direction and produce a modified cubic law with a log-normal aperture frequency distribution. The conceptual model used to derive the Neuzil-Tracy cubic law is presented in Figure 2.5.

Glover et al. (1998) perform numerical analysis on synthetic fractures generated from natural fracture profiles. They find that predicted transmissivity from the cubic law using the synthetic fractures overestimated measured transmissivity at the field scale by a factor of 2, but Reynolds equation transmissivity better matched measured field transmissivity. They define fracture transmissivity as

$$T = \frac{\rho g b^3}{12\mu} \tag{2.3}$$

where b represents either the geometric mean aperture, b_G, for the cubic law calculations or the aperture array, b_{ij}, for solving Reynolds equation. The geometric mean aperture is calculated as

$$b_G^3 = \left[\prod_{i,j=1}^{N} b_{ij}^3 \right]^{1/N^2} \tag{2.4}$$

where N is the length of one dimension of the aperture array. Notice that Glover et al. (1998) calculate the geometric mean of the cubed aperture. In other studies, including Slottke (2010) and this study, the geometric mean is taken before the aperture is cubed. This method is explained in detail in Section 3.5.

Plouraboué et al. (2000) perform experimental flow tests on artificially fractured granite and basalt with self-affine surfaces measured using mechanical profilometry to investigate deviation from the parallel plate model. They show that shear displacement of fracture surfaces increase deviations from permeability predicted by the parallel plate model.

Konzuk and Kueper (2004) evaluate recent modifications of the cubic law using experimental flow data through an artificially induced limestone fracture. Fracture morphology was measured using image analysis of an epoxy mold, similar to Hakami and Larsson (1996). Konzuk and Kueper (2004) measured the actual local aperture as tangential to a sphere (Mourzenko et al., 1995) and as the segment aperture (Oron and Berkowitz, 1998). They find that the geometric mean aperture is the only mean aperture that predicts flow to within 10% of measured flow rate. They also find that using measurements of the true aperture rather than apparent aperture increases accuracy of predicted discharge rates.

2.2.2 Reynolds equation (the local cubic law)

The second approach utilizes an equation known as Reynolds equation. Reynolds equation is taken from the study of hydrodynamic lubrication of machine ball bearings. Brown (1987) provides the first numerical treatment of flow through rock fractures using Reynolds equation. Reynolds equation is:

$$\nabla \cdot \left(\frac{\rho g b^3(x,y)}{12\mu} \nabla p \right) = 0 \tag{2.5}$$

where b(x,y) is an array of local apertures, ρ is the density of the fluid, g is gravitational acceleration, μ is dynamic viscosity, and p is the hydrodynamic fluid pressure. The volume flux is then related to pressure as

$$Q = \frac{-b^3(x,y)}{12\mu} \frac{\partial p}{\partial x} L \tag{2.6}$$

where L is the width of the fracture.

Reynolds equation is derived by assuming that the cubic law holds locally and mass is conserved. Reynolds equation is also referred to as the local cubic law in many other studies of flow through rock fractures. Brown (1987) uses fractures with surfaces generated with the same fractal dimension but different random numbers for the flow simulations and separated by a fixed distance (the fractures were not mated). The

aperture field was composed by the local mechanical aperture at each point. Brown (1987) finds that when fracture surfaces are not mated and separated by a large distance, deviation from the parallel plate model is minimal. However, as the scale of the roughness of the fracture surfaces approaches the length-scale of the fracture aperture, fracture flow as described by the Reynolds equation is much different from discharge predicted by the cubic law.

Méheust and Schmittbuhl (2003) perform numerical simulations with the Reynolds equation on randomly-generated fracture surfaces. They find that the mismatch length-scale between fracture surfaces is the most significant factor controlling flow channeling.

2.2.3 Modeling flow with the Stokes and the Navier-Stokes equations

Flow through rough fractures is described in three-dimensions using the Navier-Stokes equations. The cubic law is a solution to the Navier-Stokes equations for laminar flow between parallel plates. However, solving the Navier-Stokes equations for flow between rough fractures in three dimensions is difficult and only recently been addressed numerically. The Navier-Stokes equations can be written in steady state as

$$\rho(\nabla \mathbf{u})\mathbf{u} = \mu\nabla^2\mathbf{u} - \nabla p \tag{2.7}$$

where ρ is the density of the fluid, $\mathbf{u}$ is the velocity vector of the fluid, and p is the hydrodynamic fluid pressure. The Stokes equations are derived from the Navier-Stokes equations by ignoring the inertial forces (or assuming a laminar flow regime) and are somewhat easier to solve. The Stokes equation is

$$0 = \mu\nabla^2\mathbf{u} - \nabla p \tag{2.8}$$

Mourzenko et al. (1995) compare flow through fracture numerical results between the Stokes equations and Reynolds equation. They find that results of the Reynolds equation more closely match the Stokes equations when aperture is measured along a varying orientation (not a one-dimensional mechanical aperture). This aperture is described as the largest diameter sphere able to fit into the fracture at each point along the

fracture plane. When the apparent aperture is used, the discharge using Reynolds equation (the local cubic law) can be more than twice as large as the discharge modeled using the Stokes equations. However, when they use the true aperture measured locally, the difference between the results of the Reynolds and Stokes equations is minimal.

Zimmerman et al. (1991) investigate limitations to the Reynolds equation (the local cubic law) by comparing results to higher-order approximations to the Navier-Stokes equations for flow between sinusoidal fracture walls. Besides the requirement of laminar flow conditions (viscous forces dominating inertial forces), the Reynolds equation requires geometric conditions on the aperture. Figure 2.6 is an illustration of the two-dimensional sinusoidal fracture used in Zimmerman et al. (1991) where d_m is the mean mechanical aperture, δ is the amplitude of aperture variation and λ is the wavelength of aperture variation. For the sinusoidal fractures, the hydraulic aperture is always less than the mean mechanical aperture, an observation in agreement with Brown (1987)'s fractal-generated fractures. Zimmerman et al. (1991) conclude that, for sinusoidal fractures, the Reynolds equation is valid as long as the wavelength of aperture variation is greater than the amplitude of aperture variation, a much less restrictive condition than that given by Brown (1987). However, many natural fractures may not meet this condition.

Brush and Thomson (2003) compare 3-D Navier-Stokes, 3-D Stokes, and 2-D local cubic law (Reynold's equation) numerical flow simulations through a randomly-generated fracture with self-affine walls. For the random fracture generation, Brush and Thomson (2003) use an aperture grid measured perpendicular to the global fracture plane and also introduce a "midsurface" grid describing the local vertical position of the fracture in order to introduce effects of tortuosity and fracture undulation. In their local cubic law application, they modify the local aperture to take into account the midsurface grid (very similar to how Ge (1997) defined the 'actual' aperture). They show that for strict criteria on Reynolds number and relative roughness, the 2-D local cubic law is valid when compared to 3-D Stokes simulations.

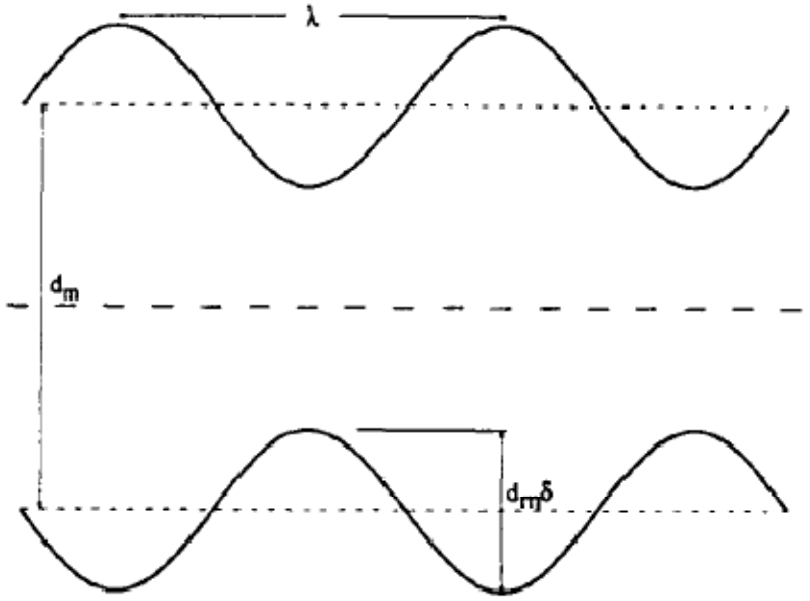

Figure 2.6 Two-dimensional sinusoidal fracture used to compare Reynolds Equation to Navier-Stokes approximations in Zimmerman et al. (1991). They find that for sinusoidal fractures, the Reynolds equation is valid as long as the wavelength of aperture variation, λ, is longer than the amplitude of aperture variation, $d_m\delta$.

Zimmerman et al. (2004) conduct experimental flow tests and high-resolution Navier-Stokes simulations on a natural sandstone fracture. They find that at Reynolds numbers above 20, flow follows a Forchheimer regime, where the hydraulic gradient is quadratic to the flow rate.

Boutt et al. (2006) considers transport of solid-phase particles (colloids) in fractures. They use a natural tuff fracture surface combined with a transparent glass plate as a fracture analog. From flow simulations using high-resolution fracture geometry, they find that colloids are trapped in low-velocity zones in the fracture flow field, on the lee side of fracture walls. These trapping zones exist due to the roughness of fracture surfaces, they do not exist for sinusoidal fractures.

Johnson et al. (2006) perform experiments and numerical flow simulations of transport in rough fracture intersections. They observe that rough intersections both increase dispersion and decrease dilution of solutes when compared to intersections of smooth parallel plate fractures.

Cardenas et al. (2007) perform two-dimensional Navier-Stokes numerical simulations through a natural fracture profile and observe turbulence eddies. Also, Cardenas et al. compare flow through the natural fracture profile with a fracture of constant aperture but equivalent to the arithmetic mean of the natural fracture aperture and find that the flow velocity through the natural fracture is slower than the equivalent parallel plate fracture.

Schmittbuhl et al. (2008) measure fracture morphology of a fresh granite fracture and model flow through the fracture. They show that long wavelengths of fracture morphology dominate aperture variability and hydraulic conductivity.

2.3 SUMMARY

Research studying flow through rock fractures has been extensive and rigorous over the past 30 years. A range of approximations and models of varying complexity have been developed for flow and transport through rock fractures. The most basic is the parallel plate model from which the cubic law is derived, where flow through a rock

fracture is predicted using a single value for fracture aperture. Refining this approach, authors tried using single value roughness factors to account for aperture variability due to roughness (Lomize, 1951; Louis, 1969; Witherspoon et al., 1980). Realizing that a single aperture value cannot be measured and applied to an entire rock fracture, and with advances in computational methods and fracture morphology measurement methods, researchers took a step back from the parallel plate model and the cubic law and modeled flow through fractures using a variable aperture field with a local cubic law (Reynolds equation) (Brown, 1987; Zimmerman et al., 1991; Mourzenko et al., 1995). With advances in measuring fracture morphology at a high resolution, other studies developed methods to characterize fracture surfaces (Brown and Scholz, 1985; Malinverno, 1990; Schmittbuhl et al., 1995; Stout, 2000; Thompson, 2005; Slottke, 2010; Robertson, 2006; Lanaro, 2000; Ketcham et al., 2010; Sharp et al., 2011). Other studies considered the possible misstep of measuring local aperture when the orientation of the fracture plane changes due to fracture roughness (Mourzenko et al., 1995; Ge, 1997; Oron and Berkowitz, 1998). Finally, with recent advances in computing, studies have investigated the validity of the assumptions required of the Reynolds equation by modeling flow through fractures with the Navier-Stokes or Stokes equations (Méheust and J. Schmittbuhl, 2000; Brush and Thomson, 2003; Robert W. Zimmerman et al., 2004; Cardenas et al., 2007; Slottke, 2010). Questions still remain with regards to which flow equations provide a "good" estimate of fracture discharge and the characterization and scaling of fracture morphology.

Chapter 3: Methodology

3.1 MEASURING THE HYDRAULIC APERTURE USING FRACTURE FLOW TESTS

Fracture permeability can be directly measured in the laboratory by performing fracture flow tests under laminar flow conditions and measuring hydraulic gradient and volumetric discharge. Under laminar flow conditions for a unit area $A = 1$, discharge, Q, is directly proportional to the hydraulic gradient, ∇h, in the relationship

$$Q \propto K \cdot \nabla h \tag{3.1}$$

where K is the constant of proportionality, the slope of the linear relationship, and described as the hydraulic conductivity.

Hydraulic conductivity is related to the properties of the fluid phase and the intrinsic permeability, k, of the porous media and described as

$$K = \frac{\rho g}{\mu} k \tag{3.2}$$

where ρ is the fluid density, g is gravitational acceleration and μ is dynamic viscosity. After accounting for the fluid properties, determining the intrinsic permeability of a fracture requires only a simple calculation.

For flow through parallel plates, the intrinsic permeability k is

$$k = \frac{b^3}{12} \tag{3.3}$$

where b is the aperture, the length-distance between the plates. The hydraulic aperture b_H is an estimation of a rock fracture's aperture determined by describing the rock fracture geometry as smooth parallel plates separated by a constant aperture.

The laboratory fracture flow apparatus has been used for fractures 10 to 2500 cm^2 in size. The experimental set-up is illustrated in Figure 3.1 and photographed in Figure 3.2. A natural rock fracture sample is collected from the field and cut with at least two opposing flat faces to be mounted to the fracture flow apparatus. The outer surface of the

rock sample is sealed with a polyurethane transparent coating. The two faces of the fracture that will not be hydraulically connected (no flow boundaries) to the flow apparatus are sealed with silicone caulk. Fracture mounting plates are glued and sealed with silicone caulk to the two hydraulically active fracture faces. Finally, the fracture is mounted to the fracture flow apparatus.

The flow apparatus consists of two reservoirs kept at a constant head. Hydraulic head is measured at the two fracture mounting plates using glass manometers. Fluid is pumped into the upper reservoir and kept at a constant head by controlling flow rate and using an overflow outlet. Discharge (volume/time) is measured from a large outlet at the lower reservoir with a digital stopwatch and a one liter graduated cylinder. Discharge is measured for flow across a range of hydraulic gradients by changing the height of the upper reservoir. Figure 3.1 is a diagram of the experimental setup.

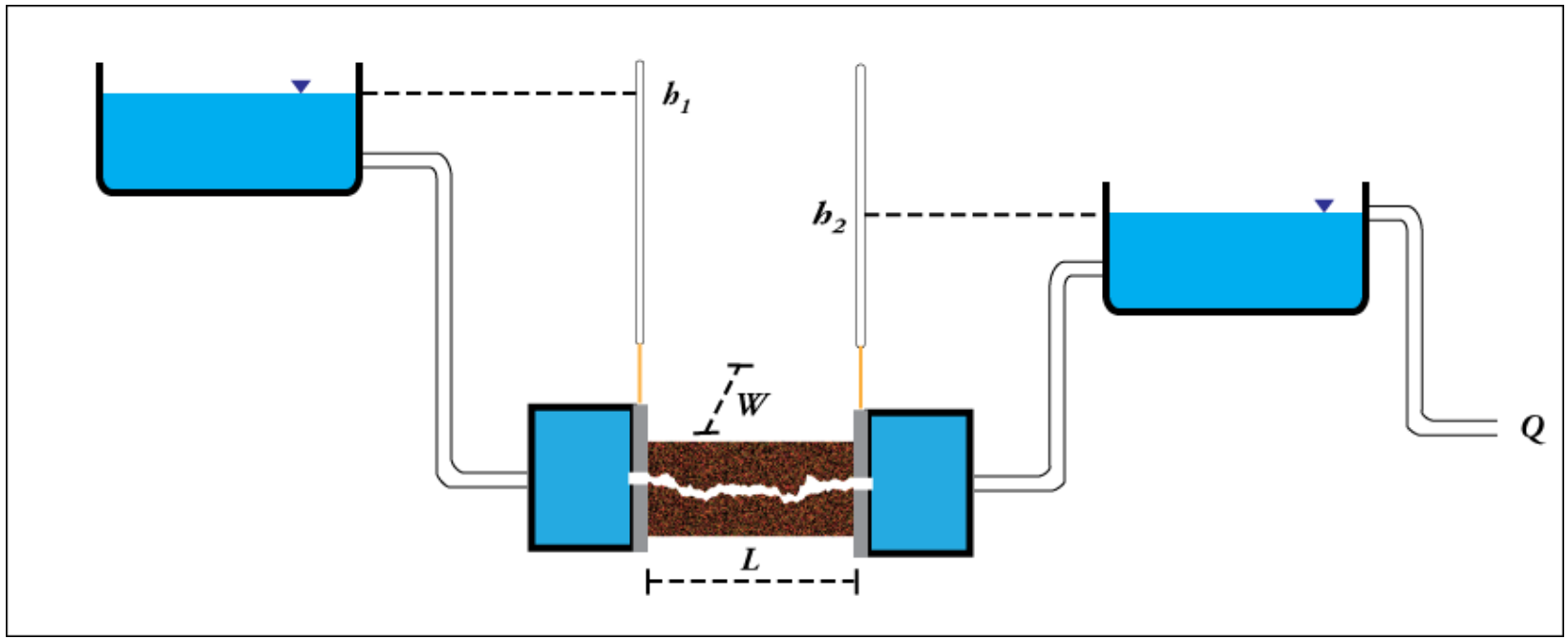

Figure 3.1 Diagram of fracture flow apparatus: h_1 is the input hydraulic head, h_2 is the output hydraulic head, W is the fracture width, L is the fracture length, and Q is the discharge. The fracture flow apparatus was designed by Thompson (2005) and modified by Slottke (2010).

3.2 MEASURING FRACTURE MORPHOLOGY USING HRXCT

Fracture morphology has been measured using mechanical and laser profilometry, optical imaging of transparent epoxy molds, and high-resolution x-ray computed tomography (HRXCT). HRXCT is a versatile and expanding field of laboratory methods to characterize rock morphology and petrography (Ketcham and Carlson, 2001; Ketcham et al., 2010). HRXCT is the only current method which allows fracture morphology to be measured while the fracture walls are mated. With other methods, the morphology of each fracture walls must be measured separately then combined as a mated fracture afterwards. Recombining the measured fracture walls with high-precision is not a simple task and introduces significant error.

X-ray computed tomography measures x-ray attenuation within the specimen as a high-resolution three-dimensional grid made up of voxels (pixels in 3-D). X-ray attenuation is controlled primarily by the material's density. Because fractures consist simply of void space within rock, resolving a fracture with HRXCT is a relatively straightforward problem of differentiating x-ray attenuation in air and x-ray attenuation in rock.

The rock fracture specimen is placed in a rotating cylinder. Figure 3.2 is a diagram of the HRXCT apparatus. The specimen is rotated as an x-ray source bombards the rock and an array of detectors measure attenuation. Specimen size is limited by the energy used by the x-ray source, the resolution required, and the size of the detector array. HRXCT data consists of grayscale 2-D image slices through the rock specimen with each pixel's brightness corresponding to the CT value. Figure 3.3 is a sample CT image slice of a sandstone rock fracture. The images are cropped to analyze only the region of interest containing the fracture.

Obtaining fracture morphology from HRXCT requires two major steps: 1) Finding and tracing the fracture through the CT volume between voxels and 2) precisely defining the fracture surface within a voxel. Two problems can complicate fracture tracing: 1) the fracture aperture approaches the resolution of the voxel spacing and 2) the

specimen contains physical obstacles such as other fractures intersecting the fracture-of-interest. For example, if the specimen contains multiple fractures which branch off of the fracture-of-interest, tracing might follow the branch and the other fracture.

Ketcham et al. (2010) review HRXCT principles and develop new methods for resolving fractures, focusing primarily on the blurring of the material across voxels. Blurring is intuitive when voxels are filled with heterogenous materials, but the majority is blurring is actually due to the HRXCT scanning itself and not the specimen. Blurring in HRXCT data can be represented by a point spread function (the spreading of a signal at a point). They review three methods for resolving fracture surfaces from HRXCT data: the Missing Attenuation method, the Peak Height method, and the Inverse Point Spread Function method.

The Missing Attenuation (MA) method assumes all x-ray attenuation is conserved in the data. The dimension of an object is measured by calibrating to standard CT values and then delineating the anomaly based on the difference between the actual CT data and the calibrated standard CT values. When calibrating to air and the local rock values, the fracture surface anomaly is delineated in the voxel by applying the relationship

$$p_i = (CT_{mat} - CT_i)/(CT_{mat} - CT_{air}) \tag{3.4}$$

where p_i is the anomaly for voxel i, CT_{mat} is the local CT value of the rock and CT_{air} is the CT value of air for the specimen (Ketcham et al., 2010).

The Peak Height (PH) method can only be applied when the width of the fracture is less than the width of the HRXCT blurring represented by the PSF. Furthermore, due to its reliance on relative calibration requiring a homogenous material, Ketcham et al. (2010) conclude it is not appropriate for rock fractures. However, Ketcham et al. develop a hybrid method combining the PH and MA methods called the Inverse Point Spread Function (IPSF) method. The IPSF method applies the PSF model for CT blurring to making a smoothing window which, combined with the rock-air-rock model of a fracture, allows missing attenuation to be measured independent of the material. However, the IPSF method is computationally intensive.

This study implements the Missing Attenuation method as used in Thompson (2005), Robertson (2006), and Slottke (2010) but with a new and more rigorous fracture tracing procedure. The new fracture tracing procedure is modified from work originally completed by Ketcham et al. (2010) and removes the need to "mask" parts of the rock as done in Slottke (2010).

Fracture tracing first requires picking the tracing path. Figure 3.4 is an illustration of a 3-D voxel grid which contains a fracture subparallel to the ***x*** and ***z*** axes. For every dimension, the tracing path contains two possible directions, forward or backward. For three dimensions, each with two directions, there are six possible tracing paths through the fracture. For the *y*-dimension, the two directions correspond to tracing one of the two fracture walls.

Using all possible fracture tracing paths is particularly important when the specimen contains multiple fractures which branch off from the specimen, or when other physical obstacles exist such as a pumice fragment within a tuff fracture. Figure 3.5 is a CT slice showing a fracture branching off of the main fracture of interest and a fracture tracing generated using only one path. Figure 3.6 is a CT image slice showing a pumice fragment in fractured tuff and a fracture tracing generated using only one path.

Once the fracture tracing is completed, the next step is resolving the fracture surface. This study implements the Missing Attenuation (MA) method. The MA method involves picking the voxel which contains the surface anomaly, and then resolving the surface at a higher precision by comparing the voxel CT value with CT values for air and rock. To make matters worse, features in CT data are often blurred across several voxels when the specimens are large in size and resolution is coarse. Furthermore, when the fracture aperture becomes smaller than the resolution of a single voxel, resolving the two separate fracture surfaces is extremely difficult. The IDL code used to generate the fracture surface height array is provided in Appendix A.

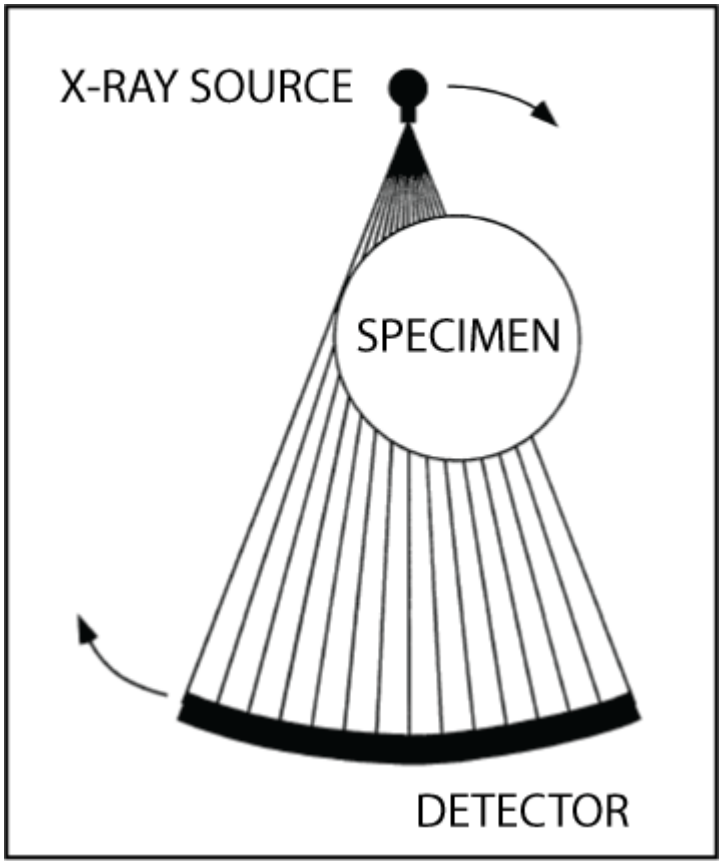

Figure 3.2 Diagram of high resolution x-ray computed tomography apparatus. The specimen is placed in a cylinder, while the x-ray source and the detector array rotate around the specimen. (Ketcham and Carlson, 2001)

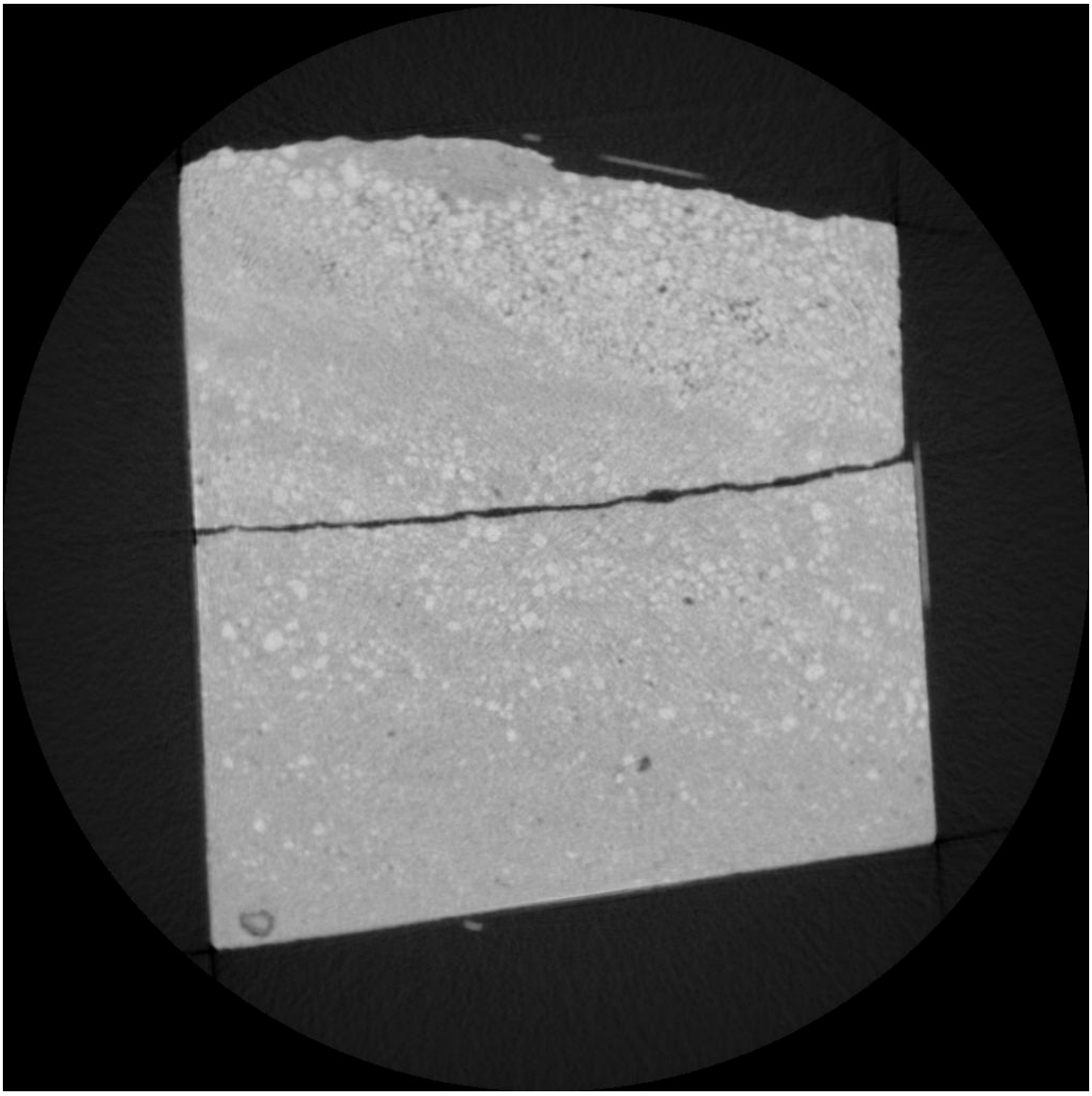

Figure 3.3 High-resolution x-ray computed tomography image slice of a natural rock fracture in Hickory Sandstone.

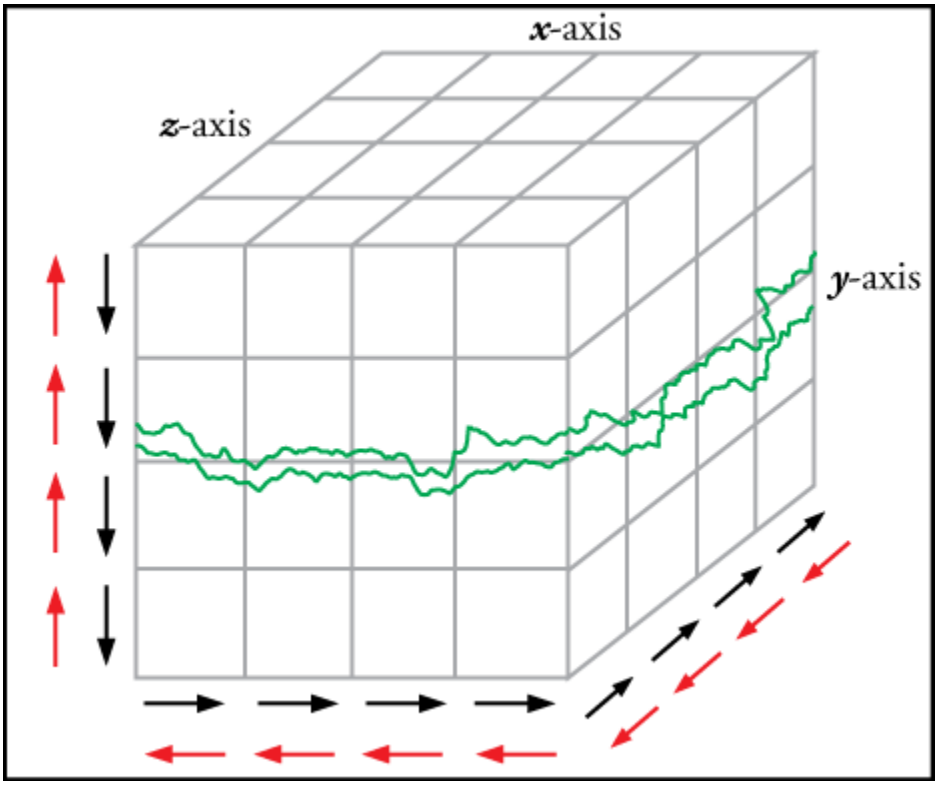

Figure 3.4 Illustration showing CT data as a 3-D grid of voxels with different directions (arrows) of fracture tracing. Each dimension has two different directions, making a total of six different paths for fracture tracing. Tracing the fracture six different times, errors from anomalies or branching fractures can be mitigated .

a)

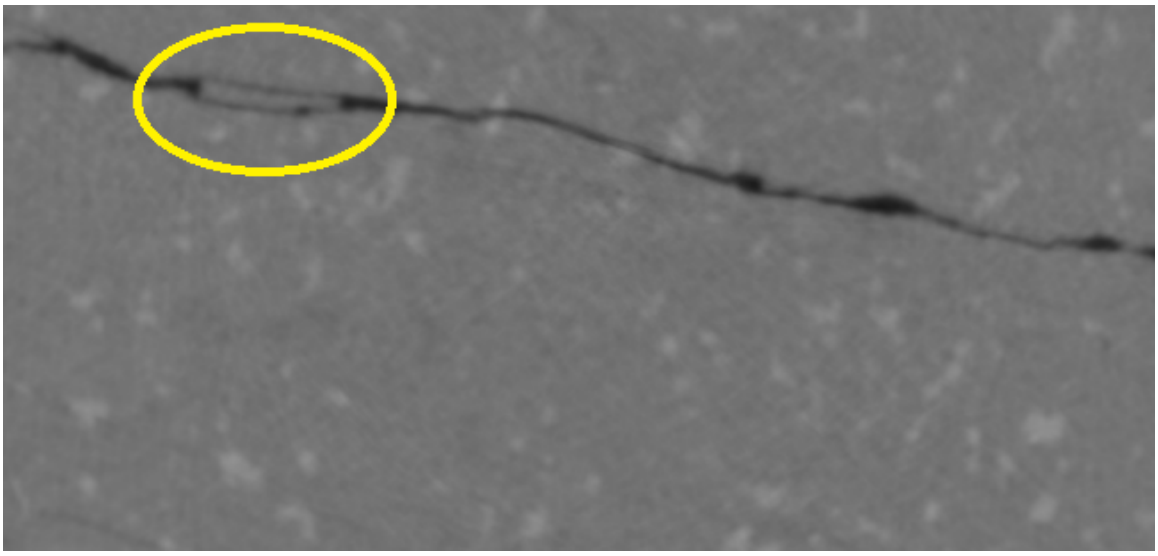

b)

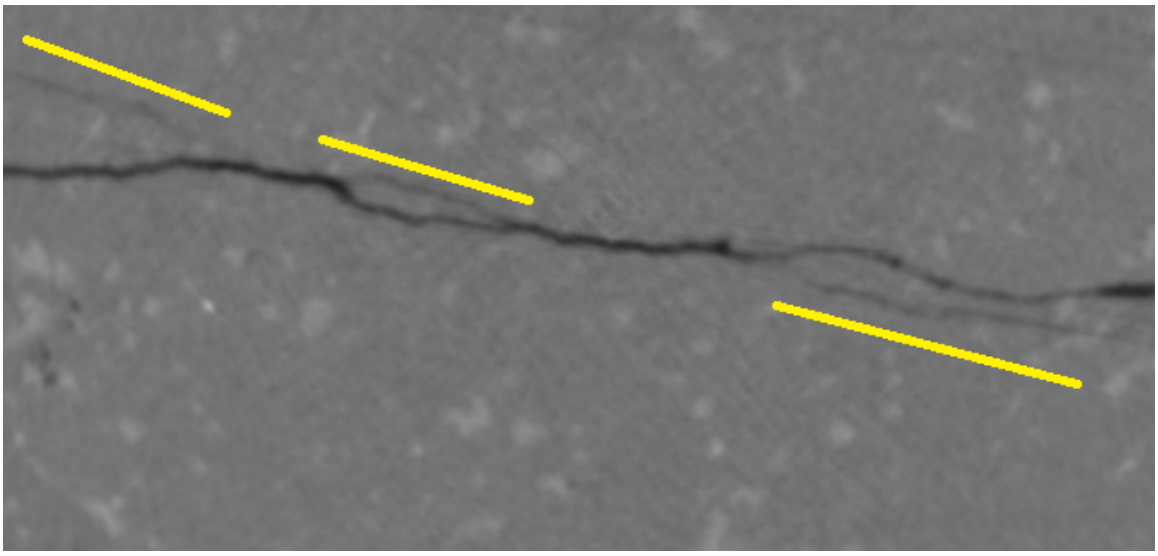

Figure 3.5 CT slices of fractured granite sample FTMGRA2 highlighting challenges in fracture resolution when other fractures intersect or branch off from the fracture of interest. (a) shows how the fracture split around a small piece of the rock, to meet back on the other side. (b) shows a second fracture intersecting the fracture of interest.

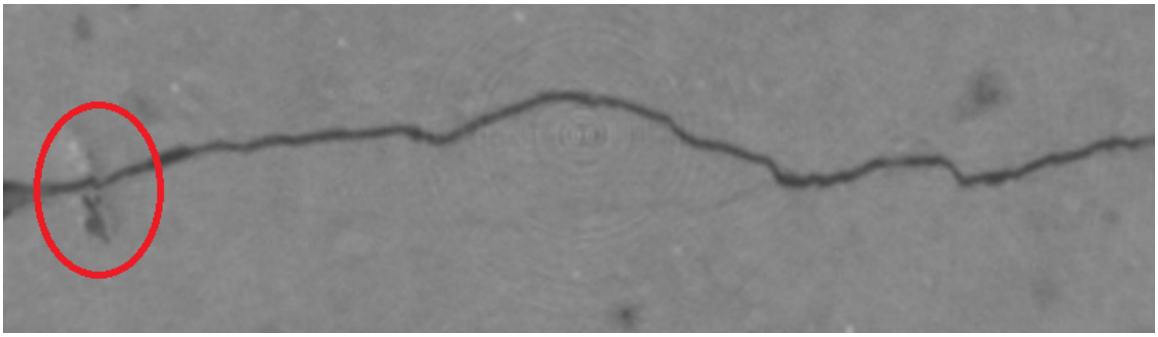

Figure 3.6 CT slice of fractured tuff CC02-2. The red circle highlights an anomaly in the matrix (a piece of pumice) which presents a challenge in resolving the morphology of the fracture-of-interest in the sample.

3.3 STATISTICAL SURFACE ROUGHNESS PARAMETERS

The standard parameters for characterizing 3-D surface roughness are the Stout or Birmingham 14 Parameters (Thomas, 1999; Stout, 2000). These 14 parameters consist of amplitude, texture, hybrid and functional parameters and are presented in Table 2.1. Not all 14 parameters are suitable for application to this study or to natural rock fractures in general because they are interested in only one particular scale size. For example, some of the Stout parameters require size be defined for summits in the surface topography. These parameters are useful for engineered surfaces manufactured at a very particular sized scale, but not for natural rock fractures that occur across a wide range of scales. However, five parameters are easy to apply to natural rock fracture CT data and are used in this study, summarized in Table 3.1.

Thompson (2005) also implements some statistical surface roughness parameters to characterize two fracture surface samples (granite and sandstone), including the RMS roughness and the arithmetic mean roughness (center-line roughness). He concludes that the utility of these statistical roughness parameters for characterizing rock fractures is questionable due to a lack of statistical stationarity.

The statistical surface roughness parameters require the planar trend of the surface to be filtered out of the data ('flattening' the surface). The MATLAB code to compute the statistical surface roughness parameters is included in Appendix B.

Table 3.1 Statistical Surface Roughness Parameters

Name	Description	Equation
Root-mean-square deviation of the surface	RMS value of surface height	$S_q = \sqrt{\frac{1}{MN}\sum_{j=1}^{N}\sum_{i=1}^{M}\lvert z^2(x_i, y_i)\rvert}$
Skewness of topography height distribution	Assymetry of surface height deviations from the mean plane	$S_{sk} = \frac{1}{MNS_q^3}\sum_{j=1}^{N}\sum_{i=1}^{M} z_{i,j}^3$
Kurtosis of topography height distribution	Peakedness or sharpness of surface height distribution	$S_{ku} = \frac{1}{MNS_q^4}\sum_{j=1}^{N}\sum_{i=1}^{M} z^4(x_i, y_j)$
Root-mean-square slope of the surface	Root mean square of the slope	$S_{\Delta q} = \sqrt{\frac{1}{(M-1)(N-1)}\sum_{j=2}^{N}\sum_{i=2}^{M}\rho_{ij}^2}$
Surface to footprint ratio	Ratio of the area of the surface over the sampling area	$S_{dr} = \frac{A}{(M-1)(N-1)\Delta x \cdot \Delta y}$

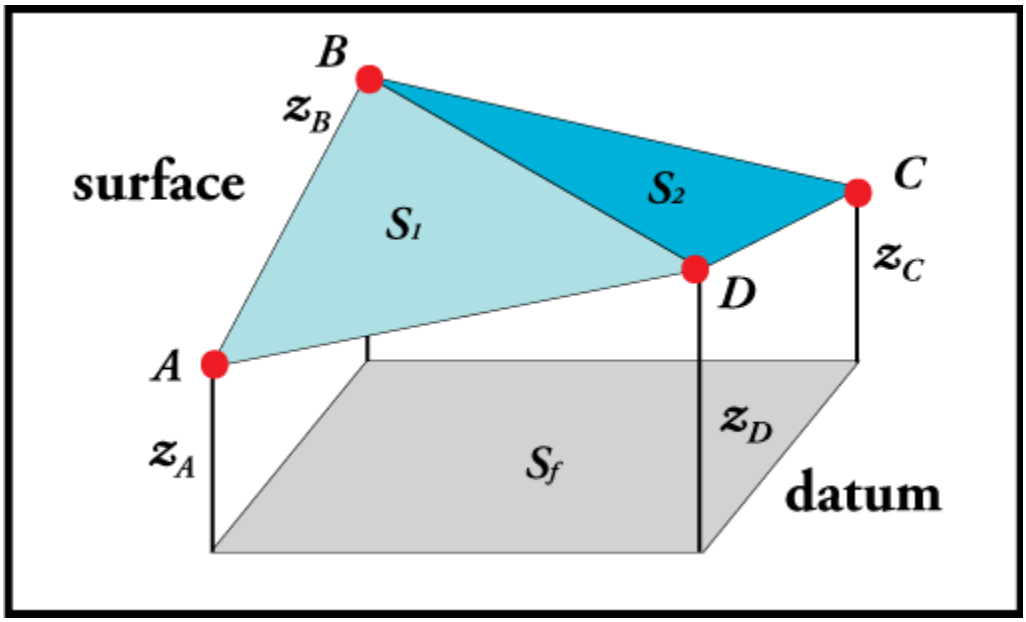

Figure 3.7 Illustration showing a gridded fracture surface such as that produced from CT data. Four points are shown: *A*, *B*, *C*, and *D* with corresponding surface height elevation *z*. The gray 'datum' is the footprint with length sides for the sampling intervals in the *x* and *y* dimensions. The blue surface can be divided into two triangles to calculate the surface to footprint ratio described in Section 3.3.1.

3.3.1 Surface to footprint ratio

The surface to footprint ratio compares the area of the surface to the area of the flat footprint beneath the surface. For a 2-D array of surface height values, the area of the surface can be determined by finding the area of the triangles between every three points, as in Figure 3.7. The major weakness of this parameter is the sensitivity to the sampling resolution of the surface data. This is discussed further in Chapter 4. The surface to footprint ratio can be determined using the equation

$$R_s = \frac{S_1 + S_2}{S_f} \tag{3.5}$$

where S_1 and S_2 are the areas of the interfacial triangles and S_f is the area of the rectangular footprint. This is implemented computationally as

$$A = \sum_{j=1}^{N-1}\sum_{i=1}^{M-1}\frac{1}{4}\left\{\left(\left[\Delta y^2 + \left(z_{i,j} - z_{i,j+1}\right)^2\right]^{1/2} + \left[\Delta y^2 + \left(z_{i+1,j+1} - z_{i+1,j}\right)^2\right]^{1/2}\right) \cdot \left(\left[\Delta x^2 + \left(z_{i,j} - z_{i+1,j}\right)^2\right]^{1/2} + \left[\Delta x^2 + \left(z_{i,j+1} - z_{i+1,j+1}\right)^2\right]^{1/2}\right)\right\} \tag{3.6}$$

$$R_s = \frac{A}{(M-1)(N-1)\Delta x \cdot \Delta y} \tag{3.7}$$

3.3.2 Root-Mean-Square (RMS) roughness

One of the most commonly used roughness parameters is the Root-Mean-Square (RMS) roughness (Stout, 2000; Brown and Scholz, 1986). The RMS roughness is the standard deviation of the surface from the mean surface plane after removing the planar trend. The RMS roughness is calculated for a measured 3-D surface grid as

$$S_q = \sqrt{\frac{1}{MN}\sum_{j=1}^{N}\sum_{i=1}^{M}\left|z^2(x_i, y_i)\right|} \tag{3.8}$$

where z is the surface height array, M is the x-dimension of the array, and N is the y-dimension of the array (Stout, 2000). Stout (2000) states that the RMS roughness is not

sensitive to the sampling intervals (the resolution of the surface height array). However, it is sensitive to the size of the sample area.

3.3.3 Surface skewness

The surface skewness describes the asymmetry of the surface height about the mean plane (or zero if the mean plane has been removed) (Stout, 2000). For a Gaussian surface, the skewness is zero. Values of skewness greater than 1 or less than -1 can indicate the existence of features such as spikes or pits, extreme outliers with otherwise flat surfaces. It is computed for a surface height array using the equation

$$S_{sk} = \frac{1}{MNS_q^3} \sum_{j=1}^{N} \sum_{i=1}^{M} z^3 (x_i, y_j) \tag{3.9}$$

with the same variables as in Equation 3.8.

3.3.4 Surface kurtosis

The surface kurtosis describes the "peakedness or sharpness" of the surface height distribution (Stout, 2000). The kurtosis of a Gaussian surface height distribution is exactly 3, while the kurtosis of sharp peaked distribution is greater than 3, and vice versa for a spread out distribution. Stout (2000) states that the surface kurtosis can be combined with the surface skewness to identify which surfaces have flat peaks but deep valleys, or vice versa. The surface kurtosis can be computed for a surface height array as

$$S_{ku} = \frac{1}{MNS_q^4} \sum_{j=1}^{N} \sum_{i=1}^{M} z^4 (x_i, y_j) \tag{3.10}$$

where the variables are the same as those used to compute the RMS roughness in Equation 3.8.

3.3.5 Root-Mean-Square slope

The root-mean-square slope parameter describes the root-mean-square slope of the surface (Stout, 2000). The slope of the surface at any point, ρ_{ij}, is calculated as

$$\rho_{ij} \approx \left[\left(\frac{z(x_i, y_j) - z(x_{i-1}, y_j)}{\Delta x} \right)^2 + \left(\frac{z(x_i, y_j) - z(x_i, y_{j-1})}{\Delta y} \right)^2 \right]^{1/2} \tag{3.11}$$

where Δx is the sampling interval along the *x*-dimension and Δy is the sampling interval along the *y*-dimension. The root-mean-square slope is calculated as

$$S_{\Delta q} = \sqrt{\frac{1}{(M-1)(N-1)} \sum_{j=2}^{N} \sum_{i=2}^{M} \rho_{ij}^2} \tag{3.12}$$

The root-mean-square slope is clearly sensitive to the sampling resolution.

3.4 FRACTAL SURFACE ROUGHNESS METHODS

Many methods have been developed to measure the fractal dimension of rough surfaces and several reviews have been completed of the limitations and accuracy of different fractal characterization methods (Kumar and Bodvarsson, 1990; Malinverno, 1990; Power and Tullis, 1991; Gallant et al., 1994; Odling, 1994; Schmittbuhl et al., 1995; Zhou and Xie, 2003). The fractal dimension, *D*, is an exponent which describes how the surface roughness changes with scale. The Hurst exponent varies linearly with the fractal dimension and is commonly used in fractal characterization methods. For 2-D profiles, the Hurst exponent, *H*, is related to the fractal dimension, *D*, by

$$D = 2 - H \tag{3.13}$$

Three different methods are used for fractal analysis in this study: the Roughness-Length Method, the First Return Probability Method, and the Power Spectral Density Method. The MATLAB code written for fractal analysis is included in Appendix B.

Malinverno (1990) introduces the roughness-length method for estimating fractal dimension. The roughness-length method calculates the RMS roughness at different

scales and calculates the Hurst exponent from the power law relationship between RMS roughness and profile length-scale. For a 2-D self-affine fractal surface profile, the RMS roughness is related to the profile length as

$$RMS(w) = Aw^H \tag{3.14}$$

where *w* is the length of the profile window, *H* is the Hurst exponent and *A* is a constant. The *RMS(w)* for a 2-D surface profile is determined using

$$RMS(w) = \frac{1}{n_w}\sum_{i=1}^{n_w}\sqrt{\frac{1}{(m_i-2)}\sum_{j\in W_i}(z(j)-\bar{z})^2} \tag{3.15}$$

where n_w is the number of profile windows of length w, m_i is the number of measured surface points within the window W_i, $z(j)$ are the residuals from the linear trend of the surface profile, and $\bar{z}$ is the mean residual. Figure 3.8 shows how the RMS roughness is calculated for a two-dimensional surface profile.

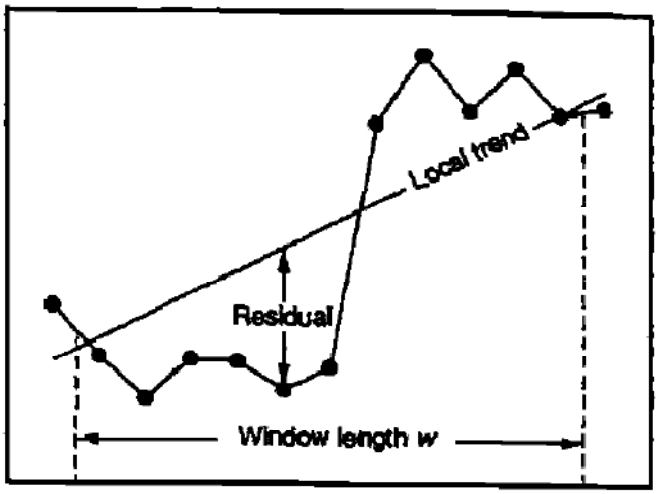

Figure 3.8 This is a diagram of a surface profile labeled with the variables required to calculate the fractal dimension with the Roughness-Length method. The residual is the surface height after the local trend is removed. The RMS roughness is calculated for the surface profile "window" of length *W*. (Malinverno, 1990)

Gallant et al. (1994) compare semi-variogram, roughness-length from Malinverno (1990), and two spectral methods for calculating the fractal dimension of rough surface profiles using two topographic profiles from a digital elevation model (DEM) at a resolution of 20m and two profiles of a soil surface at a resolution of 1mm. Gallant et al. (1994) find that the roughness-length method of Malinverno (1990) is a superior method due to it relatively easy implementation and low variability of the Hurst exponent.

Schmittbuhl et al. (1995) review six different methods to measure self-affine fractal surfaces. The box-counting and divider methods are commonly used to measure fractal dimensions of self-similar fractals, but are found to not be suitable for self-affine fractals because each dimensional axis would scale differently. Schmittbuhl et al. (1995) include the roughness-length method in their review labeled as the 'variable bandwith' method. Another set of methods reviewed by Schmittbuhl et al. (1995) are the Return Probability methods first introduced by Bouchaud et al. (1990). Figure 3.9 illustrates the difference in self-affine roughness for surface profiles of three different fractal dimensions.

The First Return Probability method for measuring the fractal dimension of a surface profile considers the horizontal distance required to intersect or 'return' to the vertical height of each x Schmittbuhl et al. (1995). The distribution of these distances found for every point in the surface profile is the First Return Probability distribution. For self-affine profiles, the First Return Probability distribution $p(d)$ with logarithmic binning scales as

$$p(d) \propto d^{H-2} \tag{3.16}$$

where d represents the distance required to return to the vertical height value for every given x in the surface profile and H is the Hurst exponent. Schmittbuhl et al. (1995) find that logarithmic binning for the probability distribution produces a higher precision for large first return distances.

The Power Spectrum method for determining the fractal dimension of self-affine fracture surfaces is introduced by Brown and Scholz (1985). The power spectrum is

computed with the Fast Fourier Transform. After applying the Fast Fourier Transform, the profile of the surface is transformed to the frequency domain and the profile is decomposed into a series of sine and cosine functions, as illustrated in Figure 3.10. The 'power' of wave-length associated with each sine and cosine function is plotted as a Power Spectral Density function. Self-affine fractals are characterized by a "red noise" power spectrum, a power law with a negative slope.

Thompson (2005) implements fractal analysis for two natural rock fractures (granite and sandstone; also included in this study). He implements Brown and Scholz (1985)'s power spectral density (PSD) method to estimate the fractal dimension. However, he concludes that the analysis has no utility for predicting flow in fractures due to the complex range of processes that affect rock fracture aperture.

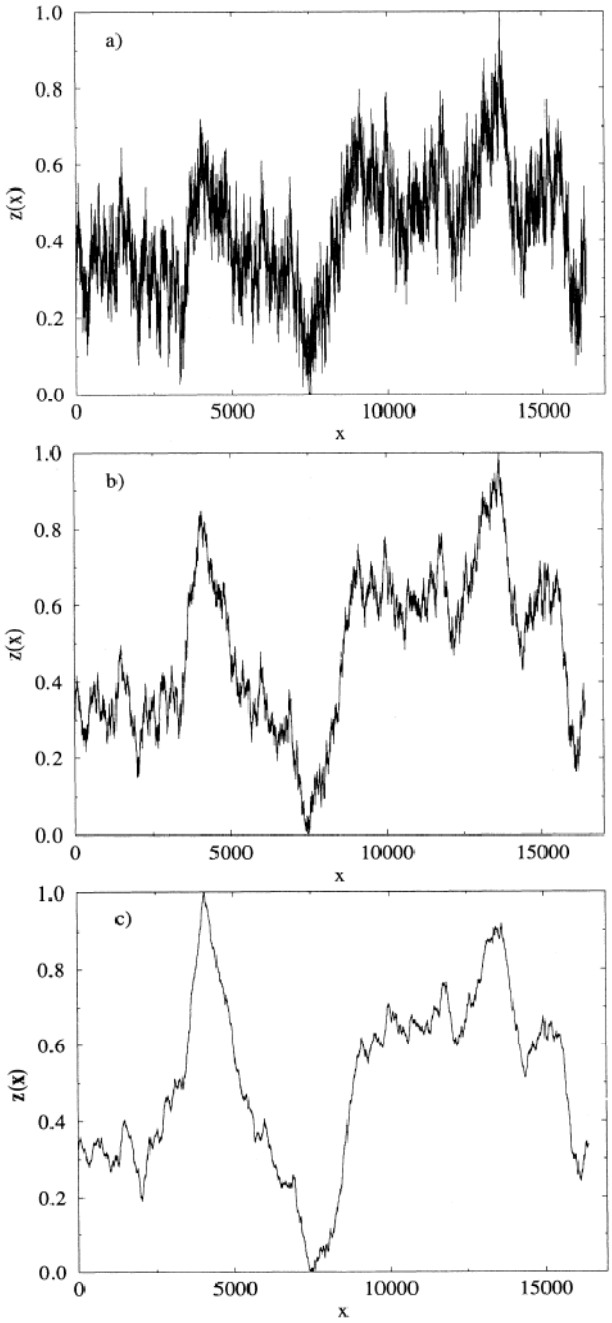

Figure 3.9 Example of three different self-affine fractal profiles with fractal dimension a) $D = 0.2$, b) $D = 0.5$, and c) $D = 0.8$ (Schmittbuhl et al., 1995)

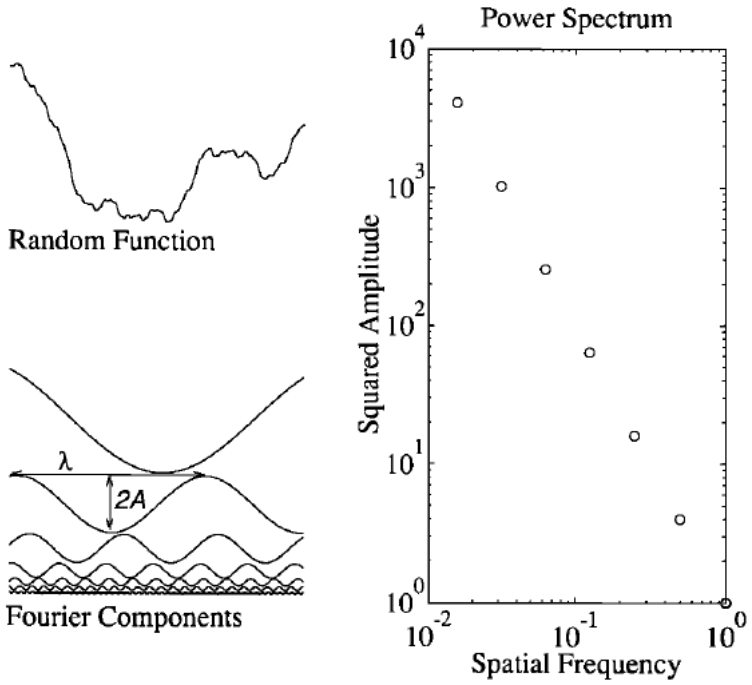

Figure 3.10 A fracture surface profile represented as some random function is decomposed into a series of Fourier sine and cosine functions. The power spectrum plots the squared amplitude against the frequency of each sine and cosine function. The spatial frequency is the inverse of the wavelength of the Fourier component. Self-affine fractal surfaces will have a negative sloping log-log power spectrum. (Brown, 1995)

3.5 DETERMINING APERTURE

Determining the fracture aperture is essential for characterizing flow through fractures. Furthermore, disagreement continues on the best standard practice for the measurement of fracture aperture. A 3-D aperture array for detailed fracture flow modeling and an average aperture that approximates the effective hydraulic aperture used in the cubic law are both useful and desired descriptions of fracture aperture. This study implements and compares different measurements of fracture aperture developed by previous researchers. The MATLAB code used for fracture aperture computation and analysis is provided in Appendix B.

3.5.1 Local aperture

Local aperture is the aperture at each point within the fracture grid. The local aperture array is calculated using the two surface grids measured from the mated fracture surfaces. A local aperture array is useful for investigating the spatial variability of fracture flow, including fluid flow rates and solute transport (dispersion, advection, and diffusion). The Reynolds equation uses the local aperture to calculate flow for the whole fracture (it is also called the local cubic law). However, calculating the local aperture is not as straightforward as one would assume, and several different methods have been introduced in the literature.

3.5.1.1 Apparent local aperture

The simplest determination of fracture aperture is a one-dimensional point-by-point measurement computing the difference between the two fracture surface grids. For rough fractures, this may be problematic when the local orientation of the fracture is not parallel to the global orientation of the surface grids. In this case, the measured aperture has been referred to as the apparent aperture (Ge, 1997). The apparent aperture is measured by finding the difference between the surface height elevations of the top and bottom surfaces at each point throughout the fracture. The surface height elevations are measured using the same coordinate system for the entire fracture.

3.5.1.2 True local aperture measurement

One approach to overcome the difficulties of measuring aperture in rough fractures is to change the orientation of the aperture measurement for every point within the fracture. Three different proposed methods for aperture measurements have been made (Ge, 1997; Oron and Berkowitz, 1998; Mourzenko et al., 1995) for fluid flow through 2-D fracture profiles.

Mourzenko et al. (1995) proposes that the aperture be measured along each point in the surface grid by finding the diameter of a circle tangent to both surface profiles. Ge (1997) proposes making a local coordinate system in the direction of average velocity, approximated by the arithmetic mean of the angle of the top and bottom surfaces. The true aperture is measured perpendicular to the local coordinate axis. Oron and Berkowitz (1998) propose ignoring small wave-length roughness when creating a local coordinate system to measure true aperture. The local aperture orientation is determined only by using the "average roughness" of the surfaces based on a calculated aspect ratio of the fracture profile.

This study implements Mourzenko et al. (1995)'s methods to determine the true aperture for 2-D fracture profiles both parallel and perpendicular to the fracture flow direction. Each of the three methods reviewed measure aperture only for a 2-D fracture profile. However, for a 3-D fracture morphology, determining the local orientation for aperture measurement requires modifying the methods developed for 2-D fracture profiles. Mourzenko et al. (1995) simply uses a sphere instead of a circle for determining the local aperture orientation for a 3-D fracture morphology.

3.5.2 Average aperture metrics

Determining a single effective aperture to estimate flow through a fracture has long been a topic of interest to hydrogeologists. The final objective is to predict the hydraulic aperture for an entire fracture from a small-scale 2-D or 3-D sample of the fracture. However, even predicting the hydraulic aperture of the fracture sample remains a difficult challenge.

Comparing the measured hydraulic aperture to different types of average apertures calculated from the local aperture array is one course of action for predicting the fracture flow rate. Three main types of averages exist: the arithmetic mean, the geometric mean, and the harmonic mean.

The arithmetic mean is the most commonly used metric to describe the average of a sample space. The arithmetic mean, b_A, for a 2-D local aperture array is calculated as

$$b_A = \frac{1}{NM}\sum_{j=1}^{N}\sum_{i=1}^{M} b(i,j) \tag{3.17}$$

where N is the number of columns in the array, M is the number of rows in the array, and $b(i,j)$ is the local aperture array. The geometric mean, b_G, for a 2-D local aperture array is calculated as

$$b_G = \sqrt[NM]{b_1 b_2 \cdots b_{NM}} \tag{3.18}$$

where the aperture array is reformed to a one-dimensional vector of length NM. Likewise, the harmonic mean for a 2-D local aperture array is calculated as

$$b_H = \frac{NM}{\sum_{i=1}^{NM}\frac{1}{b_i}} \tag{3.19}$$

One major difference between the three types of means is the sensitivity to outliers in the sample and the variability of the local aperture. The arithmetic mean is most sensitive to outliers while the harmonic mean is least sensitive to outliers. Using these three statistical averages to predict a hydraulic aperture from the local aperture array disregards any variability with regards to flow direction, assuming that aperture variability is the same in any direction.

Slottke (2010) compares the three different aperture means to experimental flow data for two natural rock fractures. He finds that the geometric mean aperture is the best predictor of the hydraulic aperture under laminar flow conditions, while the arithmetic mean aperture overpredicts discharge and the harmonic mean underpredicts discharge.

Furthermore, the mean aperture of 2-D fracture profiles varies widely and cannot predict the hydraulic aperture.

3.6 SCALING FRACTURE MORPHOLOGY PARAMETERS/MEASUREMENTS

Characterizing fracture flow in aquifers from laboratory research requires understanding how fracture flow characteristics change with scale. In this work, a scaling method is developed to study how fracture characterizations of roughness and aperture of the entire HRXCT fracture dataset changes with sub-samples of the HRXCT dataset.

Each fracture dataset includes two mated surface arrays of dimension $A \times B$. The fracture dataset is reduced to a centered, square 2-D array. This square dataset is then divided into a set of square sub-sample fractures of a range of dimension $C = 2, 4, 8, 16 \ldots 2^n$ where $C = 2^n$ is less than or equal to the shortest dimension of the original dataset. The MATLAB code used for the scaling analysis is provided in Appendix B.

3.7 MAXIMIZED APERTURE

A maximized aperture is the aperture field of a conceptual "maximum" end-member of a complete fracture generated from a single fracture surface. It assumes that the surfaces of the fracture are identical, that the mean planes of the surfaces are parallel, and that there is at least one point of contact between the surfaces. These assumptions are valid for most natural fractures observed. Most fractures at depth exist in a state of normal compressive stress and have some points of contact. Furthermore, the planar trends of mated fracture surfaces are often found to be parallel at a global scale. In the next chapter, it is demonstrated that mated fracture surfaces have nearly identical surface roughness characterizations.

The maximized aperture fracture is generated using two different methods with nearly identical results. One method involves reflecting the fracture surface across an axis parallel to the planar trend of the surface and meeting at points of contact. The other

method involves translating an identical copy of the fracture surface until the minimum surface height of the top surface is equal to the maximum surface height of the bottom surface. Figure 3.11 illustrates two maximized aperture fracture profiles generated using the reflected and translated methods. The MATLAB code written to generate the maximized aperture fracture models is provided in Appendix B.

These maximized aperture model fractures do not correspond to real fractures but, rather, are conceptual end-members which can be used to constrain predictions.

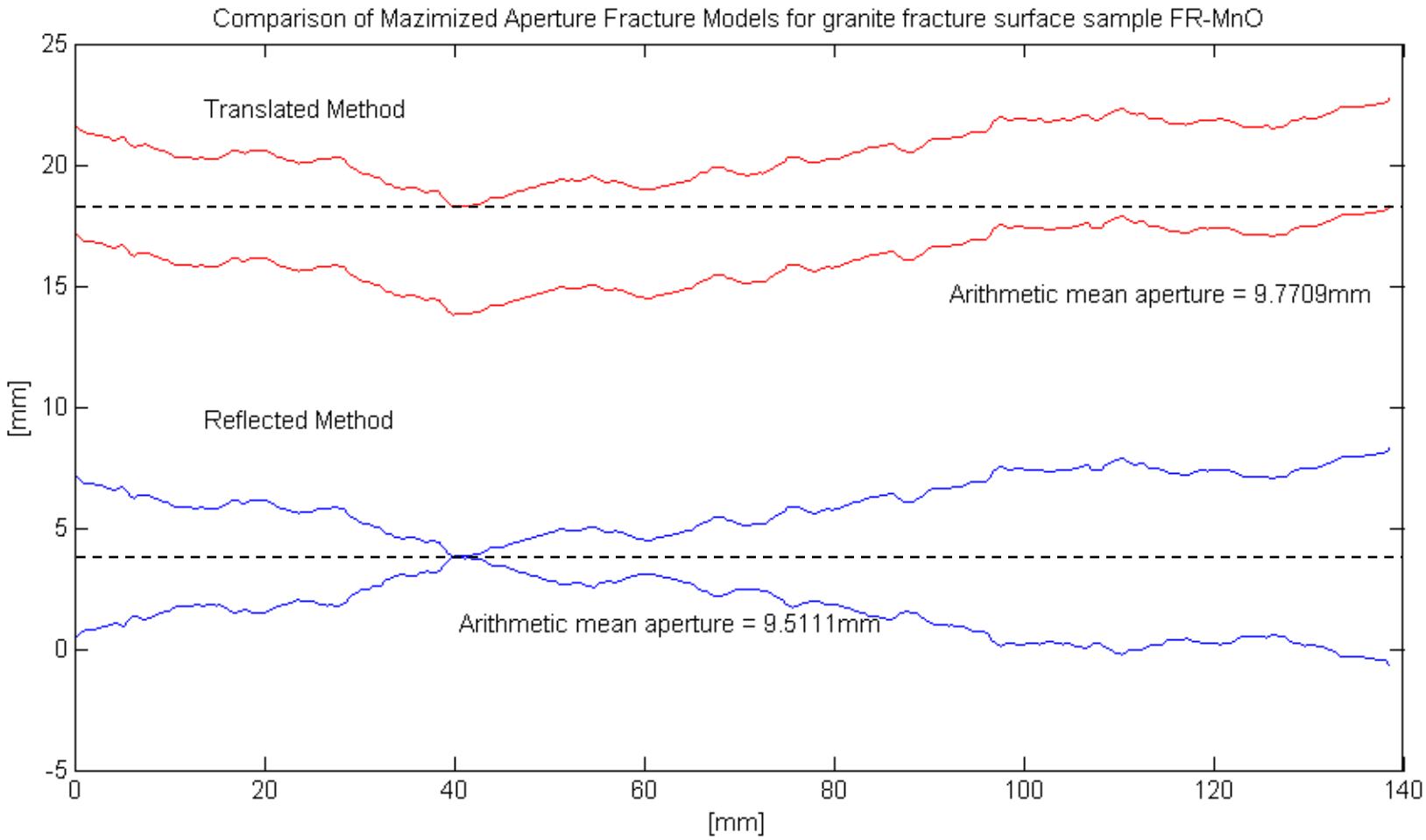

Figure 3.11 Two different maximized aperture fracture profiles generated using the translated and reflected methods. A horizontal line is drawn on the figure to help illustrate how the models are constructed.

Chapter 4: Results

This section provides an overview of the results of the study including a summary of the fracture dataset, a comparison of surface characterization methods, scaling behavior of roughness metrics, surface characterizations for the entire dataset, data from the fracture flow tests, comparisons between fracture surfaces and the hydraulic aperture, fractal characterizations of the fractures, and local aperture arrays and averages.

4.1 FRACTURE DATASET

The fracture dataset encompasses over 20 fracture surfaces and nearly 10 mated pairs of fracture surfaces from a variety of lithologies. Samples include fractures collected by Thompson (2005), Slottke (2010), and Robertson (2006). Samples contributed by this study include two mated granite fractures (coarse-grained and medium-fine grained), one mated schist fracture, and one mated sandstone fracture. Table 4.1 summarizes all of the mated fractures scanned using HRXCT. Table 4.2 summarizes all of the unmated fracture surfaces scanned using HRXCT.

Four mated fractures were contributed by this study to the HRXCT fracture dataset. FHICKSAND1 is a fracture in fine-medium grained Hickory Sandstone collected off of RM 2341 east of Lake Buchanan, in Burnet County, TX. FLLPASCH2 is a fracture in Packsaddle Schist, collected off HWY 71, 20 miles west of the junction with HWY 281, in Llano County, TX. FLLTMGRA1 is a fracture in coarse-grained Town Mountain Granite, collected at an outcrop off the Llano River off FM 3404 in Kingsland, Llano County, TX. FLLTMGRA2 is a fracture in fine-grained Oatman Creek granite collected at an outcrop off the Llano River in Llano, Llano County, TX. Also, GRV from Thompson (2005), a fine-grained fracture in Oatman Creek granite, was rescanned after it was remounted for additional flow testing by Slottke (2010).

Seven unmated fracture surfaces were contributed by this study to the HRXCT fracture dataset. LLPASCH1 is Packsaddle Schist collected off HWY 71, 20 miles west

of the junction with HWY 281, in Llano County, TX. LLQVAV1 is a quartz vein collected at an outcrop of Town Mountain Granite on the west shore of Lake Buchanan off CO RD 261. MIDGRA1 is graphic granite from the Midway Sill, collected east of Lake Buchanan off RM 2341, Burnet County, TX. W001 is porphyritic Llano ryholite (llanite) collected from Babyhead off HWY 16, Llano County, TX (Zolensky et al., 1988). W002 is granite collected at Scotts Crossing Quad, Llano River, TX. W003 is granite collected in Mason, TX. W004 is granite with a chlorite skin, collected at Wertz Dam, Marble Falls, TX. W001, W002, W003, and W004 are small samples scanned with the ultra-high resolution HRXCT machine, providing one order of magnitude higher resolution data than the other samples.

4.2 STATISTICAL SURFACE ROUGHNESS CHARACTERIZATION

Five statistical roughness metrics are implemented to characterize fracture surface roughness: the surface-to-footprint ratio, the root-mean-square (RMS) roughness, the surface skewness, the surface kurtosis, and the root-mean-square (RMS) slope. Table 4.3 summarizes the statistical surface roughness characterization for the fracture dataset. In Appendix C, plots of the surface height distribution for each sample are provided.

A series of plots of the relationships between pairs of parameters is presented in Figure 4.1. Figure 4.1 (a) is a plot of the RMS roughness versus the Surface to Footprint Ratio. This relationship shows little correlation. Higher values of either parameter would imply greater roughness, but the two parameters must describe different properties of roughness.

Figure 4.1 (b) is a plot of the Surface Kurtosis versus the Surface Skewness. This relationship shows little correlation. However, the combination of these two parameters can reveal characteristics of surfaces. For example, large values of Surface Kurtosis combined with large positive or negative values of Surface Skewness imply that the surfaces "positive" features are different from the "negative" features, or vice versa. In other words, a surface might have a flat top with deep valleys, or be relatively flat with large spikey features. Pitted features (like the space leftover from a weathered pumice

fragment in welded tuff) could create zones for eddies to occur, trapping solutes and creating longer tails in breakthrough curves (Cardenas et al., 2007).

Figure 4.1 (c) is a plot of the RMS Roughness versus the RMS Slope. There is little correlation between the parameters. The RMS Roughness measures the amplitude o of the surface height variations after the mean plane has been removed. The RMS Slope measures the change in surface slope. The RMS Slope is very sensitive to the sampling resolution while the RMS Roughness is much less so.

Figure 4.1 (d) is a plot of the RMS Slope versus the Surface to Footprint Ratio. These two parameters are highly correlated, suggesting that they basically measure the same property described differently. Larger values of the RMS Slope imply that the surface slope is highly variable. The Surface to Footprint Ratio can be affected by the amplitude of the roughness or the sampling resolution.

Sample ID	Width (cm)	Length (cm)	Area (cm^2)	Resolution (mm^2)	Description	Location	Source
CC01-3	117.920	140.250	165.383	0.0772	Welded tuff	Closed Canyon, Big Bend State Park, TX	Slottke
CC02-1	98.125	122.000	119.712	0.0681	Welded tuff	Closed Canyon, Big Bend State Park, TX	Slottke
CC02-2a	94.650	150.500	142.448	0.0590	Welded tuff	Closed Canyon, Big Bend State Park, TX	Slottke
CM03	80.460	95.000	76.437	0.0377	Welded tuff	Colorado Mesa, Big Bend State Park, TX	Slottke
FHICKSAND1	86.919	80.500	69.970	0.0343	Hickory Sandstone (medium-grained sand)	East of Lake Buchanan, off RM 2341, Burnet County, TX	Al-Johar
FLLPASCH2	74.576	159.250	118.762	0.0388	Packsaddle Schist	Llano, TX off HWY 71, 20 miles west from HWY 281	Al-Johar
FLLTMGRA1	104.892	191.500	200.869	0.0405	Coarse-grained Town Mountain Granite	Llano River, Kingsland TX FM 3404	Al-Johar
FLLTMGRA2	105.421	111.500	117.545	0.0367	Fine-grained Oatman Creek Granite	Llano River, Llano, TX	Al-Johar
FTHOMGRA	99.085	85.000	84.222	0.0296	Fine-grained Oatman Creek Granite	Llano, TX off HWY 29, 4.7 miles east from TX-16	Thompson
SSH	84.000	91.500	76.860	0.0625	Brushy Canyon Sandstone (fine-grained)	US-62/US-180 6.4 miles north of TX-54, Culberson County, Texas	Thompson

Table 4.1 Dataset of mated fractures scanned with HRXCT

Sample ID	Width (mm)	Length (mm)	Area (cm^2)	Resolution (mm^2)	Description	Location	Source
CC01-1&2	77.693	128.750	100.029	0.0404	Slab of fractured welded tuff	Closed Canyon, Big Bend State Park, TX	Slottke
CCPWTUF1	142.202	187.250	266.273	0.0512	Welded tuff	Closed Canyon, Big Bend State Park, TX	Slottke
EL1bottom	120.698	250.000	301.746	0.0772	Granite exfoliation sheet	Elberton, GA	Slottke
EL1top	120.698	250.000	301.746	0.0772	Granite exfoliation sheet	Elberton, GA	Slottke
EL2bottom	129.918	248.750	323.171	0.0771	Granite exfoliation sheet	Elberton, GA	Slottke
EL2top	123.746	249.750	309.056	0.0771	Granite exfoliation sheet	Elberton, GA	Slottke
FR-MnO	138.553	192.250	266.367	0.0775	Granite with magnesium oxide skin	Fredericksburg, TX	Slottke
FR-WRbottom	114.996	156.250	179.680	0.0775	Granite	Fredericksburg, TX	Slottke
FR-WRtop	130.494	156.250	203.896	0.0775	Granite with weathering rind	Fredericksburg, TX	Slottke
LLPASCH1	100.96	22.50	22.72	0.0373	Packsaddle Schist	Llano, TX off HWY 71, 20 miles west from HWY 281	Al-Johar
LLQVAV1	106.02	230.50	244.37	0.0416	Surface of fracture within quartz vein	West shore Lake Buchanan, off CO RO 261, Llano County, TX	Al-Johar
W001	32.546	69.682	22.679	0.0037	Llanite surface	Babyhead, Llano County, TX	Al-Johar
W002	35.500	50.695	17.997	0.0037	Granite surface	Scotts Crossing Quad, Llano River, TX	Al-Johar
W003	32.546	41.202	13.410	0.0037	Granite surface	Mason, TX	Al-Johar
W004	34.023	61.644	20.973	0.0037	Granite surface with chlorite skin	Wertz Dam, Marble Falls, TX	Al-Johar

Table 4.2 Dataset of unmated fracture surfaces scanned with HRXCT

Surface Sample	Surface to Footprint Ratio	RMS Roughness	Surface Skewness	Surface Kurtosis	RMS Slope
FR-MnO	1.048	1.63	0.78	3.27	0.33
FR-Wrbot	1.054	1.29	0.67	4.00	0.39
FHICKSANDbot	1.136	1.19	-0.97	4.80	0.57
FHICKSANDtop	1.133	1.19	-0.90	4.46	0.57
EL1bot	1.048	1.62	-0.15	2.22	0.32
EL2bot	1.049	1.19	0.53	3.77	0.33
EL1top	1.058	1.46	-0.07	2.70	0.36
EL2top	1.071	2.70	-0.18	2.40	0.42
GRVtop	1.061	0.81	0.34	2.75	0.37
GRVbot	1.063	0.81	0.54	2.98	0.39
FLLTMGRA2bot	1.298	1.10	0.07	3.11	1.28
FLLTMGRA2top	1.320	1.08	0.04	2.99	1.36
CC02-1bot	1.078	2.14	0.36	3.04	0.44
CC02-1top	1.077	2.12	0.41	3.22	0.43
CC01-1_2	1.044	1.65	0.38	2.28	0.33
CC02-2Abot	1.122	2.20	0.26	2.38	0.56
CC02-2Atop	1.120	2.14	0.26	2.40	0.56
FLLPASCH2top	1.368	1.91	-0.10	2.30	1.87
FLLPASCH2bot	1.361	1.82	0.03	2.20	1.85
W001	1.128	1.86	-0.12	1.94	0.62
W002	1.067	0.42	-0.18	2.40	0.39
W003	1.109	0.84	0.67	3.55	0.56
W004	1.132	2.01	-0.66	2.42	0.59

Table 4.3 Statistical Surface Roughness Metrics

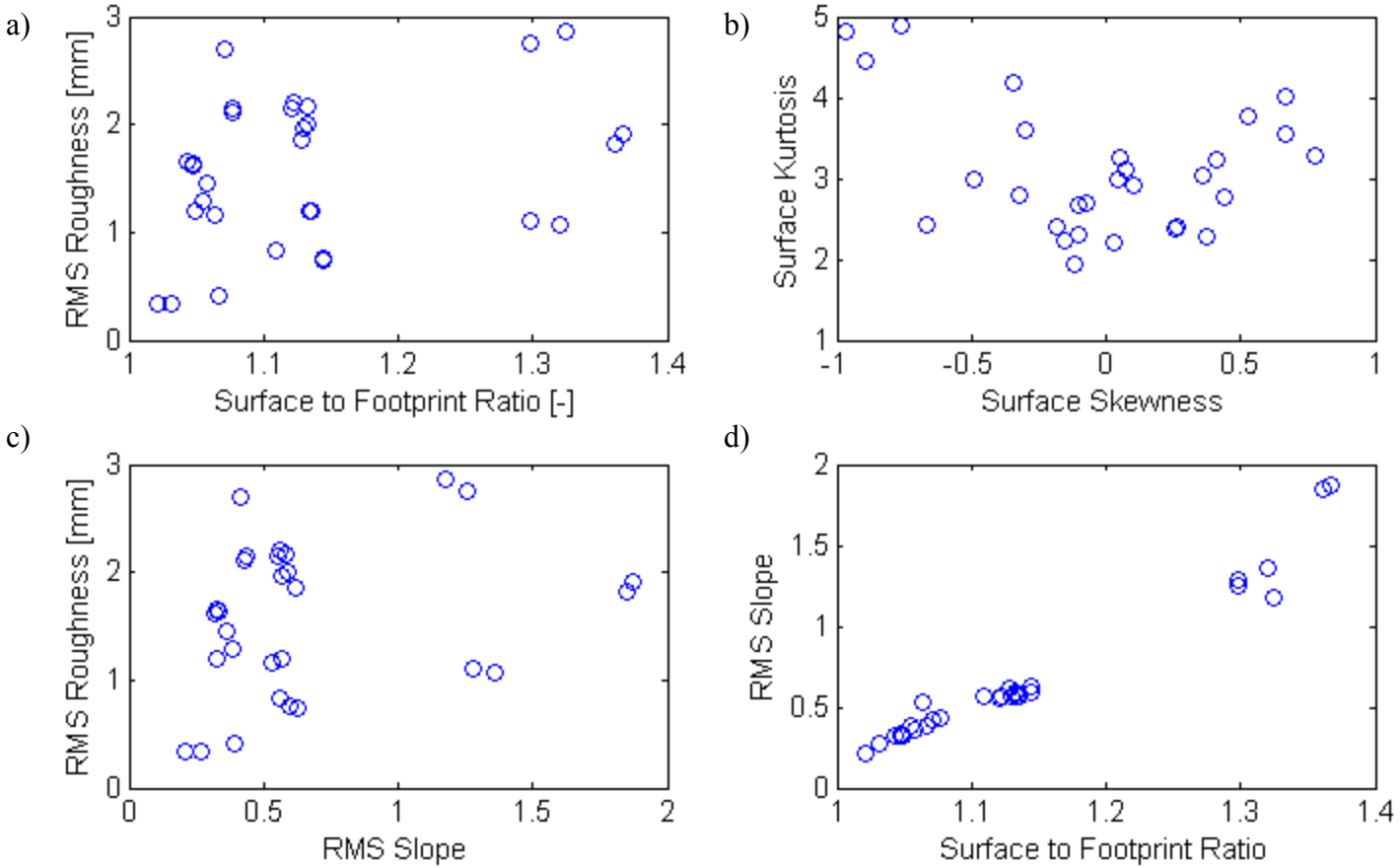

Figure 4.1 Relationships of surface roughness parameters calculated for all surface samples. No correlations can be discerned except for the RMS slope and Surface to Footprint Ratio parameters, which suggests that these two parameters describe the same property.

4.3 SCALING BEHAVIOR OF ROUGHNESS PARAMETERS

Here I present the results of scaling analysis for each statistical roughness metric for one fracture sample. Scaling analyses of statistical roughness metrics for the other surface samples are including in Appendix D. Figures 4.5-4.9 present the scaling analysis of granite fracture surface FR-MnO for the Surface-to-Footprint ratio, the RMS Roughness, the Surface Skewness, the Surface Kurtosis, and the RMS Slope, respectively.

One observation is that the different roughness parameters scale differently. Specifically, the variance of the computed roughness parameter for the group of sub-samples approaches zero differently depending on the parameter. The variance of the Surface to Footprint parameter approaches zero the fastest, then the Surface Skewness, the RMS Slope, the RMS Roughness and the Surface Kurtosis, in that order.

A second observation is that the variance relative to the magnitude of mean values for the subsamples is different depending on the parameter. The variance of the Surface to Footprint values is three orders of magnitude smaller than the mean values, the Surface Kurtosis variance values are two orders of magnitude smaller than the means, the RMS Slope and RMS Roughness variances are one order of magnitude smaller than the means, and the Surface Skewness variances are about half an order smaller than the mean values.

A third observation is how the mean values of the subsamples for the different parameters change with increasing scale. By simply looking at the change in value up to 50 cm^2 in area, the Surface to Footprint ratio decreases by 0.0006, the RMS Roughness increases by 0.2 cm, the RMS slope increases by 0.35, the Surface Skewness decreases by 0.4, and the Surface Kurtosis increases by 0.65. The extreme outlier is the Surface to Footprint ratio which changes very little with increasing scale. This is consistent with the previously stated observation of the variance of the Surface to Footprint ratio approaching zero very quickly.

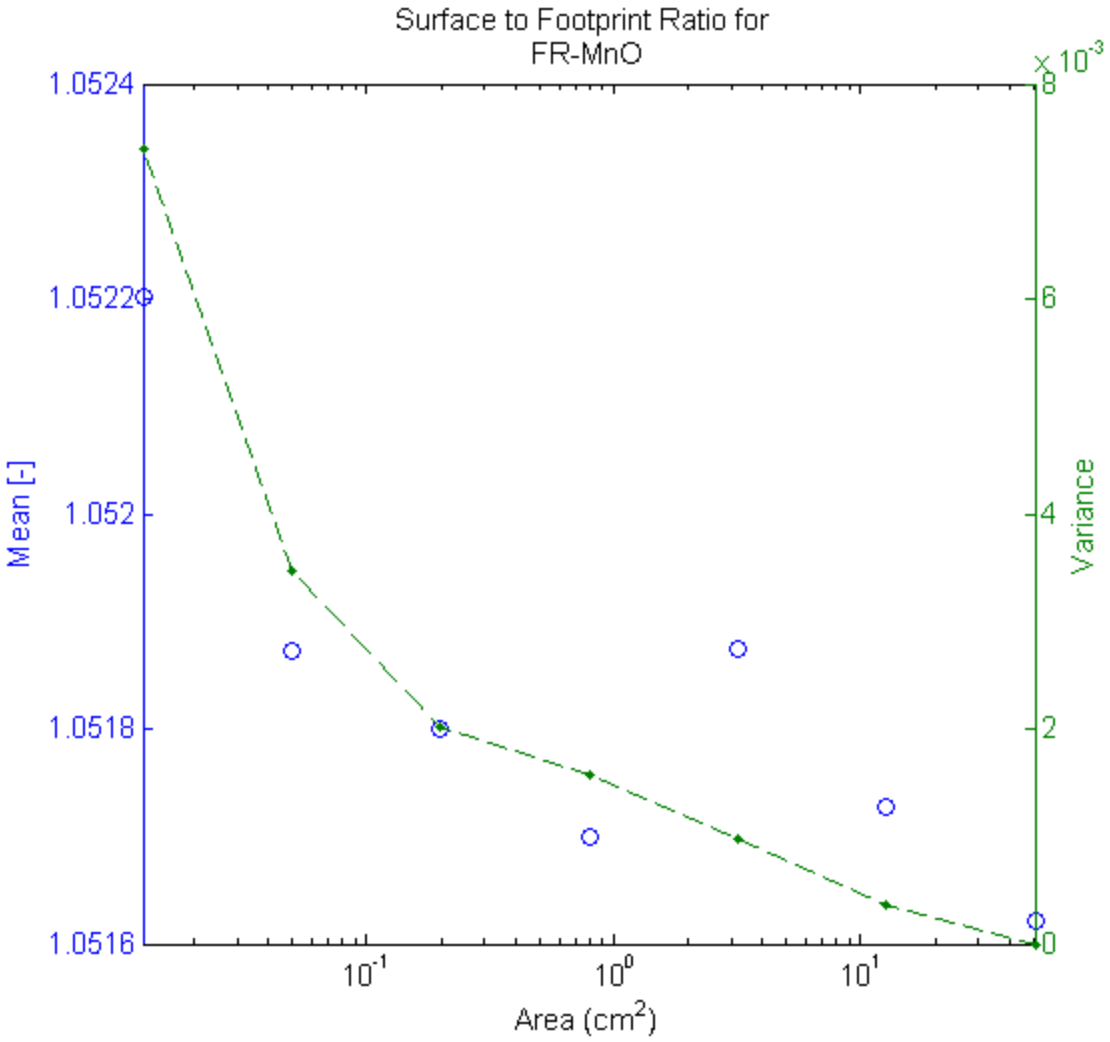

Figure 4.2 Scaling behavior of Surface to Footprint Ratio for sample FR-MnO. The surface is divided into sub-samples across a range of scales and the roughness parameter is calculated for each subsample. Each blue marker represents the arithmetic mean of the roughness parameters for each corresponding sub-sample size. The green represent the variance of the roughness parameter for the sub-samples.

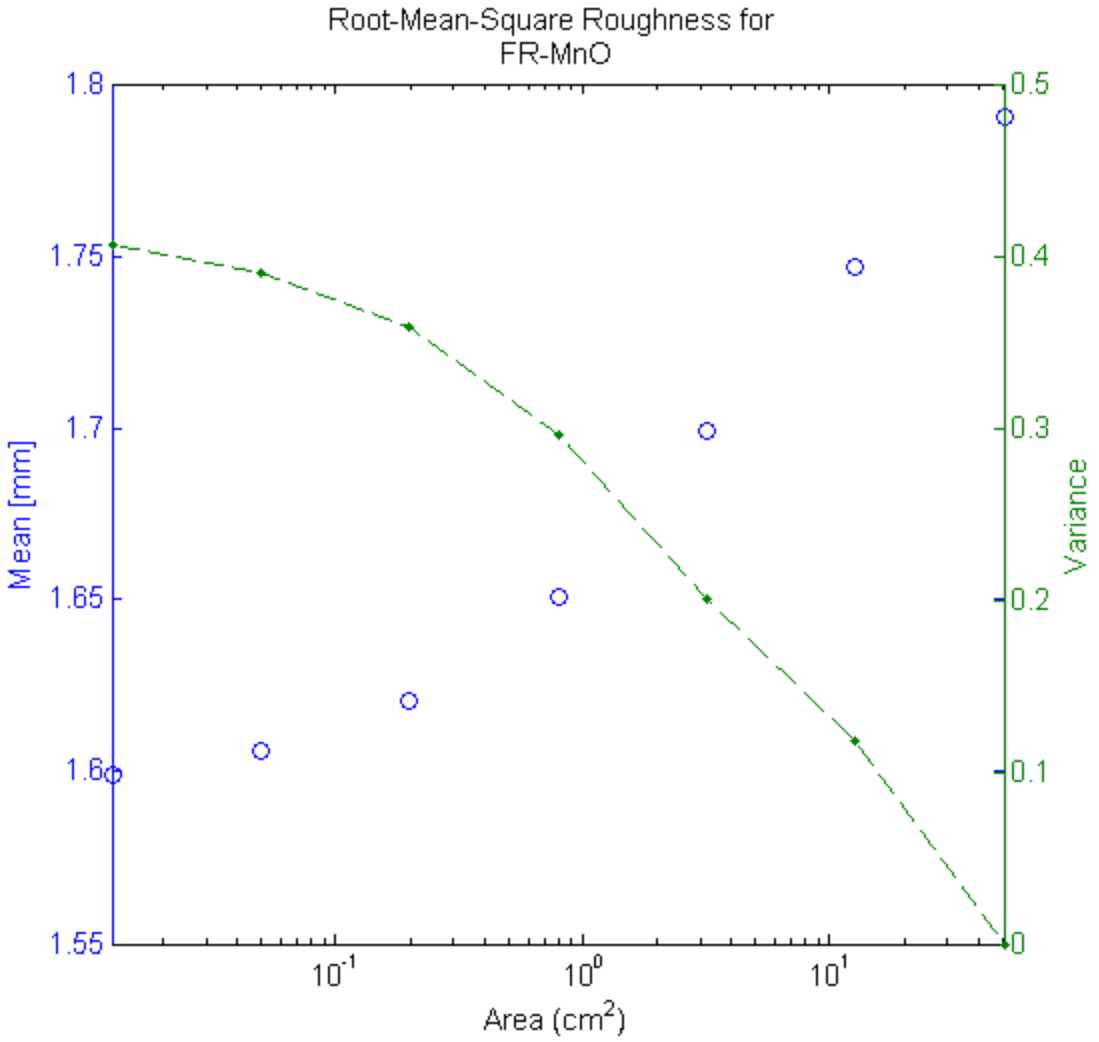

Figure 4.3 Scaling behavior of the RMS Roughness parameter for sample FR-MnO. The surface is divided into sub-samples across a range of scales and the roughness parameter is calculated for each subsample. Each blue marker represents the arithmetic mean of the roughness parameters for each corresponding sub-sample size. The green represent the variance of the roughness parameter for the sub-samples.

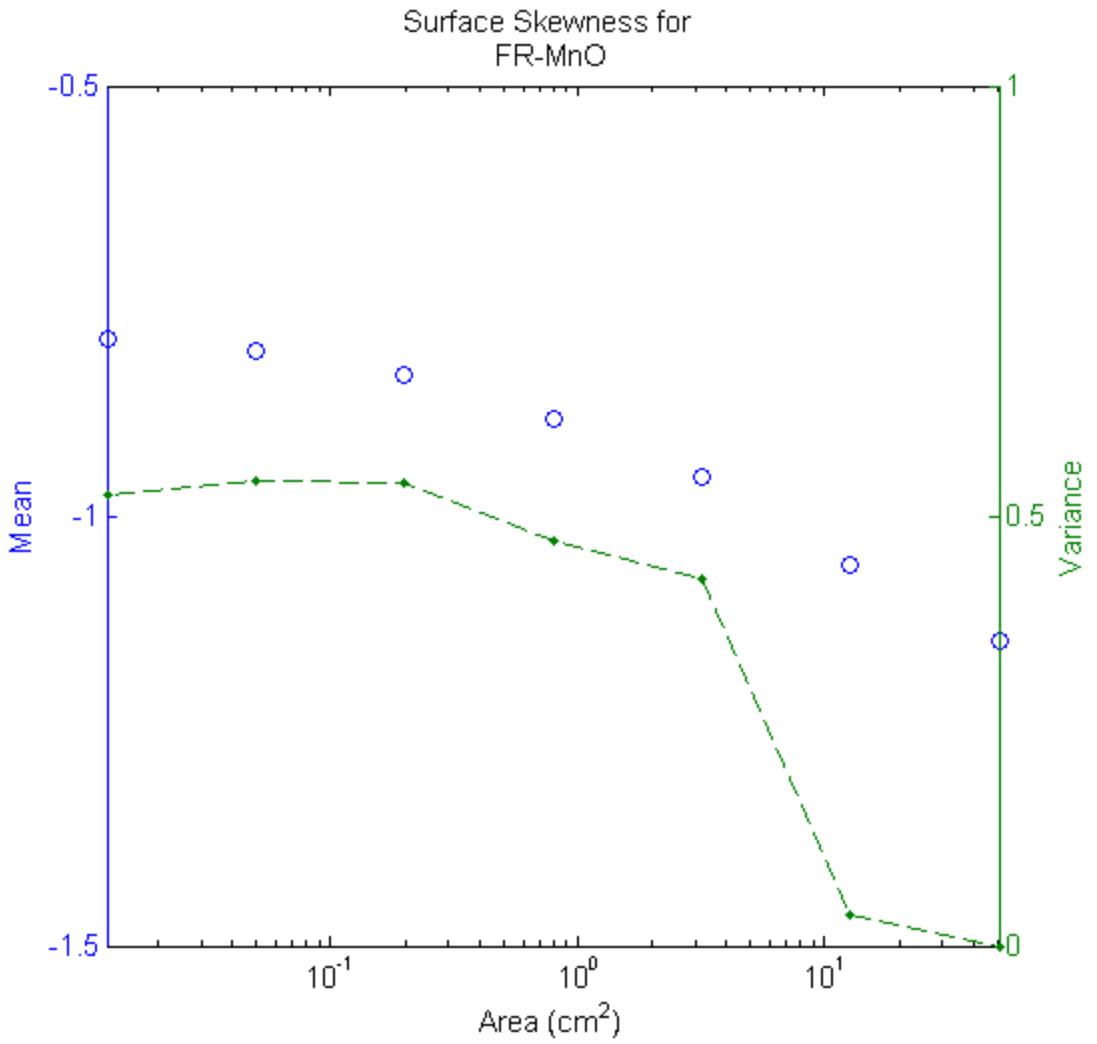

Figure 4.4 Scaling behavior of the Surface Skewness for sample FR-MnO. The surface is divided into sub-samples across a range of scales and the roughness parameter is calculated for each subsample. Each blue marker represents the arithmetic mean of the roughness parameters for each corresponding sub-sample size. The green represent the variance of the roughness parameter for the sub-samples.

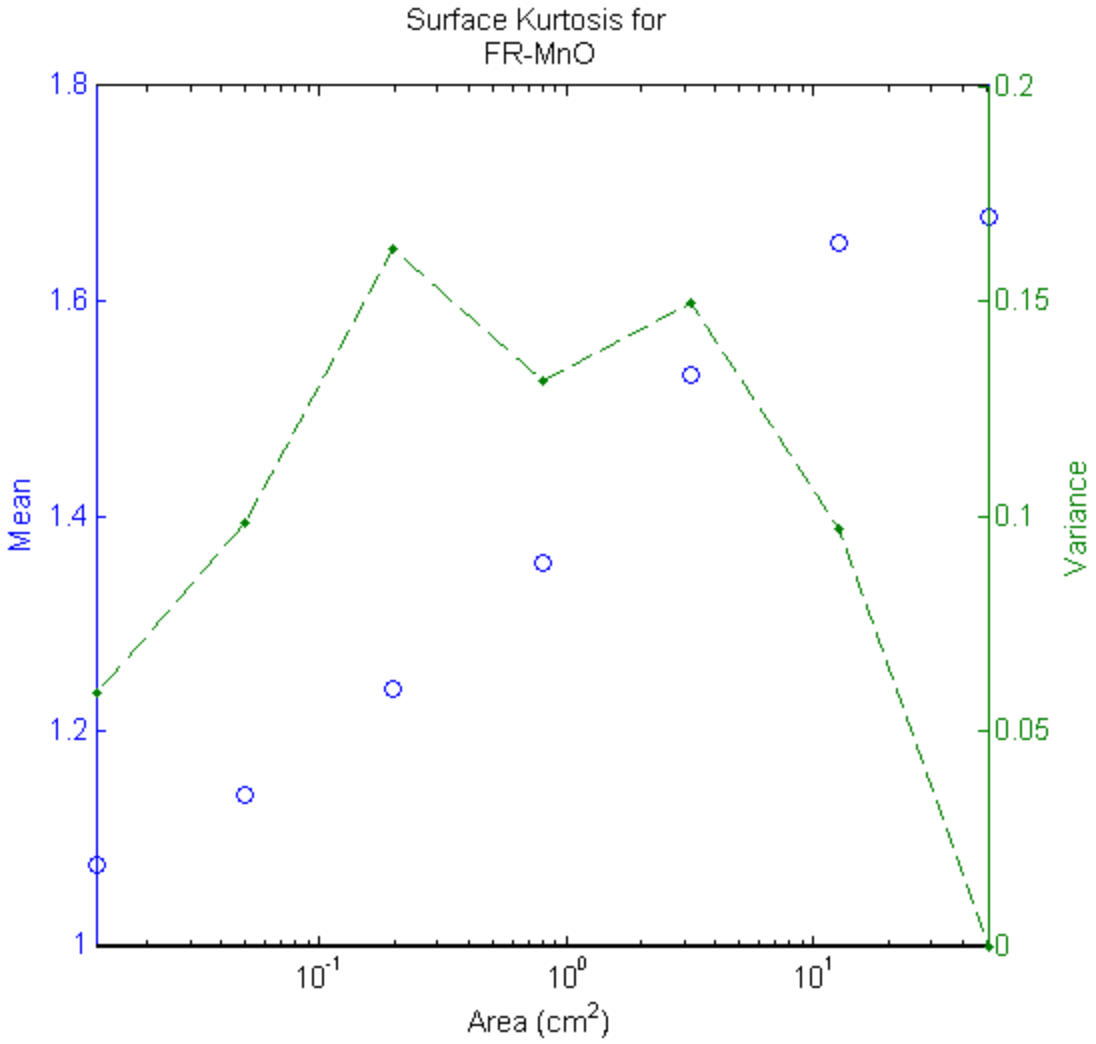

Figure 4.5 Scaling behavior of the Surface Kurtosis for sample FR-MnO. The surface is divided into sub-samples across a range of scales and the roughness parameter is calculated for each subsample. Each blue marker represents the arithmetic mean of the roughness parameters for each corresponding sub-sample size. The green represent the variance of the roughness parameter for the sub-samples.

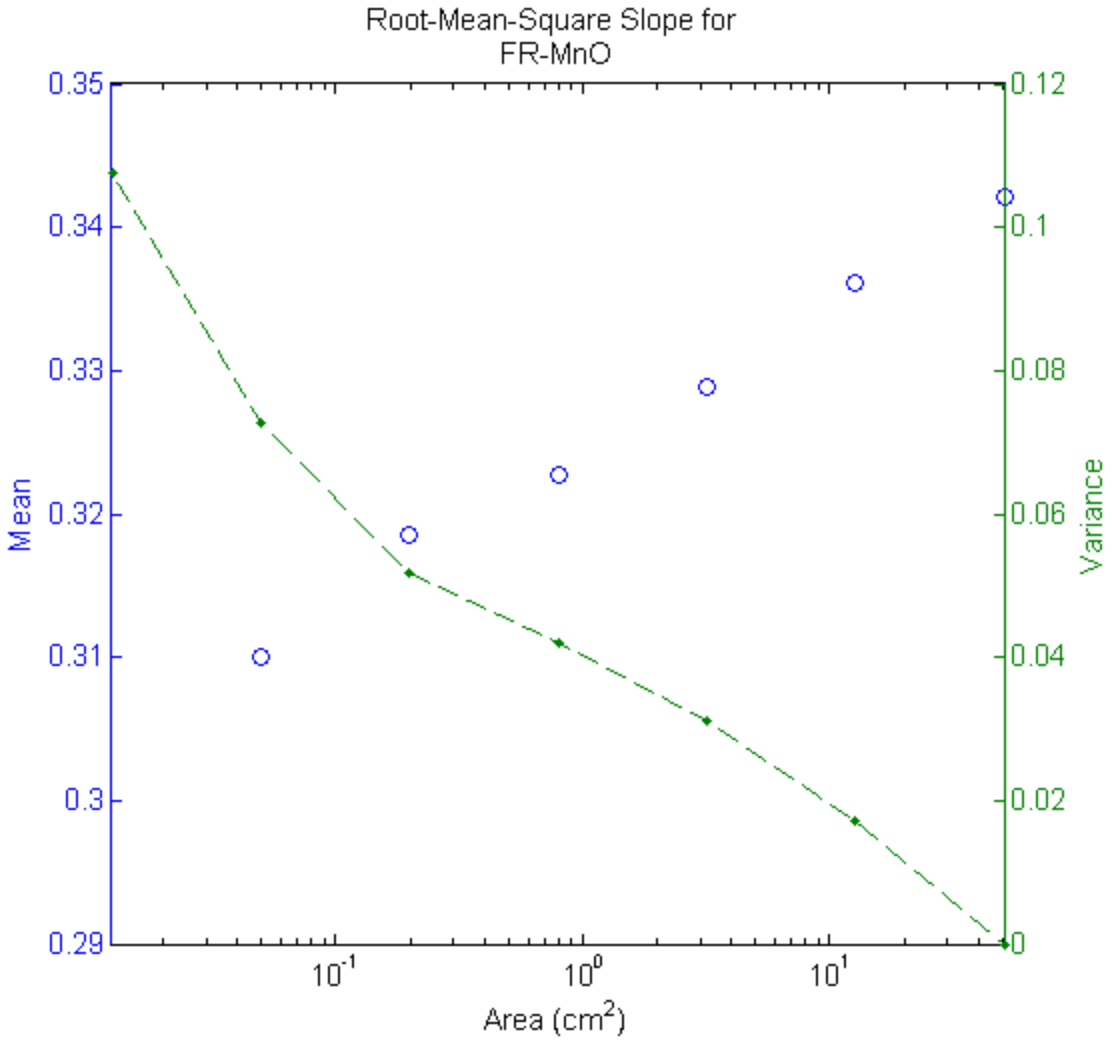

Figure 4.6 Scaling behavior of the RMS Slope for sample FR-MnO. The surface is divided into sub-samples across a range of scales and the roughness parameter is calculated for each subsample. Each blue marker represents the arithmetic mean of the roughness parameters for each corresponding sub-sample size. The green markers the variance of the roughness parameter for the sub-samples.

4.4 ROUGHNESS METRICS FOR MATED SURFACES

One important hypothesis to test is whether or not mated fracture surfaces exhibit similar roughness metrics. In Figure 4.10, statistical surface roughness parameters are calculated for each pair of mated fracture surfaces. The top and bottom surfaces (an arbitrary distinction) are plotted against each other. A strong 1:1 correlation for the mated fractures is clearly observed in the plots. This result provides validity to the assumption that mated fracture surfaces exhibit the same roughness characteristics. This is a powerful observation if the aperture of a fracture can be predicted based on the roughness of its surfaces. It is often difficult to collect both surfaces of a fracture in a mated state; other fractures are required to remove a sample from an outcrop.

4.5 APERTURES

Fracture aperture is the dominant control on fracture permeability. However, measuring and estimating fracture aperture remains difficult due to the roughness of rock fractures. Table 2.1 is a review of the different apertures used to characterize flow in fractures. The parallel plate model (Figure 1.1) has a constant aperture with flat, parallel surfaces that is easily measured by finding the difference in surface height between the two surfaces. For rock fractures, measuring the aperture is not as straightforward due to the roughness of the surfaces. After measuring the aperture locally, finding the best average aperture to predict flow in the fracture is another problem. The hydraulic aperture, the aperture computed with the cubic law after applying the parallel plate model to experimentally measured flow through a rock fracture, is less than the arithmetic mean of the local apertures (Slottke, 2010). A fracture's mechanical aperture is computed as the arithmetic mean of the local apparent aperture.

In this study, I implement Mourzenko et al. (1995)'s method to measure local aperture in two and three dimensions and compare it to the arithmetic, geometric, and harmonic means of the apparent local aperture, also computed in Slottke (2010). Figure 4.11 shows the aperture calculated for the mated fractures in the HRXCT dataset plotted against the commonly used arithmetic mean apparent aperture. For a two-dimensional

profile, Mourzenko et al. (1995)'s method involves finding the diameter of the largest circle that will be tangent to the bounding surfaces of the fracture. For three-dimensions, this is replaced with a sphere. Here, I use the arithmetic mean of the Mourzenko et al. (1995) true local apertures. I also compare these true apertures to the geometric and harmonic means of the apparent apertures. Slottke (2010) calculated the arithmetic, geometric, and harmonic mean apertures for a fracture and observed that the geometric mean was the best predictor of the hydraulic aperture for laminar flow in a fracture. Figure 4.11 shows few consistent trends, but all aperture calculations fall relatively close to each other. The arithmetic mean apparent aperture, the traditional "mechanical aperture", has the largest value for all of the mated fractures studied here. Also, all of the aperture metrics are well correlated with the arithmetic mean apparent aperture.

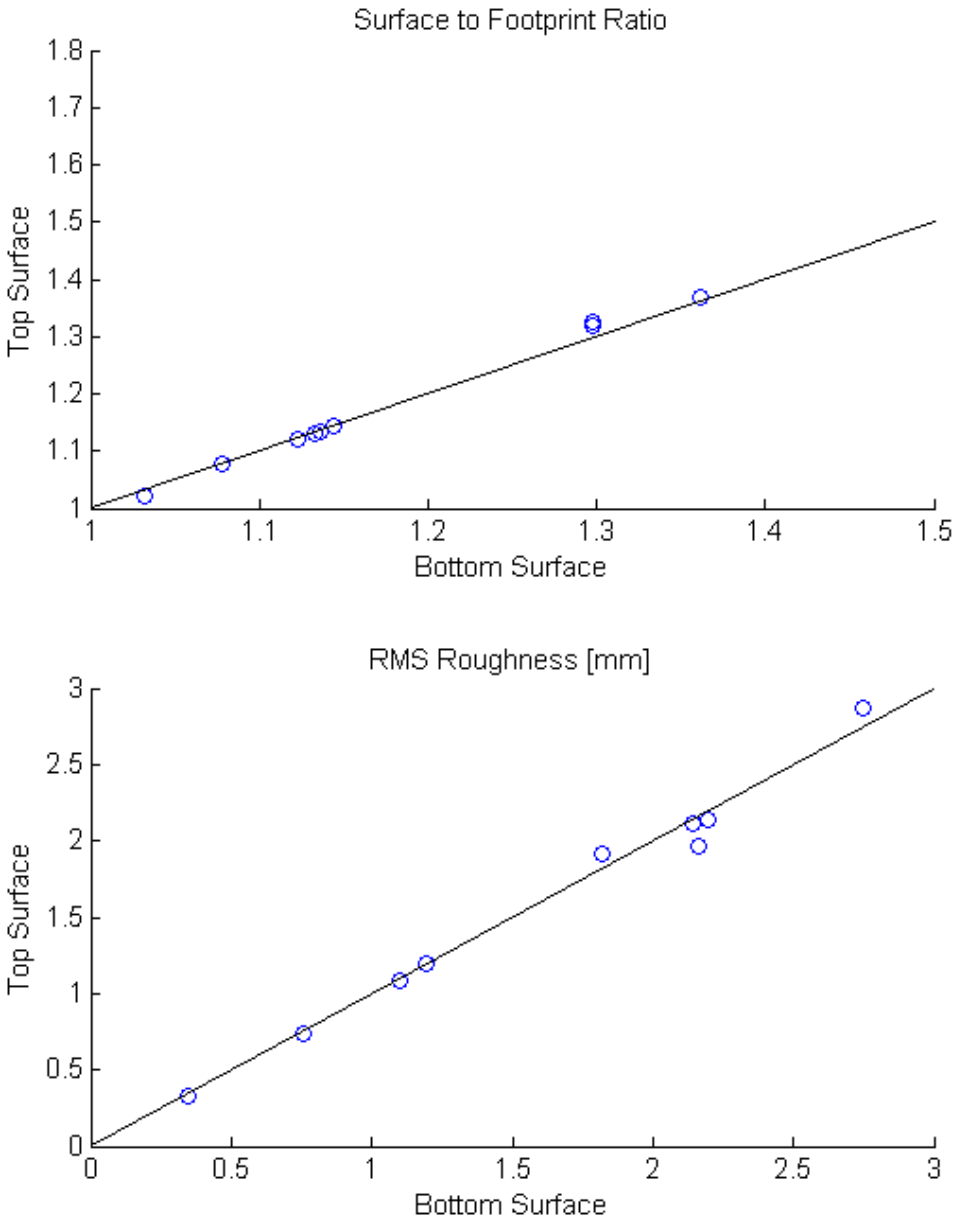

Figure 4.7 Plots comparing the Surface to Footprint Ratio and RMS Roughness metrics for mated fracture surfaces. A strong correlation is found for both metrics. A 1:1 line is plotted for comparison.

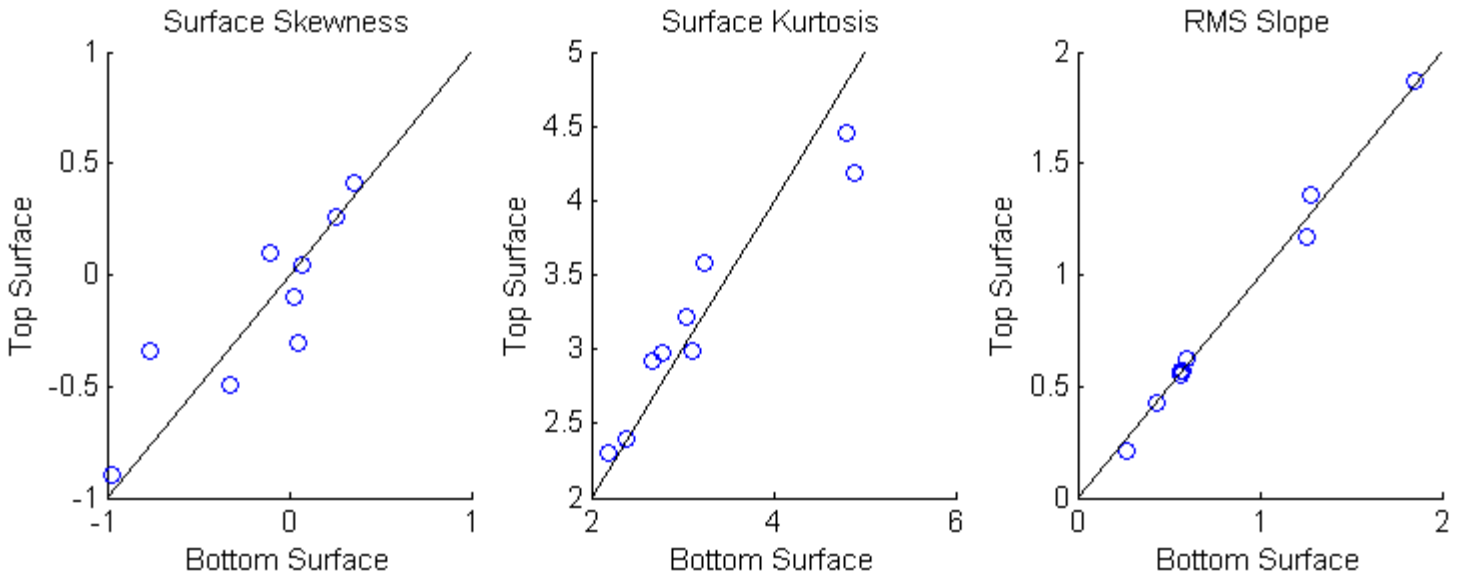

Figure 4.8 Plots comparing the Surface Skewness, Surface Kurtosis, and RMS Slope roughness metrics for mated fracture surfaces. For all metrics and all samples, a strong correlation is observed for the roughness of the top and bottom fracture surfaces. A 1:1 line is plotted for comparison.

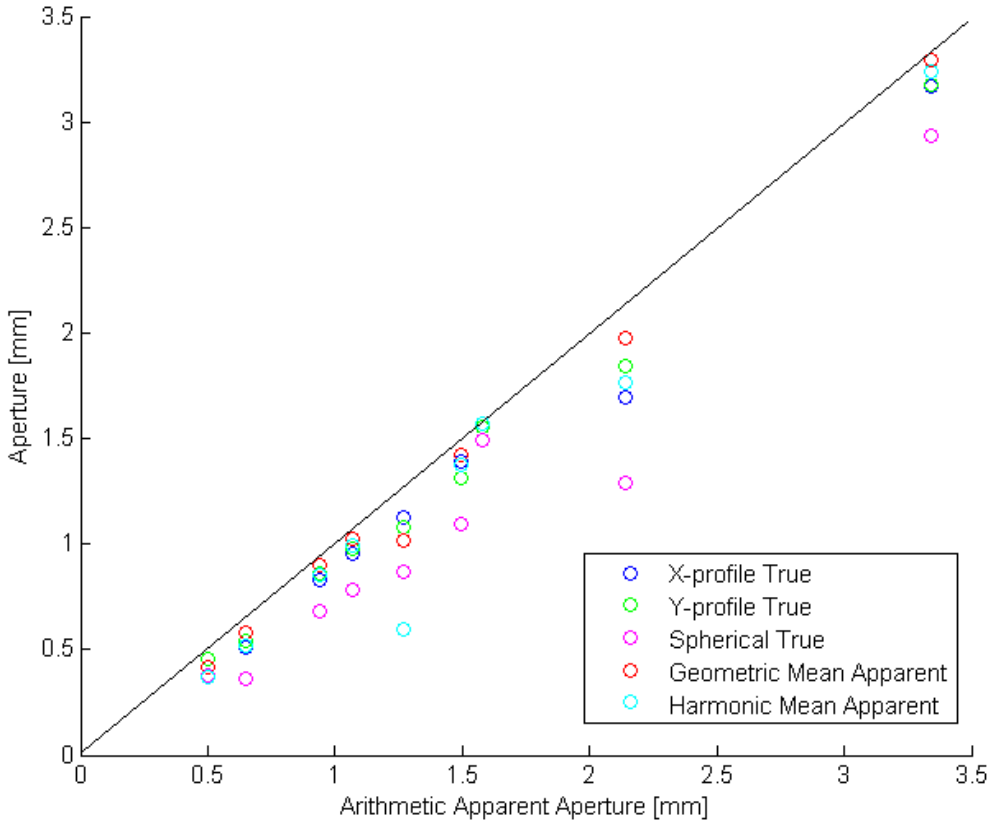

Figure 4.9 A scatter plot comparing results of different aperture calculations versus the traditional mechanical aperture (arithmetic mean of the apparent local aperture). The "x-profile true" and "y-profile true" apertures are the arithmetic mean of the true apertures calculated using Mourzenko et al. (1995)'s method from fracture profiles in the *x* and *y* dimensions, respectively. The "spherical true" aperture is the arithmetic mean of the local aperture calculated applying Mourzenko et al. (1995)'s method to three-dimensions. The "geometric mean apparent" and "harmonic mean apparent" apertures are the geometric and harmonic means of the apparent local apertures. A 1:1 line is plotted for comparison.

4.6 FRACTAL ANALYSIS OF FRACTURE MORPHOLOGY

Three different sets of figures are presented in this section. The first two sets of figures correspond to the fractal analysis of granite fracture surface FR-MnO. The last set of figures show the results of the fractal analysis for the entire dataset.

Three different fractal analysis methods are used in this study: the Roughness-Length method, the First Return Probability method, and the Power Spectral Density method. For each surface in the dataset, each fractal method is applied to each profile in the two-dimensional array of surface height values. The surface profiles are parallel either to the X or Y dimension in the array. Figures 4.12 to 4.14 show the fractal analysis for each method for granite fracture surface FR-MnO. Each fractal analysis is a log-log plot with a strong power law trend across several orders of magnitude. The Roughness-Length method plots the RMS roughness versus the width of the profile window. The First Return Probability method plots the probability to "return" to the surface height value for any given distance from the last instance of that surface height value. The Power Spectral Density method plots the power versus the wavelength surface profile. The power spectral density is found by transforming the spatial topographic series into frequency-amplitude space using the Fast Fourier Transform following the common methodology used for time series analysis. Each plot has the fractal analysis for each profile parallel to the X or Y dimension of the surface height array.

Each of the methods shows a strong power law trend for the profiles grouped together. Figures 4.15 to 4.17 plot the arithmetic mean for all profiles for each fractal analysis method. The power law trend is much clearer in these figures. The mean line for the X and Y dimension are plotted together and shows relatively strong agreement for the Roughness-Length method but less so for the First Return Probability and the Power Spectral Density methods. The two main differences between the X and Y profiles is the sampling resolution of the data along the profile and the length of the profiles (the Y dimension always the longer dimension of the surface sample). The resolution in the X

or Y dimension is generally about the same but may be greater than or less than the other depending on the fracture sample.

The Hurst exponent is calculated for each mean line of fractal analysis in the *x* and *y* dimensions. The data for all fracture surface samples is presented in Table 4.4. The Hurst exponent is found by finding the power law exponent for the 'flat' part of each line. At small scales and large scales artifacts and noise can occur causing the fractal analysis to deviate from the power law trend. This is especially true for the First Return Probability method at large scales. The artifacts and noise at the edges of the scale range are due to sampling artifacts (Schmittbuhl et al., 1995). The common Hurst exponent value for natural, self-affine rough surfaces is reported to be 0.8 (Bouchaud, 1997; Boffa et al., 1998). However, for the samples in this study, the Hurst exponent varies across a greater range. While this may be due to the limitations of the relatively short range of scale considered, these results throw into doubt the universal Hurst exponent value of 0.8 for natural fracture surfaces. Out of the three fractal analysis methods, the Roughness-Length method provides the most consistent results and describes the fractal behavior of a parameter that can be easily applied to characterizing fracture morphology.

The final set of figures (Figures 4.18 to 4.23) provides the fracture analysis of the entire fracture sample dataset. One important observation is the occurrence of two separate groups of lines for the First Return Probability and Power Spectral Density methods, but no such occurrence for the Roughness-Length method. The group of red-colored lines corresponds to granite fracture surface samples W001, W002, W003, and W004. These samples were scanned with the ultra high resolution subsystem HRXCT which produced data at a resolution an order of magnitude finer than the other samples. In the plots for the Roughness-Length method, this group of fracture samples plots with the other samples. The lack of sensitivity to sampling resolution is one reason to favor the Roughness-Length method for fractal analysis, in addition to the ease of implementation and the more intuitive nature of the method.

Surface	Roughness-Length		First Return Probability		Power Spectral Density	
	x	***y***	***x***	***y***	***x***	***y***
FR-MnO	0.700	0.681	0.734	0.735	0.946	0.894
FR-WRbot	0.618	0.619	0.527	0.614	0.757	0.690
FHICKSAND1botsurf	0.812	0.593		0.661	1.086	0.963
FHICKSAND1topsurf	0.822	0.610		0.672	1.086	0.985
sshbotsurf	0.493	0.485	0.245		0.738	0.732
sshtopsurf	0.516	0.492	0.317		0.838	0.836
EL1bot	0.626	0.650	0.448	0.663	0.820	0.851
EL2bot	0.619	0.546	0.447	0.664	0.814	0.814
EL1top	0.594	0.665	0.270	0.804	0.764	0.849
EL2top	0.658	0.746	0.571	0.726	0.859	0.933
FLLTHOMGRAbotsurf	0.698	0.555	0.237	0.420	0.964	0.917
FLLTHOMGRAtopsurf	0.714	0.553	0.081	0.414	0.955	0.887
FLLTMGRA2botsurf	0.655	0.776	0.751		0.650	0.792
FLLTMGRA2topsurf	0.646	0.762	0.765		0.636	0.787
CC01-3botsurf	0.808	0.928			0.948	1.098
CC01-3topsurf	0.827	0.931			0.959	1.084
CC02-1botsurf	0.842	0.777		0.823	1.165	1.111
CC02-1topsurf	0.834	0.770		0.830	1.177	1.120
CC01-1_2	0.764	0.830	0.747	1.010	1.032	1.003
cc02-2abot	0.815	0.771	0.760	0.756	1.209	1.154
cc02-2atop	0.819	0.777	0.688	0.769	1.208	1.178
CM03botsurf	0.809	0.667	0.498	0.618	0.886	1.036
CM03topsurf	0.805	0.678		0.647	0.987	0.997
FLLPASCH2topsurf	0.536	0.817	0.485		0.610	0.816
FLLPASCH2botsurf	0.538	0.835	0.511		0.635	0.817
LLPASCH	0.703	0.809	0.612		1.099	1.139
W001	0.781	0.780	0.689	0.612	1.205	1.119
W002	0.658	0.630	0.757	0.826	1.052	0.961
W003	0.723	0.700	0.696	0.737	1.122	1.052
W004	0.757	0.877	0.653	1.137	1.166	1.198

Table 4.4 Calculated fractal dimensions for fracture surfaces using three different methods: the Roughness-Length method, the First Return Probability method, and the Power Spectral Density method.

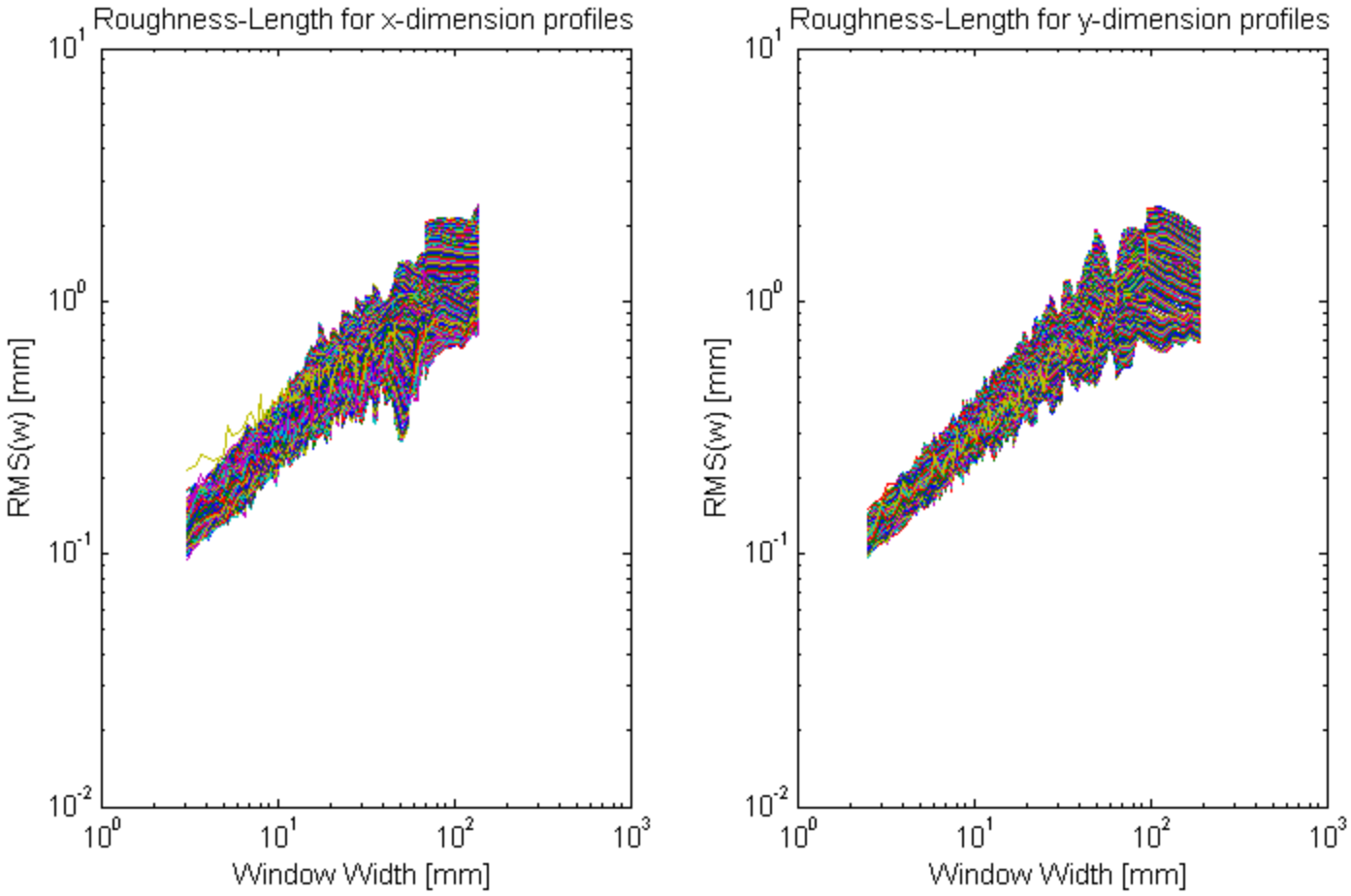

Figure 4.10 Roughness-Length fractal analysis for each surface profile of FR-MnO. Each colored line represents the roughness-length fractal analysis for each profile traverse in the surface array of sample FR-MnO.

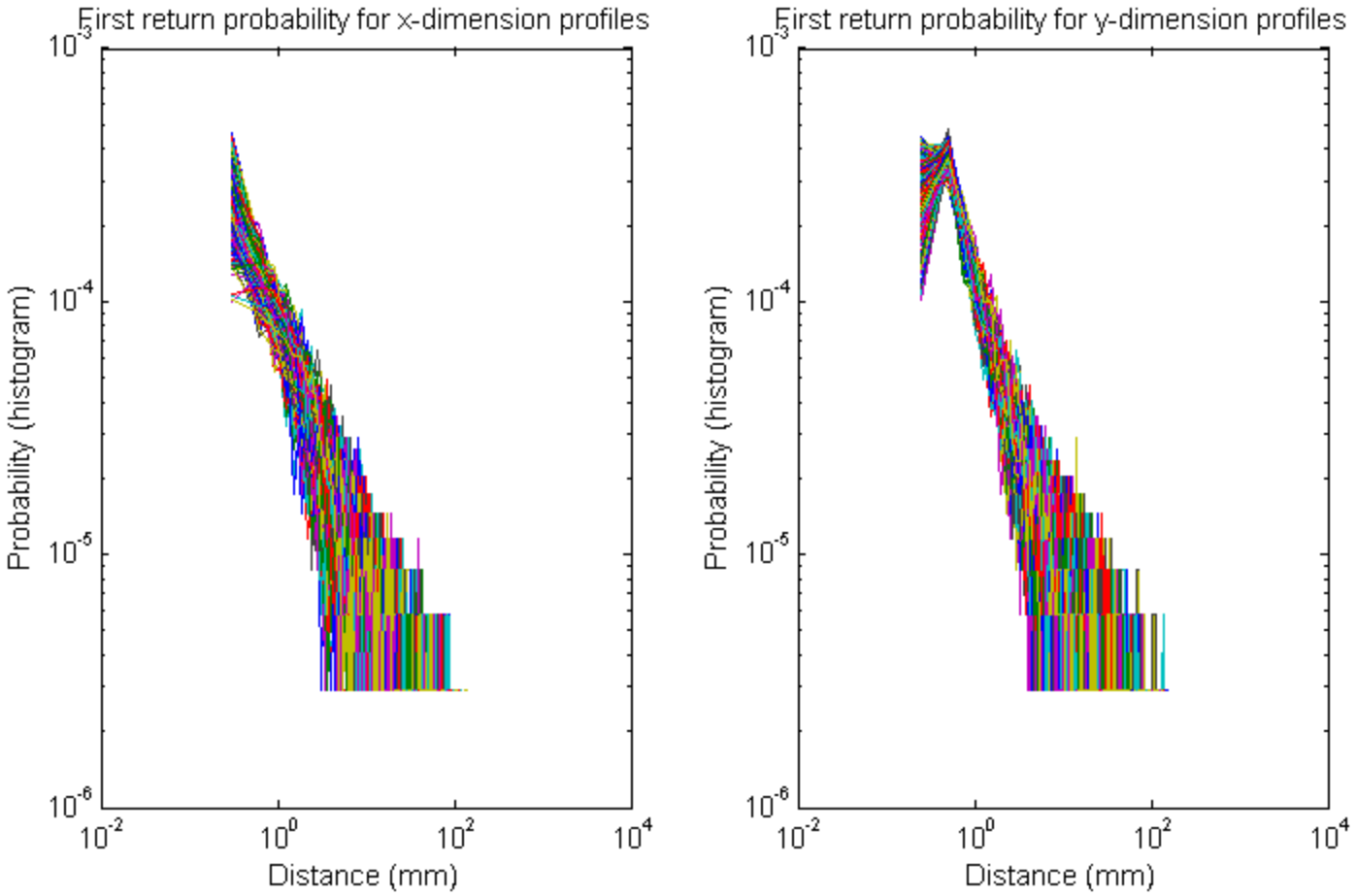

Figure 4.11 First Return Probability fractal analysis for each surface profile of FR-MnO. Each colored line represents the first return probability fractal analysis for each profile traverse in the surface array of sample FR-MnO.

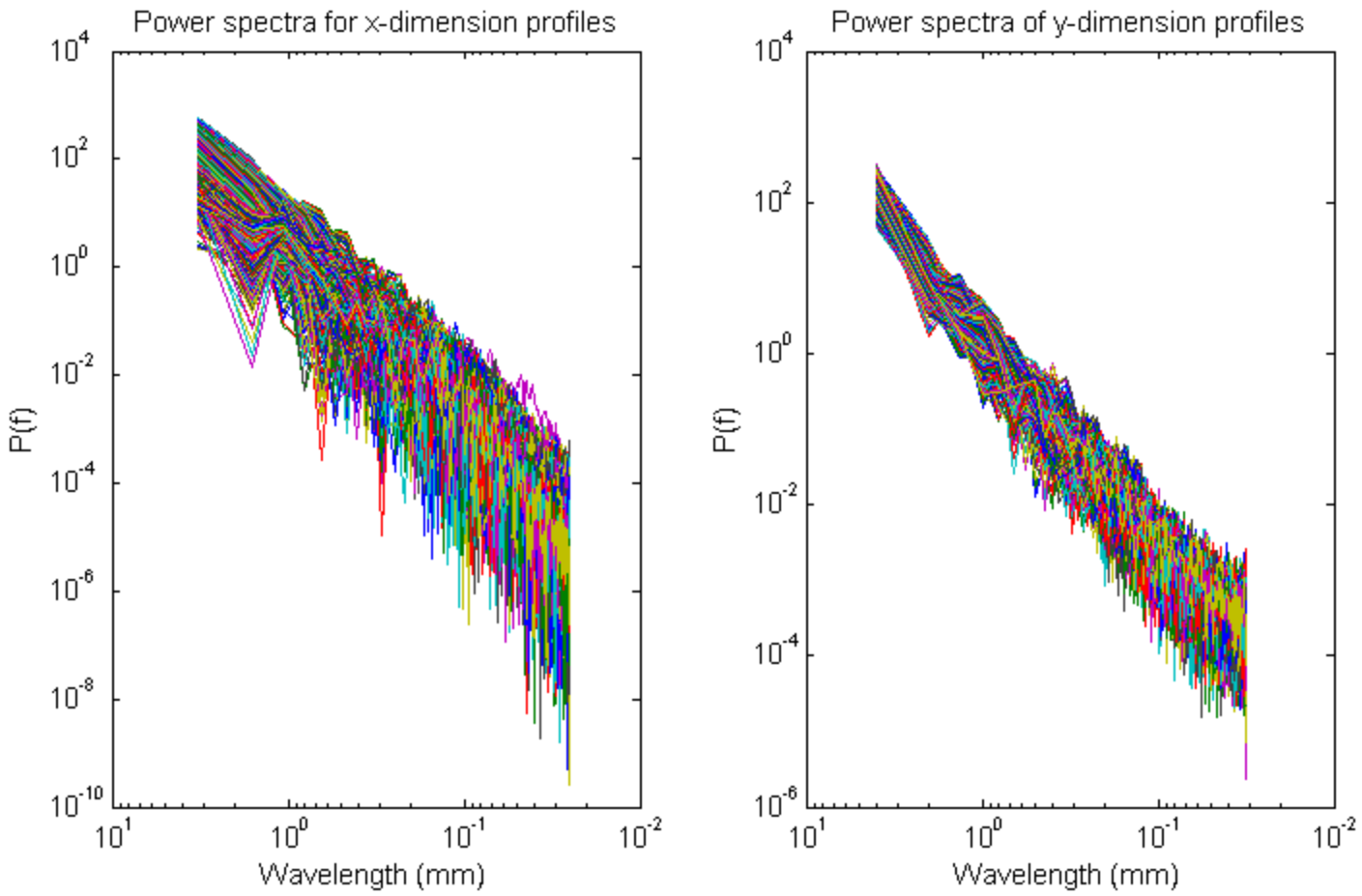

Figure 4.12 Power Spectral Density fractal analysis for each surface profile of FR-MnO. Each colored line represents the power spectral density fractal analysis for each profile traverse in the surface array of sample FR-MnO.

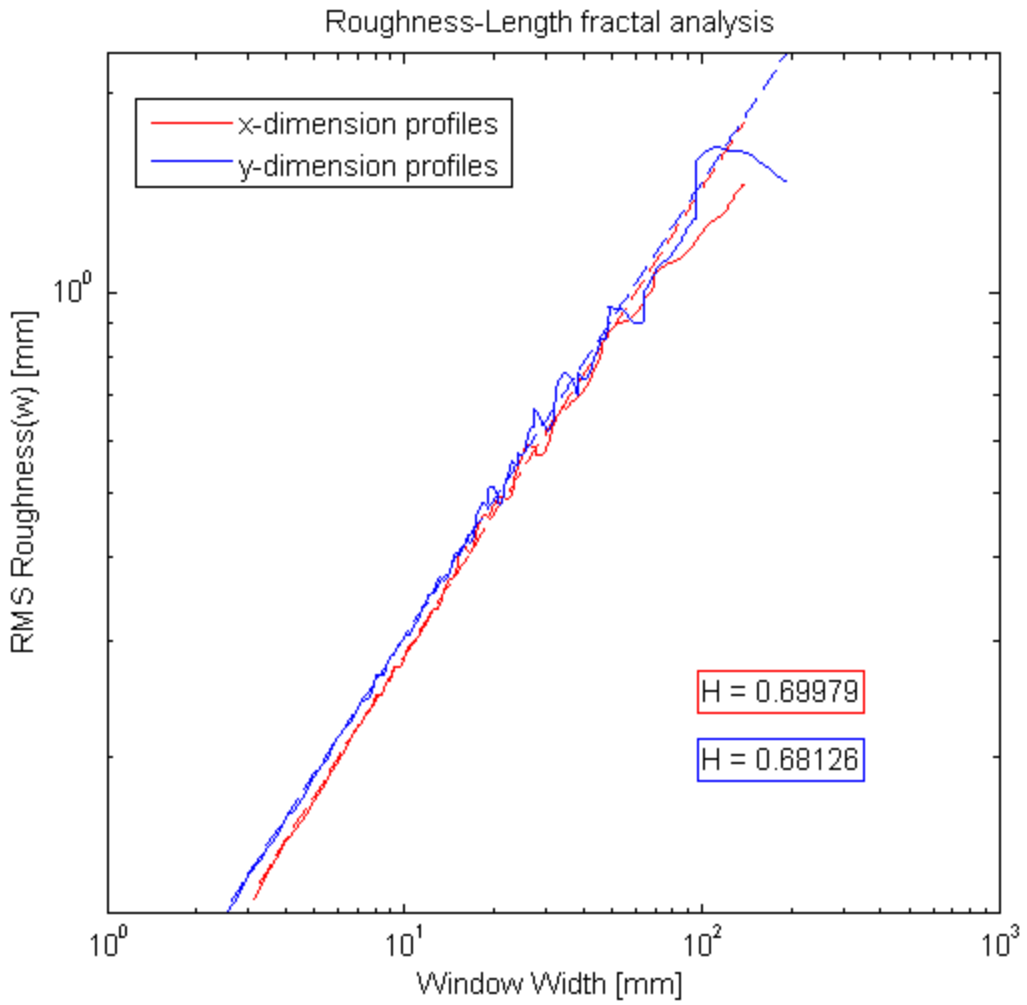

Figure 4.13 Plot of the mean Roughness-Length values for profiles parallel to the *x* and *y* dimensions for granite fracture surface sample FR-MnO. Also included are the Hurst exponents which describe the fractal behavior.

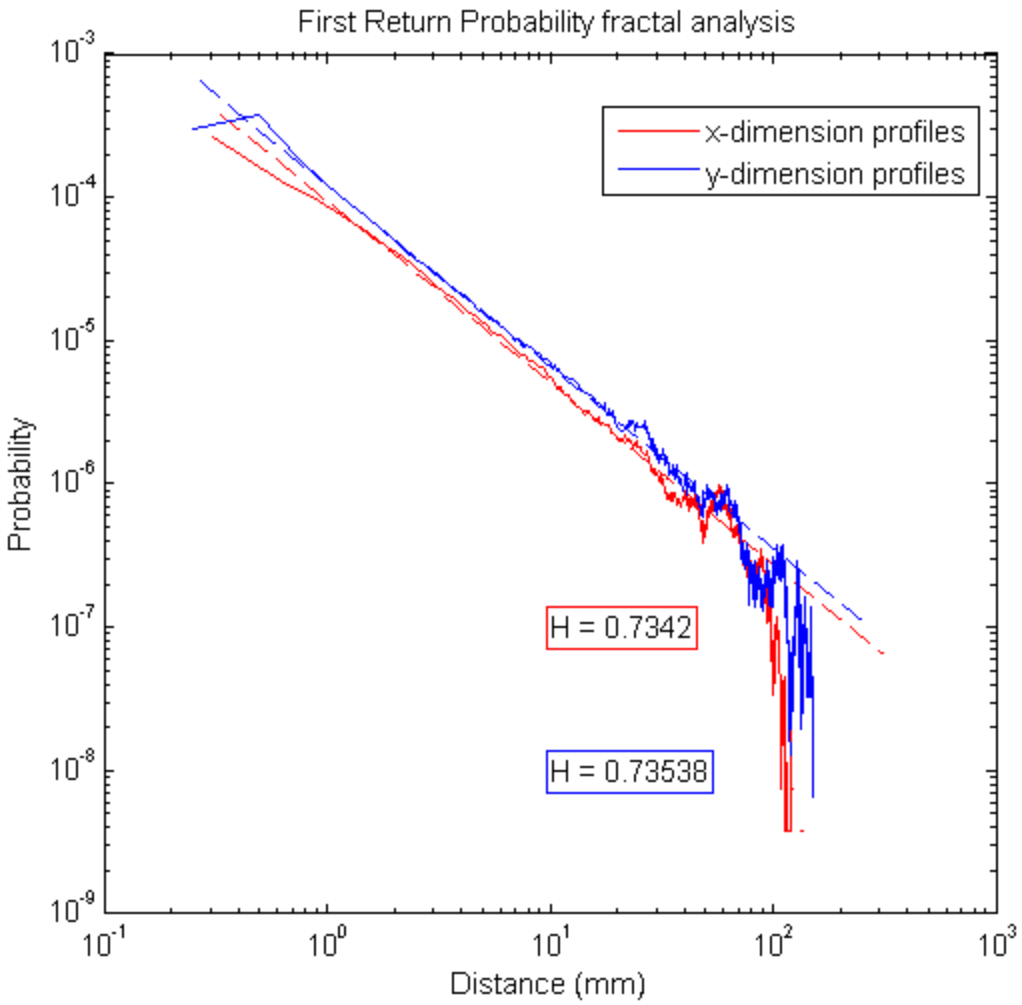

Figure 4.14 Plot of the mean First Return Probability values for profiles parallel to the *x* and *y* dimensions for granite fracture surface sample FR-MnO. Also included are the Hurst exponents which describe the fractal behavior.

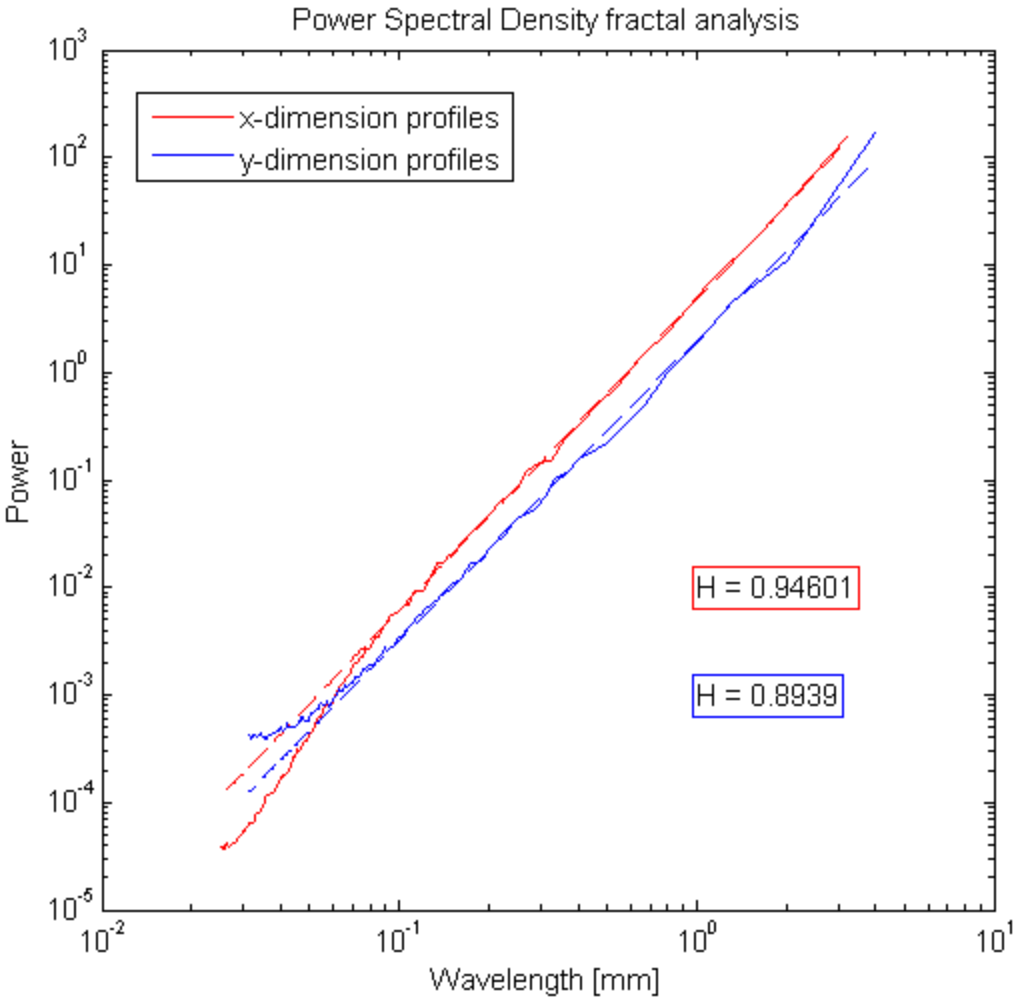

Figure 4.15 Plot of the mean Power Spectral Denisty values for profiles parallel to the *x* and *y* dimensions for granite fracture surface sample FR-MnO. Also included are the Hurst exponents which describe the fractal behavior.

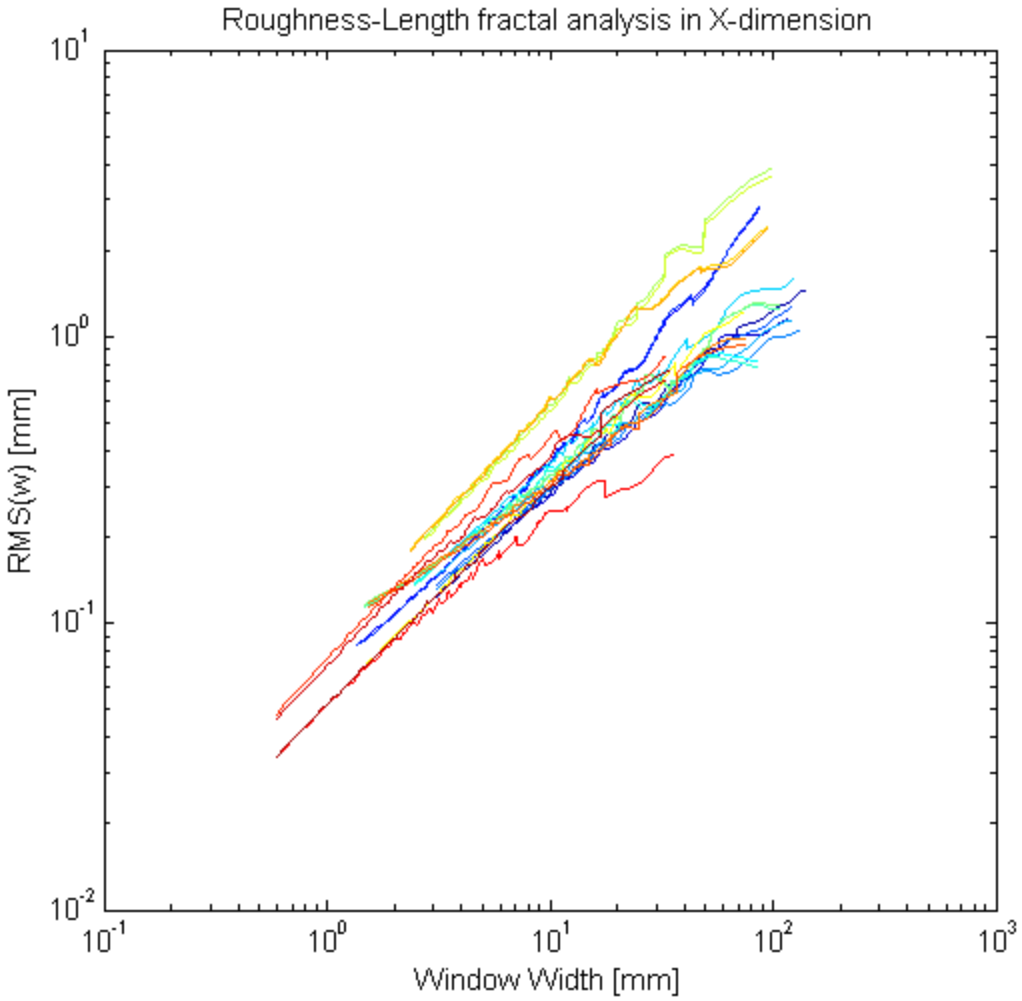

Figure 4.16 Roughness-length fractal analysis for all fracture surface samples in the *x*-dimension. Each colored line represents a different fracture surface.

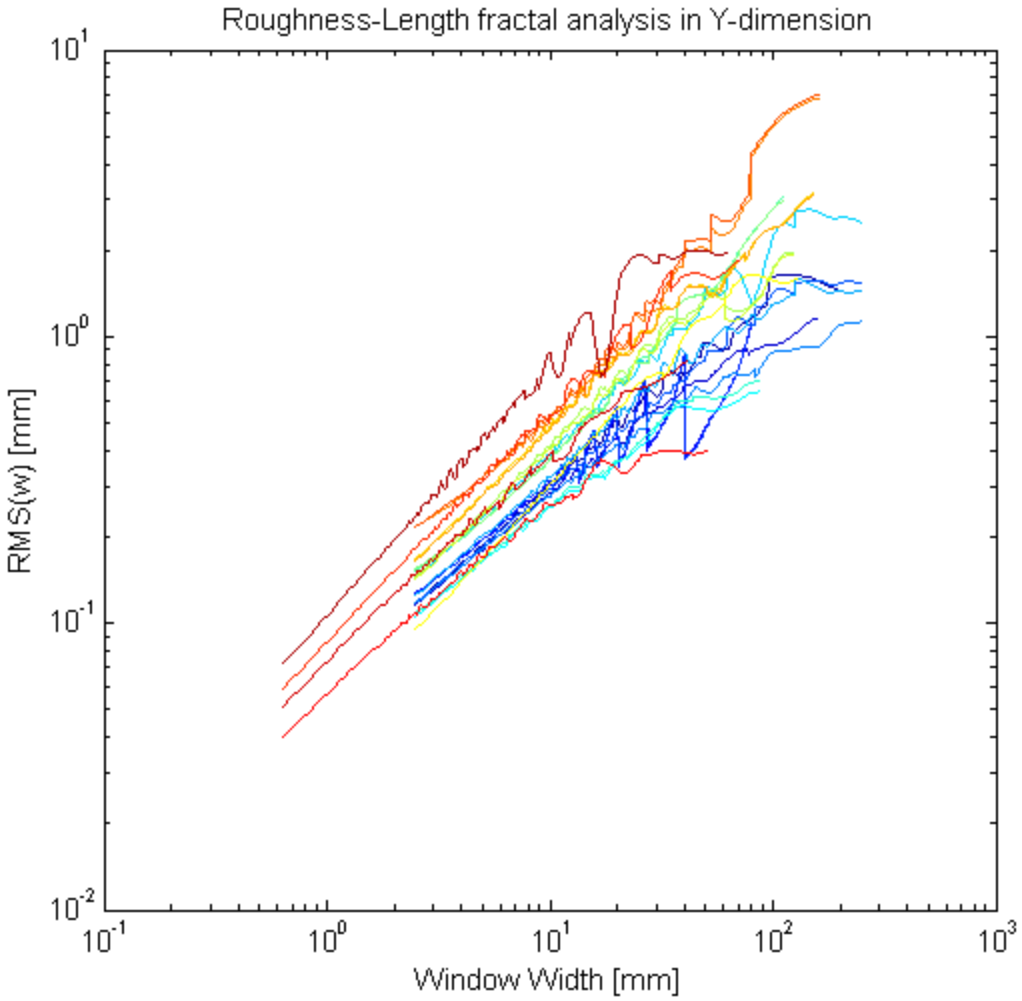

Figure 4.17 Roughness-length fractal analysis for all fracture surface samples in the *y*-dimension. Each colored line represents a different fracture surface.

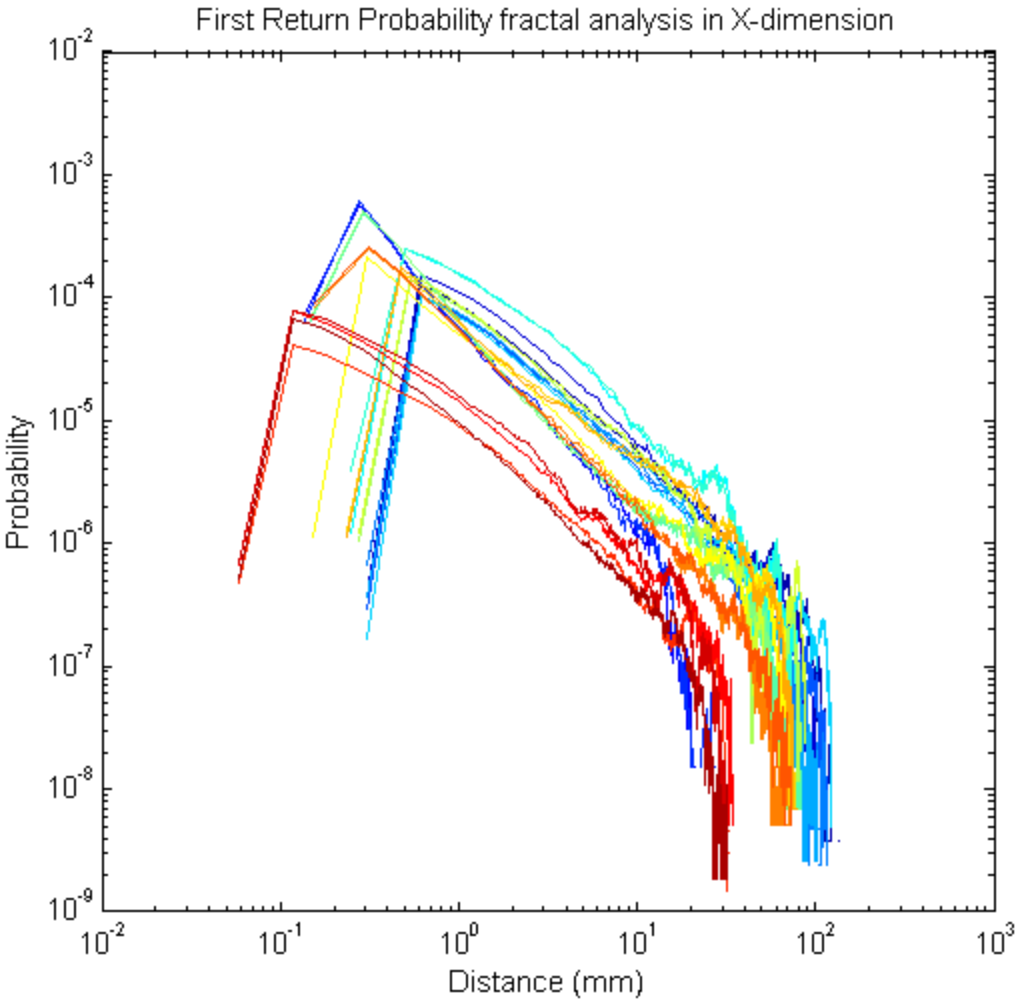

Figure 4.18 First return probability fractal analysis for all fracture surface samples in the *x*-dimension. Each colored line represents a different fracture surface.

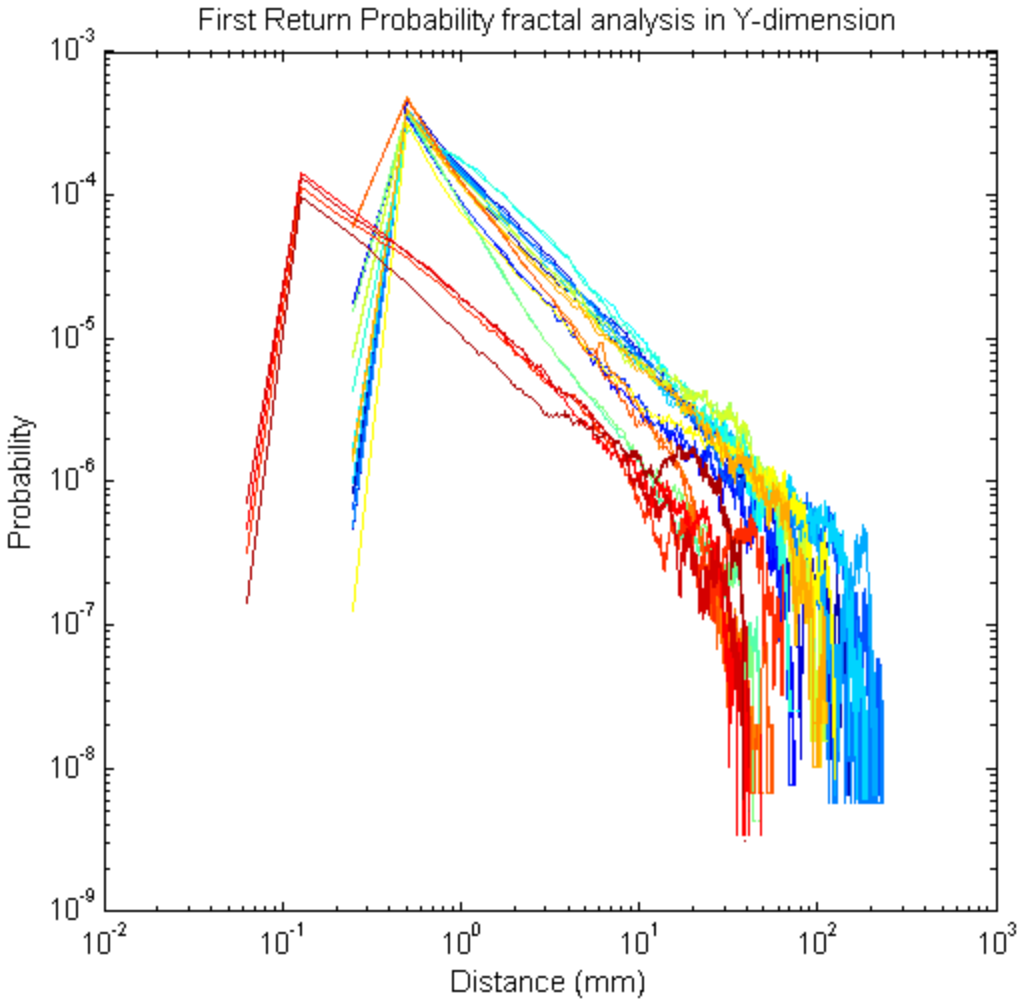

Figure 4.19 First return probability fractal analysis for all fracture surface samples in the *y*-dimension. Each colored line represents a different fracture surface.

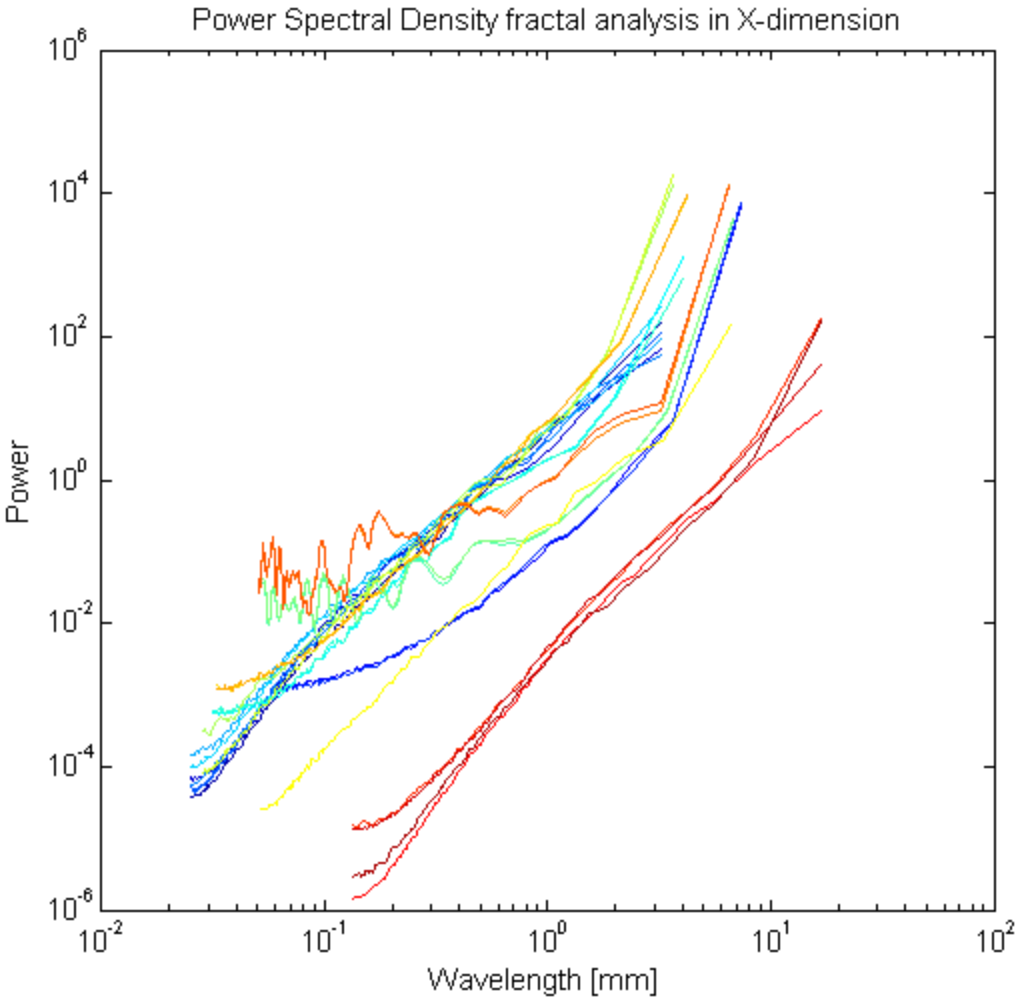

Figure 4.20 Power spectral density fractal analysis for all fracture surface samples in the *x*-dimension. Each colored line represents a different fracture surface.

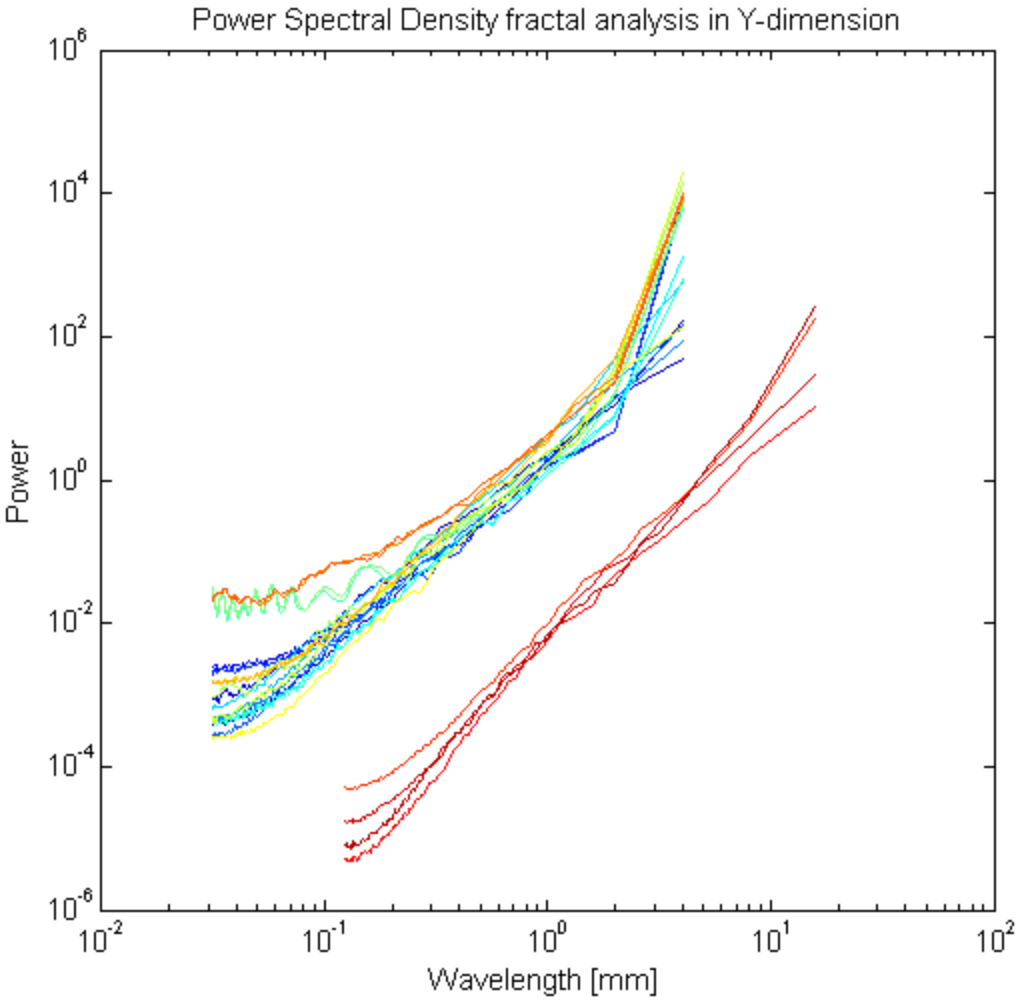

Figure 4.21 Power spectral density fractal analysis for all fracture surface samples in the *y*-dimension. Each colored line represents a different fracture surface.

4.9 MAXIMIZED APERTURE

Scaling fracture aperture is a difficult obstacle that may never be overcome. However, because fracture surface roughness is observed to be fractal and follows a power law, the maximized aperture fracture model may allow a maximum aperture limit to be determined depending on the fracture length-scale of interest. This section addresses this hypothesis. Two methods for generating the maximized aperture fracture are implemented: the reflected and translated methods, which are discussed in Section 3.7.

Commonly, only one surface is available to sample a fracture. In Section 4.4 the surface roughness characterizations of mated fractures is shown to be nearly identical. In Figure 4.24, the maximized aperture fracture is generated for both the top and bottom surfaces for the mated fractures. The maximized aperture fracture for the mated surfaces is shown to have nearly identical arithmetic mean apertures. This result shows that a maximized aperture fracture model can be generated from either mated surface without risking different results.

Even though the maximized aperture fracture is presented as a tool to constrain the fracture aperture, it is not expected to be similar to or have any correlation with the actual fracture aperture. The maximized aperture analysis provides an upper limit on a potential fracture aperture, based on the measurement of a single fracture surface. In Figure 4.25, the arithmetic mean of the maximized aperture is plotted against the real mechanical aperture for the set of mated fracture surfaces. As expected, no correlation is found to exist between the two values.

The fractal scaling of fracture surface roughness is potentially a powerful tool to predict flow through fractures. Finding a correlation between the RMS roughness and the maximized aperture allows fracture aperture to be constrained depending on length-scale. Figure 4.26 is a plot of the RMS roughness versus the arithmetic mean of the maximized aperture fracture model for all surfaces in the HRXCT dataset. Both the reflected and

translated maximized aperture models display a strong correlation with the RMS roughness of a surface.

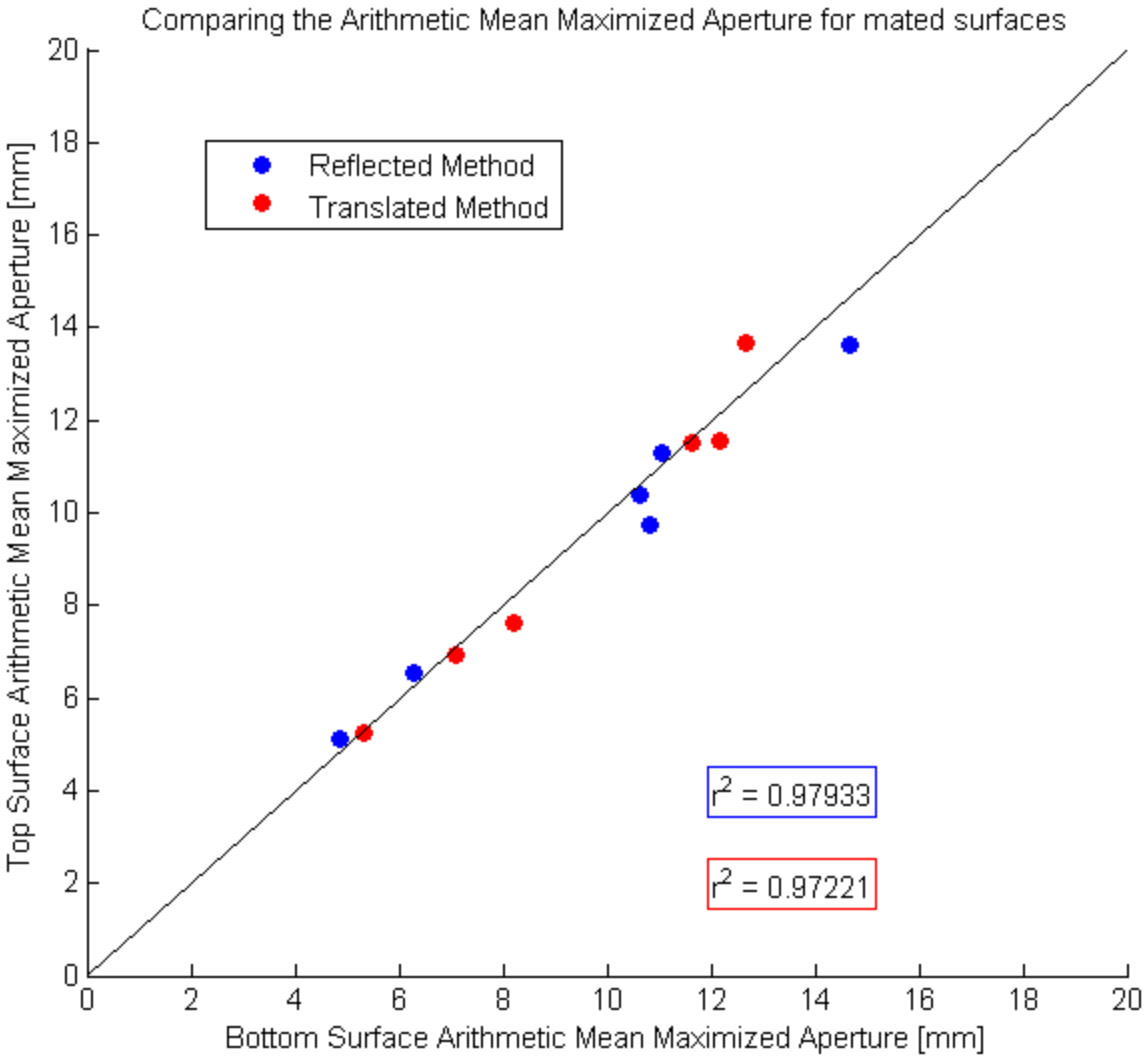

Figure 4.22 The maximized arithmetic mean apertures for each matched surface in all mated fractures are plotted against each other. A 1:1 line is also plotted for comparison. Two different methods are used to generate the maximized aperture. The reflected method is plotted in blue and the translated method is plotted in red.

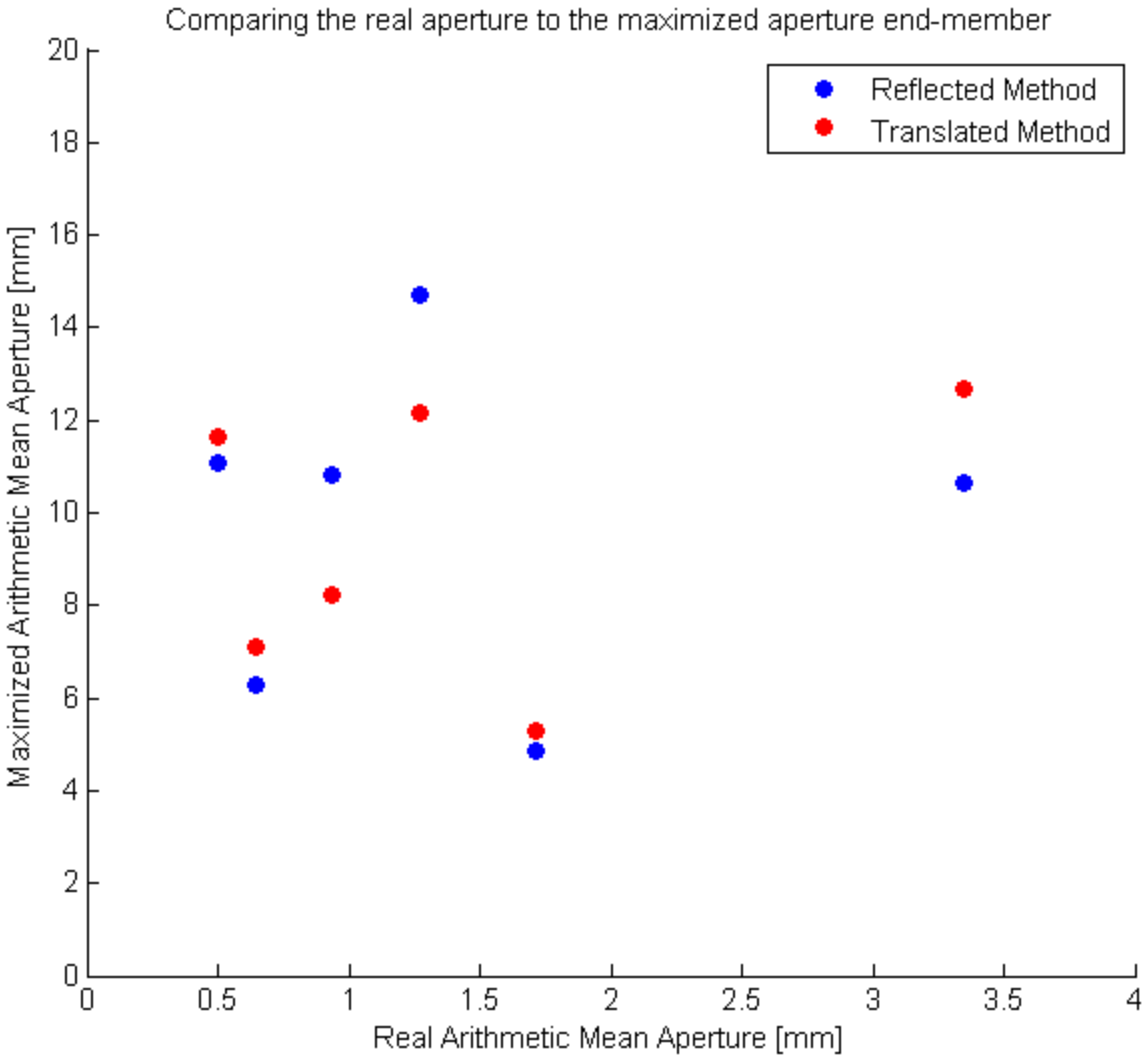

Figure 4.23 Scatter plot of the real arithmetic mean aperture versus the maximized arithmetic mean aperture determined from one surface illustrating that no correlation exist between them. Two different methods are used to generate the maximized aperture. The reflected method is plotted in blue and the translated method is plotted in red.

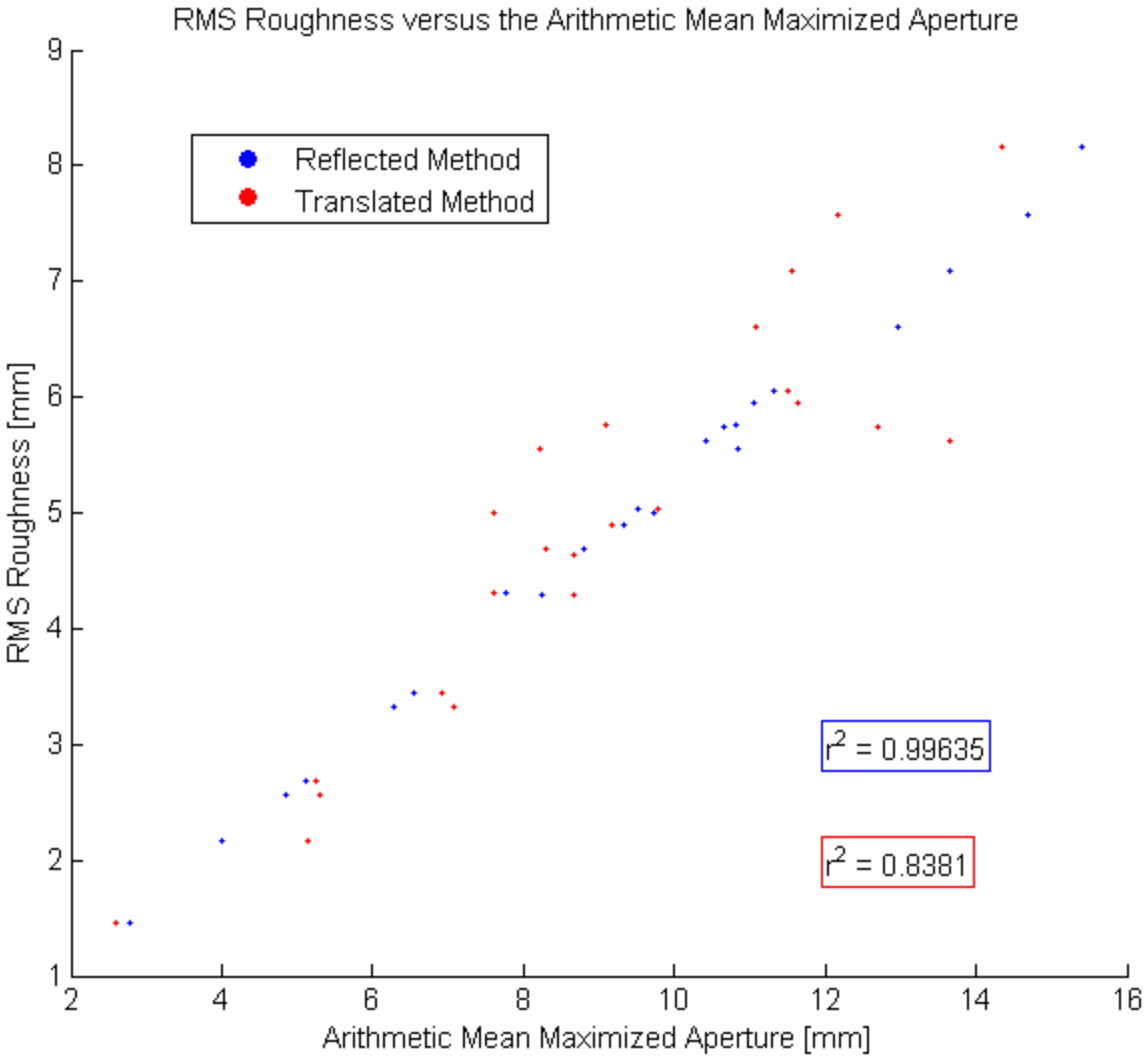

Figure 4.24 The RMS Roughness is plotted against the arithmetic mean maximized aperture for all surfaces in the dataset (mated and unmated). A strong correlation is observed. Two different methods are used to generate the maximized aperture. The reflected method is plotted in blue and the translated method is plotted in red.

Chapter 5: Conclusions

Predicting flow through fractures requires an understanding of how fracture morphology changes with scale. In a hydrogeologic sense, fractures consist of two rough surfaces, in contact and sometimes in a state of compression or shear displacement. Fractures are the result of brittle deformation (mechanical fracturing) but, for hydrogeologists, any sort of crack, such as between bedding plane partings through which fluids can flow is essentially a fracture.

The fracture aperture is the length-separation between the two rough surfaces. From the cubic law, the solution to flow between parallel plates, the discharge through a parallel plate fracture is proportional to the cube of the aperture. If the fracture surfaces are parallel to each other at a global scale, the aperture is determined by the mean separation between the two surfaces as well as the effect of the combined roughness of the two surfaces and their arrangement. However, often the two surfaces are found to be in contact at some points. In this case, the minimum separation between the two surfaces is zero and the aperture exists solely due to the effect of the combined roughness of the two surfaces and their arrangement.

Scaling fracture aperture from a sub-sample of a fracture is a difficult challenge which has yet been overcome because of the difficulty in predicting how the effect of the combined roughness of the surfaces and the arrangement of the surfaces changes with scale. However, rough surfaces are more easily characterized and fracture surfaces are observed to scale as a power law. While not providing an exact prediction, characterizing the roughness of fracture surfaces may allow a fracture aperture to be constrained between zero and a maximum value, given certain assumptions are valid. In this study, I characterize fracture surfaces measured with high-resolution x-ray computed tomography (HRXCT) using five different statistical metrics and perform fractal analysis using three different methods for both unmated and mated fracture surfaces.

It is often difficult to collect both surfaces when sampling a natural rock fracture. One hypothesis I test is to determine if mated fracture surfaces exhibit similar roughness characteristics. Figure 4.10 clearly shows that, for the five roughness metrics implemented, the fracture surfaces follow a strong 1:1 relationship. Though this hypothesis is intuitive, the experimental observation provides conclusive validity. The result is useful for studies of fracture morphology and necessary characterizations of specific fractures where collecting only half of a fracture is feasible.

Five different surface roughness metrics are implemented to characterize fracture surfaces: the surface to footprint ratio, the RMS roughness, the surface skewness, the surface kurtosis, and the RMS slope. They do not scale similarly. The surface to footprint ratio appears to reach statistical stationarity at hand-sample size scale, with the variance between sub-samples being very low. Furthermore, the surface to footprint ratio has a very strong correlation with the RMS slope, suggesting that these two parameters measure very similar properties. The RMS roughness is shown to be fractal. No direct correlation was found between aperture and surface roughness. The relationship between these two fracture properties is very complex.

Measuring aperture for rough rock fractures is not straightforward. Aperture in a rock fracture is not constant and varies widely. Calculating discharge with the Reynolds equation (the local cubic law) requires knowing the aperture locally throughout the fracture. Calculating discharge using the cubic law equation for flow between parallel plates requires finding an approximation for the hydraulic aperture. The traditional method to measure the local aperture is to simply find the difference in surface height elevation for the top and bottom surfaces. The arithmetic mean of the local aperture measured in this way is known as the mechanical aperture. The mechanical aperture is generally greater than the hydraulic aperture.

While this method of measuring the local aperture is intuitive for parallel plates, rough rock fracture may require a more sophisticated approach. Additionally, the arithmetic mean may not be the correct average to estimate the hydraulic aperture. Slottke (2010) shows that the geometric mean better predicts the hydraulic aperture. In

this study, I implement Mourzenko et al. (1995)'s method to measure the local aperture. Finding the difference in surface height elevations between the top and bottom surfaces calculates the *apparent* aperture, but not the *true* aperture. The Mourzenko aperture is measured by finding the largest diameter circle or sphere that is tangent to the two fracture surfaces. I also calculate the geometric and harmonic means of the apparent aperture. For the fractures in this study, the arithmetic mean of the apparent local aperture, the mechanical aperture, is always the largest aperture. All of the various aperture metrics produce similar values, but there are no consistent trends to differentiate them.

Three different methods of fracture analysis are used to determine whether the fracture surfaces collected for this study scale as a power law. Even though the fracture surfaces are natural and have been affected by secondary processes after their mechanical genesis in the form of fracture skin, all of the fracture surfaces are fractal. However, two of the fractal analysis methods are sensitive to the sampling resolution of the surface height data: the Power Spectral Density method and the First Return Probability method. The lines for surfaces sampled at an order of magnitude finer resolution are displaced from the group of other surfaces. For the Roughness-Length fractal analysis method, the finer-resolution measured surfaces simply plot over a different range of scale.

The Roughness-Length fractal analysis method computed the RMS roughness for surface profiles of widths across scales. The power law behavior of the RMS roughness is a useful result for scaling fracture morphology. The RMS roughness correlates strongly with two models to determine the maximum mean aperture of a fracture based on the roughness of its surfaces. Computing the RMS roughness and determining its scaling behavior for a given fracture surface sample allows fracture roughness to be predicted based on the fracture length-scale of interest.

By finding the roughness scaling law of a fracture and with knowledge of the fracture's length, a maximum aperture can be computed to constrain the potential permeability of the fracture. For example, these results suggest that the maximum mean aperture for a fracture one kilometer long can be constrained based on a hand-sample of

one of the fracture surfaces. Fracture permeability is controlled by aperture, so the permeability of a fracture would be constrained by finding the maximum aperture that could exist for any particular length fracture. Predicting fracture permeability in a field-scale setting is exceptionally difficult and the methods formulated in this study provide additional tools to apply when real data is limited and direct methods of measurement are not possible.

Appendix A: IDL Code

```
; MMA_AIR_ROCK estimates the x-ray attenuation values of air and rock
; using histograms of different bin sizes.  The maximum value of air
; and minimum value of rock are necessary for resolving the fracture
; surface.

PRO MMA_AIR_ROCK,tiffdirectory
hstack = B3D_ReadTiffs('tif',directory=tiffdirectory,/NO_LOOK, /NOPTR)
szstack=SIZE(hstack)
minrock = FLTARR(1)
maxair= FLTARR(1)

FOR i=1,10 DO BEGIN
minrock = FLTARR(1)
maxair= FLTARR(1)
binsz=i*1000
hist=HISTOGRAM(hstack[*,*,*],BINSIZE=binsz,min=5, max=max(hstack))
window,i
plot,hist
szhist = SIZE(hist)
onepercent=TOTAL(hist)*.01
x=FINDGEN(szhist(1))^0
y=onepercent*x
oplot,y
limit = WHERE(hist GT onepercent)
szlimit=SIZE(limit)
k=0
WHILE maxair EQ 0 DO BEGIN
IF limit[k+1]-limit[k] GT 1 THEN BEGIN
  maxair=(limit[k])*binsz
  minrock=(limit[k+1])*binsz
  avgair=MEAN([limit[k]*binsz,limit[0]*binsz])
  avgrock=MEAN([limit[k+1]*binsz,limit[(szlimit[1]-1)]*binsz])
  midpt=MEAN([avgair,avgrock],/DOUBLE)
ENDIF
k=k+1
ENDWHILE
print,"Bin Size: ",binsz," Minrock: ",minrock," Maxair: ", maxair,"
Midpt: ", midpt
ENDFOR
END

; MMA_MASTER_SURFACE is the master procedure for resolving the fracture
; surface from the CT data and outputting in text files.

PRO MMA_MASTER_SURFACE, xzres, yres, filename, filedirectory,
maxair,minrock
print, "Reading in the TIFFS"
```

```
stack = B3D_READTIFFS("tif", directory=filedirectory, /NO_LOOK,/NOPTR)
stack=reverse(stack,2)
print, "Getting the raw surface"
MMA_GET_RAW_SURFACE, stack, surf, xzres, yres, maxair, minrock, xvect,
yvect

OPENW,ounit,filename+".txt", /GET_LUN
szxvect=SIZE(xvect)
szyvect=SIZE(yvect)
PRINTF, ounit, "x","  ","y"," ","z"
FOR j=0,szyvect[1]-1 DO BEGIN
  FOR k=0,szxvect[1]-1 DO BEGIN
    PRINTF, ounit, xvect[k], yvect[j], surf[k,j]
  ENDFOR
ENDFOR
FREE_LUN,ounit

print, "Finished"
END

; MMA_GET_RAW_SURFACE Retrieves the top surface from a stack of sliced
; rock. This is the actual surface on the rock, including the planar
; trend. Modified from RK_GetVertSurface.pro

PRO MMA_GET_RAW_SURFACE, stack, surf, xzres, yres,maxair,minrock,
xvect, yvect
szstack=SIZE(stack)
surf=FLTARR(szstack[1],szstack[3])

midpt=MEAN([maxair,minrock])
FOR i=0,szstack[1]-1 DO BEGIN
  FOR j=0,szstack[3]-1 DO BEGIN
     line = REFORM(stack[i,*,j])
     k=0
     WHILE (line[k] LT midpt) DO k=k+1
     interface = k - 1.0 + float(line[k] - line[k-1])/float(line[k] -
maxair)
     surf[i,j] = (szstack[2]-interface) * xzres
  ENDFOR
ENDFOR

xvect=FINDGEN(szstack[1])*xzres
yvect=FINDGEN(szstack[3])*yres
SHADE_SURF,surf,xvect,yvect
END

; MMA_MASTER_FRACTURE is the master procedure to resolve the fracture
; of interest in the CT image slices and output the surface topography
; to text files.

PRO MMA_MASTER_FRACTURE, rockmin, airmax, xzres, yres, filename,
tiffdirectory
```

```
start=SYSTIME(/SECONDS)
print, "Reading in the TIFFS"
stack = B3D_READTIFFS("tif",directory=tiffdirectory, /NO_LOOK,/NOPTR)

print, "Getting the raw surface"
MMA_GET_RAW_FRACTURE,stack,rockmin,airmax,
topsurf,botsurf,xzres,yres,xvect,yvect

OPENW,ounit,filename+"topsurf.txt", /GET_LUN
szxvect=SIZE(xvect)
szyvect=SIZE(yvect)
PRINTF, ounit, "x","  ","y"," ","z"
FOR j=0,szyvect[1]-1 DO BEGIN
  FOR k=0,szxvect[1]-1 DO BEGIN
    PRINTF, ounit, xvect[k], yvect[j], topsurf[k,j]
  ENDFOR
ENDFOR
FREE_LUN,ounit

OPENW,ounit,filename+"botsurf.txt", /GET_LUN
szxvect=SIZE(xvect)
szyvect=SIZE(yvect)
PRINTF, ounit, "x","  ","y"," ","z"
FOR j=0,szyvect[1]-1 DO BEGIN
  FOR k=0,szxvect[1]-1 DO BEGIN
    PRINTF, ounit, xvect[k], yvect[j], botsurf[k,j]
  ENDFOR
ENDFOR
FREE_LUN,ounit

print, "Finished"
stop= SYSTIME(/SECONDS)
print,stop-start
END

; MMA_GET_RAW_FRACTURE retrieves the fracture surfaces from a stack of
; CT image slices.  Fracture tracing is done in six different
; direction, then different combinations are computed.  The user must ;
; pick the best one to use for picking the fracture surface.
; Modified from RK_GetVertSurface.pro

PRO MMA_GET_RAW_FRACTURE, stack, rockmin, airmax, topsurf, botsurf,
xzres, yres, xvect, yvect
midpt=mean([rockmin,airmax])
szstack=SIZE(stack)
topsurf=FLTARR(szstack[1],szstack[3])
botsurf=topsurf
midcrack=[[[topsurf]],[[topsurf]],[[topsurf]],[[topsurf]]]
; PART ONE: Finding the middle of the fracture
stacko=stack
stack1=reverse(stacko,3)
stack3=reverse(stacko,1)
```

```
tiny=0
wo=7
FOR j=0,szstack[3]-1 DO BEGIN
   FOR i=0,szstack[1]-1 DO BEGIN
       IF (i EQ 0) AND (j EQ 0) THEN BEGIN
         line = REFORM(stacko[i,*,j])
         minVal = Min(line, mid)
         midcrack[i,j,0]=mid
         line = REFORM(stack1[i,*,j])
         minVal = Min(line, mid)
         midcrack[i,j,1]=mid
         line = REFORM(stacko[i,*,j])
         minVal = Min(line, mid)
         midcrack[i,j,2]=mid
         line = REFORM(stack3[i,*,j])
         minVal = Min(line, mid)
         midcrack[i,j,3]=mid
       ENDIF ELSE IF i EQ 0 THEN BEGIN
         wb=wo
         wf=wo
IF (midcrack[i,j-1,0]-wo) LE 0 THEN wb = wo-abs(midcrack[i,j-1,0]-wo)-1
IF (midcrack[i,j-1,0]+wo) GE szstack[2]-1 THEN wf = wo-abs(szstack[2]-
wo-midcrack[i,j-1,0]-1)-1
1,0]+wf),j])
         minVal = Min(line, mid)
         midcrack[i,j,0]=mid+(midcrack[i,j-1,0]-wb)
         wb=wo
         wf=wo
IF (midcrack[i,j-1,1]-wo) LE 0 THEN wb = wo-abs(midcrack[i,j-1,1]-wo)-1
IF (midcrack[i,j-1,1]+wo) GE szstack[2]-1 THEN wf = wo-abs(szstack[2]-
wo-midcrack[i,j-1,1]-1)-1
line = REFORM(stack1[i,(midcrack[i,j-1,1]-wb):(midcrack[i,j-
1,1]+wf),j])
         minVal = Min(line, mid)
         midcrack[i,j,1]=mid+(midcrack[i,j-1,1]-wb)
         wb=wo
         wf=wo
IF (midcrack[i,j-1,2]-wo) LE 0 THEN wb = wo-abs(midcrack[i,j-1,2]-wo)-1
         IF (midcrack[i,j-1,2]+wo) GE szstack[2]-1 THEN wf = wo-
abs(szstack[2]-wo-midcrack[i,j-1,2]-1)-1
         line = REFORM(stacko[i,(midcrack[i,j-1,2]-wb):(midcrack[i,j-
1,2]+wf),j])
         minVal = Min(line, mid)
         midcrack[i,j,2]=mid+(midcrack[i,j-1,2]-wb)
         wb=wo
         wf=wo
IF (midcrack[i,j-1,3]-wo) LE 0 THEN wb = wo-abs(midcrack[i,j-1,3]-wo)-1
         IF (midcrack[i,j-1,3]+wo) GE szstack[2]-1 THEN wf = wo-
abs(szstack[2]-wo-midcrack[i,j-1,3]-1)-1
         line = REFORM(stack3[i,(midcrack[i,j-1,3]-wb):(midcrack[i,j-
1,3]+wf),j])
         minVal = Min(line, mid)
```

```
          midcrack[i,j,3]=mid+(midcrack[i,j-1,3]-wb)
        ENDIF ELSE IF j EQ 0 THEN BEGIN
          wb=wo
          wf=wo
          IF (midcrack[i-1,j,0]-wo) LE 0 THEN wb = wo-abs(midcrack[i-
1,j,0]-wo)-1
          IF (midcrack[i-1,j,0]+wo) GE szstack[2]-1 THEN wf = wo-
abs(szstack[2]-wo-midcrack[i-1,j,0]-1)-1
          line = REFORM(stacko[i,(midcrack[i-1,j,0]-wb):(midcrack[i-
1,j,0]+wf),j])
          minVal = Min(line, mid)
          midcrack[i,j,0]=mid+(midcrack[i-1,j,0]-wb)
          wb=wo
          wf=wo
          IF (midcrack[i-1,j,1]-wo) LE 0 THEN wb = wo-abs(midcrack[i-
1,j,1]-wo)-1
          IF (midcrack[i-1,j,1]+wo) GE szstack[2]-1 THEN wf = wo-
abs(szstack[2]-wo-midcrack[i-1,j,1]-1)-1
          line = REFORM(stack1[i,(midcrack[i-1,j,1]-wb):(midcrack[i-
1,j,1]+wf),j])
          minVal = Min(line, mid)
          midcrack[i,j,1]=mid+(midcrack[i-1,j,1]-wb)
          wb=wo
          wf=wo
          IF (midcrack[i-1,j,2]-wo) LE 0 THEN wb = wo-abs(midcrack[i-
1,j,2]-wo)-1
          IF (midcrack[i-1,j,2]+wo) GE szstack[2]-1 THEN wf = wo-
abs(szstack[2]-wo-midcrack[i-1,j,2]-1)-1
          line = REFORM(stacko[i,(midcrack[i-1,j,2]-wb):(midcrack[i-
1,j,2]+wf),j])
          minVal = Min(line, mid)
          midcrack[i,j,2]=mid+(midcrack[i-1,j,2]-wb)
          wb=wo
          wf=wo
          IF (midcrack[i-1,j,3]-wo) LE 0 THEN wb = wo-abs(midcrack[i-
1,j,3]-wo)-1
          IF (midcrack[i-1,j,3]+wo) GE szstack[2]-1 THEN wf = wo-
abs(szstack[2]-wo-midcrack[i-1,j,3]-1)-1
          line = REFORM(stack3[i,(midcrack[i-1,j,3]-wb):(midcrack[i-
1,j,3]+wf),j])
          minVal = Min(line, mid)
          midcrack[i,j,3]=mid+(midcrack[i-1,j,3]-wb)
        ENDIF ELSE BEGIN
          wb=wo
          wf=wo
          IF (midcrack[i,j-1,0]-wo) LE 0 THEN wb = wo-abs(midcrack[i,j-
1,0]-wo)-1
          IF (midcrack[i,j-1,0]+wo) GE szstack[2]-1 THEN wf = wo-
abs(szstack[2]-wo-midcrack[i,j-1,0]-1)-1
          line = REFORM(stacko[i,(midcrack[i,j-1,0]-wb):(midcrack[i,j-
1,0]+wf),j])
          minVal = Min(line, mid)
```

```
          midcrack[i,j,0]=mid+(midcrack[i,j-1,0]-wb)
          wb=wo
          wf=wo
          IF (midcrack[i,j-1,1]-wo) LE 0 THEN wb = wo-abs(midcrack[i,j-
1,1]-wo)-1
          IF (midcrack[i,j-1,1]+wo) GE szstack[2]-1 THEN wf = wo-
abs(szstack[2]-wo-midcrack[i,j-1,1]-1)-1
          line = REFORM(stack1[i,(midcrack[i,j-1,1]-wb):(midcrack[i,j-
1,1]+wf),j])
          minVal = Min(line, mid)
          midcrack[i,j,1]=mid+(midcrack[i,j-1,1]-wb)
          wb=wo
          wf=wo
          IF (midcrack[i-1,j,2]-wo) LE 0 THEN wb = wo-abs(midcrack[i-
1,j,2]-wo)-1
          IF (midcrack[i-1,j,2]+wo) GE szstack[2]-1 THEN wf = wo-
abs(szstack[2]-wo-midcrack[i-1,j,2]-1)-1
          line = REFORM(stacko[i,(midcrack[i-1,j,2]-wb):(midcrack[i-
1,j,2]+wf),j])
          minVal = Min(line, mid)
          midcrack[i,j,2]=mid+(midcrack[i-1,j,2]-wb)
          wb=wo
          wf=wo
          IF (midcrack[i-1,j,3]-wo) LE 0 THEN wb = wo-abs(midcrack[i-
1,j,3]-wo)-1
          IF (midcrack[i-1,j,3]+wo) GE szstack[2]-1 THEN wf = wo-
abs(szstack[2]-wo-midcrack[i-1,j,3]-1)-1
          line = REFORM(stack3[i,(midcrack[i-1,j,3]-wb):(midcrack[i-
1,j,3]+wf),j])
          minVal = Min(line, mid)
          midcrack[i,j,3]=mid+(midcrack[i-1,j,3]-wb)
        ENDELSE
        ENDFOR
ENDFOR

midcrack[*,*,1]=reverse(midcrack[*,*,1],2)
midcrack[*,*,3]=reverse(midcrack[*,*,3],1)
midcrackm=FLTARR(szstack[1],szstack[3],3)
midcrackm[0:floor((szstack[1]-1)/2),*,0]=midcrack[0:floor((szstack[1]-
1)/2),*,2]
midcrackm[ceil((szstack[1]-1)/2):(szstack[1]-
1),*,0]=midcrack[ceil((szstack[1]-1)/2):(szstack[1]-1),*,3]
midcrackm[*,0:floor((szstack[3]-
1)/2),1]=midcrack[*,0:floor((szstack[3]-1)/2),2]
midcrackm[*,ceil((szstack[3]-1)/2):(szstack[3]-
1),1]=midcrack[*,ceil((szstack[3]-1)/2):(szstack[3]-1),3]

FOR j=0,szstack[3]-1 DO BEGIN
   FOR i=0,szstack[1]-1 DO BEGIN
   IF midcrackm[i,j,1]-midcrackm[i,j,0] NE 0 AND i NE 0 AND j NE 0 AND
j NE szstack[3]-1 AND i NE szstack[1]-1 THEN BEGIN
```

```
    midcrackm[i,j,2]=median([midcrackm[i-1,j-1,0],midcrackm[i-1,j-
1,1],midcrackm[i-1,j+1,0],midcrackm[i-1,j+1,1],midcrackm[i+1,j-
1,0],midcrackm[i+1,j-1,1],midcrackm[i+1,j+1,0],midcrackm[i+1,j+1,1]])
   ENDIF ELSE IF midcrackm[i,j,1]-midcrackm[i,j,0] NE 0 AND j EQ 0 AND
i NE 0 AND i NE szstack[1]-1 THEN BEGIN
    midcrackm[i,j,2]=median([midcrackm[i-
1,j+1,0],midcrackm[i+1,j+1,1]])
   ENDIF ELSE IF midcrackm[i,j,1]-midcrackm[i,j,0] NE 0 AND i EQ 0 AND
j NE 0 AND j NE szstack[3]-1 THEN BEGIN
    midcrackm[i,j,2]=median([midcrackm[i+1,j-
1,0],midcrackm[i+1,j+1,1]])
   ENDIF ELSE IF midcrackm[i,j,1]-midcrackm[i,j,0] NE 0 AND j EQ
szstack[3]-1 AND i NE 0 AND i NE szstack[1]-1 THEN BEGIN
    midcrackm[i,j,2]=median([midcrackm[i-1,j-1,0],midcrackm[i+1,j-
1,1]])
   ENDIF ELSE IF midcrackm[i,j,1]-midcrackm[i,j,0] NE 0 AND i EQ
szstack[1]-1 AND j NE 0 AND j NE szstack[3]-1 THEN BEGIN
    midcrackm[i,j,2]=median([midcrackm[i-1,j+1,0],midcrackm[i-1,j-
1,1]])
   ENDIF ELSE midcrackm[i,j,2]=midcrackm[i,j,0]
   ENDFOR
ENDFOR

stack=stacko
xvect=FINDGEN(szstack[1])*xzres
yvect=FINDGEN(szstack[3])*yres
window, 1
SHADE_SURF,(szstack[3]-midcrack[*,*,1])*xzres,xvect,yvect
midcrack=midcrack[*,*,1]

; PART TWO: Finding the surfaces from the middle of the fracture
FOR j=0,szstack[3]-1 DO BEGIN
  FOR i=0,szstack[1]-1 DO BEGIN
     line = REFORM(stack[i,*,j])
     b=midcrack[i,j]
     t=midcrack[i,j]
     ma=midcrack[i,j]
     WHILE (line[t] LT rockmin) AND t GT 0 DO t=t-1
     WHILE (line[b] LT rockmin) AND b LT szstack[2]-1 DO b=b+1
     bot=b-1+float(line[b]-line[b-1])/float(line[b]-airmax)
     top=t+1-float(line[t]-line[t+1])/float(line[t]-airmax)
     topsurf[i,j]=(szstack[2]-top)*xzres
     botsurf[i,j]=(szstack[2]-bot)*xzres
  ENDFOR
ENDFOR

window, 2
SHADE_SURF,topsurf,xvect,yvect
window, 3
SHADE_SURF,botsurf,xvect,yvect

END
```

Appendix B: MATLAB Code

```
function [] = figures()
close all
tic
directory='D:\IDL\';
surfaces=importdata('surfaces.txt');
fractures=importdata('fractures.txt');

% Section 4.1: Probability Distribution of Surface Heights
for i=1:length(surfaces)
    m=importdata(char(strcat(directory,surfaces(i),'.txt')));
    [surf,dx,dy]=get_surf(m.data(:,1),m.data(:,2),m.data(:,3));
    surf=remove_planar_trend(surf,dx,dy);
    szsurf=size(surf);
    [n,xout]=hist(reshape(surf,1,szsurf(1)*szsurf(2)),30);
    n=n/(szsurf(1)*szsurf(2))*100;
    figure
    bar(xout,n)
    title(['Histogram for surface ' char(surfaces(i))])
    ylabel('Relative Frequency [%]')
    xlabel('Surface height [mm]')
end

% Section 4.2: Comparison of Statistical Roughness Metrics
for i=1:length(surfaces)

[roughness(i,:),res(i,:)]=rough(char(strcat(directory,surfaces(i),...
    '.txt')));
end
% save
% out=[surfaces roughness];
% xlswrite('roughnessdata.xls', out);

% FIGURE 1 RMS ROUGHNESS VS. SURFACE TO FOOTPRINT RATIO
figure
subplot(2,2,1)
plot(roughness(:,1),roughness(:,2),'o')
ylabel('RMS Roughness [mm]')
xlabel('Surface to Footprint Ratio [-]')
% FIGURE 2 SURFACE KURTOSIS VS. SURFACE SKEWNESS
subplot(2,2,2)
plot(roughness(:,3),roughness(:,4),'o')
ylabel('Surface Kurtosis')
xlabel('Surface Skewness')
% FIGURE 3 RMS ROUGHNESS VS. RMS SLOPE
subplot(2,2,3)
plot(roughness(:,5),roughness(:,2),'o')
ylabel('RMS Roughness [mm]')
xlabel('RMS Slope')
```

```
% FIGURE 4 RMS SLOPE VS SUFACE TO FOOTPRINT RATIO
subplot(2,2,4)
plot(roughness(:,1),roughness(:,5),'o')
ylabel('RMS Slope')
xlabel('Surface to Footprint Ratio')

%SECTION 4.2 Scaling Roughness Parameters
for i=1:1%length(surfaces)
    [surf,dx,dy]=scaling(directory,surfaces(i));
end

%SECTION 4.3 Roughness Metrics for Mated Fractures
%FIGURES Top Vs. Bottom for the 5 roughness metrics
j=1;
for i=1:2:length(fractures)
    file=char(strcat(directory,fractures(i),'.txt'));
    m=importdata(file);
    [botsurf,dx,dy]=get_surf(m.data(:,1),m.data(:,2),m.data(:,3));
    file=char(strcat(directory,fractures(i+1),'.txt'));
    m=importdata(file);
    [topsurf,dx,dy]=get_surf(m.data(:,1),m.data(:,2),m.data(:,3));
    topsurf=remove_planar_trend(topsurf,dx,dy);
    botsurf=remove_planar_trend(botsurf,dx,dy);
    r_bot(j,:)=master_surface_analysis(botsurf,dx,dy);
    r_top(j,:)=master_surface_analysis(topsurf,dx,dy);
    j=j+1;
end
figure
% FIGURE Surface to Footprint Ratio
subplot(2,1,1)
scatter(r_bot(:,1),r_top(:,1)),hold on
plot(1:.5:1.5,1:.5:1.5,'black'),hold on
title('Surface to Footprint Ratio')
xlabel('Bottom Surface')
ylabel('Top Surface')
% FIGURE RMS Roughness
subplot(2,1,2)
scatter(r_bot(:,2),r_top(:,2)),hold on
plot(0:3,0:3,'black'),hold on
title('RMS Roughness [mm]')
xlabel('Bottom Surface')
ylabel('Top Surface')
% FIGURE Surface Skewness
figure
subplot(1,3,1)
scatter(r_bot(:,3),r_top(:,3)),hold on
plot(-1:1,-1:1,'black'),hold on
title('Surface Skewness')
xlabel('Bottom Surface')
ylabel('Top Surface')
% FIGURE Surface Kurtosis
subplot(1,3,2)
```

```
scatter(r_bot(:,4),r_top(:,4)),hold on
plot(2:5,2:5,'black'),hold on
title('Surface Kurtosis')
xlabel('Bottom Surface')
ylabel('Top Surface')
% FIGURE RMS Slope
subplot(1,3,3)
scatter(r_bot(:,5),r_top(:,5)),hold on
plot(0:2.5,0:2.5,'black'),hold on
title('RMS Slope')
xlabel('Bottom Surface')
ylabel('Top Surface')

%SECTION 4.7 Comparing apertures
Plotting the different apertures against the hydraulic aperture makes
the
most sense.
Plotting apparent aperture to true profile aperture
j=1;
for i=1:2:length(fractures)
    file=char(strcat(directory,fractures(i),'.txt'));
    m=importdata(file);
    [botsurf,dx,dy]=get_surf(m.data(:,1),m.data(:,2),m.data(:,3));
    file=char(strcat(directory,fractures(i+1),'.txt'));
    m=importdata(file);
    [topsurf,dx,dy]=get_surf(m.data(:,1),m.data(:,2),m.data(:,3));
    a=get_aperture(botsurf,topsurf,dx,dy);
    apparent_ap(j)=a(1,1);
    geo_apparent_ap(j)=a(2,1);
    harm_apparent_ap(j)=a(3,1);
    true_x_ap(j)=a(1,2);
    true_y_ap(j)=a(1,3);
    true_surf_ap(j)=a(1,4);
    surf=topsurf;
    remove_planar_trend(surf,dx,dy);
    roughness(j,:)=master_surface_analysis(surf,dx,dy);
    j=j+1;
end
figure
scatter(apparent_ap,true_x_ap,'blue'), hold on
scatter(apparent_ap,true_y_ap,'green'), hold on
scatter(apparent_ap,true_surf_ap,'magenta'),hold on
scatter(apparent_ap,geo_apparent_ap,'red'),hold on
scatter(apparent_ap,harm_apparent_ap,'cyan'),hold on
xlabel('Arithmetic Apparent Aperture [mm]')
ylabel('True/Apparent Aperture [-]')
legend('X-profile True','Y-profile True','Spherical True','Geometric
Mean Apparent','Harmonic Mean Apparent')
```

```
%SECTION 4.8  FRACTAL ANALYSIS OF FRACTURE SURFACES
%FIGURE Fractal plots of profiles and the mean for the x and y
dimensions
map = colormap(jet(length(surfaces)));
data=ones(length(surfaces),6);
for i=1:length(surfaces)
    file=char(strcat(directory,surfaces(i),'.txt'));
    m=importdata(file);
    [surf,dx,dy]=get_surf(m.data(:,1),m.data(:,2),m.data(:,3));
    [lengths_x,FRL_x,lengths_y,FRL_y]=fractalrl(surf,dx,dy);
    [wave_x,PSD_x,wave_y,PSD_y]=fractalpsd(surf,dx,dy);
    [distance_x,FRP_x,distance_y,FRP_y]=fractalfrp(surf,dx,dy);
%FIGURES Two sets of figures will be produced.
%     figure(481)
%     loglog(lengths_x,FRL_x,'color',map(i,:)), hold on
%     figure(482)
%     loglog(lengths_y,FRL_y,'color',map(i,:)), hold on
%     figure(483)
%     loglog(wave_x,PSD_x,'color',map(i,:)),hold on
%     figure(484)
%     loglog(wave_y,PSD_y,'color',map(i,:)),hold on
%     figure(485)
%     loglog(distance_x,FRP_x,'color',map(i,:)),hold on
%     figure(486)
%     loglog(distance_y,FRP_y,'color',map(i,:)),hold on

    figure
    subplot(1,3,1)
    p(1)=loglog(lengths_x,FRL_x,'red'); hold on
    coeff=estimate_fractal_dim(lengths_x,FRL_x);
    line=10.^(log10(lengths_x)*coeff(1)+coeff(2));
    p(2)=plot(lengths_x,line,'--r');hold on
    r=['H = ' num2str(coeff(1))];
    text(10^2,10^-.6,num2str(r),'EdgeColor','red')
    RLx=coeff(1);
    p(3)=loglog(lengths_y,FRL_y,'blue'); hold on
    coeff=estimate_fractal_dim(lengths_y,FRL_y);
    line=10.^(log10(lengths_y)*coeff(1)+coeff(2));
    p(4)=plot(lengths_y,line,'--b');hold on
    r=['H = ' num2str(coeff(1))];
    RLy=coeff(1);
    text(10^2,10^-.7,num2str(r),'EdgeColor','blue')
    xlabel('Window Width [mm]')
    ylabel('RMS Roughness(w) [mm]')
    title(['Roughness-Length fractal analysis for ' char(surfaces(i))])
    legend([p(1) p(3)],'x-dimension profiles','y-dimension profiles')

    subplot(1,3,2)
    p(1)=loglog(wave_x,PSD_x,'red');hold on
    coeff=estimate_fractal_dim(wave_x,PSD_x);
    PSDx=coeff(1)/2-.5;
    line=10.^(log10(wave_x)*coeff(1)+coeff(2));
```

```
    p(2)=plot(wave_x,line,'--r');hold on
    r=['H = ' num2str((coeff(1)/2-.5))];
    text(1,10^-2,num2str(r),'EdgeColor','red')
    p(3)=loglog(wave_y,PSD_y,'blue');hold on
    coeff=estimate_fractal_dim(wave_y,PSD_y);
    PSDy=coeff(1)/2-.5;
    line=10.^(log10(wave_y)*coeff(1)+coeff(2));
    p(4)=plot(wave_y,line,'--b');hold on
    r=['H = ' num2str((coeff(1)/2-.5))];
    text(1,10^-3,num2str(r),'EdgeColor','blue')
    xlabel('Wavelength [mm]')
    ylabel('Power')
    title(['Power Spectral Density fractal analysis for '
char(surfaces(i))])
    legend([p(1) p(3)],'x-dimension profiles','y-dimension profiles')

    subplot(1,3,3)
    p(1)=loglog(distance_x,FRP_x,'red');hold on
    coeff=estimate_fractal_dim(distance_x,FRP_x);
    FRPx=coeff(1)+2;
    line=10.^(log10(distance_x)*coeff(1)+coeff(2));
    p(2)=plot(distance_x,line,'--r');hold on
    r=['H = ' num2str(coeff(1)+2)];
    text(10,10^-7,num2str(r),'EdgeColor','red')
    p(3)=loglog(distance_y,FRP_y,'blue');hold on
    coeff=estimate_fractal_dim(distance_y,FRP_y);
    FRPy=coeff(1)+2;
    line=10.^(log10(distance_y)*coeff(1)+coeff(2));
    p(4)=plot(distance_y,line,'--b');hold on
    r=['H = ' num2str(coeff(1)+2)];
    text(10,10^-8,num2str(r),'EdgeColor','blue')
    xlabel('Distance (mm)')
    ylabel('Probability')
    title(['First Return Probability fractal analysis for '
char(surfaces(i))])
    legend([p(1) p(3)],'x-dimension profiles','y-dimension profiles')
    data(i,:)=[RLx,RLy,FRPx,FRPy,PSDx,PSDy];
end
save
figure(481)
xlabel('Window Width [mm]')
ylabel('RMS(w) [mm]')
title('Roughness-Length fractal analysis in X-dimension')
figure(482)
xlabel('Window Width [mm]')
ylabel('RMS(w) [mm]')
title('Roughness-Length fractal analysis in Y-dimension')
figure(483)
xlabel('Wavelength [mm]')
ylabel('Power')
title('Power Spectral Density fractal analysis in X-dimension')
figure(484)
```

```
xlabel('Wavelength [mm]')
ylabel('Power')
title('Power Spectral Density fractal analysis in Y-dimension')
figure(485)
xlabel('Distance (mm)')
ylabel('Probability')
title('First Return Probability fractal analysis in X-dimension')
figure(486)
xlabel('Distance (mm)')
ylabel('Probability')
title('First Return Probability fractal analysis in Y-dimension')

% SECTION 3.9/4.9 MAXIMIZED APERTURE
% FIGURE 3.7 Illustration of two different methods to compute maximized
% aperture
for i=1:length(surfaces)
    file=char(strcat(directory,surfaces(i),'.txt'));
    m=importdata(file);
    [surf,dx,dy]=get_surf(m.data(:,1),m.data(:,2),m.data(:,3));

  %FIGURE 3.7 Illustration of two different methods to compute
maximized
  %aperture
    surf=remove_planar_trend(surf,dx,dy);
    surf=surf+abs(min(min(surf)));
    profA1=surf(1,:);
    profA2=surf(1,:).*(-1)+2*min(profA1);
    profB1=surf(1,:)+10;
    profB2=surf(1,:)+10+max(surf(1,:))-min(surf(1,:));
    plot((1:length(profA1)).*dx,profA1, 'b'),hold on;
    plot((1:length(profA2)).*dx,profA2,'b'),hold on;
    plot((1:length(profB1)).*dx,profB1,'r'),hold on;
    plot((1:length(profB2)).*dx,profB2,'r'),hold on;
  %FIGURE RMS versus MAX AP for all fracture surface samples
    [maxap1(i),maxap2(i)]=maximized_aperture(surf,dx,dy);
    rms(i)=root_mean_square(surf,dx,dy);
end

figure
scatter(maxap1,rms,5,'blue','filled'),hold on
r=corrcoef(maxap1,rms);
r=r(1,2)^2;
r=['r^2 = ' num2str(r)];
text(12,3,num2str(r),'EdgeColor','blue')
scatter(maxap2,rms,5,'red','filled'),hold on
r=corrcoef(maxap2,rms);
r=r(1,2)^2;
r=['r^2 = ' num2str(r)];
text(12,2,num2str(r),'EdgeColor','red')
xlabel('Arithmetic Mean Maximized Aperture [mm]')
ylabel('RMS Roughness [mm]')
```

```
title('RMS Roughness versus the Arithmetic Mean Maximized Aperture')
legend('Reflected Method','Translated Method')

j=1;
for i=1:2:length(fractures)
    file=char(strcat(directory,fractures(i),'.txt'));
    m=importdata(file);
    [botsurf,dx,dy]=get_surf(m.data(:,1),m.data(:,2),m.data(:,3));
    file=char(strcat(directory,fractures(i+1),'.txt'));
    m=importdata(file);
    [topsurf,dx,dy]=get_surf(m.data(:,1),m.data(:,2),m.data(:,3));
    [b_maxap_r(j),b_maxap_tr(j)]=maximized_aperture(botsurf,dx,dy);
    [t_maxap_r(j),t_maxap_tr(j)]=maximized_aperture(topsurf,dx,dy);
    a=get_aperture(botsurf,topsurf,dx,dy);
    arith_mean_ap(j)=a(1,1);
    j=j+1;
end
% FIGURE MAX AP Top vs. Bottom
figure
scatter(b_maxap_r,t_maxap_r,'blue','filled'),hold on
r=corrcoef(b_maxap_r,t_maxap_r);
r=r(1,2)^2;
r=['r^2 = ' num2str(r)];
text(12,4,num2str(r),'EdgeColor','blue')
scatter(b_maxap_tr,t_maxap_tr,'red','filled'),hold on
r=corrcoef(b_maxap_tr,t_maxap_tr);
r=r(1,2)^2;
r=['r^2 = ' num2str(r)];
text(12,2,num2str(r),'EdgeColor','red')
plot(0:20,0:20,'black'),hold on
xlabel('Bottom Surface Arithmetic Mean Maximized Aperture [mm]')
ylabel('Top Surface Arithmetic Mean Maximized Aperture [mm]')
title('Comparing the Arithmetic Mean Maximized Aperture for mated
surfaces')
legend('Reflected Method','Translated Method')

% FIGURE Maximized Aperture (bot,ref) vs. Real Aperture (arithmetic
means)
figure
scatter(arith_mean_ap,b_maxap_r,'blue','filled'),hold on
scatter(arith_mean_ap,b_maxap_tr,'red','filled'),hold on
axis([0 4 0 20])
xlabel('Real Arithmetic Mean Aperture [mm]')
ylabel('Maximized Arithmetic Mean Aperture [mm]')
title('Comparing the real aperture to the maximized aperture end-
member')
legend('Reflected Method','Translated Method')


toc
end
```

```
function [r,res]=rough(file)
m=importdata(file);
[surf,dx,dy]=get_surf(m.data(:,1),m.data(:,2),m.data(:,3));
surf=remove_planar_trend(surf,dx,dy);
r=master_surface_analysis(surf,dx, dy);
res=dx*dy;
end

function [surf,dx,dy]=scaling(directory,file)
m=importdata(char(strcat(directory,file,'.txt')));
[surf,dx,dy]=get_surf(m.data(:,1),m.data(:,2),m.data(:,3));
surf=remove_planar_trend(surf,dx,dy);
scales(surf,dx,dy,file);
end

function [maxap1,maxap2]=maximized_aperture(surf,dx,dy)
    surf=remove_planar_trend(surf,dx,dy);
    surf=surf+abs(min(min(surf)));
    surfA1=surf;
    surfA2=surf.*(-1)+2*min(min(surfA1));
    surfB1=surf;
    surfB2=surf+max(max(surf))-min(min(surf));
    a1=get_aperture(surfA1,surfA2,dx,dy);
    a2=get_aperture(surfB1,surfB2,dx,dy);
    maxap1=a1(1,1);
    maxap2=a2(1,1);
end

function [coeff]=estimate_fractal_dim(x,y)
start=1;
finish=int32(length(x)/4);
coeff=polyfit(log10(x(start:finish)),log10(y(start:finish)),1);

end
function [distance_x,avghistogramx,distance_y,avghistogramy] =
fractalfrp(rocksurf,dx,dy)
%FRACTALFRP Finds the average fractal dimension for x dimension and y
%dimension
szsurf=size(rocksurf);
length_y=szsurf(1);
length_x=szsurf(2);

%Find fractal dimension using x profiles
d=rocksurf;
for i=1:length_y,
    for j=1:(length_x-1),
        if rocksurf(i,j) > rocksurf(i,j+1)
            count=1;
            while count~=0 && rocksurf(i,j+count) < rocksurf(i,j)
                count=count+1;
```

```
                if j+count > length_x
                    count=0;
                end
            end
            d(i,j)=count;
        else
            count=1;
            while count~=0 && rocksurf(i,j+count) > rocksurf(i,j)
                count=count+1;
                if j+count > length_x
                    count=0;
                end
            end
            d(i,j)=count;
        end
    end
end
logbinx=1:1000;
histogram=hist(d',logbinx);
histogram=histogram./sum(sum(histogram));
distance_x=logbinx*dx;

% figure
% subplot(1,2,1)
% loglog(distance_x,histogram')
% xlabel('Distance (mm)')
% ylabel('Probability (histogram)')
% title('First return probability for x-dimension profiles')

avghistogramx=mean(histogram',1);
line=polyfit(log10(logbinx(5:50)),log10(avghistogramx(5:50)),1);
fracdim_x=line(1)+2;
c=avghistogramx(10)/(logbinx(10)^line(1));

%Find fractal dimension using y profiles
d=rocksurf;
for j=1:length_x,
    for i=1:(length_y-1),
        if rocksurf(i,j) > rocksurf(i+1,j)
            count=1;
            while count~=0 && rocksurf(i+count,j) < rocksurf(i,j)
                count=count+1;
                if i+count > length_y
                    count=0;
                end
            end
            d(i,j)=count;
        else
            count=1;
            while count~=0 && rocksurf(i+count,j) > rocksurf(i,j)
                count=count+1;
```

```
                if i+count > length_y
                    count=0;
                end
            end
            d(i,j)=count;
        end
    end
end
logbiny=1:1000;
histogram=hist(d,logbiny);
histogram=histogram./sum(sum(histogram));
distance_y=logbiny*dy;

% subplot(1,2,2)
% loglog(distance_y,histogram)
% xlabel('Distance (mm)')
% ylabel('Probability (histogram)')
% title('First return probability for y-dimension profiles')

avghistogramy=mean(histogram',1);
line=polyfit(log10(logbiny(5:50)),log10(avghistogramy(5:50)),1);
fracdim_y=line(1)+2;
c=avghistogramy(10)/(logbiny(10)^line(1));

% figure
% loglog(distance_x,avghistogramx,distance_y,avghistogramy)
% xlabel('Distance (mm)')
% ylabel('Probability')
% title('Mean First Return Probability')
% legend('X profiles','Y profiles')

end

function [wave_x,avgpsd_x,wave_y,avgpsd_y] = fractalpsd(rocksurf,dx,dy)
%FRACTALPSD Finds the average fractal dimension for x dimension and y
%dimension using the power spectral density method
szsurf=size(rocksurf);
length_y=szsurf(1);
length_x=szsurf(2);

%psd in the x direction
psd_x=psd(rocksurf(1,:))';
for i=2:length_y,
    psd_x=[psd_x; psd(rocksurf(i,:))'];
end
szpsd=size(psd_x);
nyquist=1/2/dx;
frequency_x=((0:(szpsd(2)-1))/(2*nyquist));

% figure
% subplot(1,2,1)
```

```
% loglog(frequency_x.^-1,psd_x)
% set(gca,'XDir','reverse')
% xlabel('Wavelength (mm)')
% ylabel('P(f)')
% title('Power spectra for x-dimension profiles')

avgpsd_x=mean(psd_x,1);
frequency_x(1)=[];
wave_x=frequency_x.^-1;
avgpsd_x(1)=[];
line=polyfit(log10(frequency_x(2:30)),log10(avgpsd_x(2:30)),1);
fracdim_x=(line(1)+1)/(-2)
c=avgpsd_x(10)/(frequency_x(10)^line(1));

% subplot(2,2,2)
% loglog(frequency_x.^-1,avgpsd_x,frequency_x(2:30).^-
1,c*frequency_x(2:30).^line(1))
% set(gca,'XDir','reverse')
% xlabel('Wavelength (mm)')
% ylabel('P(f)')
% title('Mean power spectrum for x-dimension profiles')

%psd in the y direction
psd_y=psd(rocksurf(:,1))';
for i=2:length_x,
    psd_y=[psd_y; psd(rocksurf(:,i))'];
end
szpsd=size(psd_y);
nyquist=1/2/dy;
frequency_y=((0:(szpsd(2)-1))/(2*nyquist));


% subplot(1,2,2)
% loglog(frequency_y.^-1,psd_y)
% set(gca,'XDir','reverse')
% xlabel('Wavelength (mm)')
% ylabel('P(f)')
% title('Power spectra of y-dimension profiles')

avgpsd_y=mean(psd_y,1);


frequency_y(1)=[];
wave_y=frequency_y.^-1;
avgpsd_y(1)=[];
line=polyfit(log10(frequency_y),log10(avgpsd_y),1);
fracdim_y=(line(1)+1)/(-2)
c=avgpsd_y(10)/(frequency_y(10)^line(1));

% subplot(2,2,4)
```

```
% loglog(frequency_y.^-1,avgpsd_y,frequency_y(2:30).^-
1,c*frequency_y(2:30).^line(1))
% set(gca,'XDir','reverse')
% xlabel('Wavelength (mm)')
% ylabel('P(f)')
% title('Mean power spectrum for y-dimension profiles')

% figure
% loglog(frequency_x.^-1,avgpsd_x,frequency_y.^-1,avgpsd_y)
% set(gca,'XDir','reverse')
% xlabel('Wavelength [mm]')
% ylabel('Power')
% title('Mean Power Spectral Density')
% legend('X profiles','Y profiles')

end

function [xvalues,meanRMSx,yvalues,meanRMSy] = fractalrl(surf,dx,dy)
%FRACTALRL Finds the average fractal dimension for x dimension and y
%dimension using the roughness-length method

szsurf=size(surf);
length_x=szsurf(2);
length_y=szsurf(1);

xvalues=(10:length_x).*dx;
yvalues=(10:length_y).*dy;

RMSall=[];
for i=1:length_y,
    RMSprofile=[];
    for w=10:length_x,
        profile=surf(i,:);
        numbands=idivide(int32(length(profile)),w);
        allbands=0;
        for j=0:(numbands-1),
            band=profile(1+j*w:(j+1)*w);
            mband=mean(band);
            vband=0;
            for k=1:w,
                vband=vband+(band(k)-mband)^2;
            end
            vband=vband/(double(w)-2);
            vband=sqrt(vband);
            allbands=allbands+vband;
        end
          numbands=double(numbands);
          RMSw=allbands/numbands;
          RMSprofile=[RMSprofile,RMSw];
    end
    RMSall=[RMSall;RMSprofile];
```

```
end
RMSallx=RMSall;
meanRMSx=mean(RMSallx,1);

% figure
% subplot(1,2,1)
% loglog(xvalues,RMSallx)
% xlabel('Window Width [mm]')
% ylabel('RMS(w) [mm]')
% title('Roughness-Length for x-dimension profiles')


RMSall=[];
for i=1:length_x,
    RMSprofile=[];
    for w=10:length_y,
        profile=surf(:,i);
        numbands=idivide(int32(length(profile)),w);
        allbands=0;
        for j=0:(numbands-1),
            band=profile(1+j*w:(j+1)*w);
            mband=mean(band);
            vband=0;
            for k=1:w,
                vband=vband+(band(k)-mband)^2;
            end
            vband=vband/(double(w)-2);
            vband=sqrt(vband);
            allbands=allbands+vband;
        end
          numbands=double(numbands);
          RMSw=allbands/numbands;
          RMSprofile=[RMSprofile,RMSw];
    end
    RMSall=[RMSall;RMSprofile];
end
RMSally=RMSall;
meanRMSy=mean(RMSally,1);

% subplot(1,2,2)
% loglog(yvalues,RMSally)
% xlabel('Window Width [mm]')
% ylabel('RMS(w) [mm]')
% title('Roughness-Length for y-dimension profiles')
%
% figure
% loglog(xvalues,meanRMSx,yvalues,meanRMSy)
% xlabel('Window Width [mm]')
% ylabel('RMS(w) [mm]')
% title('Mean Roughness-Length')
% ylim([10^-1 10^0.3])
```

```
% legend('X profiles', 'Y profiles')

end

function [a] = get_aperture(surf1,surf2,dx,dy)

% This function calculates the aperture for two gridded surfaces,
% one-dimensionally, two-dimensionally, and three-dimensionally.

if max(max((surf1))) > max(max(surf2)),
    topsurf=surf1;
    botsurf=surf2;
else
    topsurf=surf2;
    botsurf=surf1;
end
szsurf=size(botsurf);

%plot(1:szsurf(2),botsurf(1,:),1:szsurf(2),topsurf(1,:))

% Aperture calculated one-dimensionally by subtracting the bottom
surface
% grid from the top surface grid.

oneDap=topsurf-botsurf;

% Aperture calculated two-dimensionally, parallel to the x-direction
% (within the plane of the CT slice).  At each point on the bottom
surface,
% a circle is grown until it tangentially touches the two surfaces.

twoDxap=oneDap;
for y=1:szsurf(1);

%   Left edge
    x=1;
    tr=[(x+1)*dx,topsurf(y,x+1)];
    t0=[x*dx,topsurf(y,x)];
    b0=[x*dx,botsurf(y,x)];
    twoDxap(y,x)=abs(det([tr-t0;b0-t0]))/norm(tr-t0);

    for x=2:szsurf(2)-1;

        tr=[(x+1)*dx,topsurf(y,x+1)];
        t0=[x*dx,topsurf(y,x)];
        b0=[x*dx,botsurf(y,x)];
        dr=abs(det([tr-t0;b0-t0]))/norm(tr-t0);

        tl=[(x-1)*dx,topsurf(y,x-1)];
```

```
        dl=abs(det([tl-t0;b0-t0]))/norm(tl-t0);

        if dr <= dl
            twoDxap(y,x)=dr;
        else
            twoDxap(y,x)=dl;
        end
    end

%   Right edge
    x=szsurf(2);
    tl=[(x-1)*dx,topsurf(y,x-1)];
    t0=[x*dx,topsurf(y,x)];
    b0=[x*dx,botsurf(y,x)];
    twoDxap(y,x)=abs(det([tl-t0;b0-t0]))/norm(tl-t0);
end

% Aperture calculated two-dimensionally, parallel to the y-direction
% (perpendicular to the plane of the CT slice).

twoDyap=oneDap;
for x=1:szsurf(2);

%   Front edge
    y=1;
    tr=[(y+1)*dy,topsurf(y+1,x)];
    t0=[y*dy,topsurf(y,x)];
    b0=[y*dy,botsurf(y,x)];
    twoDyap(y,x)=abs(det([tr-t0;b0-t0]))/norm(tr-t0);

    for y=2:szsurf(1)-1;
        tr=[(y+1)*dy,topsurf(y+1,x)];
        t0=[y*dy,topsurf(y,x)];
        b0=[y*dy,botsurf(y,x)];
        dr=abs(det([tr-t0;b0-t0]))/norm(tr-t0);

        tl=[(y-1)*dy,topsurf(y-1,x)];
        dl=abs(det([tl-t0;b0-t0]))/norm(tl-t0);

        if dr <= dl
            twoDyap(y,x)=dr;
        else
            twoDyap(y,x)=dl;
        end
    end

%   Back edge
    y=szsurf(1);
    tl=[(y-1)*dy,topsurf(y-1,x)];
    t0=[y*dy,topsurf(y,x)];
```

```
    b0=[y*dy,botsurf(y,x)];
    twoDyap(y,x)=abs(det([tl-t0;b0-t0]))/norm(tl-t0);
end

% Three-dimensional aperture is found by finding the tangent plane for
a
% sphere created at each point from the bottom surface. This is
otherwise
% known as finding the distance from a point to a plane.  For every
% interior point on the bottom surface grid, there are 16 different
planes
% which could

threeDap=oneDap;
dist=ones(1,44);

for y=2:szsurf(1)-1;
    for x=2:szsurf(2)-1;


        xp=x*dx;
        yp=y*dy;
        zp=botsurf(y,x);

        x0=x*dx;
        y0=y*dy;
        z0=topsurf(y,x);

        x1=(x-1)*dx;
        y1=(y-1)*dy;
        z1=topsurf(y-1,x-1);

        x2=x*dx;
        y2=(y-1)*dy;
        z2=topsurf(y-1,x);

        x3=(x+1)*dx;
        y3=(y-1)*dy;
        z3=topsurf(y-1,x+1);

        x4=(x+1)*dx;
        y4=y*dy;
        z4=topsurf(y,x+1);

        x5=(x+1)*dx;
        y5=(y+1)*dy;
        z5=topsurf(y+1,x+1);

        x6=x*dx;
        y6=(y+1)*dy;
```

```
        z6=topsurf(y+1,x);

        x7=(x-1)*dx;
        y7=(y+1)*dy;
        z7=topsurf(y+1,x-1);

        x8=(x-1)*dx;
        y8=y*dy;
        z8=topsurf(y,x-1);

dist(1)=point_plane_distance(xp,yp,zp,x6,y6,z6,x7,y7,z7,x8,y8,z8);
dist(2)=point_plane_distance(xp,yp,zp,x6,y6,z6,x0,y0,z0,x8,y8,z8);
dist(3)=point_plane_distance(xp,yp,zp,x0,y0,z0,x8,y8,z8,x7,y7,z7);
dist(4)=point_plane_distance(xp,yp,zp,x0,y0,z0,x6,y6,z6,x7,y7,z7);
dist(5)=point_plane_distance(xp,yp,zp,x1,y1,z1,x2,y2,z2,x8,y8,z8);
dist(6)=point_plane_distance(xp,yp,zp,x2,y2,z2,x8,y8,z8,x0,y0,z0);
dist(7)=point_plane_distance(xp,yp,zp,x1,y1,z1,x2,y2,z2,x0,y0,z0);
dist(8)=point_plane_distance(xp,yp,zp,x1,y1,z1,x8,y8,z8,x0,y0,z0);
dist(9)=point_plane_distance(xp,yp,zp,x2,y2,z2,x3,y3,z3,x4,y4,z4);
dist(10)=point_plane_distance(xp,yp,zp,x2,y2,z2,x0,y0,z0,x4,y4,z4);
dist(11)=point_plane_distance(xp,yp,zp,x0,y0,z0,x2,y2,z2,x3,y3,z3);
dist(12)=point_plane_distance(xp,yp,zp,x3,y3,z3,x4,y4,z4,x0,y0,z0);
dist(13)=point_plane_distance(xp,yp,zp,x4,y4,z4,x5,y5,z5,x6,y6,z6);
dist(14)=point_plane_distance(xp,yp,zp,x6,y6,z6,x0,y0,z0,x4,y4,z4);
dist(15)=point_plane_distance(xp,yp,zp,x0,y0,z0,x4,y4,z4,x5,y5,z5);
dist(16)=point_plane_distance(xp,yp,zp,x0,y0,z0,x6,y6,z6,x5,y5,z5);
dist(17)=point_space_distance(xp,yp,zp,x0,y0,z0);
dist(18)=point_space_distance(xp,yp,zp,x1,y1,z1);
dist(19)=point_space_distance(xp,yp,zp,x2,y2,z2);
dist(20)=point_space_distance(xp,yp,zp,x3,y3,z3);
dist(21)=point_space_distance(xp,yp,zp,x4,y4,z4);
dist(22)=point_space_distance(xp,yp,zp,x5,y5,z5);
dist(23)=point_space_distance(xp,yp,zp,x6,y6,z6);
dist(24)=point_space_distance(xp,yp,zp,x7,y7,z7);
dist(25)=point_space_distance(xp,yp,zp,x8,y8,z8);
dist(26)=point_edge_distance([xp,yp,zp],[x0,y0,z0],[x1,y1,z1]);
dist(27)=point_edge_distance([xp,yp,zp],[x0,y0,z0],[x2,y2,z2]);
dist(28)=point_edge_distance([xp,yp,zp],[x0,y0,z0],[x8,y8,z8]);
dist(29)=point_edge_distance([xp,yp,zp],[x1,y1,z1],[x8,y8,z8]);
dist(30)=point_edge_distance([xp,yp,zp],[x1,y1,z1],[x2,y2,z2]);
dist(31)=point_edge_distance([xp,yp,zp],[x0,y0,z0],[x4,y4,z4]);
dist(32)=point_edge_distance([xp,yp,zp],[x0,y0,z0],[x3,y3,z3]);
dist(33)=point_edge_distance([xp,yp,zp],[x2,y2,z2],[x3,y3,z3]);
dist(34)=point_edge_distance([xp,yp,zp],[x4,y4,z4],[x3,y3,z3]);
dist(35)=point_edge_distance([xp,yp,zp],[x2,y2,z2],[x4,y4,z4]);
dist(36)=point_edge_distance([xp,yp,zp],[x0,y0,z0],[x5,y5,z5]);
dist(37)=point_edge_distance([xp,yp,zp],[x0,y0,z0],[x6,y6,z6]);
dist(38)=point_edge_distance([xp,yp,zp],[x6,y6,z6],[x4,y4,z4]);
dist(39)=point_edge_distance([xp,yp,zp],[x5,y5,z5],[x6,y6,z6]);
dist(40)=point_edge_distance([xp,yp,zp],[x5,y5,z5],[x4,y4,z4]);
dist(41)=point_edge_distance([xp,yp,zp],[x0,y0,z0],[x7,y7,z7]);
dist(42)=point_edge_distance([xp,yp,zp],[x8,y8,z8],[x6,y6,z6]);
```

```
dist(43)=point_edge_distance([xp,yp,zp],[x8,y8,z8],[x7,y7,z7]);
dist(44)=point_edge_distance([xp,yp,zp],[x6,y6,z6],[x7,y7,z7]);
threeDap(y,x)=min(dist);
    end
end
m_oneDap=reshape(oneDap,1,szsurf(1)*szsurf(2));
m_twoDxap=reshape(twoDxap,1,szsurf(1)*szsurf(2));
m_twoDyap=reshape(twoDyap,1,szsurf(1)*szsurf(2));
m_threeDap=reshape(threeDap,1,szsurf(1)*szsurf(2));

m_oneDap=replace_zeros(m_oneDap);
m_twoDxap=replace_zeros(m_twoDxap);
m_twoDyap=replace_zeros(m_twoDyap);
m_threeDap=replace_zeros(m_threeDap);

a=[];
a(1,1)=mean(m_oneDap);
a(1,2)=mean(m_twoDxap);
a(1,3)=mean(m_twoDyap);
a(1,4)=mean(m_threeDap);
a(2,1)=geomean(m_oneDap);
a(2,2)=geomean(m_twoDxap);
a(2,3)=geomean(m_twoDyap);
a(2,4)=geomean(m_threeDap);
a(3,1)=harmmean(m_oneDap);
a(3,2)=harmmean(m_twoDxap);
a(3,3)=harmmean(m_twoDyap);
a(3,4)=harmmean(m_threeDap);

%min(min(oneDap))

end

function [L] =
point_plane_distance(xp,yp,zp,x1,y1,z1,x2,y2,z2,x3,y3,z3)

%   Finds the distance from a point to a plane.

    normal=cross([x1,y1,z1]-[x2,y2,z2],[x1,y1,z1]-[x3,y3,z3]);
    A=normal(1);
    B=normal(2);
    C=normal(3);
    D=dot(normal,[x1,y1,z1]);
    L=abs(A*xp+B*yp+C*zp-D)/sqrt(A^2+B^2+C^2);
end

function[L] = point_space_distance(x1,y1,z1,x2,y2,z2)
    L=sqrt((x1-x2)^2+(y1-y2)^2+(z1-z2)^2);
end
```

```
function[d] = point_edge_distance(p,e1,e2)
    d=norm(cross(e1-e2,p-e2))/norm(e1-e2);
end

function[array]=replace_zeros(array)
i=find(array==0);
array(i)=inf;
lownum=min(array);
array(i)=lownum/2;
end

function [r] = master_surface_analysis(surf,dx,dy)

r=ones(1,5);
r(1)=roughnessratio(surf,dx,dy);
r(2)=root_mean_square(surf,dx,dy);
r(3)=surface_skewness(surf,dx,dy);
r(4)=surface_kurtosis(surf,dx,dy);
r(5)=root_mean_square_slope(surf,dx,dy);

end

function [surf] = remove_planar_trend(surf,dx,dy)

szsurf=size(surf);

xvect=[0:dx:(szsurf(2)*dx)];
yvect=[0:dy:(szsurf(1)*dy)];

m=szsurf(2);
n=szsurf(1);

xbar=0;
ybar=0;
zbar=0;

for k=1:m,
    xbar=xbar+xvect(k);
end
xbar=xbar/m;

for l=1:n,
    ybar=ybar+yvect(l);
end
ybar=ybar/n;

for l=1:n,
    for k=1:m,
        zbar=zbar+surf(l,k);
    end
```

```
end
zbar=zbar/(m*n);

bnum=0;
bden=0;

for k=1:m,
    for l=1:n,
    bnum=bnum+xvect(k)*(surf(l,k)-zbar);
    end
end

for k=1:m,
    for l=1:n,
        bden=bden+xvect(k)*(xvect(k)-xbar);
    end
end

b=bnum/bden;

cnum=0;
cden=0;

for k=1:m,
    for l=1:n,
        cnum=cnum+yvect(l)*(surf(l,k)-zbar);
    end
end

for k=1:m,
    for l=1:n,
    cden=cden+yvect(l)*(yvect(l)-ybar);
    end
end
c=cnum/cden;

a=zbar-b*xbar-c*ybar;

for k=1:m,
    for l=1:n,
        surf(l,k)=surf(l,k)-(a+b*xvect(k)+c*yvect(l));
    end
end
end

function [Sq] = root_mean_square(surf,dx,dy)

% ROOT_MEAN_SQUARE ROUGHNESS

szsurf=size(surf);
```

```
length_y=szsurf(1);
length_x=szsurf(2);

Sq=0;
for j=1:length_y,
    for i=1:length_x,
        Sq=Sq+surf(j,i)^2;
    end
end
Sq=Sq/(length_x*length_y);
Sq=sqrt(Sq);
end

function [Sdq] = root_mean_square_slope(surf,dx,dy)

% ROOT_MEAN_SQUARE_SLOPE

szsurf=size(surf);
length_y=szsurf(1);
length_x=szsurf(2);

Sdq=0;

for j=2:length_y,
    for i=2:length_x,
        Sdq=Sdq+((surf(j,i)-surf(j,(i-1)))/dx)^2+((surf(j,i)-surf((j-
1),i))/dy)^2;
    end
end

Sdq=sqrt(Sdq/((length_x-1)*(length_y-1)));

end

function [Sdq] = root_mean_square_slope(surf,dx,dy)

% ROOT_MEAN_SQUARE_SLOPE

szsurf=size(surf);
length_y=szsurf(1);
length_x=szsurf(2);

Sdq=0;

for j=2:length_y,
    for i=2:length_x,
        Sdq=Sdq+((surf(j,i)-surf(j,(i-1)))/dx)^2+((surf(j,i)-surf((j-
1),i))/dy)^2;
    end
end
```

```
Sdq=sqrt(Sdq/((length_x-1)*(length_y-1)));

end

function [Sdq] = scales(surf,dx,dy,surfacename)

% SCALE_STATS

szsurf=size(surf);
minszsurf=min(szsurf);

if minszsurf > 8192,
    error('ITS A BIG ONE!')
elseif minszsurf > 4096,
    surfsurf=surf(1:4096,1:4096);
    width=2.^(2:12);
elseif minszsurf > 2048,
    surfsurf=surf(1:2048,1:2048);
    width=2.^(2:11);
elseif minszsurf > 1024,
    surfsurf=surf(1:1024,1:1024);
    width=2.^(2:10);
elseif minszsurf > 512,
    surfsurf=surf(1:512,1:512);
    width=2.^(2:9);
elseif minszsurf > 256,
    surfsurf=surf(1:256,1:256);
    width=2.^(2:8);
else
    error('ITS TOO DAMN SMALL!')
end

szsurfsurf=size(surfsurf);
xx=szsurfsurf(2);
yy=szsurfsurf(1);

for k=1:length(width),

    w=width(k);
    scratch=0;
    count=1;

    for i=1:w:xx,
        for j=1:w:yy,
            scratch(1,count)=roughnessratio(surfsurf(j:(j+w-1),i:(i+w-
1)),dx,dy);
            scratch(2,count)=root_mean_square(surfsurf(j:(j+w-
1),i:(i+w-1)),dx,dy);
```

```
            scratch(3,count)=surface_skewness(surfsurf(j:(j+w-
1),i:(i+w-1)),dx,dy);
            scratch(4,count)=surface_kurtosis(surfsurf(j:(j+w-
1),i:(i+w-1)),dx,dy);
            scratch(5,count)=root_mean_square_slope(surfsurf(j:(j+w-
1),i:(i+w-1)),dx,dy);
        count=count+1;
        end
    end

   rr(1,k)=w^2*dx*dy/100;
   rr(2,k)=mean(scratch(1,:));
   rr(3,k)=var(scratch(1,:));

   rms(1,k)=w^2*dx*dy/100;
   rms(2,k)=mean(scratch(2,:));
   rms(3,k)=var(scratch(2,:));

   ss(1,k)=w^2*dx*dy/100;
   ss(2,k)=mean(scratch(3,:));
   ss(3,k)=var(scratch(3,:));

   sk(1,k)=w^2*dx*dy/100;
   sk(2,k)=mean(scratch(4,:));
   sk(3,k)=var(scratch(4,:));

   rmss(1,k)=w^2*dx*dy/100;
   rmss(2,k)=mean(scratch(5,:));
   rmss(3,k)=var(scratch(5,:));

end

figure
[RRAX,RRMEAN,RRVAR]=plotyy(rr(1,:),rr(2,:),rr(1,:),rr(3,:)./abs(rr(2,:)
),'semilogx');
set(get(RRAX(1),'Ylabel'),'String','Mean [-]')
set(get(RRAX(2),'Ylabel'),'String','Variance')
xlabel('Area (cm^2)')
title(['Surface to Footprint Ratio for ' surfacename])
set(RRMEAN,'Marker','o', 'LineStyle','none')
set(RRVAR,'Marker','.', 'LineStyle','--')
set(RRAX(1),'xlim',[0 max(rr(1,:))]);
set(RRAX(2),'xlim',[0 max(rr(1,:))]);

figure
[RMSAX,RMSMEAN,RMSVAR]=plotyy(rms(1,:),rms(2,:),rms(1,:),rms(3,:)./abs(
rms(2,:)),'semilogx');
set(get(RMSAX(1),'Ylabel'),'String','Mean [mm]')
set(get(RMSAX(2),'Ylabel'),'String','Variance')
xlabel('Area (cm^2)')
```

```
title(['Root-Mean-Square Roughness for ' surfacename])
set(RMSMEAN,'Marker','o', 'LineStyle','none')
set(RMSVAR,'Marker','.', 'LineStyle','--')
set(RMSAX(1),'xlim',[0 max(rms(1,:))]);
set(RMSAX(2),'xlim',[0 max(rms(1,:))]);


figure
[SSAX,SSMEAN,SSVAR]=
plotyy(ss(1,:),ss(2,:),ss(1,:),ss(3,:)./abs(ss(2,:)),'semilogx');
set(get(SSAX(1),'Ylabel'),'String','Mean')
set(get(SSAX(2),'Ylabel'),'String','Variance')
xlabel('Area (cm^2)')
title(['Surface Skewness for ' surfacename])
set(SSMEAN,'Marker','o', 'LineStyle','none')
set(SSVAR,'Marker','.', 'LineStyle','--')
set(SSAX(1),'xlim',[0 max(ss(1,:))]);
set(SSAX(2),'xlim',[0 max(ss(1,:))]);

figure
[SKAX,SKMEAN,SKVAR]=plotyy(sk(1,:),sk(2,:),sk(1,:),sk(3,:)./abs(sk(2,:)
),'semilogx');
set(get(SKAX(1),'Ylabel'),'String','Mean')
set(get(SKAX(2),'Ylabel'),'String','Variance')
xlabel('Area (cm^2)')
title(['Surface Kurtosis for ' surfacename])
set(SKMEAN,'Marker','o', 'LineStyle','none')
set(SKVAR,'Marker','.', 'LineStyle','--')
%set(SKAX(2),'ylim',[0 .6])
set(SKAX(1),'xlim',[0 max(sk(1,:))]);
set(SKAX(2),'xlim',[0 max(sk(1,:))]);

figure
[RMSSAX,RMSSMEAN,RMSSVAR]=plotyy(rmss(1,:),rmss(2,:),rmss(1,:),rmss(3,:
)./abs(rmss(2,:)),'semilogx');
set(get(RMSSAX(1),'Ylabel'),'String','Mean')
set(get(RMSSAX(2),'Ylabel'),'String','Variance')
xlabel('Area (cm^2)')
title(['Root-Mean-Square Slope for ' surfacename])
set(RMSSMEAN,'Marker','o', 'LineStyle','none')
set(RMSSVAR,'Marker','.', 'LineStyle','--')
%set(RMSSAX(2),'ylim',[0 .6])
set(RMSSAX(1),'xlim',[0 max(rmss(1,:))]);
set(RMSSAX(2),'xlim',[0 max(rmss(1,:))]);
end



function [Sku] = surface_kurtosis(surf,dx,dy)
% SURFACE_KURTOSIS
```

```
szsurf=size(surf);
length_y=szsurf(1);
length_x=szsurf(2);
Sku=0;
for j=1:length_y,
    for i=1:length_x,
        Sku=Sku+surf(j,i)^4;
    end
end
Sq=root_mean_square(surf,dx,dy);
Sku=Sku/(length_x*length_y*Sq^4);
end

function [Ssk] = surface_skewness(surf,dx,dy)
% SURFACE_SKEWNESS
szsurf=size(surf);
length_y=szsurf(1);
length_x=szsurf(2);
Ssk=0;
for j=1:length_y,
    for i=1:length_x,
        Ssk=Ssk + surf(j,i)^3;
    end
end
Sq=root_mean_square(surf,dx,dy);
Ssk=Ssk/(length_x*length_y*Sq^3);
end
```

Appendix C: Statistical Roughness Analysis

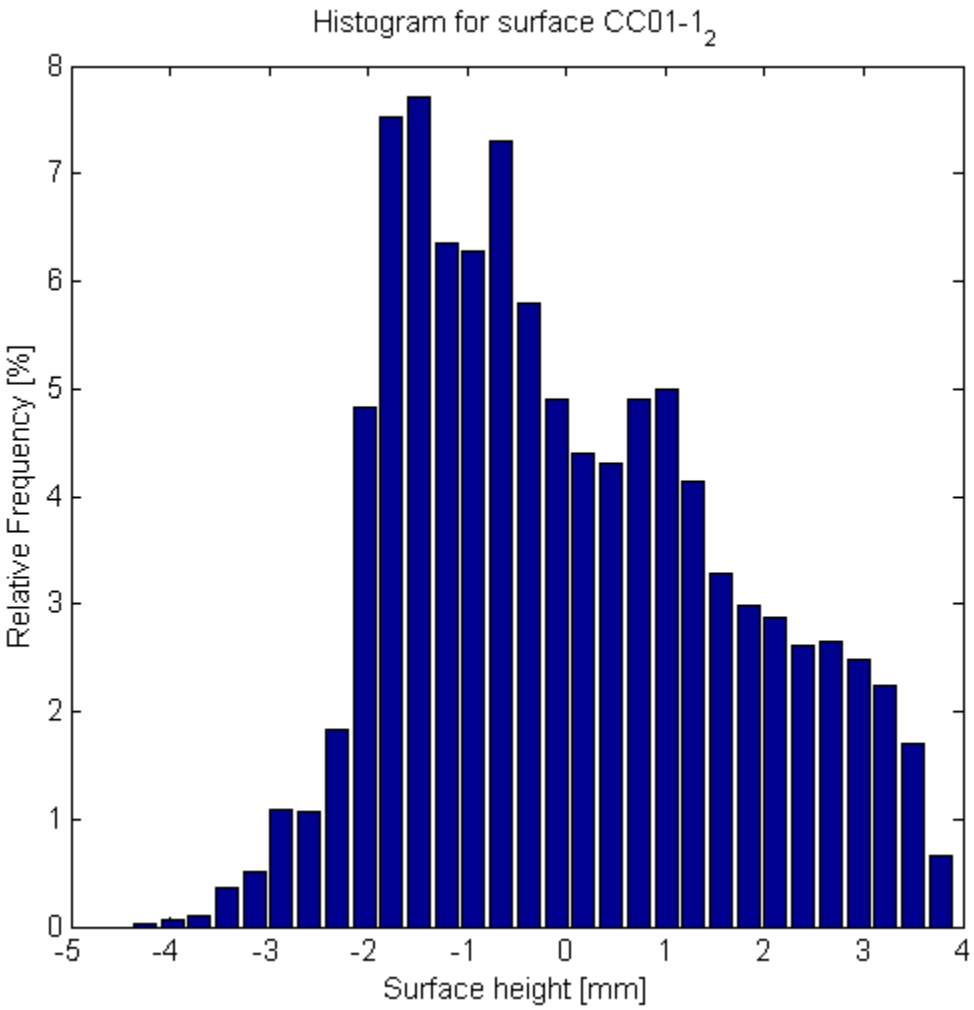

Figure C.1 Surface height frequency distribution for surface sample CC01-1_2

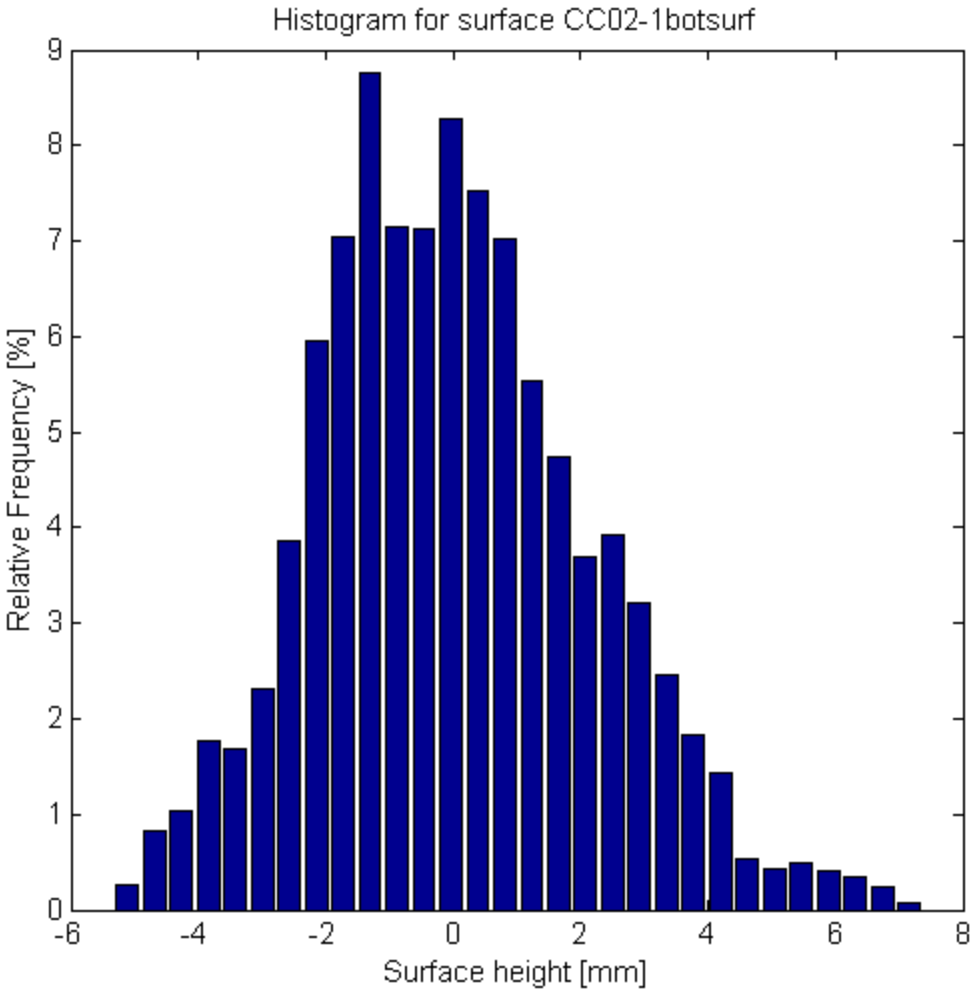

Figure C.2 Surface height frequency distribution for surface sample CC02-1botsurf

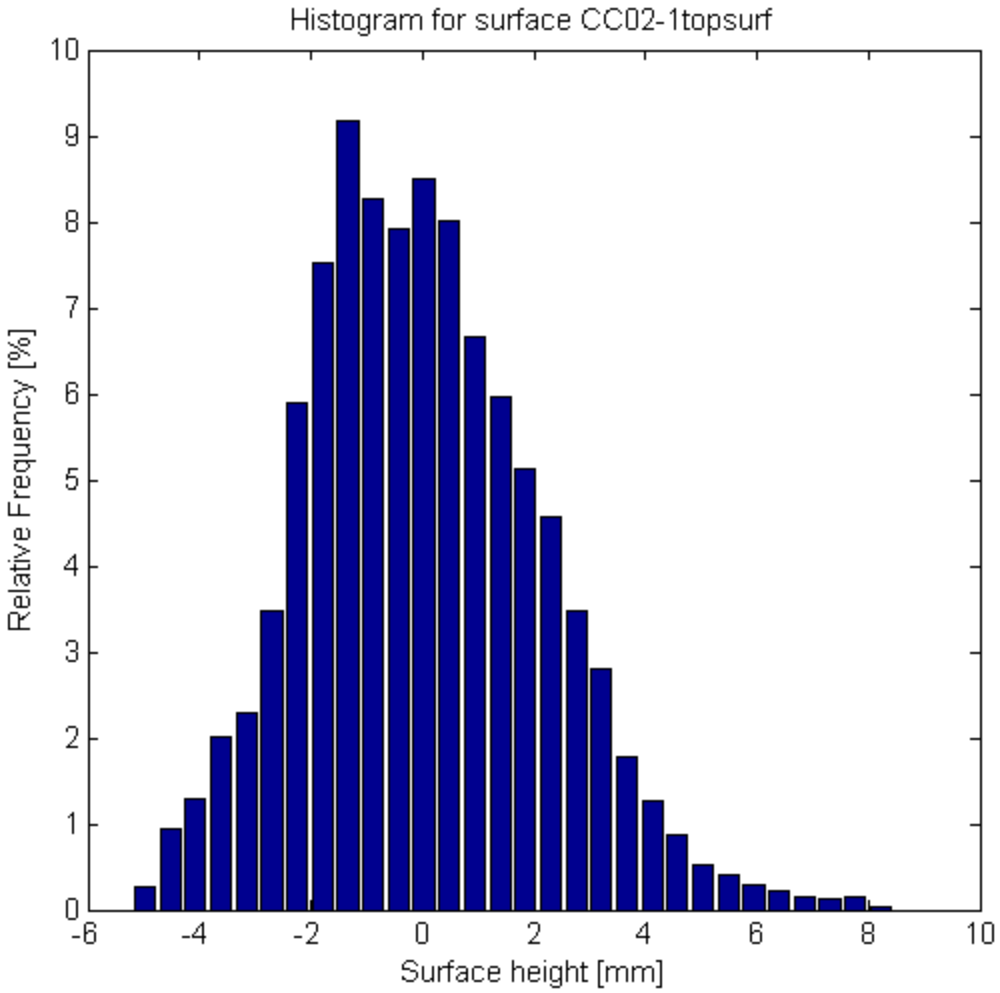

Figure C.3 Surface height frequency distribution for surface sample CC02-1topsurf

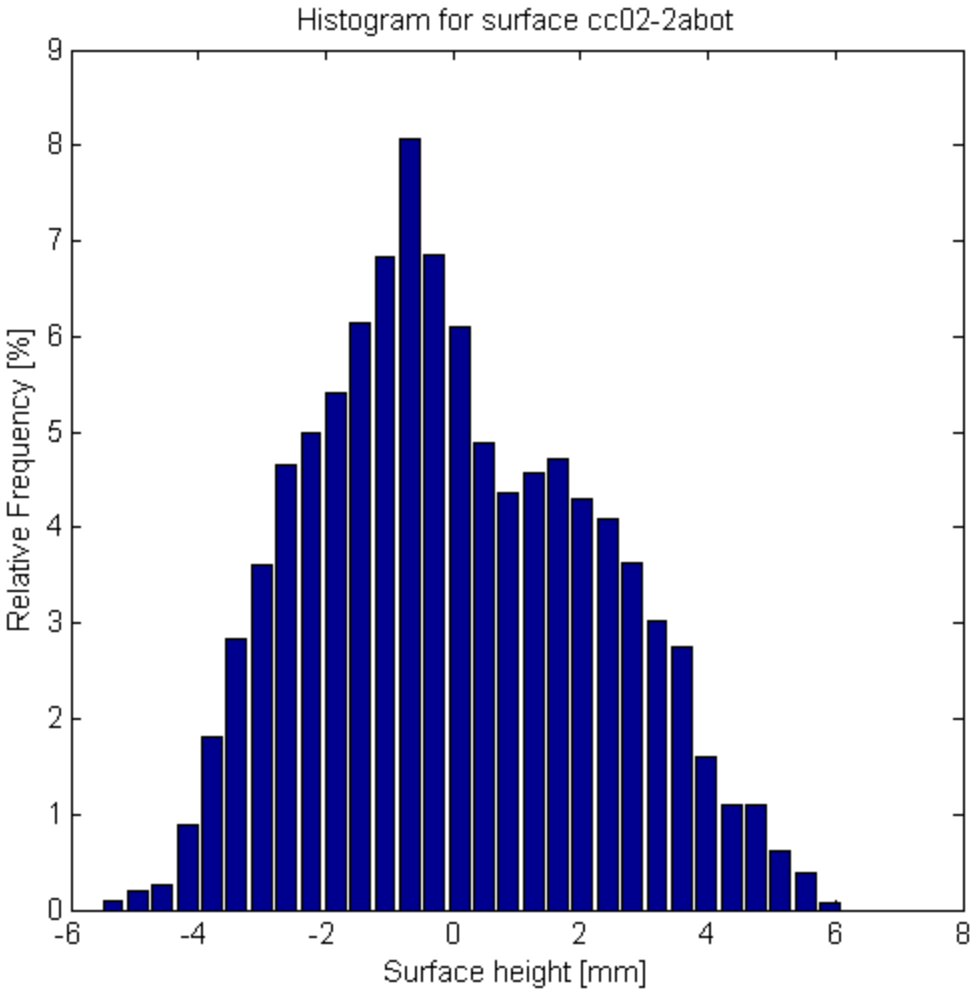

Figure C.4 Surface height frequency distribution for surface sample CC02-2abot

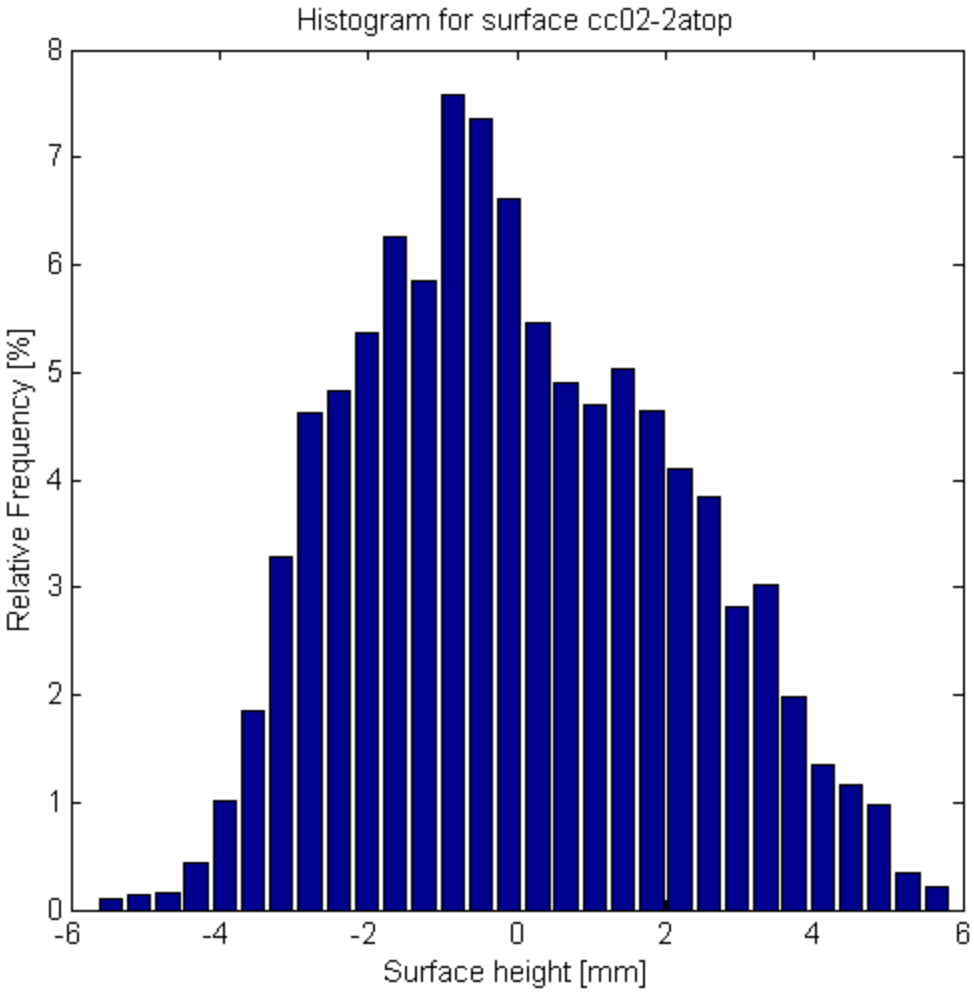

Figure C.5 Surface height frequency distribution for surface sample CC02-2atop

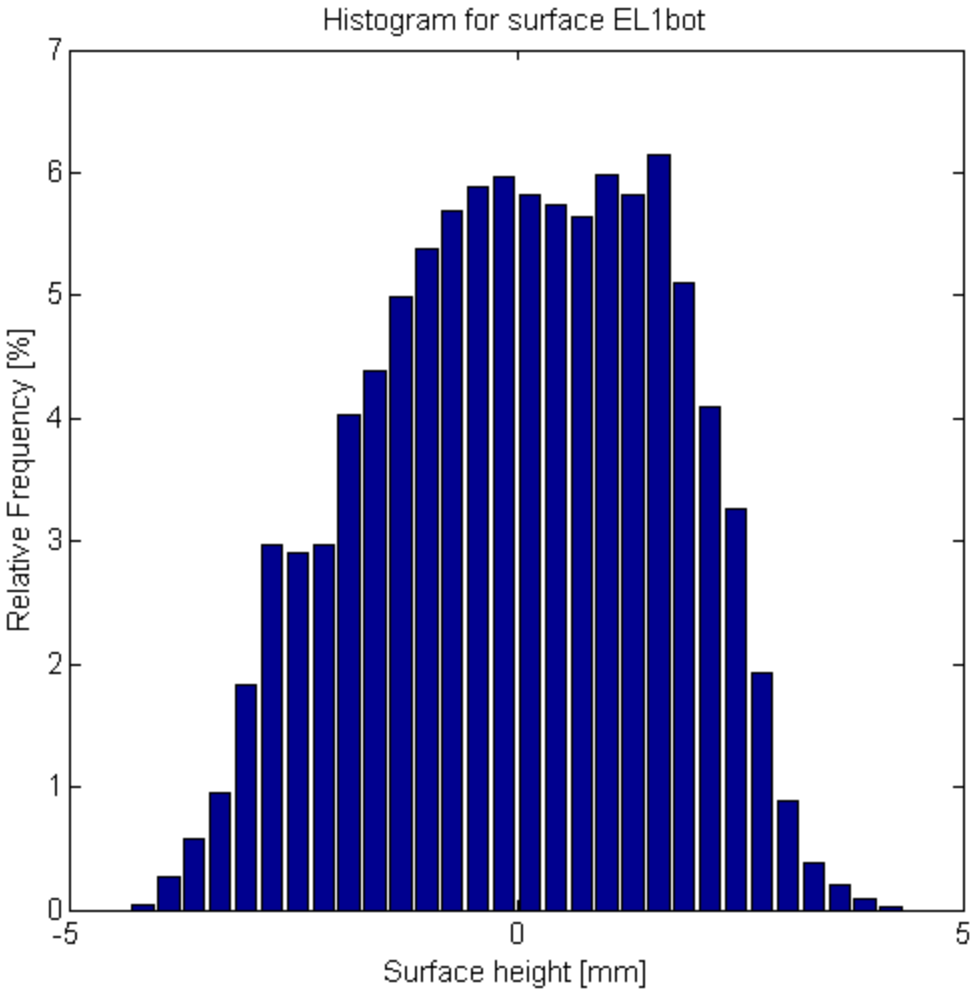

Figure C.6 Surface height frequency distribution for surface sample EL1bot

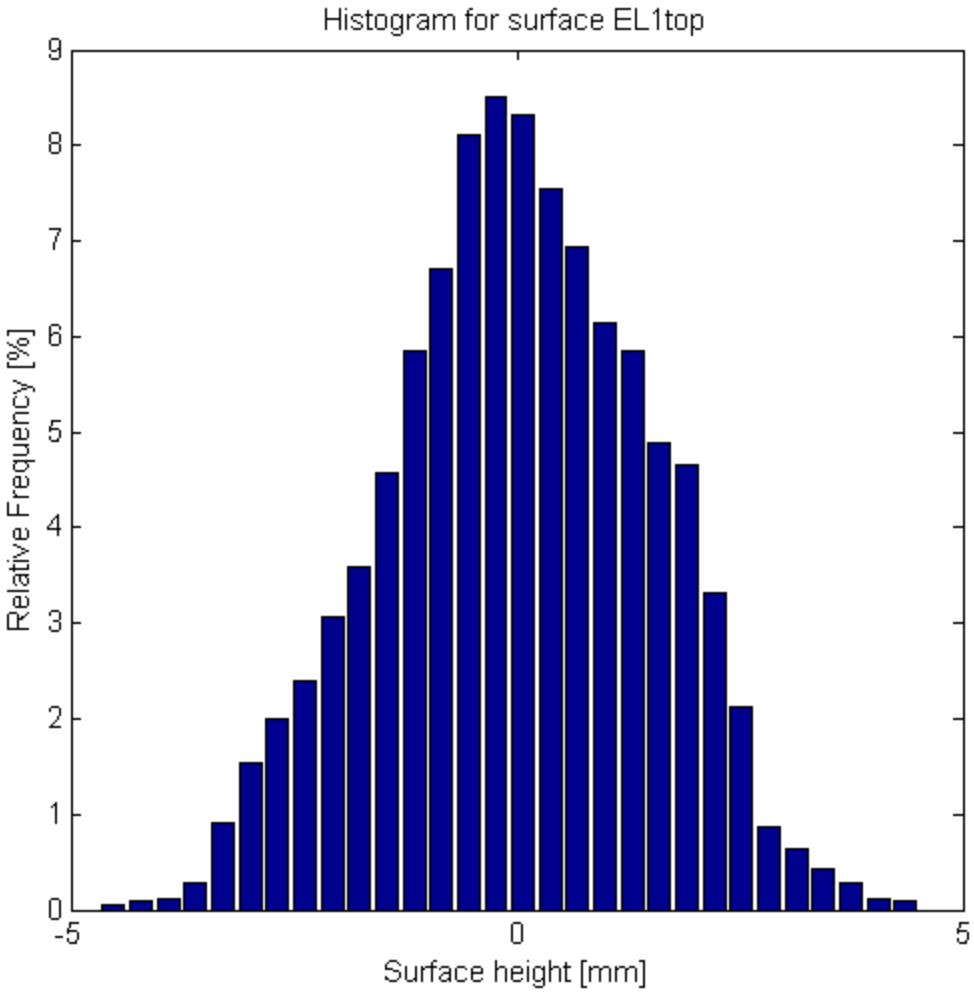

Figure C.7 Surface height frequency distribution for surface sample EL1top

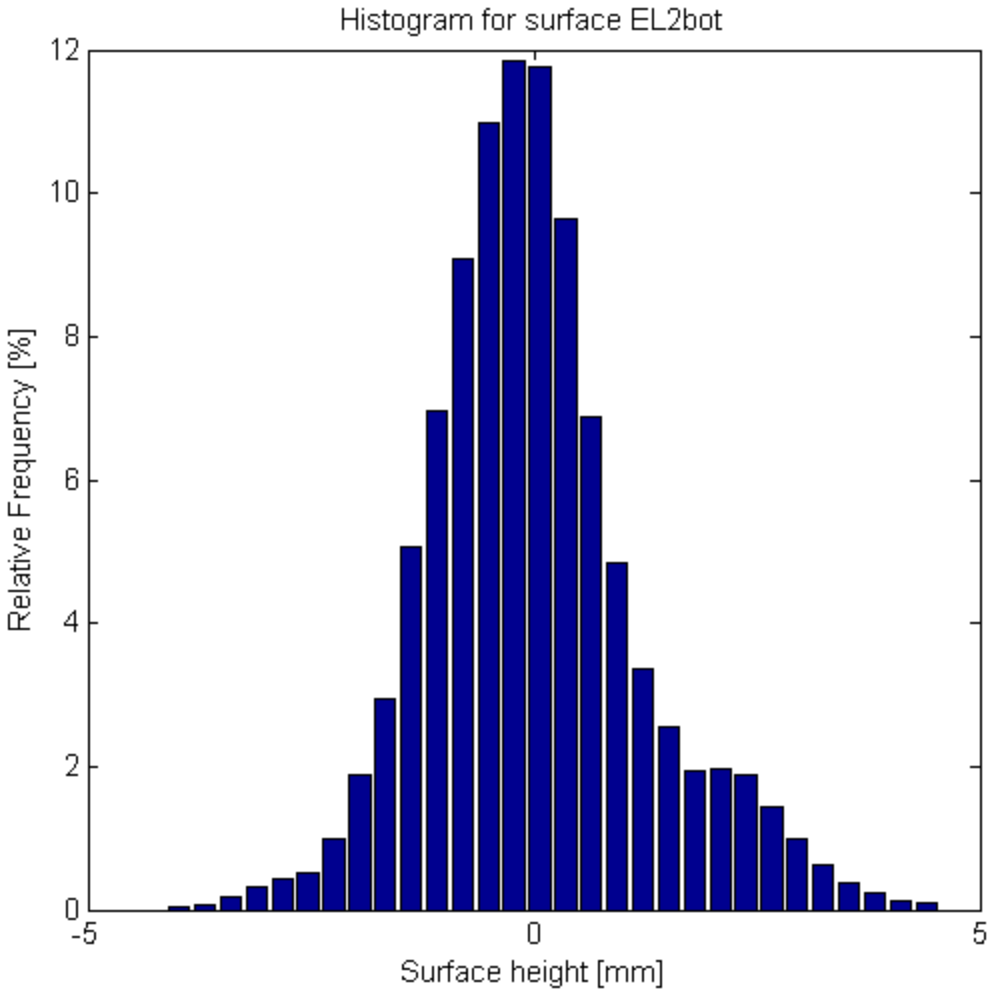

Figure C.8 Surface height frequency distribution for surface sample EL2bot

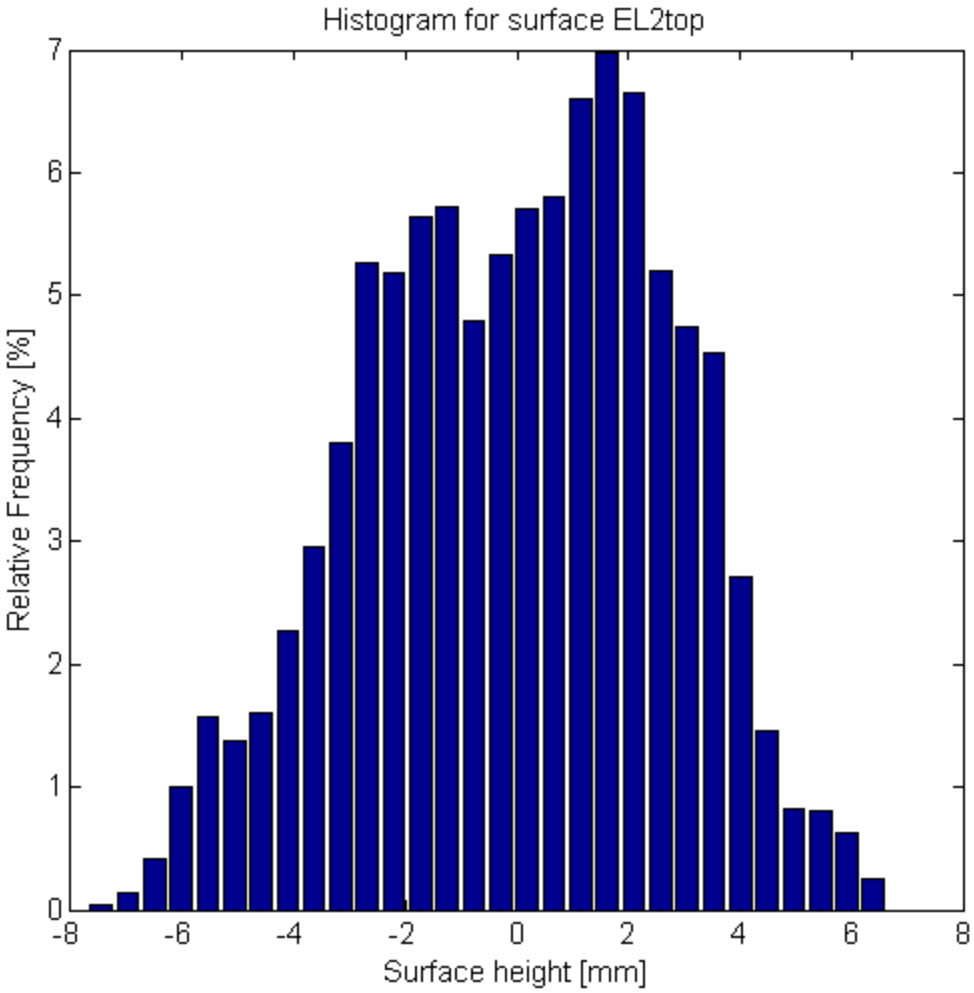

Figure C.9 Surface height frequency distribution for surface sample EL2top

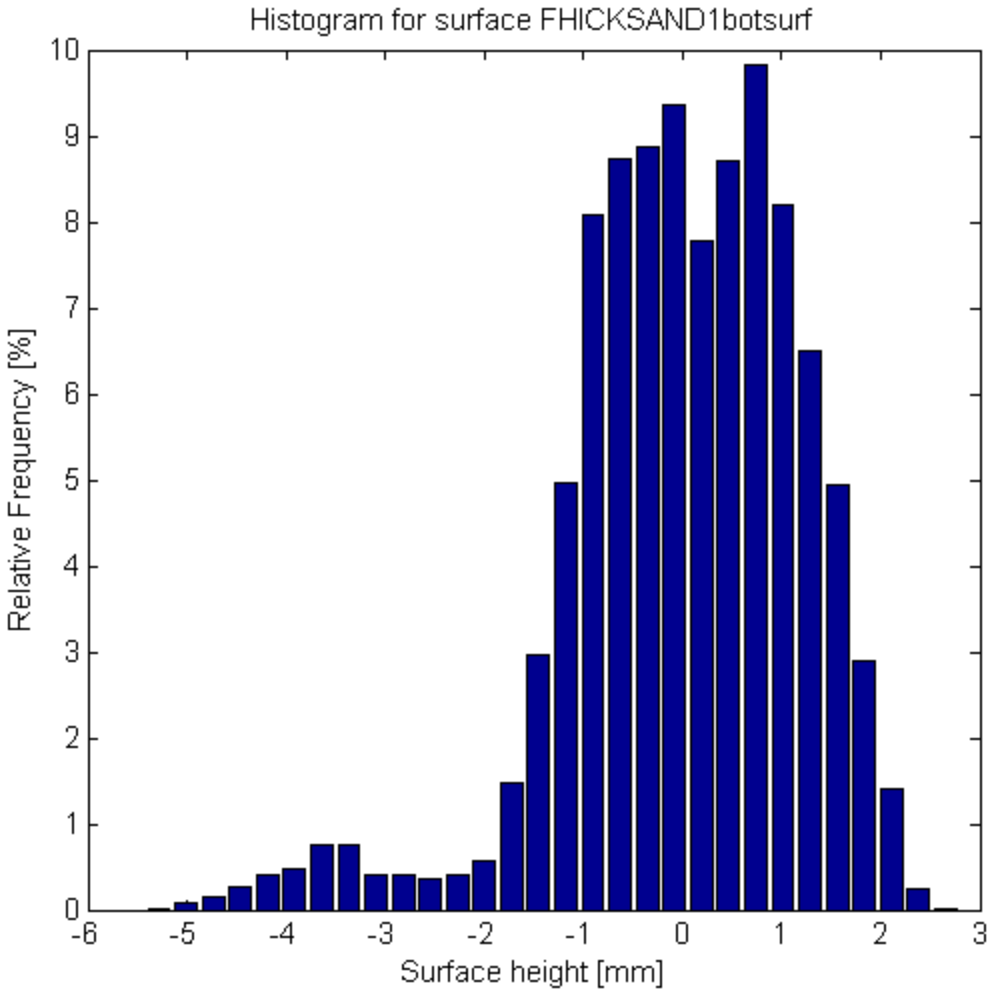

Figure C.10 Surface height frequency distribution for surface sample FHICKSAND1bot

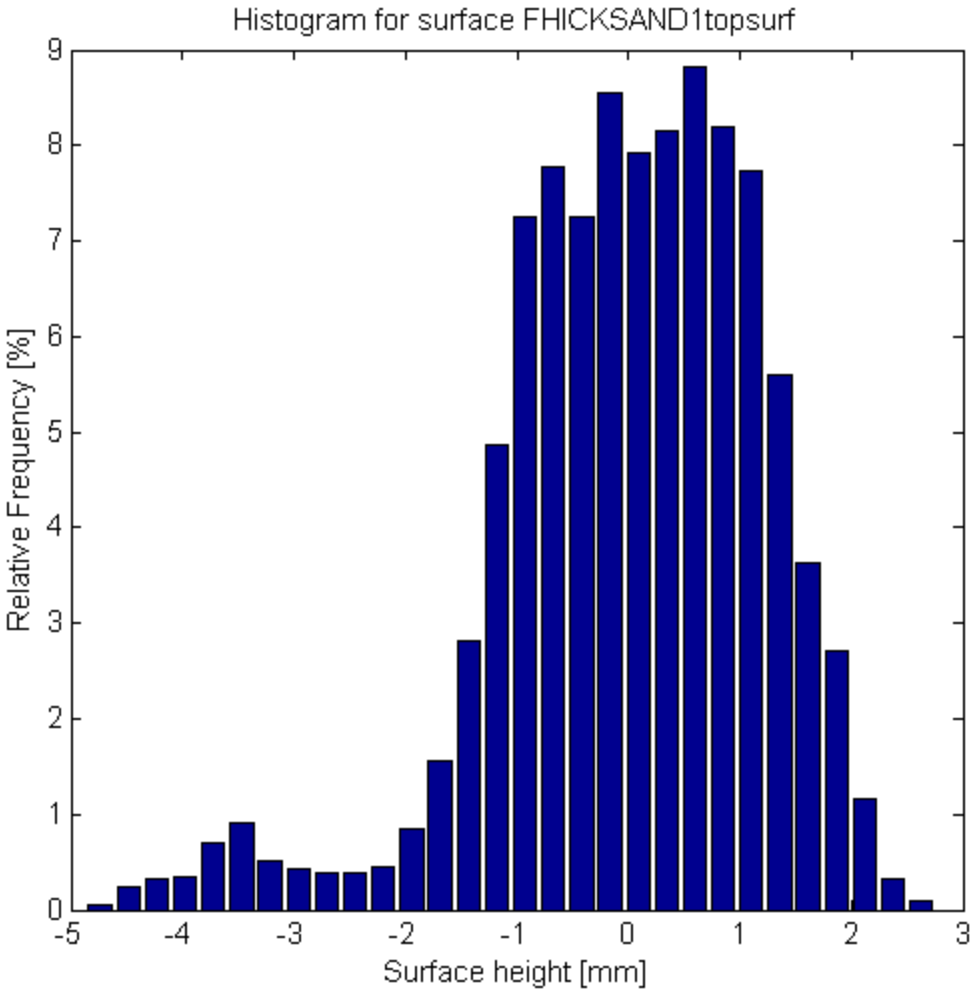

Figure C.11 Surface height frequency distribution for surface sample FHICKSAND1TOP

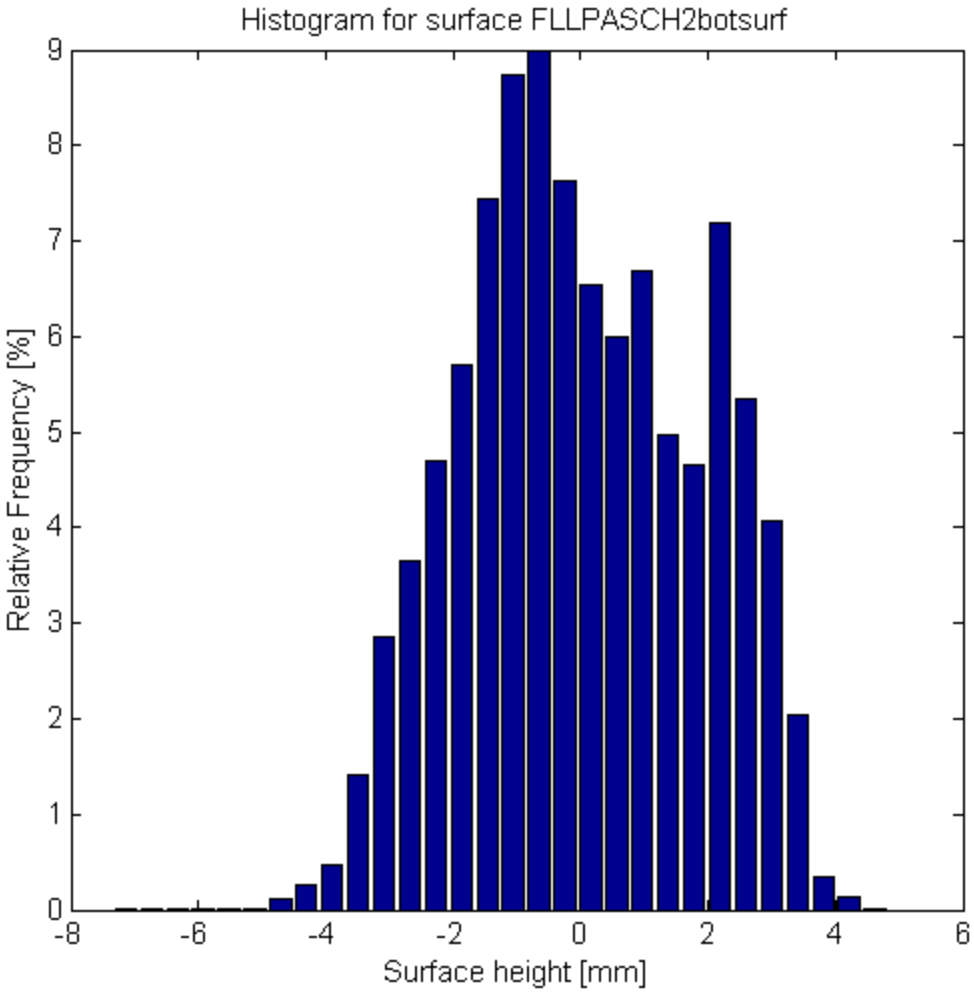

Figure C.12 Surface height frequency distribution for surface sample FLLPASCH2BOTSURF

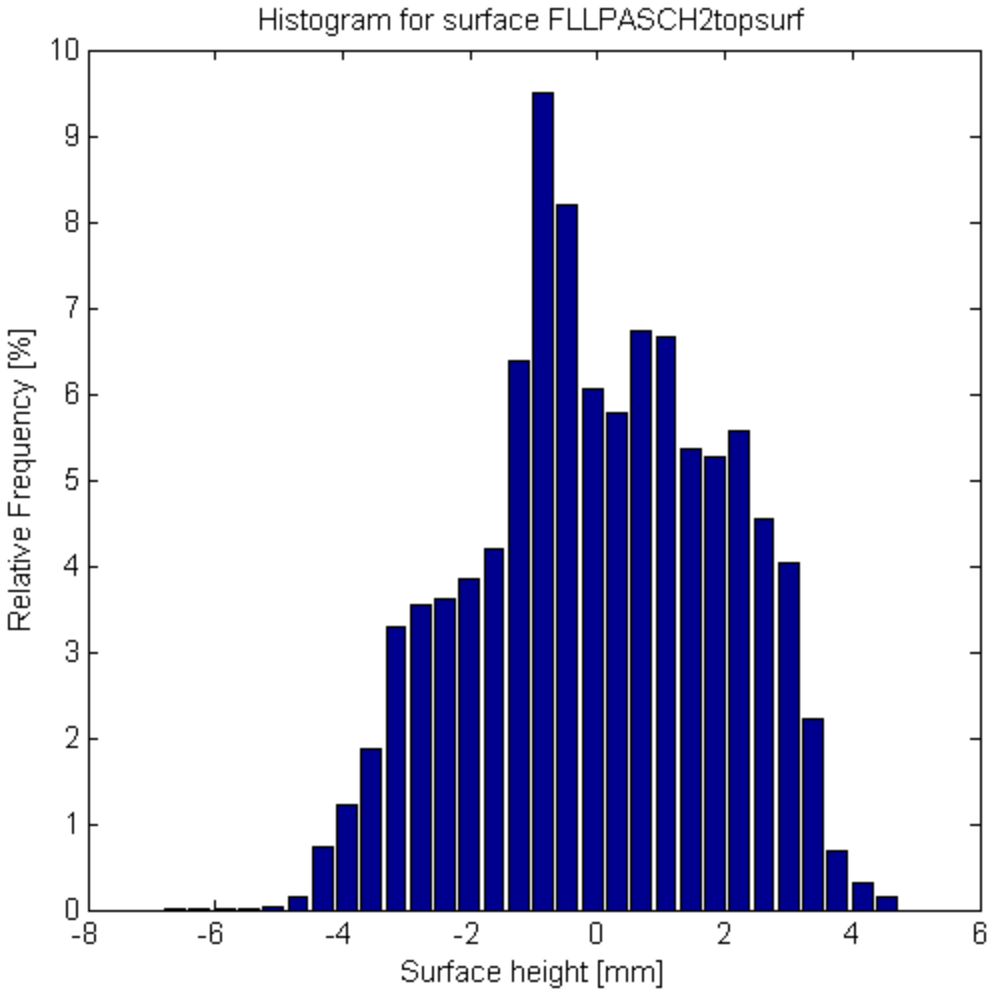

Figure C.13 Surface height frequency distribution for surface sample FLLPASCH2TOPSURF

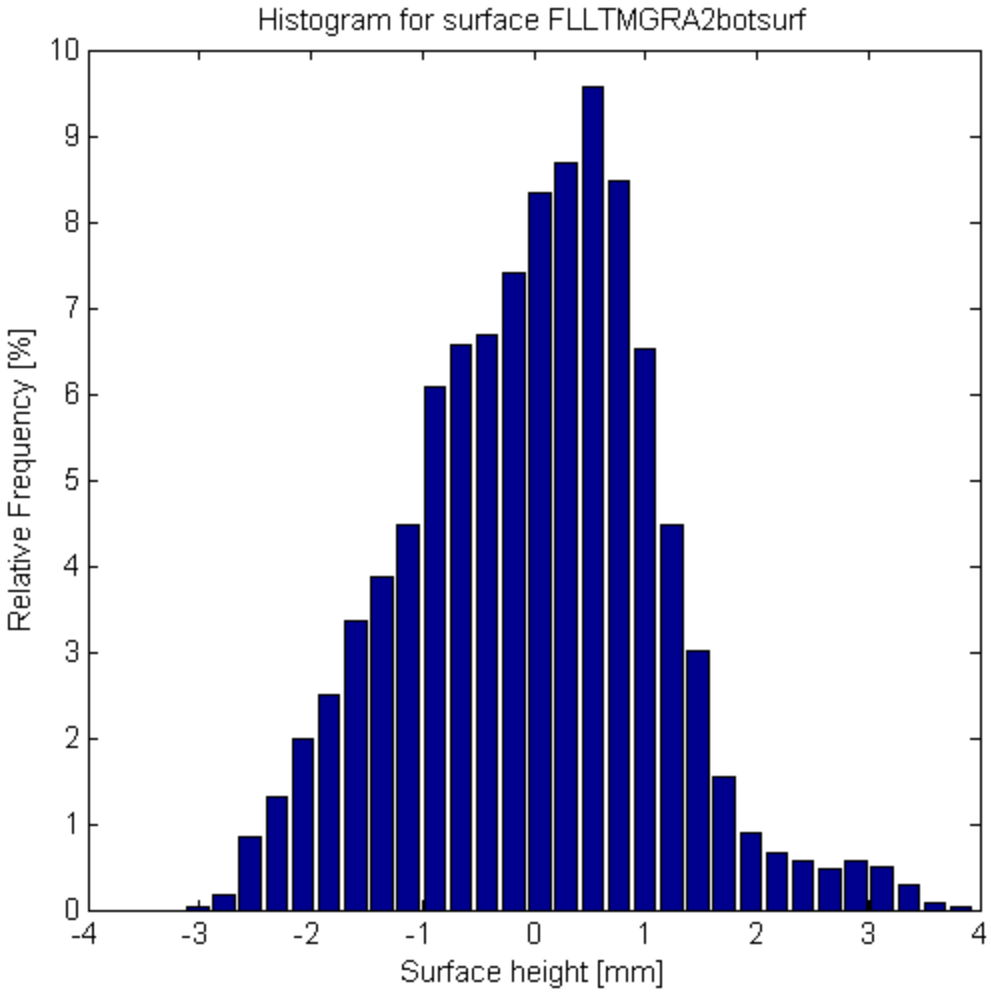

Figure C.14 Surface height frequency distribution for surface sample FLLTMGRA2BOTSURF

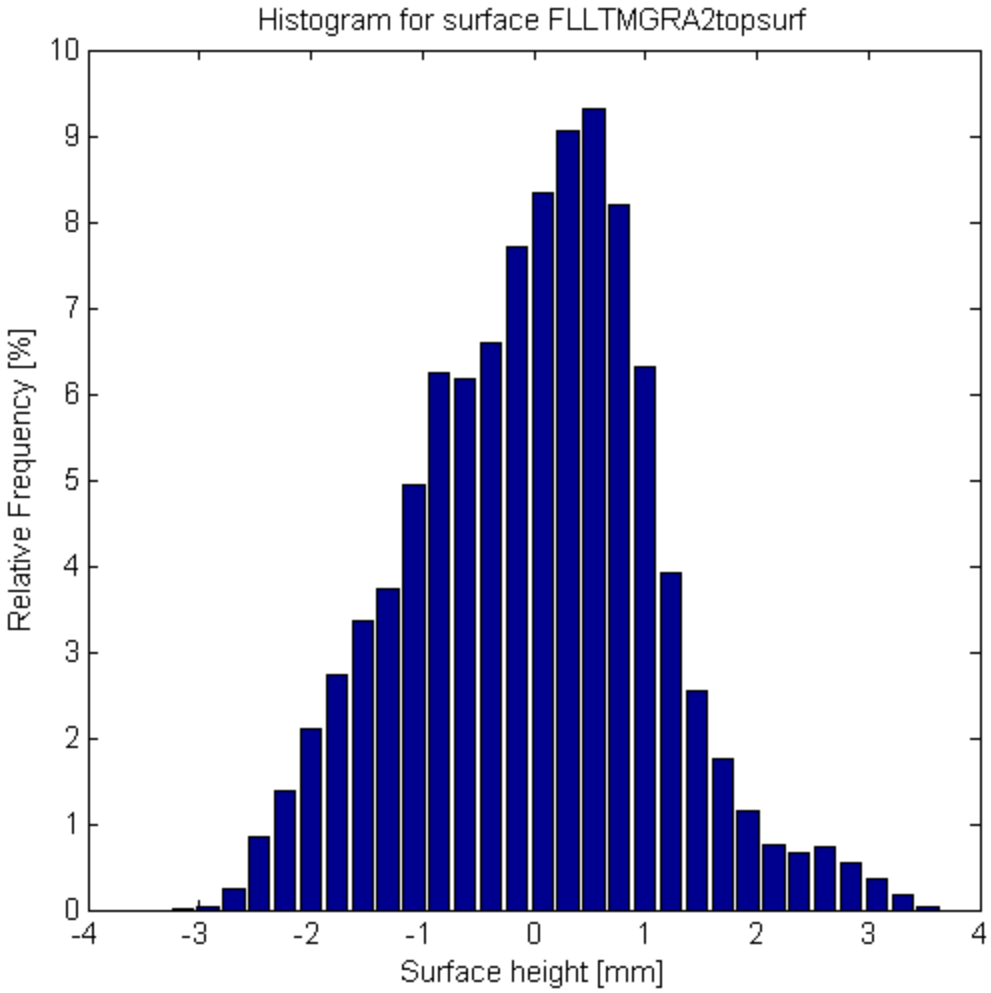

Figure C.15 Surface height frequency distribution for surface sample FLLTMGRA2TOPSURF

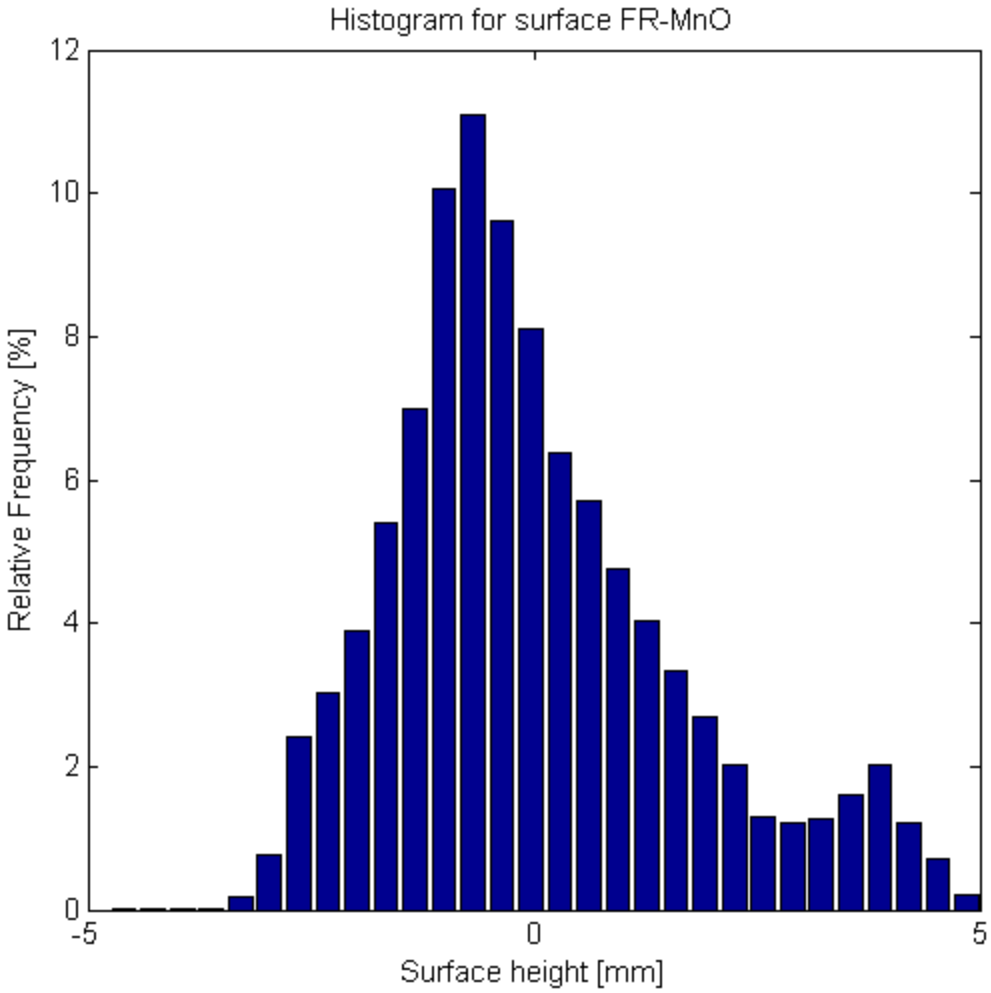

Figure C.16 Surface height frequency distribution for surface sample FR-MnO

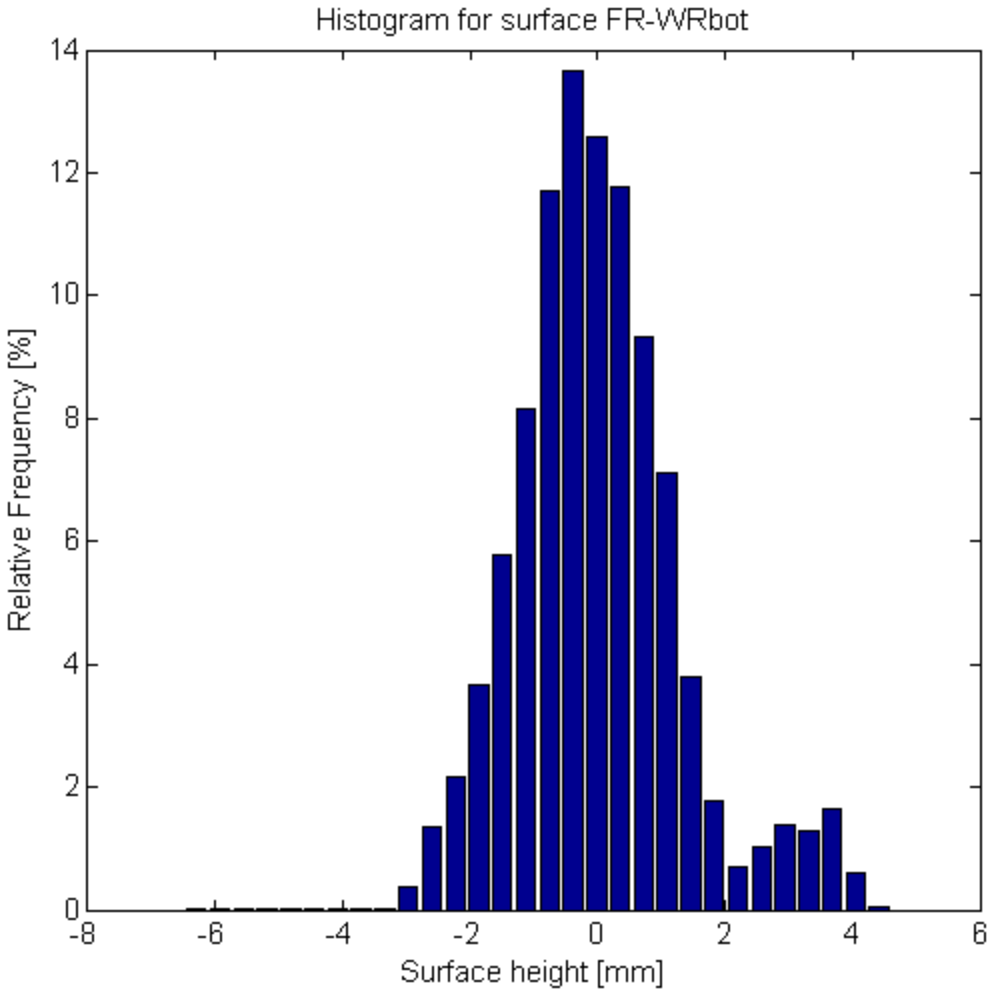

Figure C.17 Surface height frequency distribution for surface sample FR-WRbot

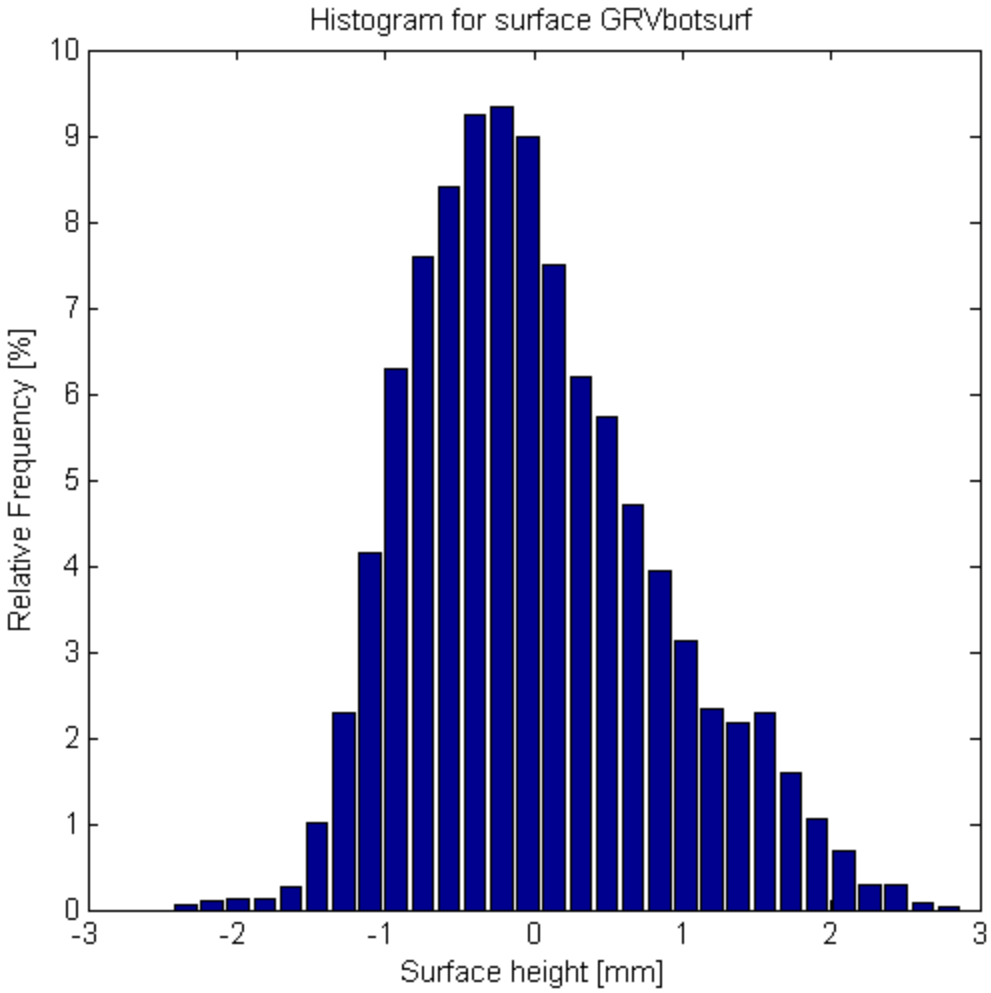

Figure C.18 Surface height frequency distribution for surface sample GRVbotsurf

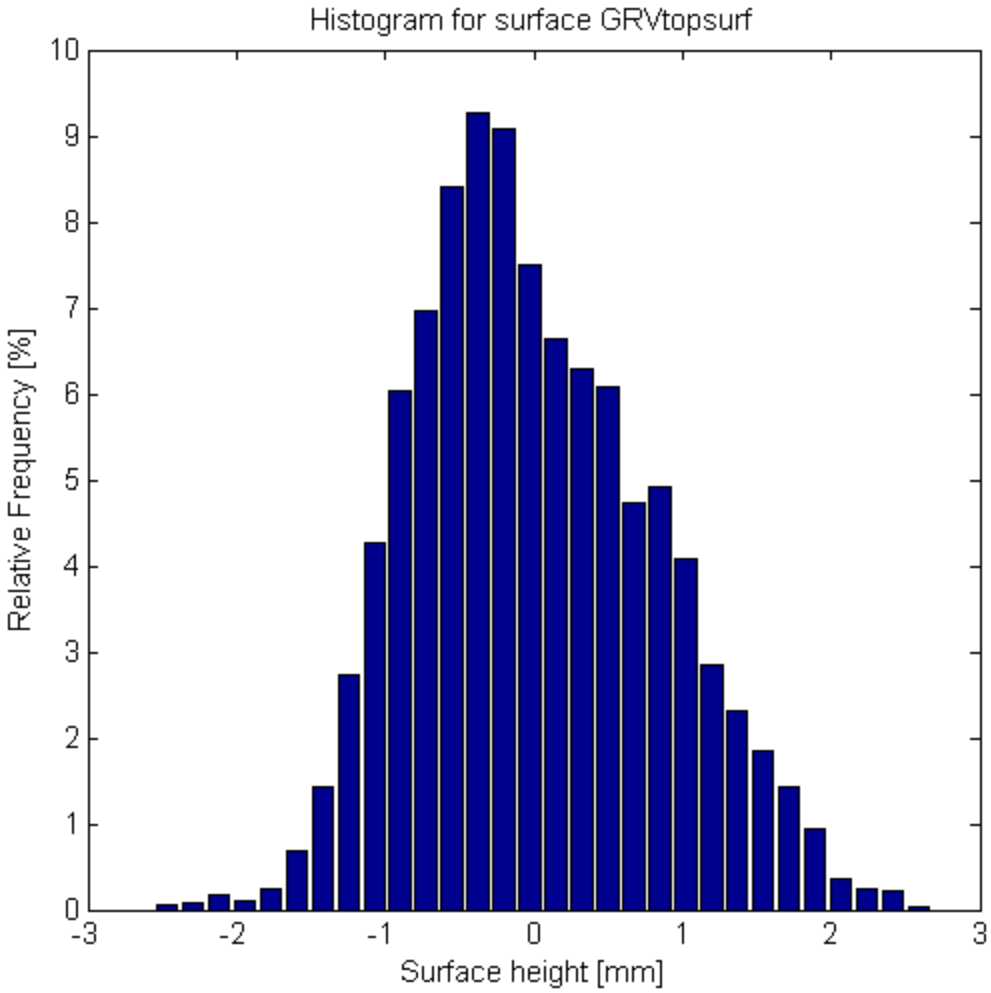

Figure C.19 Surface height frequency distribution for surface sample GRVtopsurf

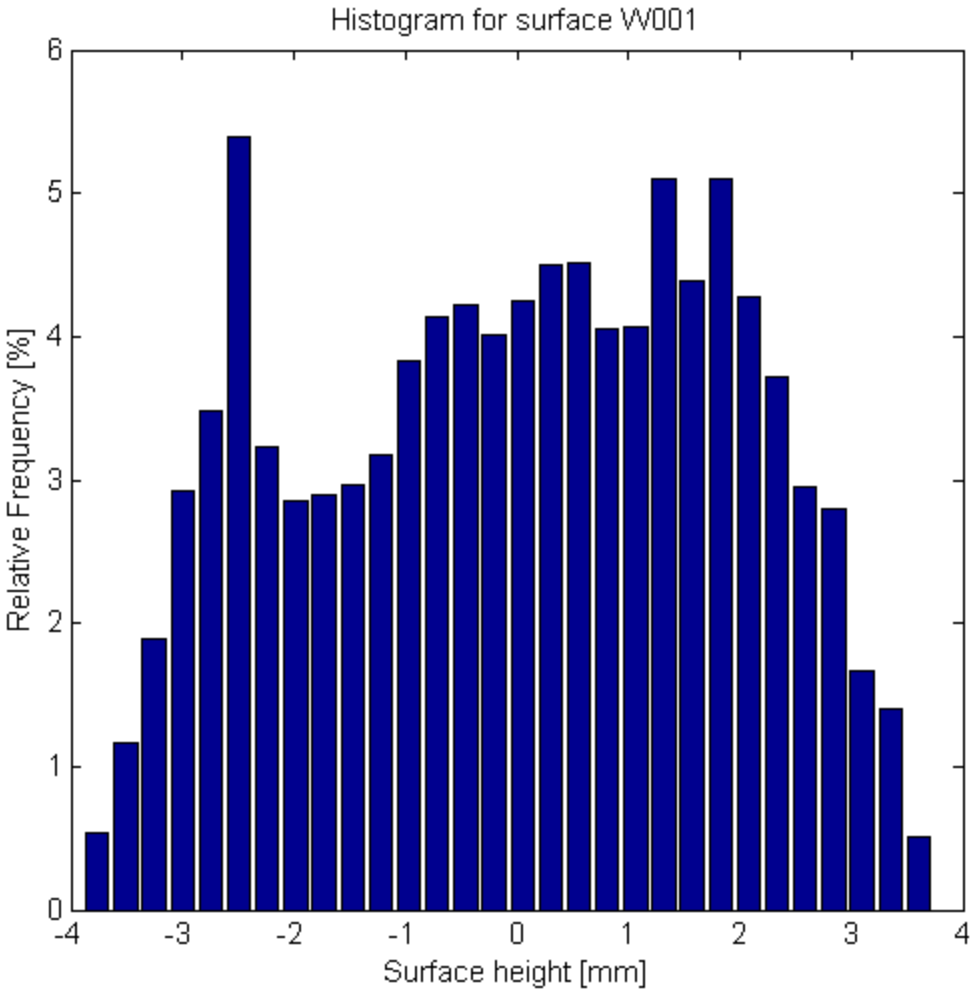

Figure C.20 Surface height frequency distribution for surface sample W001

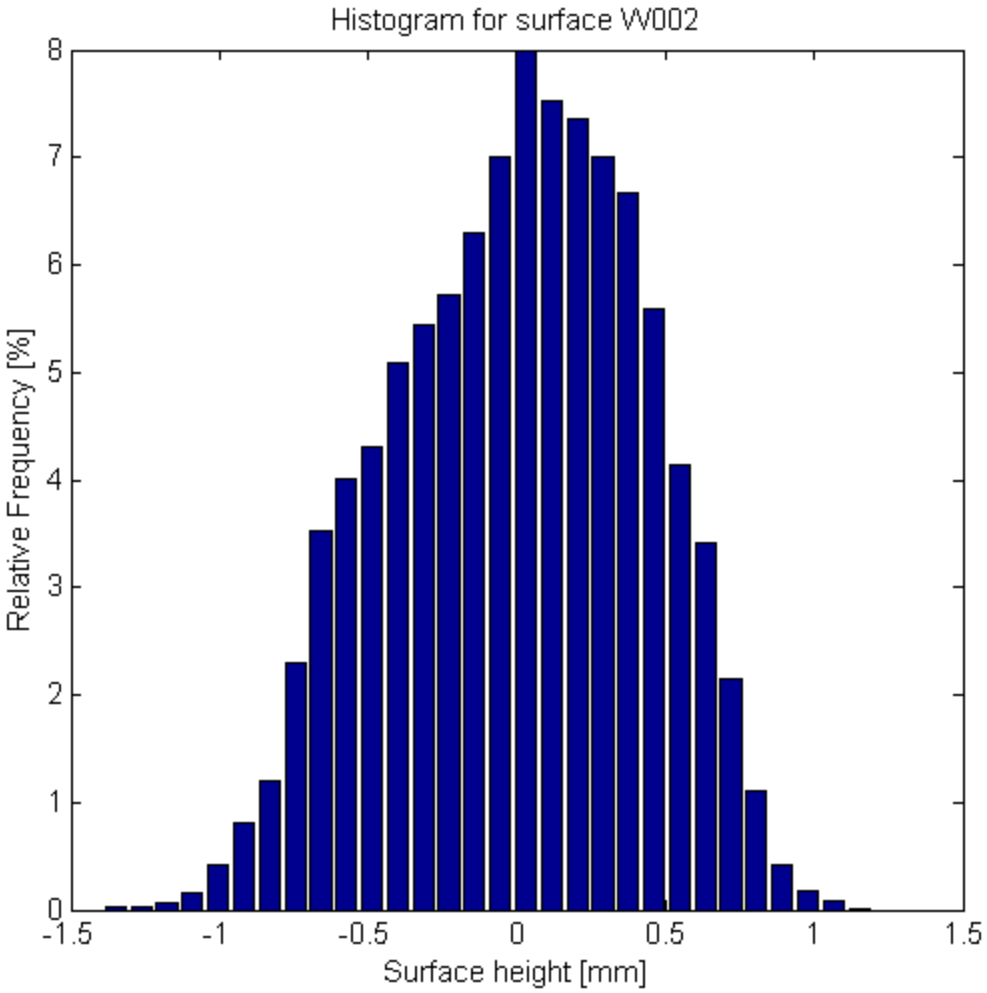

Figure C.21 Surface height frequency distribution for surface sample W002

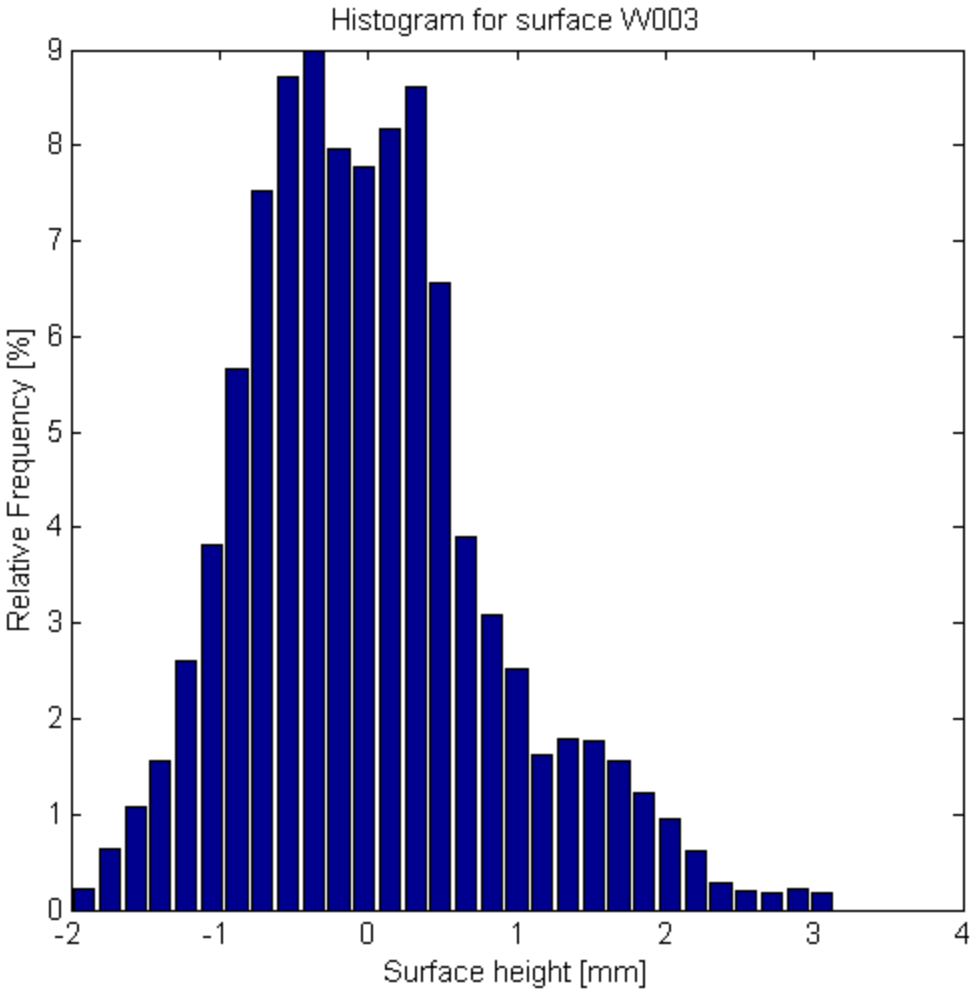

Figure C.22 Surface height frequency distribution for surface sample W003

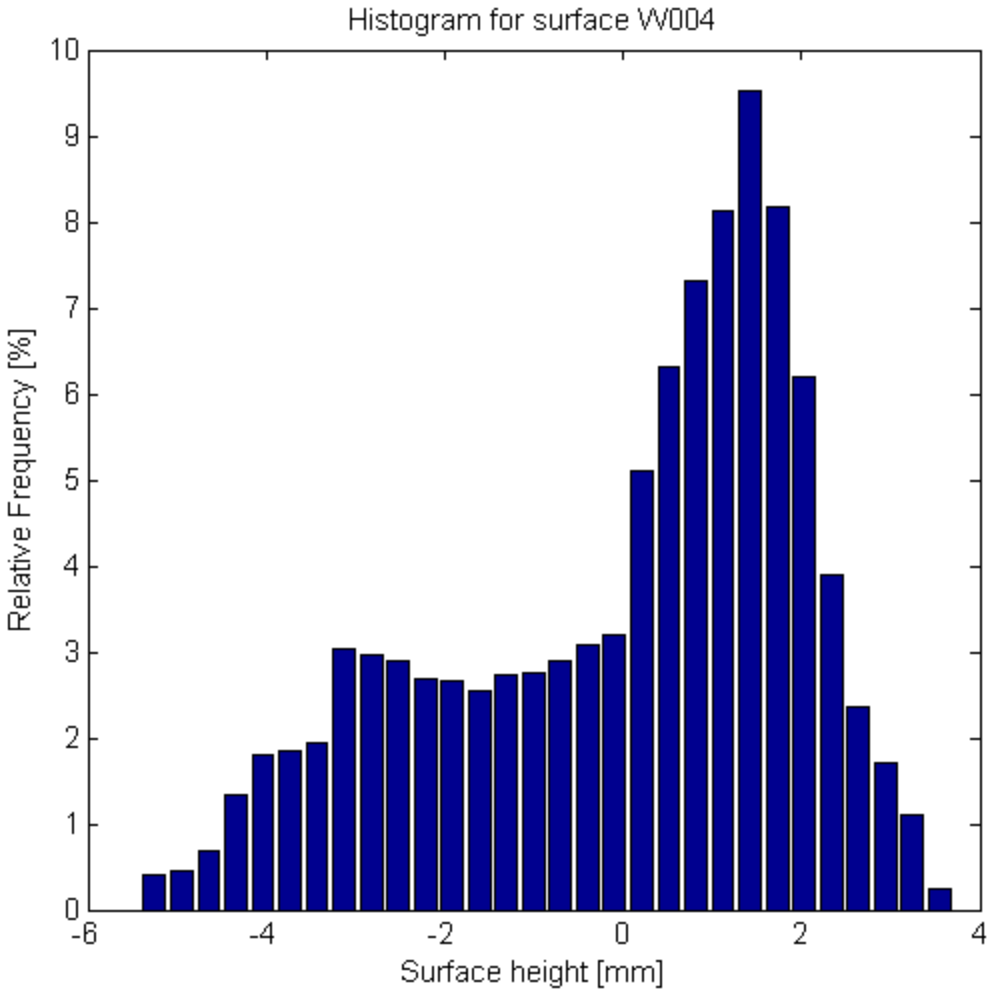

Figure C.23 Surface height frequency distribution for surface sample W004

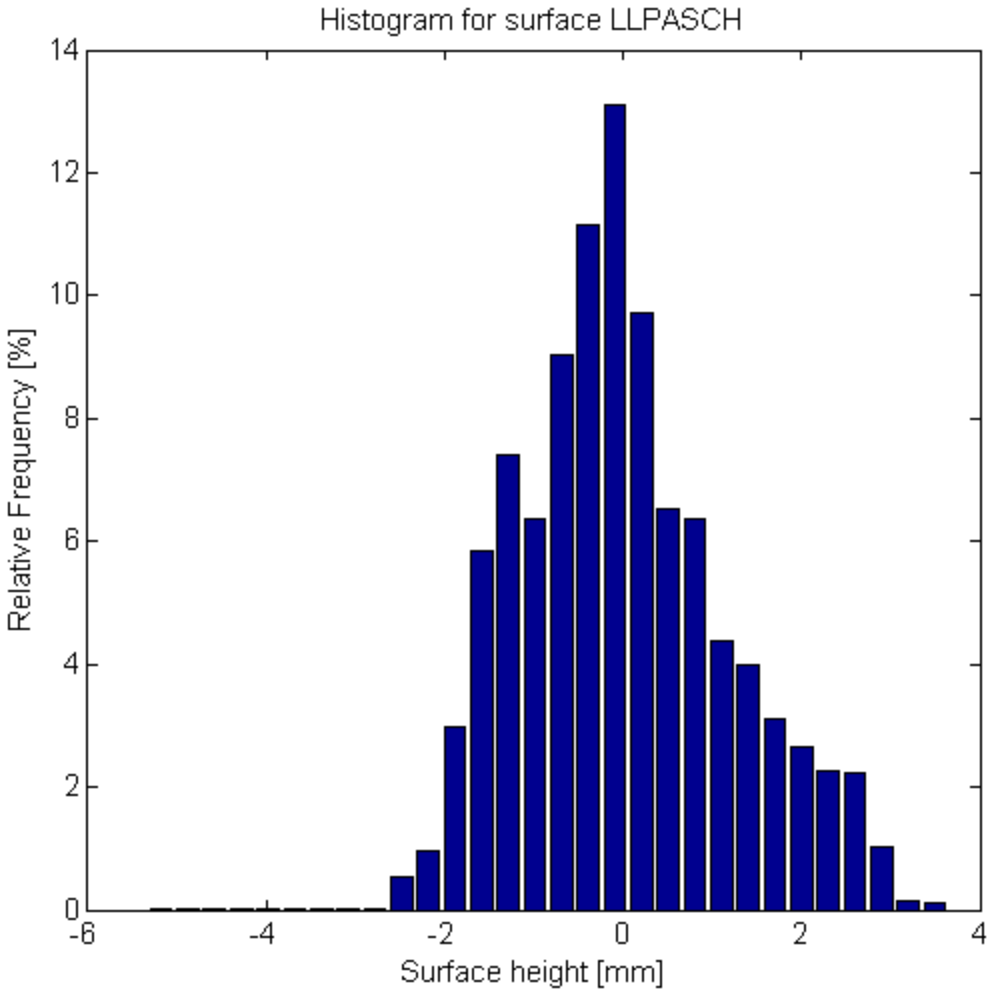

Figure C.24 Surface height frequency distribution for surface sample LLPASCH1

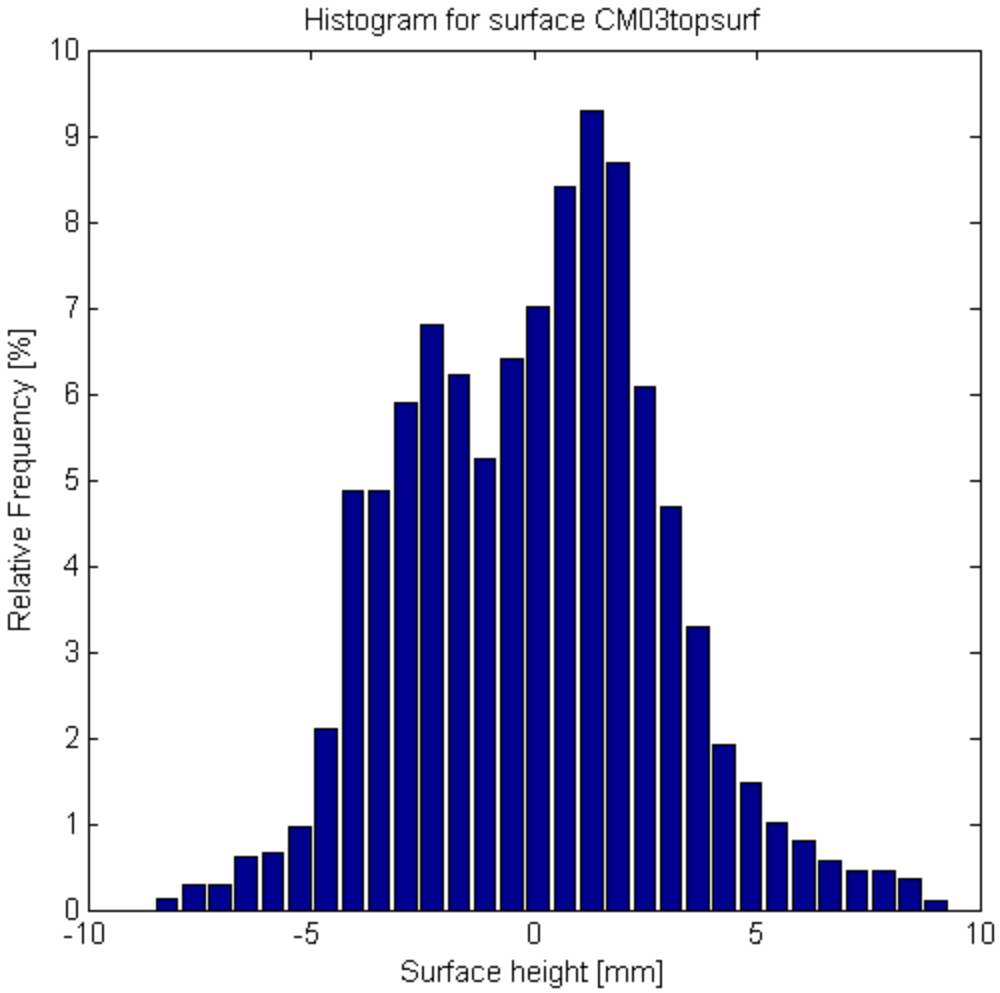

Figure C.25 Surface height frequency distribution for surface sample CM03topsurf

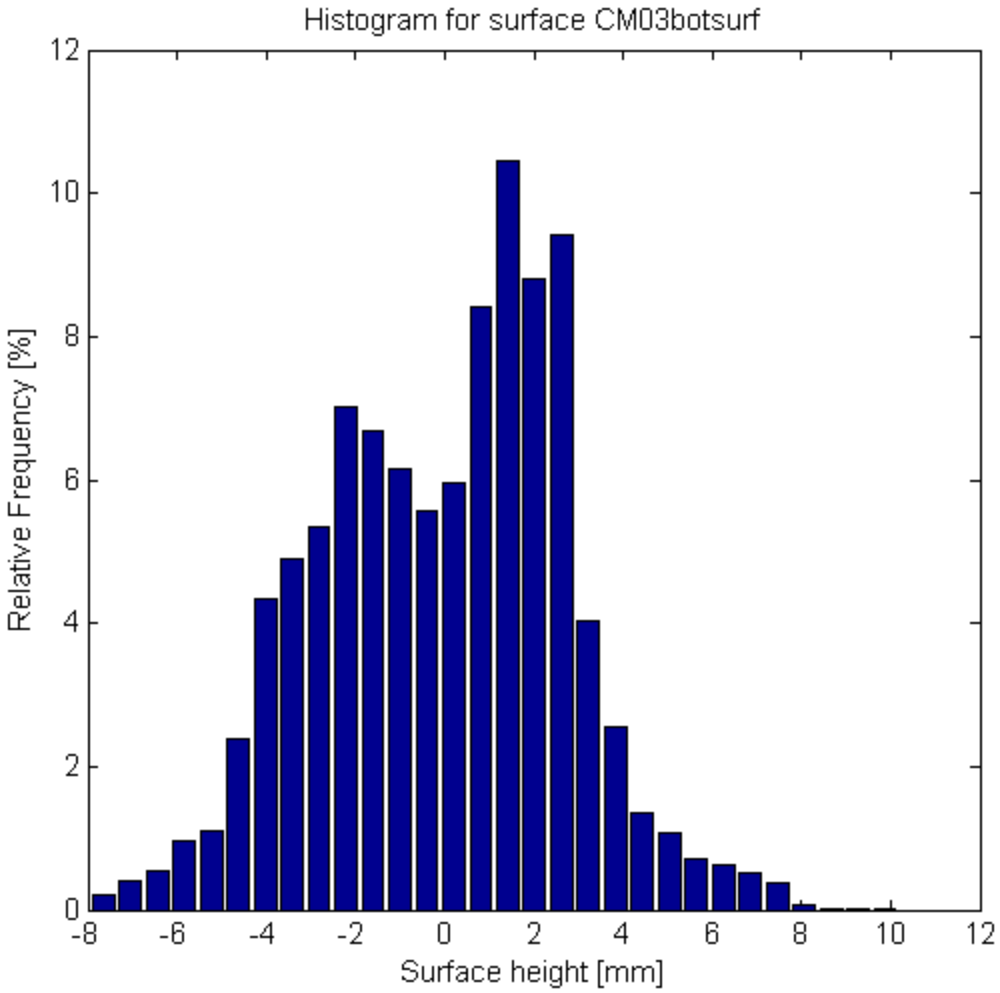

Figure C.26 Surface height frequency distribution for surface sample CM03botsurf

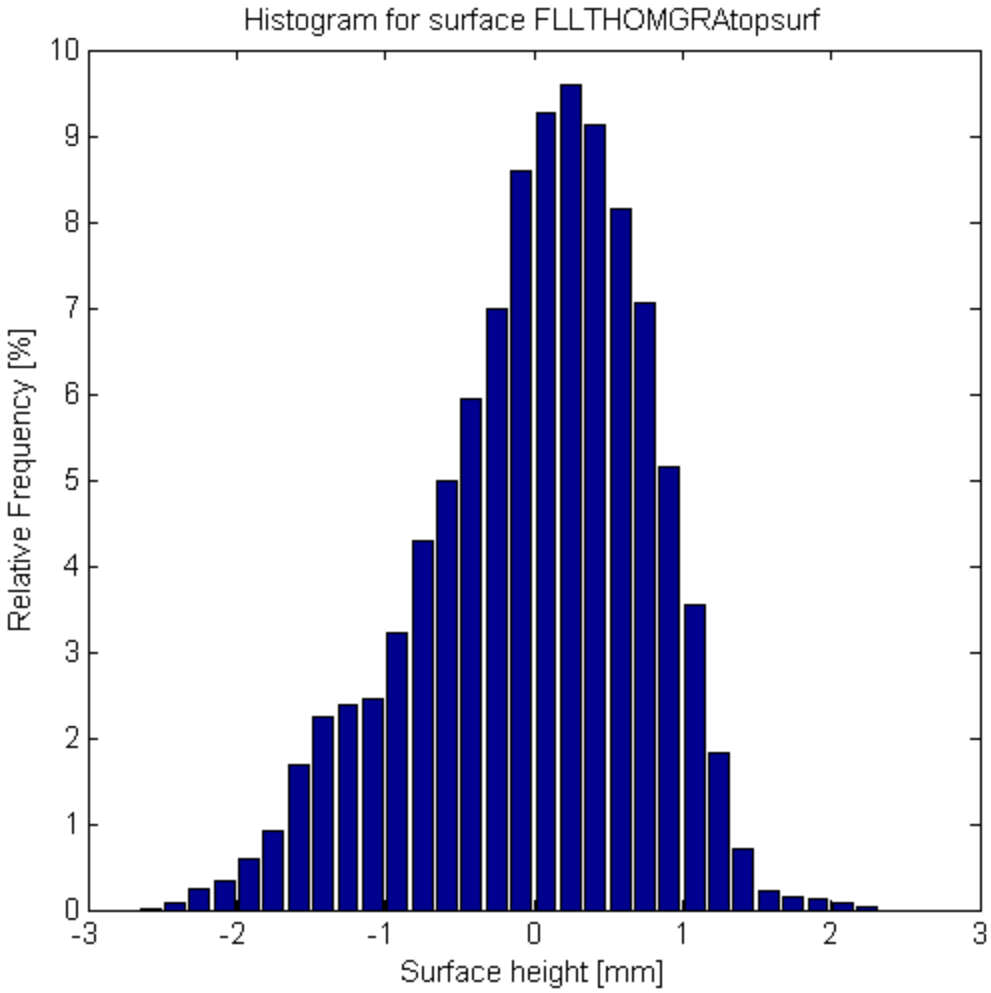

Figure C.27 Surface height frequency distribution for surface sample FLLTHOMGRAtopsurf

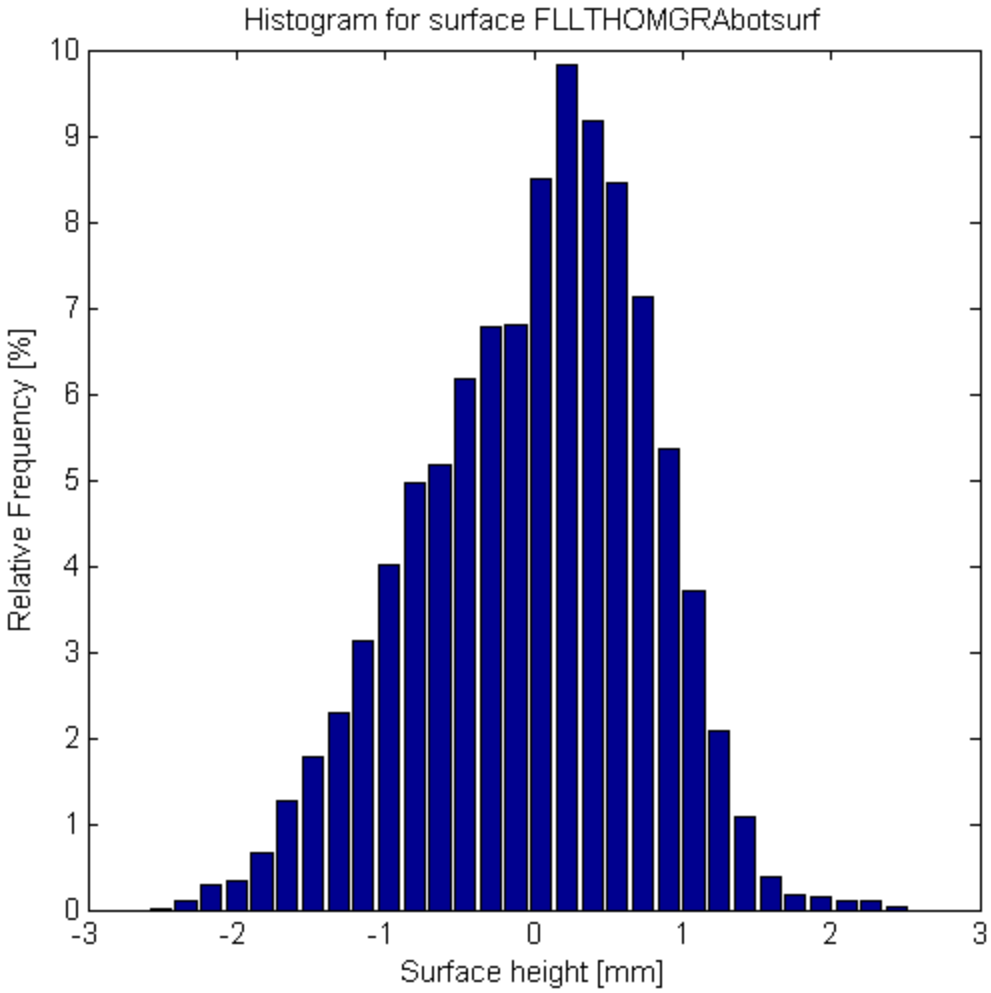

Figure C.28 Surface height frequency distribution for surface sample FLLTHOMGRAbotsurf

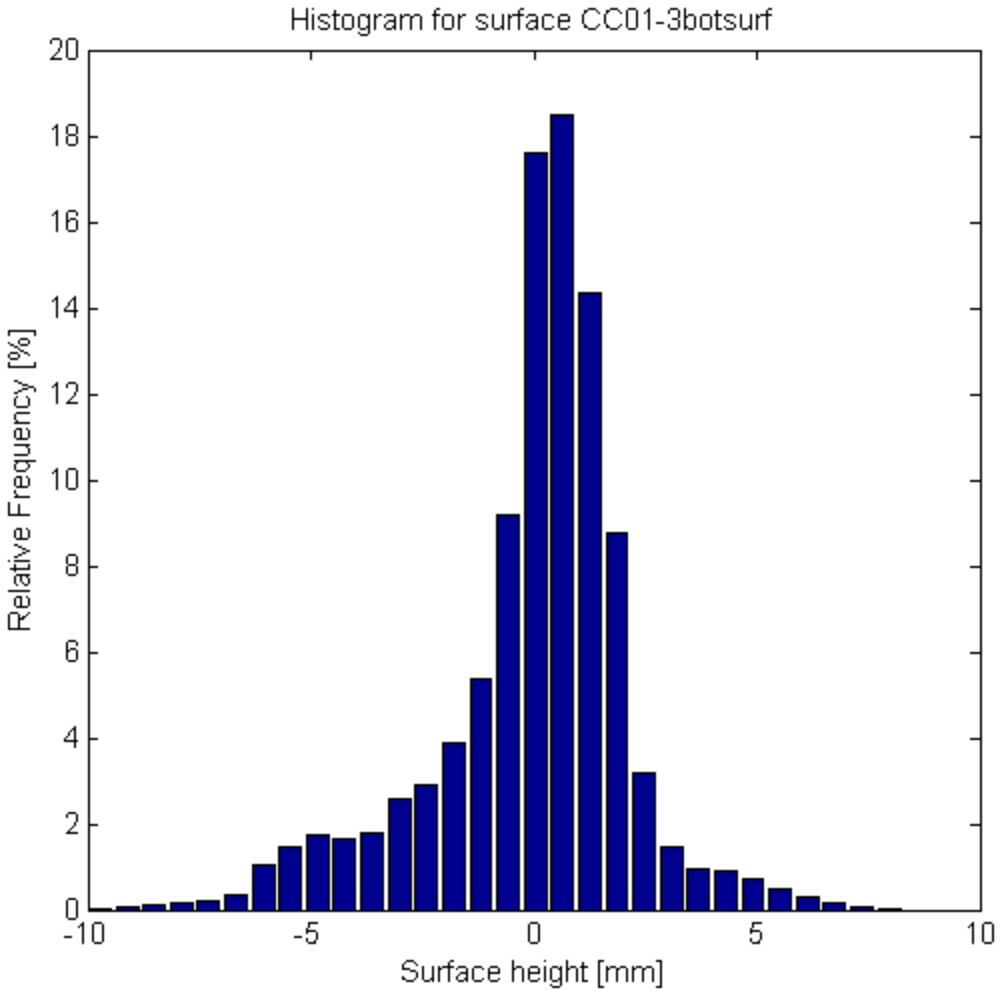

Figure C.29 Surface height frequency distribution for surface sample CC01-3botsurf

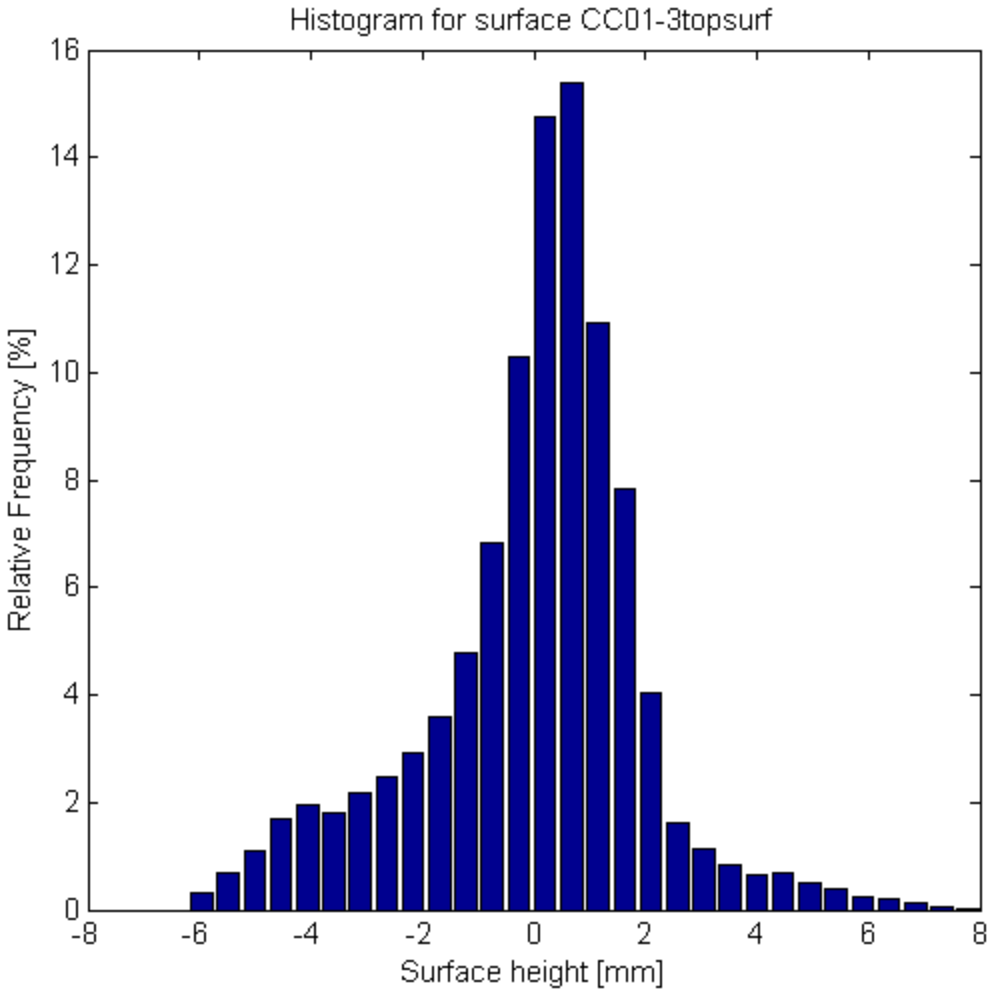

Figure C.30 Surface height frequency distribution for surface sample CC01-3topsurf

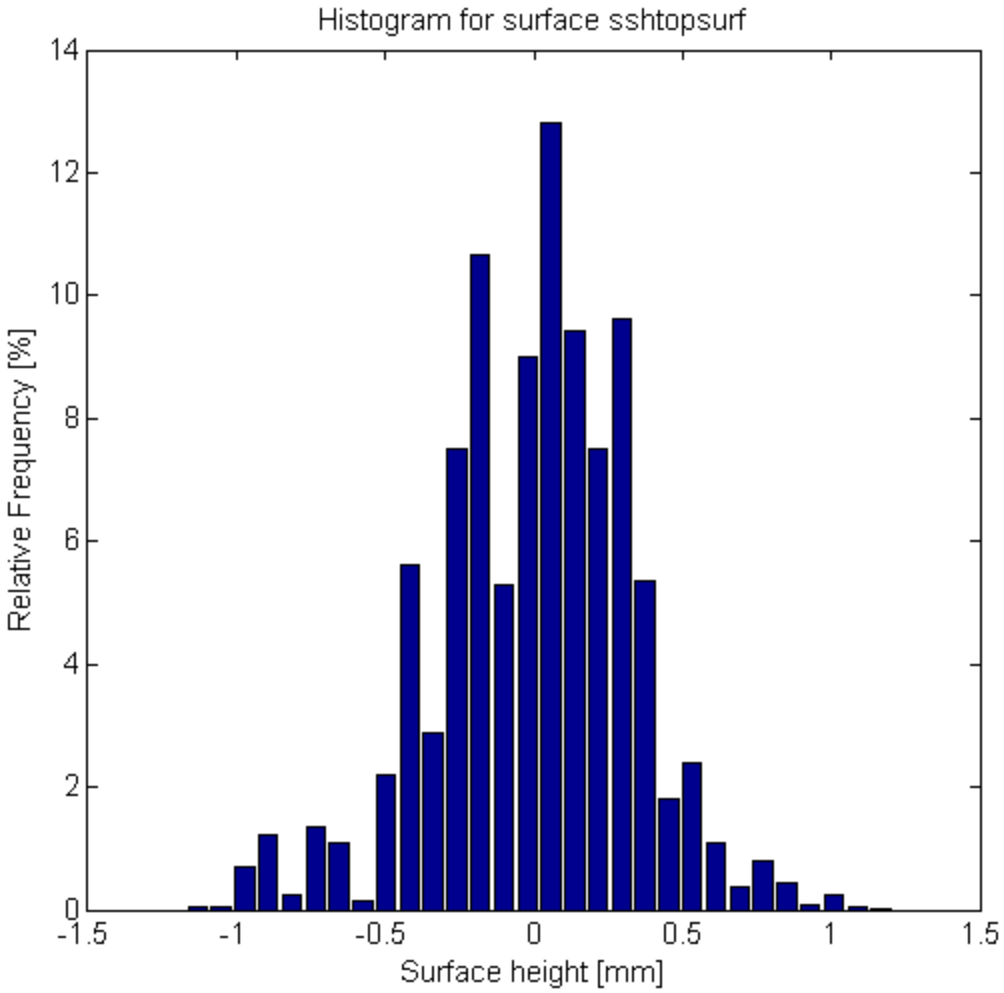

Figure C.31 Surface height frequency distribution for surface sample SSHtopsurf

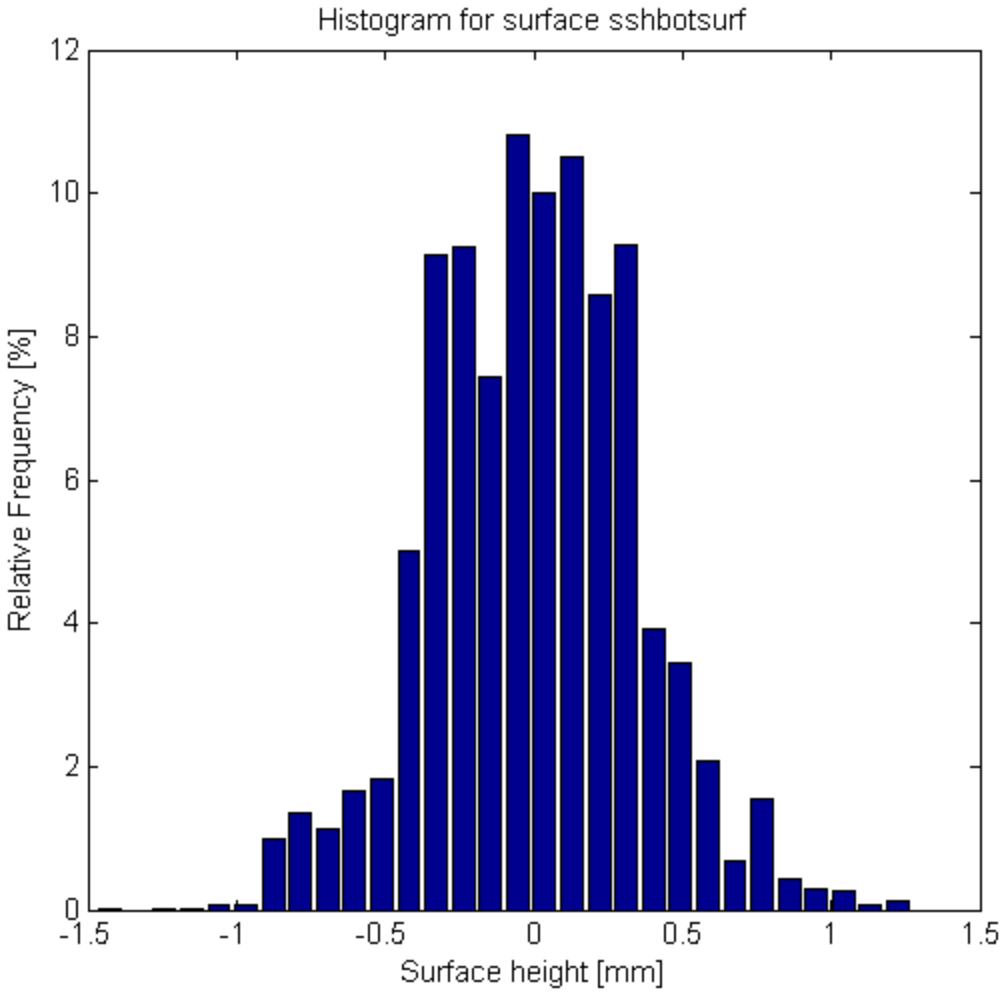

Figure C.32 Surface height frequency distribution for surface sample SSHbotsurf

Appendix E: Fractal Surface Analysis

Figures E.1 to E.16 are the fractal surface analyses for 16 surface samples. The plots consist of fractal analysis using the Roughness-Length method, the First Return Probability method, and the Power Spectral Density method. The Hurst exponent is calculated by fitting a power law to the 'flat' part of each plot. Each plot consists of the arithmetic mean of the fractal analysis applied to each profile transect in the x and y dimensions.

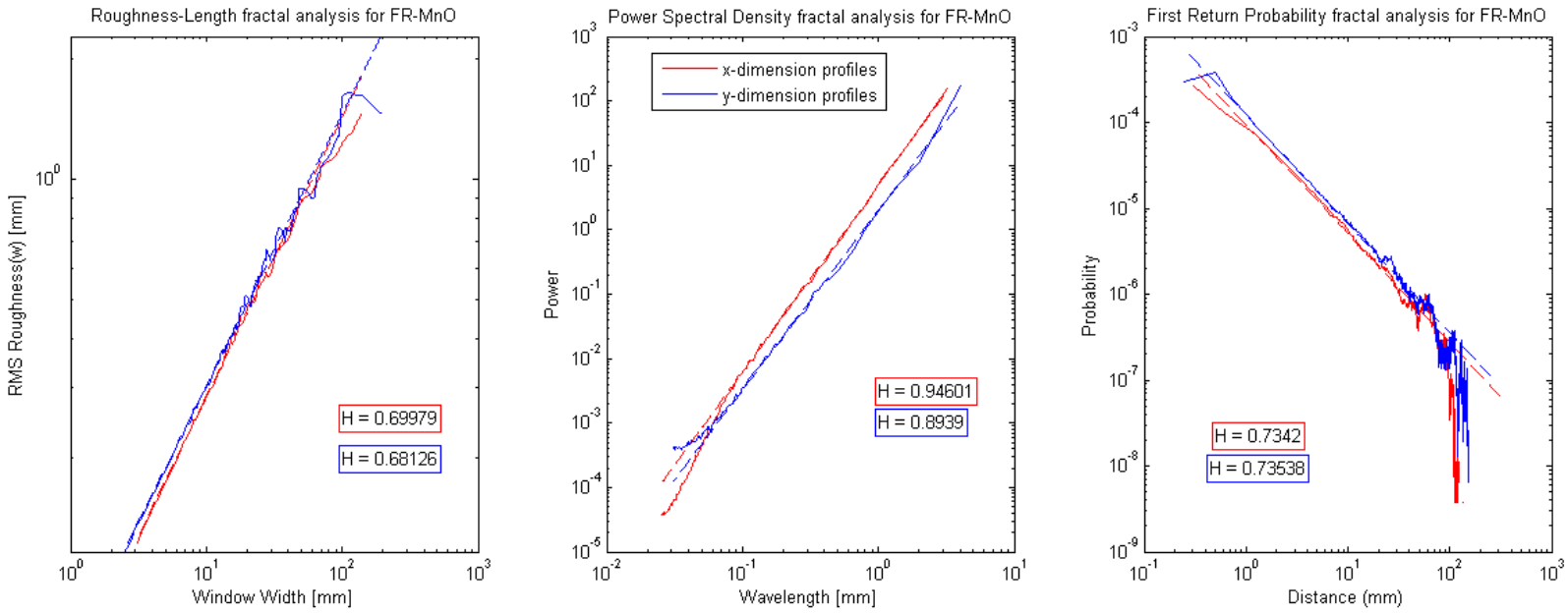

Figure E.1 Fractal surface analysis for sample FR-MnO

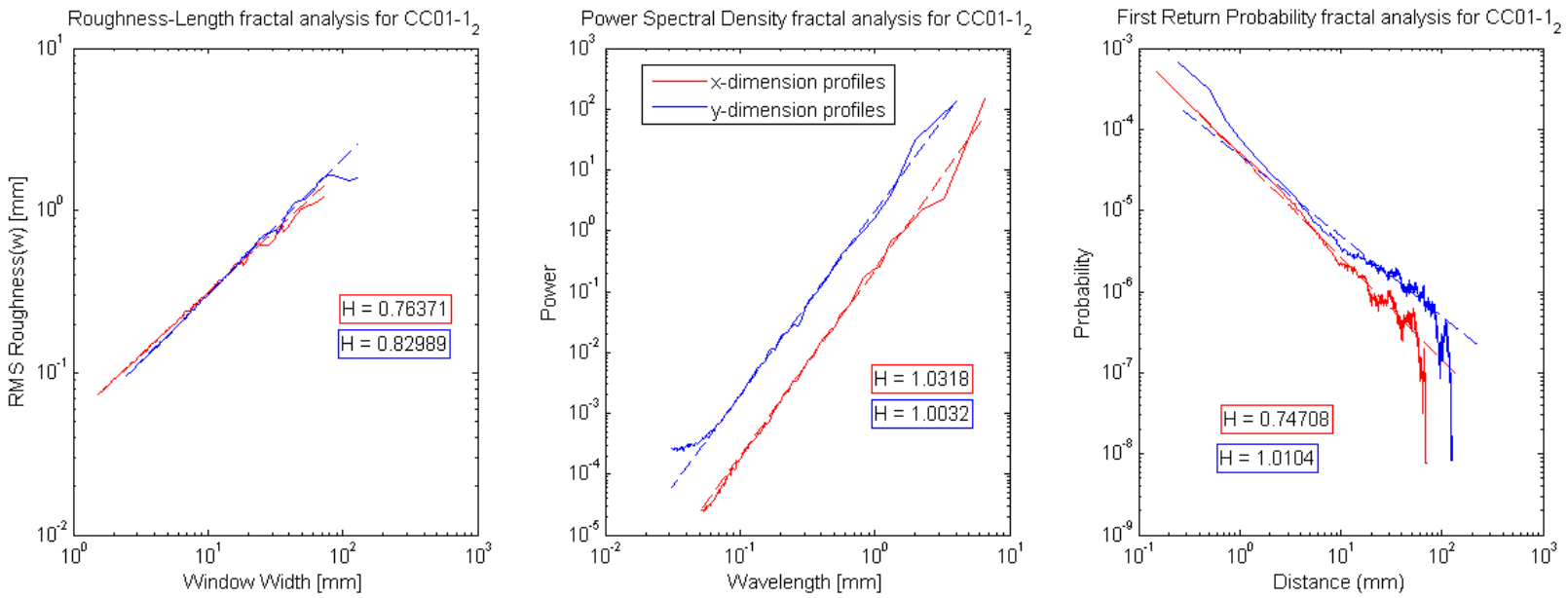

Figure E.2 Fractal surface analysis for sample CC01-1_2

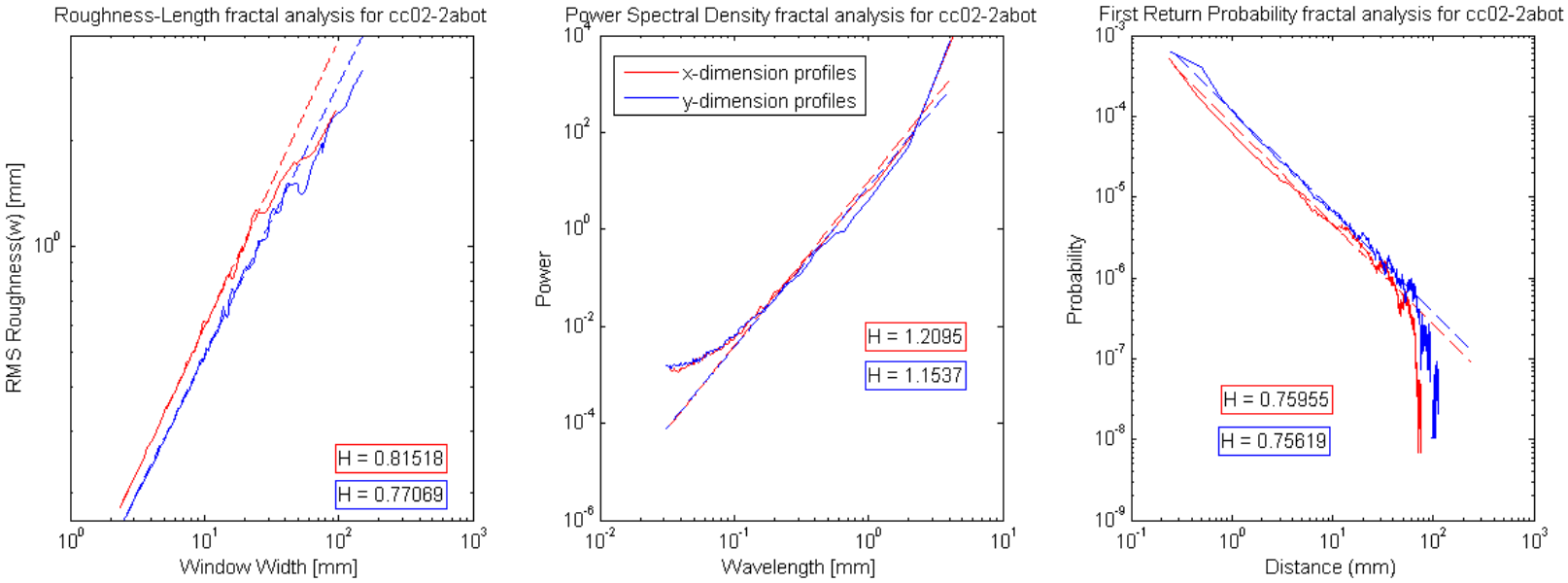

Figure E.3 Fractal surface analysis for sample CC02-2abot

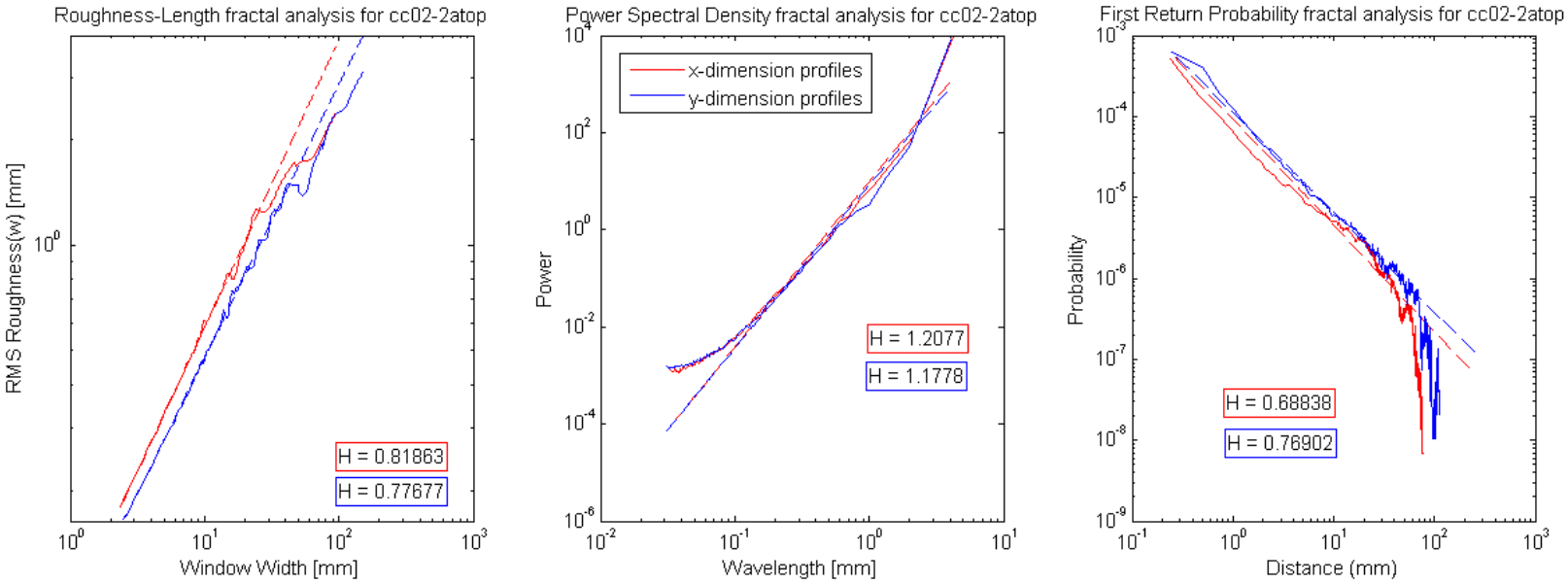

Figure E.4 Fractal surface analysis for sample CC02-2atop

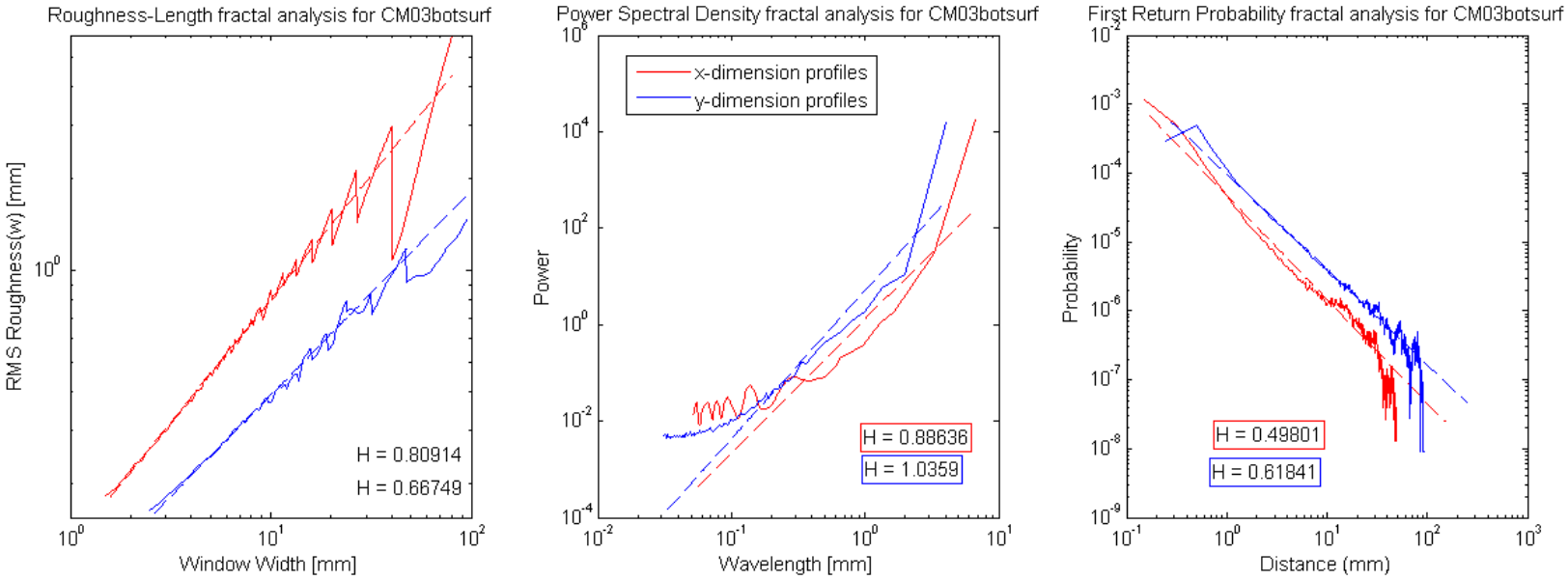

Figure E.5 Fractal surface analysis for sample CM03botsurf

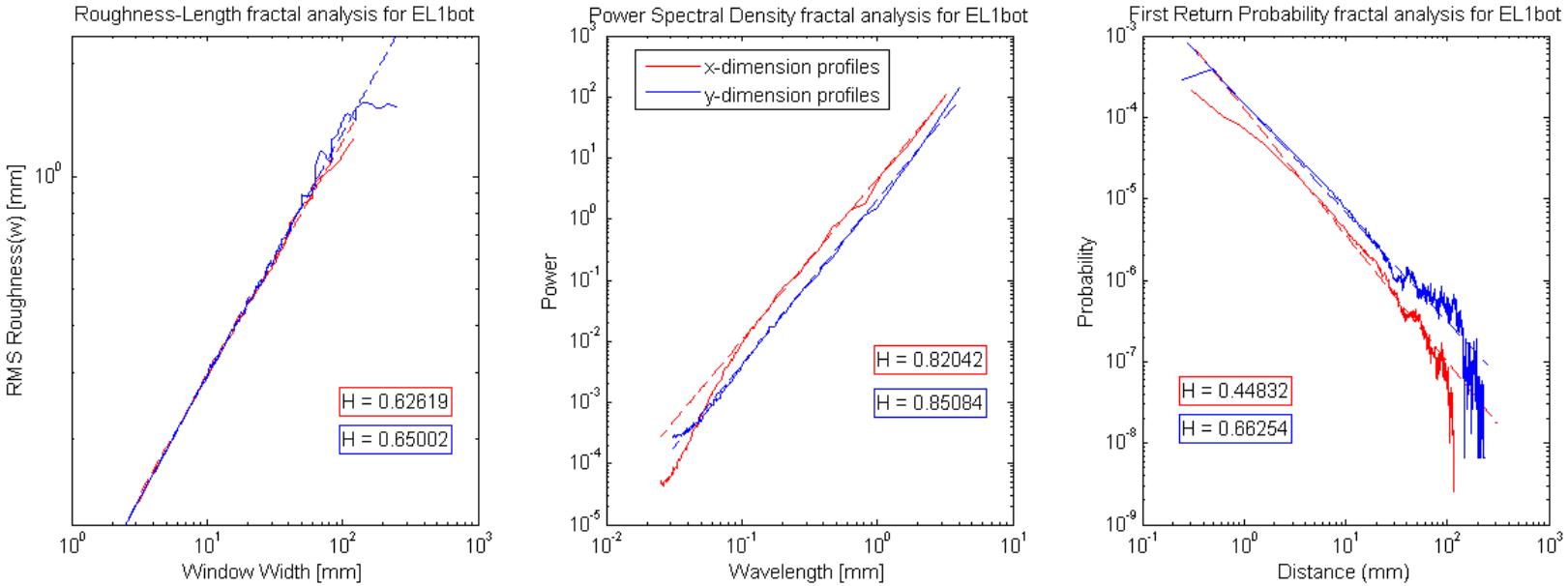

Figure E.6 Fractal surface analysis for sample EL1bot

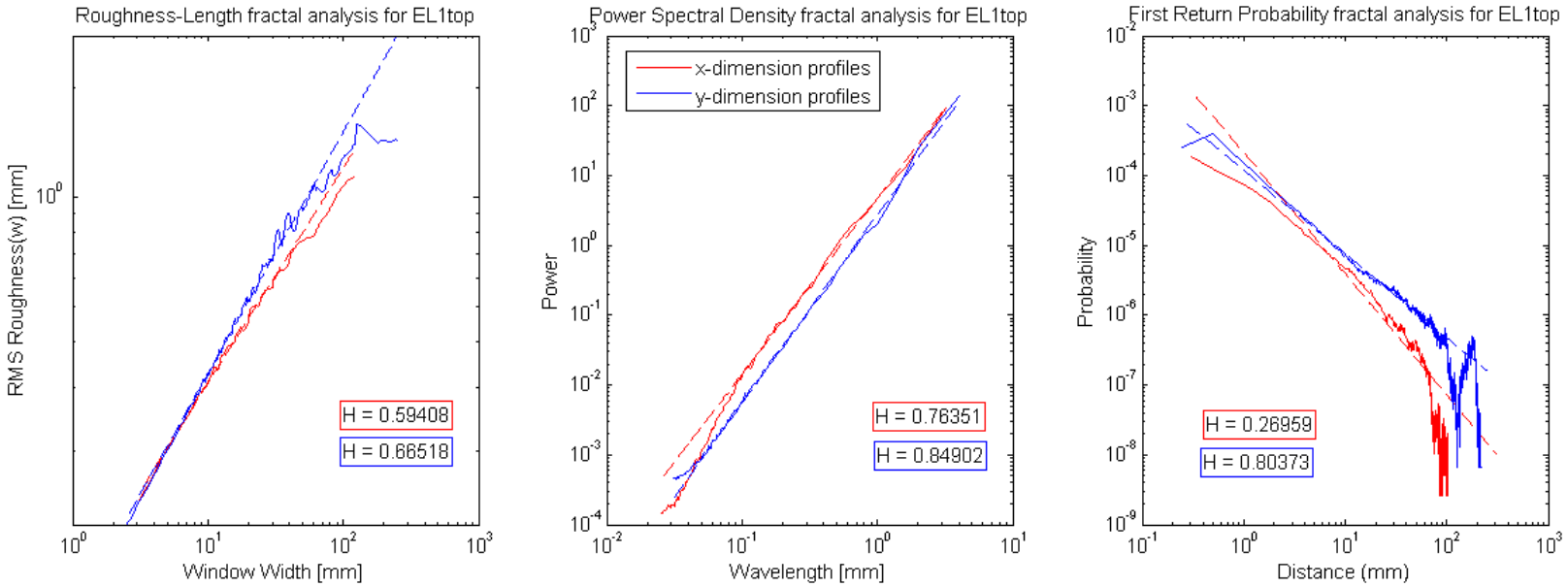

Figure E.7 Fractal surface analysis for sample EL1top

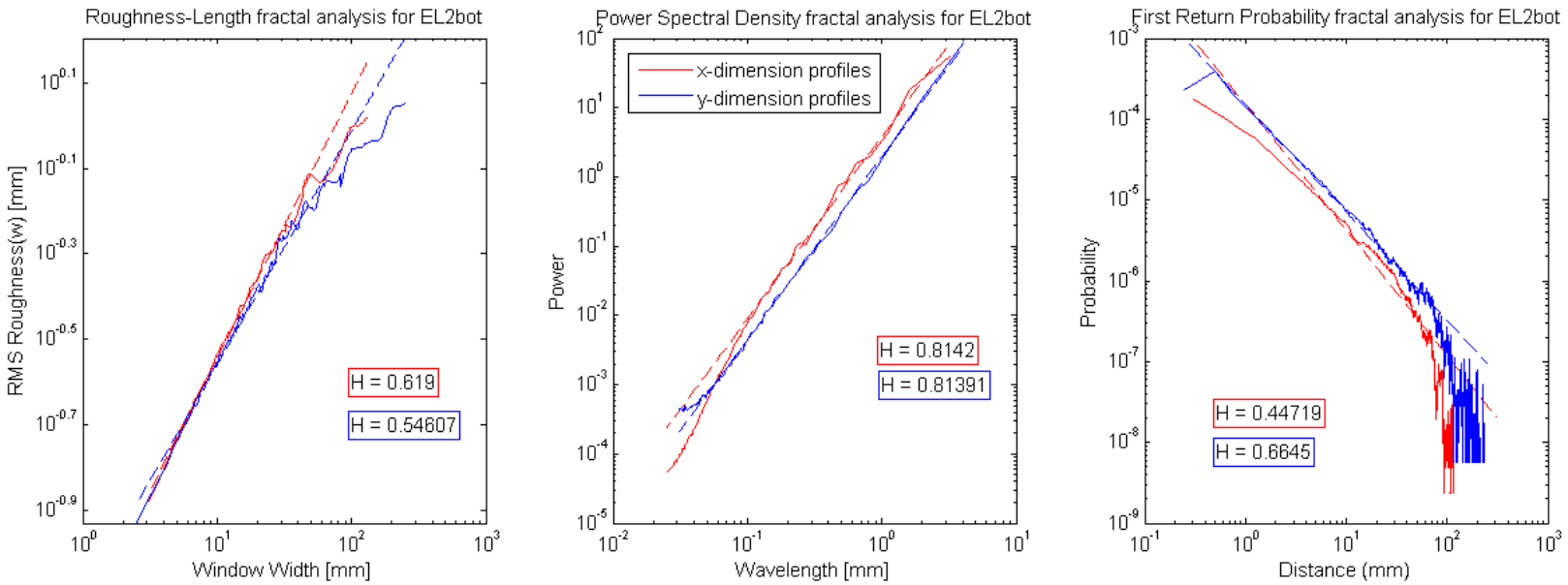

Figure E.8 Fractal surface analysis for sample EL2bot

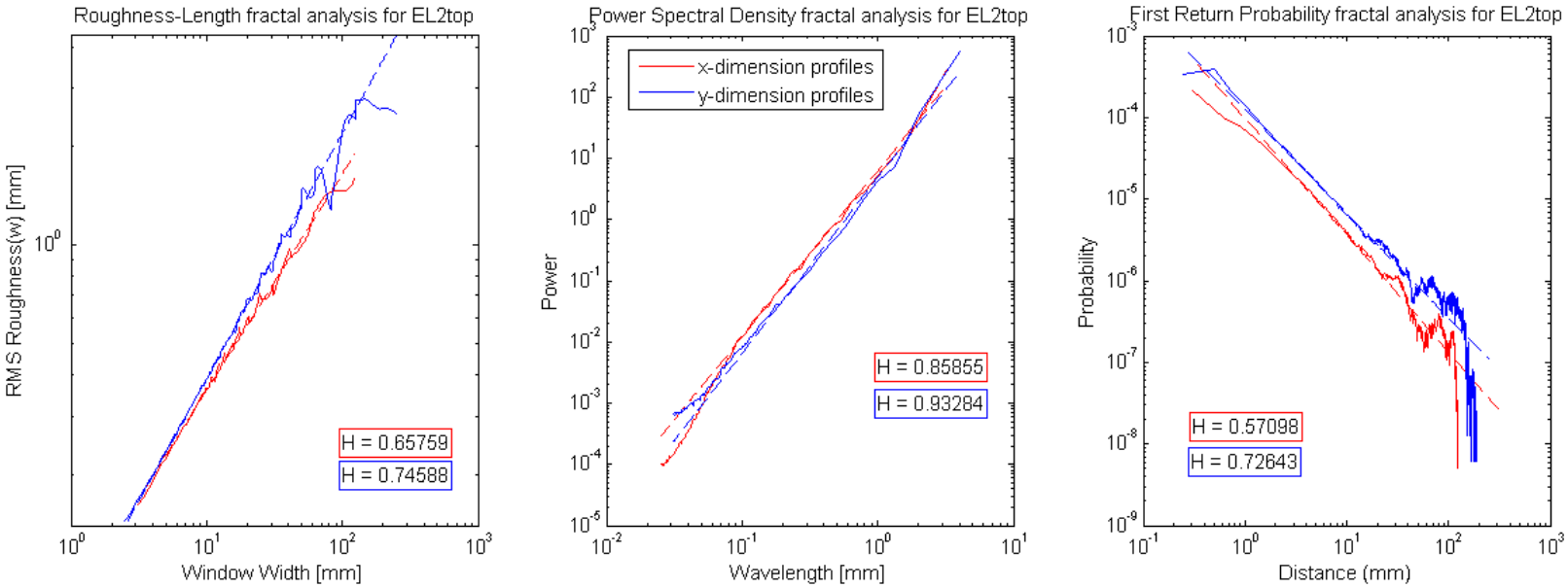

Figure E.9 Fractal surface analysis for sample EL2top

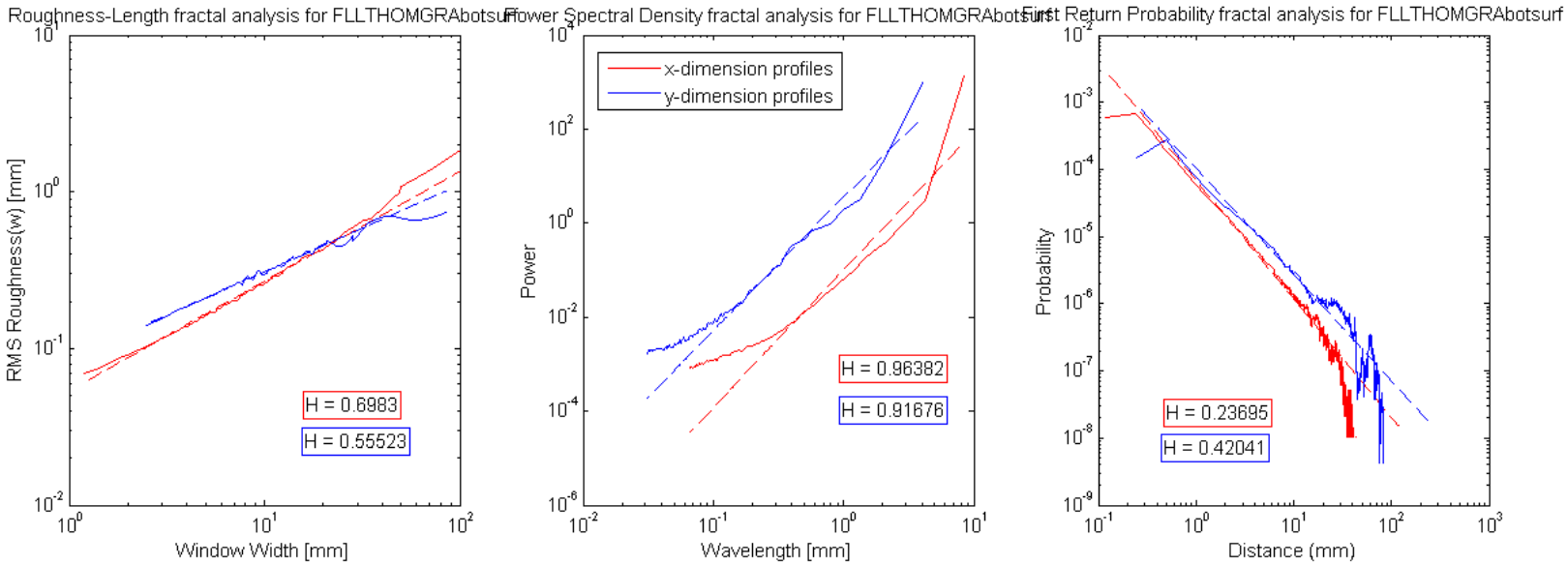

Figure E.10 Fractal surface analysis for sample FLLTHOMGRAbotsurf

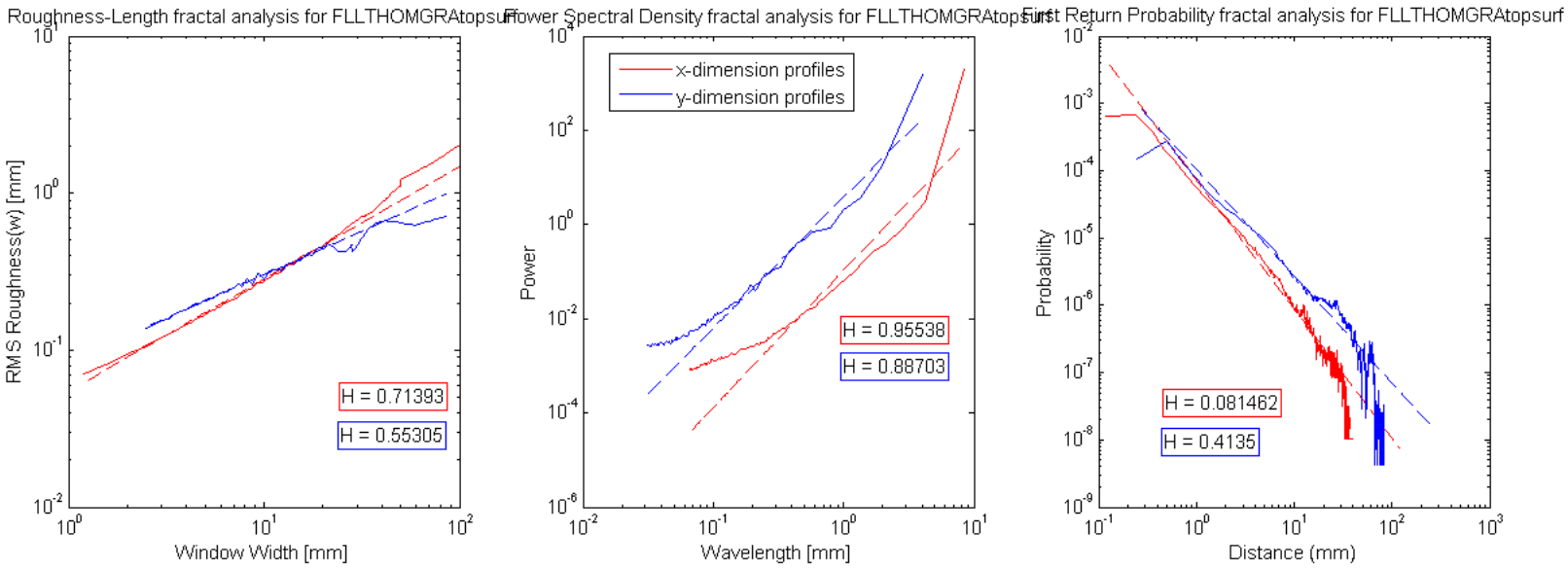

Figure E.11 Fractal surface analysis for sample FLLTHOMGRAtopsurf

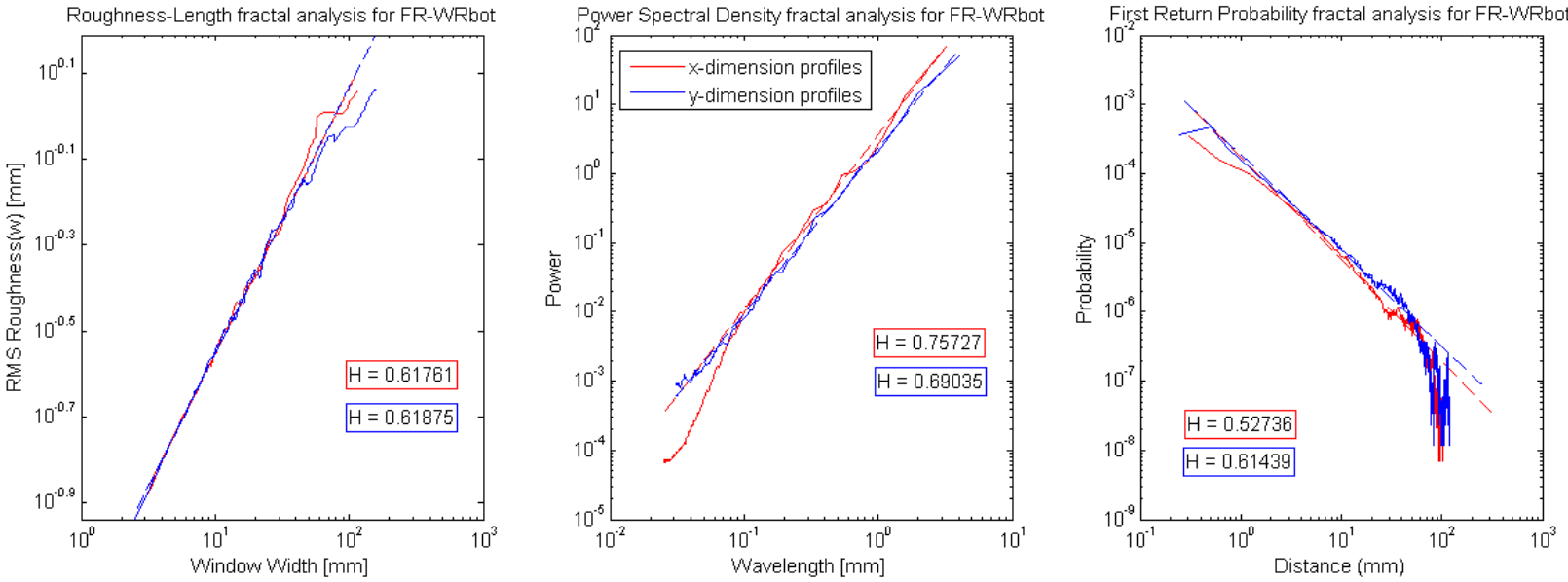

Figure E.12 Fractal surface analysis for sample FR-WRbot

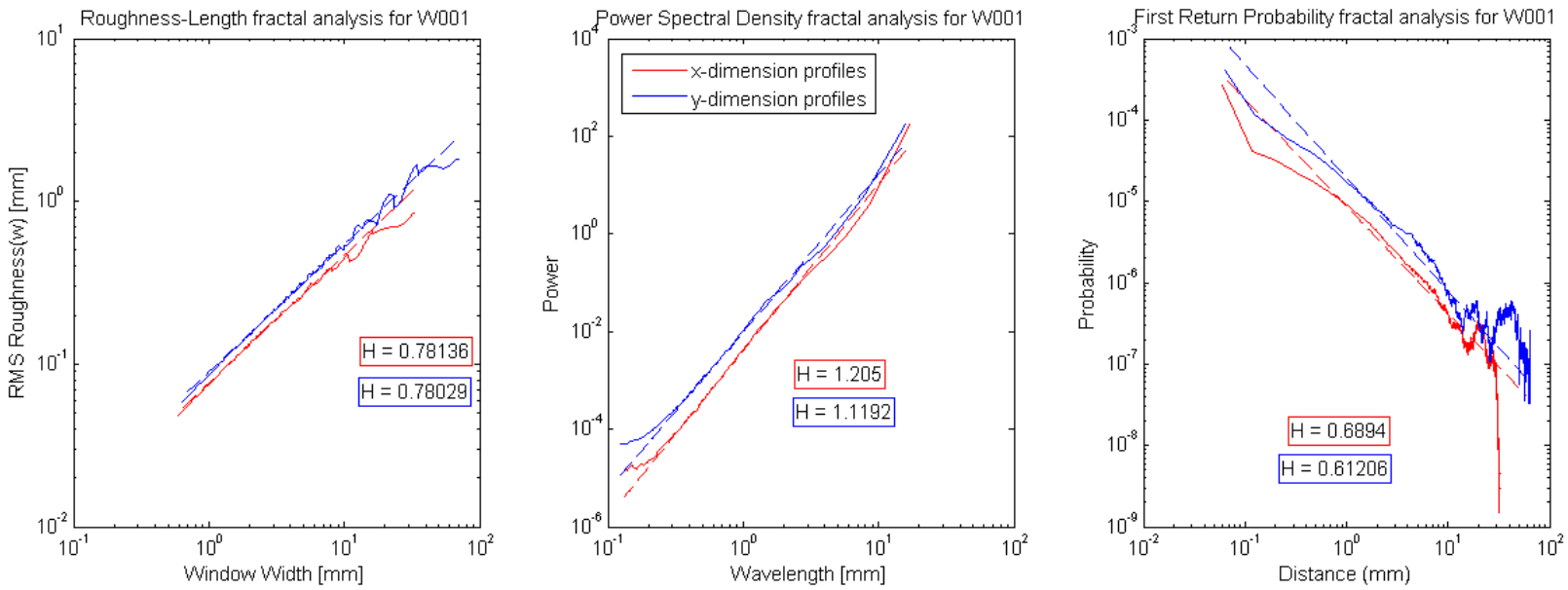

Figure E.13 Fractal surface analysis for sample W001

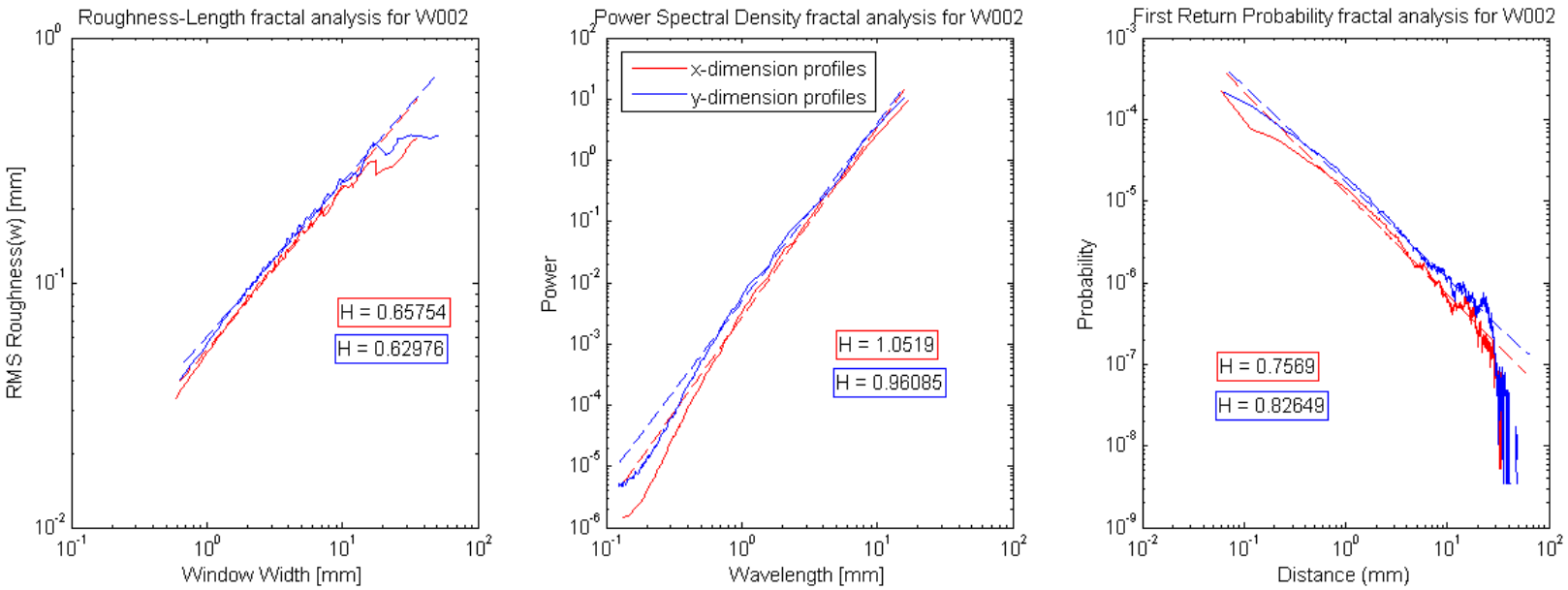

Figure E.14 Fractal surface analysis for sample W002

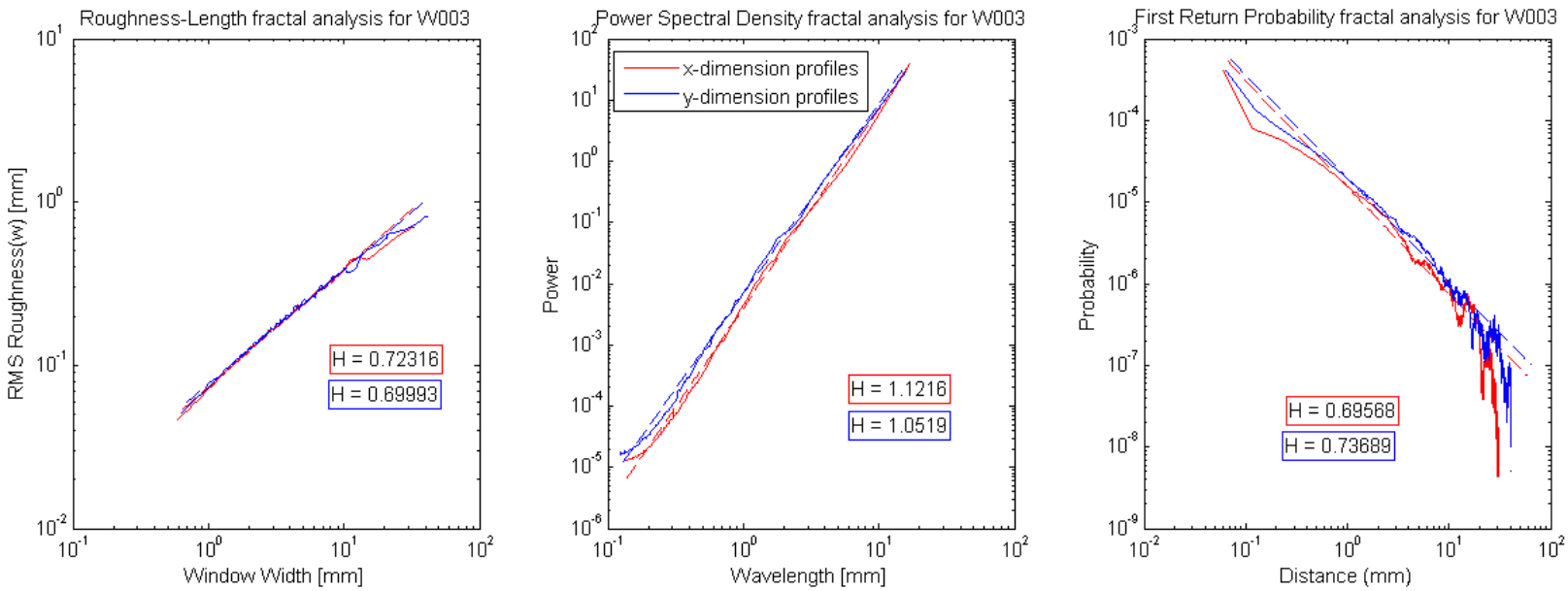

Figure E.15 Fractal surface analysis for sample W003

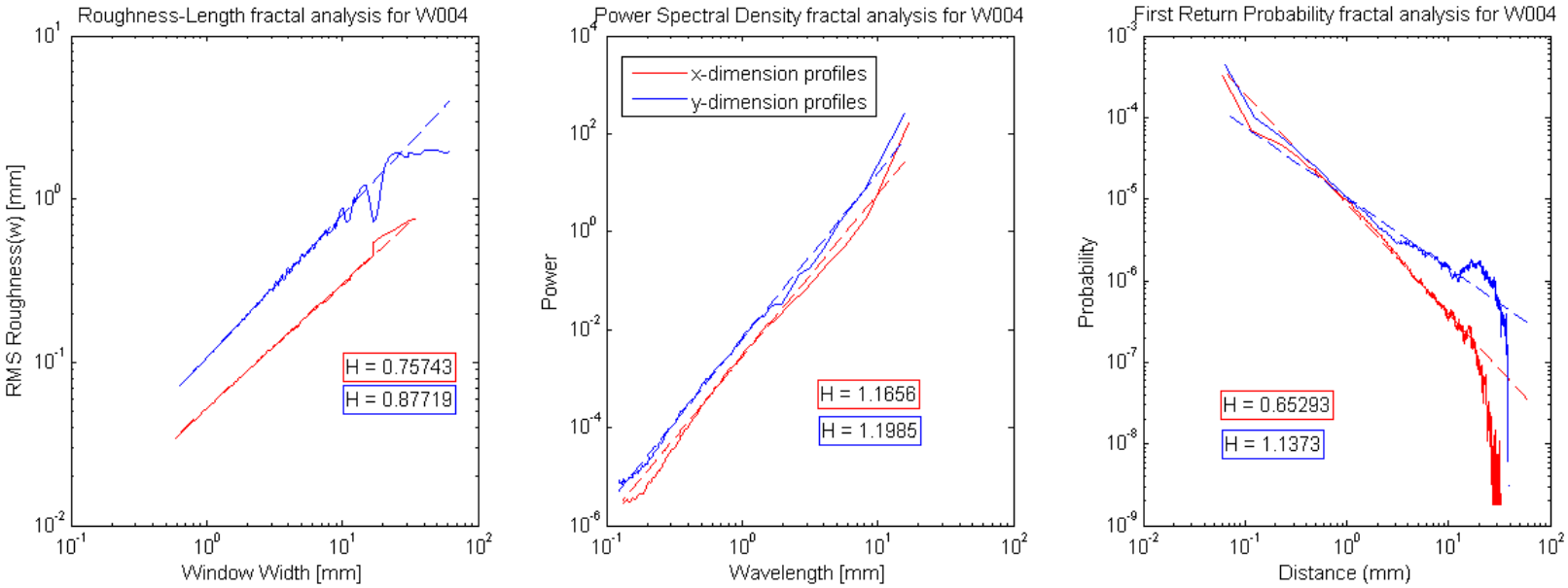

Figure E.16 Fractal surface analysis for sample W004

References

Amitrano, D., and Schmittbuhl, J., 2002, Fracture roughness and gouge distribution of a granite shear band: Journal of Geophysical Research, v. 107, no. B12, p. 2375.

Auradou, H., 2006, Flow channeling in a single fracture induced by shear displacement: Geothermics, v. 35, no. 5-6, p. 588-576.

Barton, N., and de Quadros, E., 1997, Joint Aperture and Roughness in the Prediction of Flow and Groutability of Rock Masses: International Journal of Rock Mechanics and Mining Sciences and Geomechanics Abstracts, v. 34, p. 700.

Boffa, J., Allain, C., and Hulin, J., 1998, Experimental analysis of fracture rugosity in granular and compact rocks: European Physical Journal: Applied Physics, v. 2, no. 3, p. 281-289.

Bouchaud, E., Lapasset, G., and Planès, J., 1990, Fractal Dimension of Fractured Surfaces: A Universal Value?: Europhysics Letters (EPL), v. 13, no. 1, p. 73-79.

Bouchaud, E., 1997, Scaling properties of cracks: Journal of Physics: Condensed Matter, v. 9, no. 21, p. 4319-4344.

Boutt, D.F., Grasselli, G., Fredrich, J.T., Cook, B.K., and Williams, J.R., 2006, Trapping zones: The effect of fracture roughness on the directional anisotropy of fluid flow and colloid transport in a single\line fracture: Geophysical Research Letters, v. 33, p. L21402.

Brown, S., Caprihan, A., and Hardy, R., 1998, Experimental observation of fluid flow channels in a single fracture: Journal of Geophysical Research, v. 103, no. B3, p. PAGES 5125–5132.

Brown, S.R., 1987, Fluid Flow Through Rock Joints: The Effect of Surface Roughness: Journal of Geophysical Research, v. 92, no. B2, p. PAGES 1337–1347.

Brown, S.R., 1995, Simple mathematical model of a rough fracture: Journal of Geophysical Research, v. 100, no. B4, p. 5941–5952.

Brown, S.R., and Scholz, C.H., 1985, Broad Bandwidth Study of the Topography of Natural Rock Surfaces:

Brown, S.R., and Scholz, C.H., 1986, Closure of Rock Joints: Journal of Geophysical

Research, v. 91, no. B5, p. PAGES 4939–4948.

Brush, D.J., and Thomson, N.R., 2003, Fluid flow in synthetic rough-walled fractures: Navier-Stokes, Stokes, and local cubic law simulations: Water Resources Research, v. 39, no. 4, p. 1085.

Cardenas, M.B., Slottke, D.T., Ketcham, R.A., and Sharp, J.M. Jr., 2007, Navier-Stokes flow and transport simulations using real fractures shows heavy tailing due to eddies: Geophysical Research Letters, v. 34, p. L14404.

Chen, Z., Narayan, S.P., Yang, Z., and Rahman, S.S., 2000, An experimental investigation of hydraulic behaviour of fractures and joints in granitic rock: International Journal of Rock Mechanics and Mining Sciences, v. 37, no. 7, p. 1061-1071.

Fu, L., Milliken, K., and Sharp, J.M. Jr., 1994, Porosity and permeability variations in fractured and liesegang-banded Breathitt sandstones (Middle Pennsylvanian), eastern Kentucky; diagenetic controls and implications for modeling dual-porosity systems: Journal of Hydrology, v. 154, no. (1-4), p. p. 351-381.

Fuller, C.M., and Sharp, J.M. Jr., 1992, Permeability and fracture patterns in extrusive volcanic rocks; implications from the welded Santana Tuff, Trans-Pecos Texas: GSA Bulletin, v. 104, no. 11.

Gallant, J., Moore, I., Hutchinson, M., and Gessler, P., 1994, Estimating fractal dimension of profiles: A comparison of methods: Mathematical Geology, v. 26, no. 4, p. 455-481.

Garner, T., Phyu, T., Robinson, N., and Sharp, J.M. Jr., 2007, Sensitivity of fracture skin properties on solute transport and back diffusion in fractured media, *in* Groundwater in Fractured Rocks, Taylor & Francis, London.

Ge, S., 1997, A governing equation for fluid flow in rough fractures: Water Resources Research, v. 33, no. 1, p. PAGES 53–61.

Glover, P.W.J., Matsuki, K., Hikima, R., and Hayashi, K., 1998, Fluid flow in synthetic rough fractures and application to the Hachimantai geothermal hot dry rock test site: Journal of Geophysical Research, v. 103, no. B5, p. 9621–9635.

Gustafson, G., and Krásný, J., 1994, Crystalline Rock Aquifers: Their Occurrence, Use And Importance: Hydrogeology Journal, v. 2, no. 2, p. 64-75.

Hakami, E., and Larsson, E., 1996, Aperture measurements and flow experiments on a

single natural fracture: International Journal of Rock Mechanics and Mining Science & Geomechanics Abstracts, v. 33, no. 4, p. 395-404.

Isakov, E., Ogilvie, S.R., Taylor, C.W., and Glover, P.W.J., 2001, Fluid flow through rough fractures in rocks I: high resolution aperture determinations: Earth and Planetary Science Letters, v. 191, no. 3-4, p. 267-282.

Johnson, J., Brown, S., and Stockman, H., 2006, Fluid flow and mixing in rough-walled fracture intersections: Journal of Geophysical Research, v. 111, p. B12206.

Ketcham, R.A., and Carlson, W.D., 2001, Acquisition, optimization and interpretation of X-ray computed tomographic imagery: applications to the geosciences: Computers & Geosciences, v. 27, no. 4, p. 381-400.

Ketcham, R.A., Slottke, D.T., and Sharp, J.M. Jr., 2010, Three-dimensional measurement of fractures in heterogeneous materials using high-resolution X-ray computed tomography: Geosphere, v. 6, no. 5, p. 499-514.

Konzuk, J.S., and Kueper, B.H., 2004, Evaluation of cubic law based models describing single-phase flow through a rough-walled fracture: Water Resources Research, v. 40, p. W02402.

Krásný, J., and Sharp, J.M. Jr., 2007, Hydrogeology of fractured rocks from particular fractures to regional approaches: State-of-the-art and future challenges, *in* Groundwater in Fractured Rocks, Selected Papers on Hydrogeology, London.

Kreisel, I., 1996, Fracture skins and their effect on solute transport in a fractured porous medium, with examples from the Brushy Canyon Formation in West Texas: Unpublished Master's Thesis, The University of Texas at Austin.

Kumar, S., and Bodvarsson, G.S., 1990, Fractal study and simulation of fracture roughness: Geophysical Research Letters, v. 17, no. 6, p. PAGES 701–704.

Lanaro, F., 2000, A random field model for surface roughness and aperture of rock fractures: International Journal of Rock Mechanics and Mining Sciences, v. 37, no. 8, p. 1195-1210.

Lee, H.S., and Cho, T.F., 2002, Hydraulic Characteristics of Rough Fractures in Linear Flow under Normal and Shear Load: Rock Mechanics and Rock Engineering, v. 35, no. 4, p. 299-318.

Lomize, G.M., 1951, Flow in Fractured Rocks: Gosenergoizdat, Moscow.

Louis, C., 1969, A study of groundwater flow in jointed rock and its influence on the stability of rock masses: Imperial College, London.

Malinverno, A., 1990, A simple method to estimate the fractal dimension of a self-affine series: Geophysical Research Letters, v. 17, no. 11, p. PAGES 1953–1956.

Mandelbrot, B.B., 1977, The Fractal Geometry of Nature: Freeman, New York.

Marrett, R., Ortega, O.J., and Kelsey, C.M., 1999, Extent of power-law scaling for natural fractures in rock: Geology, v. 27, no. 9, p. 799 -802.

McKay, L.D., Gillham, R.W., and Cherry, J.A., 1993, Field experiments in a fractured clay till: 2. Solute and colloid transport: Water Resources Research, v. 29, no. 12, p. PP. 3879-3890.

Méheust, Y., and Schmittbuhl, J., 2000, Flow Enhancement of a Rough Fracture: Geophysical Research Letters, v. 27, no. 18, p. 2989–2992.

Méheust, Y., and Schmittbuhl, J., 2003, Scale Effects Related to Flow in Rough Fractures: Pure and Applied Geophysics, v. 160, no. 5, p. 1023-1050.

Moench, A.F., 1984, Double-Porosity Models for a Fissured Groundwater Reservoir With Fracture Skin: Water Resources Research, v. 20, no. 7, p. PP. 831-846.

Mourzenko, V., Thovert, J., and Adler, P., 1995, Permeability of a Single Fracture; Validity of the Reynolds Equation: Journal de Physique II, v. 5, no. 3, p. 18 pages.

Neuzil, C.E., and Tracy, J.V., 1981, Flow Through Fractures: Water Resources Research, v. 17, no. 1, p. PAGES 191–199.

Nicholl, M.J., Rajaram, H., Glass, R.J., and Detwiler, R., 1999, Saturated Flow in a Single Fracture: Evaluation of the Reynolds Equation in Measured Aperture Fields: Water Resources Research, v. 35, no. 11, p. PAGES 3361–3373.

Odling, N.E., 1994, Natural fracture profiles, fractal dimension and joint roughness coefficients: Rock Mechanics and Rock Engineering, v. 27, no. 3, p. 135-153.

Oron, A.P., and Berkowitz, B., 1998, Flow in rock fractures: The local cubic law assumption reexamined: Water Resources Research, v. 34, p. 2811-2826.

Plouraboué, F., Kurowski, P., Boffa, J., Hulin, J., and Roux, S., 2000, Experimental study of the transport properties of rough self-affine fractures: Journal of Contaminant Hydrology, v. 46, no. 3-4, p. 295-318.

Power, W.L., and Tullis, T.E., 1991, Euclidean and Fractal Models for the Description of Rock Surface Roughness: Journal of Geophysical Research, v. 96, no. B1, p. PAGES 415–424.

Renshaw, C.E., 1995, On the relationship between mechanical and hydraulic apertures in rough-walled fractures: Journal of Geophysical Research, v. 100, no. B12, p. 636.

Robertson, W., 2006, Characterization of Fracture Roughness Using Computed Tomography: Unpublished Undergraduate Thesis, The University of Texas at Austin.

Robinson, N.I., Sharp, J.M. Jr., and Kreisel, I., 1998, Contaminant transport in sets of parallel finite fractures with fracture skins: Journal of Contaminant Hydrology, v. 31, no. 1-2, p. 83-109.

Sayles, R.S., and Thomas, T.R., 1978, Surface topography as a nonstationary random process: Nature, v. 271, no. 5644, p. 431-434.

Schmittbuhl, J., Steyer, A., Jouniaux, L., and Toussaint, R., 2008, Fracture morphology and viscous transport: International Journal of Rock Mechanics and Mining Sciences, v. 45, no. 3, p. 422-430.

Schmittbuhl, Jean, Jean-Pierre Vilotte, and St?phane Roux. 1995. Reliability of self-affine measurements. *Physical Review E* 51, no. 1 (January 1): 131. doi:10.1103/PhysRevE.51.131.

Sharp, J.M. Jr., 1993, Fractured aquifers/reservoirs; approaches, problems and opportunities: Memoires - Association Internationale des Hydrogeologues = Memoires - International Association of Hydrogeologists, v. 24, p. 23-38.

Sharp, J.M. Jr., Slottke, D.T., and Ketcham, R.A., 2011, Prediction of fracture roughness and other hydraulic properties: Is upscaling possible?: Selected papers, 37th Congress, International Association of Hydrogeologists, v. in press.

Slottke, D.T., 2010, Surface Roughness of Natural rock Fractures: Implications for Prediction of Fluid Flow: Unpublished Doctoral Dissertation, The University of Texas at Austin.

Stout, K.J., 2000, Development of Methods for the Characterisation of Roughness in Three Dimensions (Ultra Precision Technology): Butterworth-Heinemann.

Thomas, T.R., 1999, Rough Surfaces:

Thompson, C., 2005, Investigation of surface roughness of natural rock fractures using high-resolution X-ray computed tomography and laboratory flow test measurements [M.S.]: Univeristy of Texas at Austin.

Thompson, M.E., and Brown, S.R., 1991, The Effect of Anisotropic Surface Roughness on Flow and Transport in Fractures: Journal of Geophysical Research, v. 96, no. B13, p. PAGES 21,923–21,932.

Tsang, Y.W., and Witherspoon, P.A., 1983, The Dependence of Fracture Mechanical and Fluid Flow Properties on Fracture Roughness and Sample Size: Journal of Geophysical Research, v. 88, no. B3, p. 2359–2366.

Witherspoon, P.A., Wang, J.S.Y., Iwai, K., and Gale, J.E., 1980, Validity of Cubic Law for Fluid Flow in a Deformable Rock Fracture: Water Resources Research, v. 16, no. 6, p. 1016–1024.

Zhou, H., and Xie, H., 2003, Direct Estimation of the Fractal Dimensions of a Fracture Surface of Rock.: Surface Review & Letters, v. 10, no. 5, p. 751.

Zimmerman, R.W., Kumar, S., and Bodvarsson, G.S., 1991, Lubrication theory analysis of the permeability of rough-walled fractures: International Journal of Rock Mechanics and Mining Science & Geomechanics Abstracts, v. 28, no. 4, p. 325-331.

Zimmerman, R.W., Al-Yaarubi, A., Pain, C.C., and Grattoni, C.A., 2004, Non-linear regimes of fluid flow in rock fractures: International Journal of Rock Mechanics and Mining Sciences, v. 41, no. Supplement 1, p. 163-169.

Zimmerman, R.W., and Bodvarsson, G.S., 1996, Hydraulic conductivity of rock fractures: Transport in Porous Media, v. 23, no. 1, p. 1-30.

Zolensky, M.E., Sylvester, P.J., and Paces, J.B., 1988, Origin and significance of blue coloration in quartz from Llano Rhyolite (llanite), north-central Llano County, Texas: American Mineralogist, v. 73, no. 3-4, p. 313-323.

Vita

Mishal Adam Mansour Al-Johar grew up in Orange County, California and Sugar Land, Texas. He graduated from Stephen F. Austin High School and completed an undergraduate degree at The University of Texas at Austin. After working as a Staff Geologist at Delta Consultants in Austin, TX, he returned to The University of Texas at Austin to work on characterizing and scaling fracture roughness, following the work of Donald Slottke, Wendy Robertson, and Clark Thompson.

mishal.aljohar@gmail.com

This thesis was typed by the author.